Integration of a nanostructured photothermal interface in photovoltaic-thermoelectric energy devices

Sébastien Hanauer

THÈSE

En vue de l'obtention du
DOCTORAT DE L'UNIVERSITÉ DE TOULOUSE

Délivré par l'Université Toulouse 3 - Paul Sabatier

Présentée et soutenue par

Sébastien HANAUER

Le 16 octobre 2023

Intégration d'une interface photothermique nanostructurée dans des systèmes de cogénération photovoltaïque-thermoélectrique

---

Ecole doctorale : **GEETS - Génie Electrique Electronique,Télécommunications et Santé : du système au nanosystème**

Spécialité : **Photonique et Systèmes Optoélectroniques**

Unité de recherche :
LAAS - Laboratoire d'Analyse et d'Architecture des Systèmes

Thèse dirigée par
Inès REVOL et Alexandre Dmitriev

Jury

M. Rodolphe VAILLON, Rapporteur
Mme Zhuoying CHEN, Rapporteure
M. Arnaud ARBOUET, Examinateur
M. Soufiane EL OUALID, Examinateur
Mme Inès REVOL, Co-directrice de thèse
M. Alexandre DMITRIEV, Co-directeur de thèse

Integration of a nanostructured photothermal interface in photovoltaic-thermoelectric energy devices

Abstract

As the conversion efficiencies of industrially mature photovoltaic technologies continue to increase, they are approaching the theoretical limit of 33 % for single-junction solar cells. In practice, up to 50 % of the incident solar energy is still lost or dissipated as heat within the photovoltaic (PV) cell. An innovative approach to recover this lost energy and ultimately surpass the efficiency limit of the single-junction cell is to combine the solar cell with a thermoelectric generator (TEG), a device capable of converting heat flux into energy. However, the energy conversion efficiency of these photovoltaic-thermoelectric (PV-TE) systems remains currently limited.

To demonstrate a breakthrough in the efficiency of PV-TE systems, we propose a new approach based on the integration of a nanostructured photothermal interface between the solar cell and the thermoelectric generator. This interface is meant to absorb the energy of infrared photons transmitted through the solar cell and convert it into thermal energy to increase the electrical power produced by the thermoelectric generator. The objective of this thesis is to design a photothermal interface made of thermoplasmonic nanoantennas for solar infrared absorption and to study the impact of its integration on the performance of a PV-TE device.

The first part of this thesis focuses on the design and fabrication of isolated nanoantennas. Numerical simulations are used to calculate the optical properties of nanoantennas with different shapes, dimensions, and compositions, in order to identify the optimal structures for solar infrared absorption. Nanofabrication techniques are employed to realize these structures, and their topography is then characterized to assess the impact of manufacturing defects on their optical properties.

The second part of the thesis concentrates on the experimental realization of photothermal interfaces. Samples covered with nanoantennas are fabricated using colloidal lithography to demonstrate the heating resulting from an ensemble of interacting particles. The temperature of these interfaces under solar infrared illumination is measured using an infrared camera. The influence of the substrate and encapsulation layer on the photothermal properties of the interfaces is also discussed.

At last, the development of a multiphysics model of a PV-TE system incorporating a nanostructured photothermal interface is presented. This numerical tool allows to simulate the coupling of optical, thermal, and electrical phenomena occurring within a PV-TE device. In particular, it is used to calculate the heating of isolated photothermal interfaces under solar illumination, which is compared to the experimental results measured in the previous part. Finally, this model, validated by comparison to the literature, will be used to calculate the impact of the integration of a photothermal interface on the electrical power generated by a PV-TE device.

Intégration d'une interface photothermique nanostructurée dans des systèmes de cogénération photovoltaïque-thermoélectrique

Résumé

Alors que les rendements de conversion des filières photovoltaïques continuent d'augmenter, ils se rapprochent de la limite théorique de 33 % pour une cellule solaire à simple jonction. En pratique, jusqu'à 50 % de l'énergie solaire incidente est encore perdue ou dissipée sous forme de chaleur dans la cellule photovoltaïque (PV). Une approche originale pour récupérer cette énergie perdue, et ainsi dépasser le rendement de conversion limite de la cellule à simple jonction, consiste à combiner la cellule solaire avec un générateur thermoélectrique (TEG), un dispositif capable de convertir un flux de chaleur en énergie. Cependant, le rendement de conversion énergétique de ces systèmes de cogénération photovoltaïque-thermoélectrique (PV-TE) reste actuellement limité.

Afin de démontrer une rupture dans l'efficacité du système PV-TE, nous proposons une nouvelle approche basée sur l'intégration d'une interface photothermique nanostructurée entre la cellule solaire et le générateur thermoélectrique. Cette interface est destinée à absorber l'énergie des photons infrarouges transmis à travers la cellule solaire et à la convertir en énergie thermique pour augmenter la puissance électrique produite par le générateur thermoélectrique. L'objectif de cette thèse est de concevoir une interface photothermique à base de nanoantennes thermoplasmoniques pour l'absorption infrarouge solaire, et d'étudier l'impact de son intégration sur les performances d'un système PV-TE.

La première partie de cette thèse porte sur la conception et fabrication de nanoantennes isolées. Des simulations numériques sont utilisées pour calculer les propriétés optiques de nanoantennes de différentes formes, dimensions et compositions, afin d'identifier les structures optimales pour l'absorption infrarouge solaire. Des techniques de nanofabrication sont employées pour réaliser ces structures, dont la topographie est ensuite caractérisée afin d'analyser l'impact des défauts de fabrication sur leurs propriétés optiques.

La deuxième partie de la thèse se concentre sur la réalisation expérimentale d'interfaces photothermiques. Des échantillons recouverts de nanoantennes sont fabriqués par lithographie colloïdale, afin de démontrer l'échauffement résultant d'un ensemble de particules en interaction. La température de ces interfaces sous illumination infrarouge solaire est mesurée à l'aide d'une caméra infrarouge. L'impact du substrat et de la couche d'encapsulation sur les propriétés photothermiques des interfaces est également discuté.

Enfin, le développement d'un modèle multiphysique de système PV-TE intégrant une interface photothermique nanostructurée est présenté. Cet outil numérique permet de simuler le couplage des phénomènes optiques, thermiques et électriques ayant lieu dans un dispositif PV-TE. Il est notamment utilisé pour calculer l'échauffement d'interfaces isolées sous illumination solaire, pour comparaison aux résultats expérimentaux de la partie précédente. Finalement, ce modèle, validé par comparaison à la littérature, sera utilisé pour calculer l'impact de l'intégration d'une interface photothermique sur la puissance électrique générée par un dispositif PV-TE.

List of Publications and Communications

International peer reviewed journals

- S. Hanauer, I. Massiot, A. Mlayah, F. Carcenac, J.-B. Doucet, S. Beldjoudi, I. Faniayeu, A. Dmitriev, "Photothermal Conversion of Solar Infrared Radiation by Plasmonic Nanoantennas for Photovoltaic-Thermoelectric Hybrid Devices", *ACS Applied Energy Materials*, 2023, *10.1021/acsaem.2c03724*.
- S. Hanauer et al., "Multiphysics modelling tool for hybrid photovoltaic-thermoelectric devices integrating a photothermal interface", Article in preparation.

International conferences

- S. Hanauer, I. Massiot, A. Mlayah, S. Beldjoudi, F. Carcenac, J.-B. Doucet, E. Daran, I. Faniayeu, A. Dmitriev, "Harvesting of infrared solar energy by thermoplasmonic nanoantenna for enhanced photovoltaic-thermoelectric systems". Poster presentation at *META 2022 - Metamaterials, Photonic Crystals and Plasmonics*, Torremolinos, Spain *Jul.* 2022.
`https://hal.laas.fr/hal-03756637`
- S. Hanauer, A. Mlayah, F. Carcenac, J.-B. Doucet, E. Daran, A. Dmitriev, I. Massiot, "Harvesting of IR solar energy by thermoplasmonic nanoantennas". Poster presentation at *PEP21 - Summer School on Photothermal Effects in Plasmonics*, Porquerolles, *Oct.* 2021.
`https://hal.laas.fr/hal-03627756`

National conferences

- S. Hanauer, I. Massiot, A. Mlayah, F. Carcenac, J.-B. Doucet, S. Beldjoudi, I. Faniayeu, A. Dmitriev, "Conception et intégration d'une interface photothermique nanostructurée au sein de dispositifs de cogénération photovoltaïque-thermoélectrique". Oral presentation at *JNRSE 2023 - Journées Nationales sur la Récupération et le Stockage de l'Energie*, Paris, *Jun.* 2023.
`https://hal.science/hal-04127933`
- S. Hanauer, I. Massiot, A. Mlayah, F. Carcenac, J.-B. Doucet, S. Beldjoudi, I. Faniayeu, A. Dmitriev, Interface photothermique à base de nanoantennes thermoplasmoniques pour la récupération d'énergie infrarouge solaire au sein de dispositifs hybrides photovoltaïquesthermoélectriques". Oral presentation at *Journées Plénières du Groupe de Recherche NAME (NAnoMaterials for Energy applications)*, Lyon, *Oct.* 2022.
`https://hal.science/hal-04128261`
- S. Hanauer, A. Mlayah, F. Carcenac, J.-B. Doucet, E. Daran, I. Faniayeu, A. Dmitriev, I. Massiot, "Interface photothermique à base de nano-antennes thermoplasmoniques pour la cogénération photovoltaïque-thermoélectrique". Oral presentation at *OPTIQUE Conference*, Nice, *Jul.* 2022.
`https://hal.science/hal-03756678`

Remerciements

Au terme de ce voyage, je tiens à exprimer ma profonde gratitude envers toutes les personnes qui ont contribué de près ou de loin à la réalisation de cette thèse de doctorat. Leurs conseils éclairés, leur soutien indéfectible et leur engagement ont été des piliers essentiels dans la concrétisation de ce travail de recherche.

En premier lieu, je souhaite exprimer ma reconnaissance envers mes directeurs de thèse, Inès Revol et Alexandre Dmitriev, dont l'encadrement, la disponibilité et la passion pour la recherche ont été des sources inestimables d'inspiration tout au long de cette aventure scientifique.

Je tiens également à remercier chaleureusement Rodolphe Vaillon et Zhuoying Chen d'avoir accepté de consacrer leur temps et leur expertise en tant que rapporteurs de ma thèse. Leurs remarques constructives et leurs éclairages ont grandement enrichi ce travail.

Un merci particulier à Arnaud Arbouet et Soufiane El Oualid qui ont accepté de jouer le rôle d'examinateurs. Leurs précieuses suggestions et leur intérêt pour mes recherches ont été des éléments cruciaux dans l'élaboration de ce manuscrit.

Adnen Mlayah mérite une reconnaissance spéciale pour son aide inlassable tout au long de cette thèse, ainsi que pour sa participation active à l'encadrement. Sa collaboration a été un atout majeur dans la progression de mes travaux.

Je souhaite exprimer ma gratitude envers Franck Carcenac et Jean-Baptiste Doucet pour leur soutien dans le domaine de la fabrication en salle blanche. Leur expertise a grandement contribué à la qualité et à la rigueur des expérimentations réalisées.

Un sincère remerciement à Ihar Faniayeu et Rafael Cichelero pour leur accueil chaleureux et leur précieuse assistance à l'université de Göteborg. Leur collaboration a enrichi mes perspectives de recherche et a permis des échanges fructueux.

Enfin, une mention spéciale à Sélyan Beldjoudi et Ali Msahazi Ahamada, les deux stagiaires de master que j'ai eu la chance d'encadrer. Leur engagement, leur curiosité intellectuelle et leur contribution ont été des éléments clés dans la réalisation de certaines parties de ce travail.

Je souhaite également remercier les membres de l'équipe PHOTO pour leurs conseils avisés, les discussions informelles qui m'ont permis de prendre du recul sur mon sujet, et les séances de jeux bien utiles à la décontraction.

Un immense merci à mes amis et à ma famille pour leur soutien indéfectible et leurs encouragements pendant cette période.

En conclusion, ma gratitude va à tous ceux qui ont contribué, de près ou de loin, à la réussite de cette thèse. Leurs efforts conjugués ont façonné ce travail et ont contribué à son aboutissement. Merci infiniment.

List of Acronyms

AFM Atomic Force Microscopy

AR Aspect Ratio

AZO Aluminum-doped Zinc Oxide

CIGS Copper Indium Gallium Selenide

DDA Discrete Dipole Approximation

DSSC Dye-Sensitized Solar Cell

EBL Electron-Beam Lithography

EVA Ethylene Vinyl Acetate

FFT Fast Fourier Transform

FPA Focal Plane Array

FT Fourier Transform

FTIR Fourier Transform Infrared

HCL Hole-mask Colloidal Lithography

IBM Intermediate Band Material

IPA Isopropyl Alcohol

IR Infrared

LED Light-Emitting Diode

LSP Localized Surface Plasmon

LSPR Localized Surface Plasmon Resonance

MIBK Methyl Isobutyl Ketone

NA Nanoantenna

NIL Nanoimprint Lithography

PDMS Polydimethylsiloxane

PERC Passivated Emitter and Rear-Contact

PMMA Poly(Methyl Methacrylate)

PS Polystyrene

PTI Photothermal Interface

PV Photovoltaic

PV-TE Photovoltaic-Thermoelectric

PVC Photovoltaic Cell

PVD Physical Vapor Deposition

SEM Scanning Electron Microscopy

SPP Surface Plasmon Polariton

SSA Solar Selective Absorber

TEG Thermoelectric Generator

UV Ultraviolet

Contents

General Introduction

As the global energy demand is rising, the pursuit of self-sustaining energy systems is of paramount importance. A compelling strategy involves harnessing ambient energy sources, with solar energy standing as the most abundant and readily available. Solar photovoltaics (PV) has emerged as a cornerstone of electricity generation due to its cost-effectiveness (0.2 $/W in 2020 for silicon modules [1]). However, the conversion efficiency of solar cells is inherently limited by intrinsic losses (record efficiency for silicon solar cell: 26.7 % [2]), which necessitates innovative approaches to optimize their performance.

The efficiency of single-junction PV cells is impeded by two primary sources of losses: the thermalization of high-energy photons, which leads to temperature elevation and reduction of the overall efficiency, and the lack of absorption of low-energy photons. Addressing these challenges has stimulated diverse strategies aimed at enhancing the utilization of solar spectrum by PV cells, including the development of multi-junction architectures.

A novel strategy that has recently been explored for augmenting the efficiency of single-junction solar cells involves combining photovoltaic conversion with thermoelectric generation. While experimental photovoltaic-thermoelectric (PV-TE) systems have demonstrated increased power generation as compared to standalone PV cells, the potential efficiency gains remain low, largely due to the limited conversion efficiency of thermoelectric generators (TEGs), typically below 8 % at ambient temperatures.

Surprisingly, the pivotal role of the interface connecting the PV cell and the TEG has been relatively overlooked until recently. This interface can be tailored to facilitate efficient heat extraction from the solar cell towards the TEG. Furthermore, introducing a photothermal conversion layer capable of absorbing solar infrared radiation and transforming it into heat offers a way to enhance the TEG's power output through controlled heating of the contact interface. Although a handful of studies have explored photothermal interfaces in PV-TE systems, none have addressed the specific spectral design of such interfaces to optimally match the solar infrared spectrum for efficient light harvesting.

In light of these gaps in research, this thesis proposes the conceptualization of a photothermal interface made of thermoplasmonic nanoantennas for integration in PV-TE cogeneration system, as represented in Figure 1. The overall objective is to investigate the impact of integrating such an interface within a PV-TE system, with

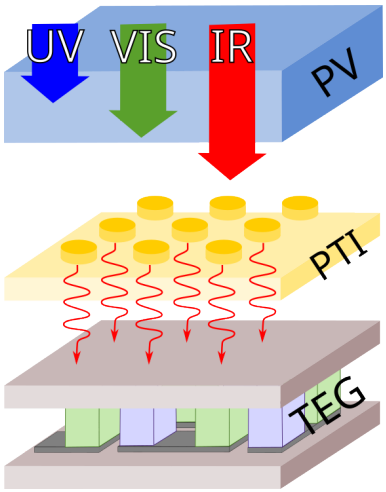

Figure 1: Schematics of a hybrid photovoltaic-thermoelectric device, including a nanostructured photothermal interface to convert solar infrared radiation into heat. In the actual device, the three components are in physical contact. Reprinted with permission from ACS Appl. Energy Mater. 2023, 6, 4, 2128–2133. Copyright 2023 American Chemical Society.

a focus on its influence on system performance. The use of nanoantennas offers a unique path to tailor the absorption spectrum of the interface to match with the solar spectrum transmitted through the PV cell. It simultaneously allows to reduce the thickness of the interface, which in turn translates to reduced thermal resistance between the PV cell and the TEG.

The difficulties with this strategy lie in creating an efficient nanostructured photothermal interface. In order to identify the optimal nanoantennas, it is necessary to characterize or simulate their photothermal properties. Moreover, optical, thermal and electrical effects occurring within a PV-TE device should also be taken into account when designing the interface. Fabrication of nanoantennas can also prove to be a difficult task, often introducing design limitations and structural defects.

Thesis outline

The **first chapter** of this thesis introduces the limits of PV cell and how they can be overcome by PV-TE cogeneration devices. Fundamentals and applications of thermoplasmonic nanoantennas are also presented.

Chapter 2 describes the numerical and experimental methods used in the framework of this thesis.

The **third chapter** is dedicated to the numerical study of isolated nanoantennas for solar infrared absorption. The optical properties of nanoantennas with various shapes, sizes and compositions are simulated to identify the structures best suited for the application. The impact of fabrication defects is also discussed in this chapter.

In **chapter 4**, we tackle the fabrication and characterization of large scale nanostructured photothermal interfaces. A home-made experimental setup is used to measure the heating of these interfaces under solar infrared illumination, and the results pave the way for optimizing their temperature increase.

The **last chapter** presents the multiphysics model we propose to study PV-TE device integrating a nanostructured photothermal interface. This model is aimed at quantifying the impact of the PTI on the power output of the global device.

Contribution

The work presented in this thesis results from the fruitful collaboration of several individuals from LAAS, my host laboratory, and Gothenburg University, where I spent 2 months in 2022.

The fabrication of nanoantennas was made either at the LAAS cleanroom, or at the Nanofabrication Laboratory, at Chalmers University of Technology in Sweden, depending on the technique used.

At LAAS, **Franck Carcenac**, cleanroom engineer, developed an electron-beam lithography process according to the specific needs of the project. He taught me how to use the electron-beam writer so that I could fabricate the samples presented in Chapter 3. The metal covering these samples was deposited by **Ludovic Salvagnac** using Physical Vapor Deposition.

Ali Msahazi Ahamada, during his Master 2 internship, developed a NanoImprint Lithography process to replicate 150 nm-high nanoantennas, under the supervision of **Jean-Baptiste Doucet**, cleanroom engineer and technical coordinator of the thesis.

The photothermal interfaces presented in Chapter 4 were made in the Nanofabrication Laboratory cleanroom. **Dr. Ihar Faniayeu**, from Gothenburg University, taught me the Hole-mask Colloidal Lithography process, which I used to fabricate the samples. The optical characterization of these samples was done using a spectroscopy setup made by **Dr. Rafael Cichelero**.

The other measurements were done at LAAS, where I made all the Scanning Electron Microscopy and Atomic Force Microscopy images available in this manuscript.

I supervised the Master 1 internship of **Sélyan Beldjoudi**, which focused on the photothermal characterization setup described in Section 2.3.3. After developing the measurement protocol, he determined the emissivity of the samples by FTIR spectroscopy, and used the setup to record their heating under solar illumination. His results are discussed in Section 4.4.

On the computing side, I personally conducted the numerical simulations using the Discrete Dipole Approximation, after being trained by **Prof. Adnen Mlayah**,

and I also developed the multiphysics model described in Chapter 5.

Chapter 1

Context, motivations and objectives

In this first chapter, we describe how photovoltaic-thermoelectric devices integrating a nanoantenna-based photothermal interface can be used to overcome intrinsic limitations of mono-junction photovoltaic cells. The first part of this chapter presents the fundamentals of photovoltaic conversion and highlights intrinsic limitations of mono-junction cells, before listing some strategies used to overcome these limitations. The working principle of thermoelectric generator is also described. Then, we conduct a literature review on photovoltaic-thermoelectric cogeneration, introducing the history of the concept and discussing the controversy on its viability, before focusing on the physical interface between the photovoltaic cell and the thermoelectric generator. Finally, we describe how thermoplasmonic nanoantennas are efficient photothermal converters used in a variety of applications, including solar energy harvesting.

Contents

1.1 Working principle of mono-junction photovoltaic cells

In the last decades, the growing demand for renewable energy sources has propelled the development of photovoltaic (PV) technology as a viable solution for sustainable power generation. Among the various types of PV cells, mono-junction photovoltaic cells have been the first to be developed and are widely spread due to their simplicity and cost-effectiveness. This section aims to provide a comprehensive understanding of the working principle of mono-junction PV cells and elucidate their intrinsic limitations, including the bandgap of the semiconductors used, the thermalization mechanism, and the effects of heat on cell performance.

1.1.1 Limitations of mono-junction PV cells

The fundamental working principle of mono-junction PV cells relies on the photovoltaic effect, which is the generation of a voltage difference or electrical potential across a material in response to incident light. Mono-junction PV cells, also known as single-junction PV cells, consist of a single semiconductor material that serves as both the optical absorber and the energy converter. The most commonly used semiconductor materials for mono-junction PV cells are silicon (Si), gallium arsenide (GaAs), copper indium gallium selenide (CIGS) and cadmium telluride (CdTe).

In semiconductors, electrons are confined to two electronic bands: the valence band and the conduction band, which are separated by an energy range devoid of allowed electronic states. In order for an electron from the valence band to be promoted to the conduction band, it needs to gain an amount of energy at least equal to the difference between the highest energy level of the valence band and the lowest energy level of the conduction band. This energy difference between the top of the valence band and the bottom of the conduction band is called the bandgap, and is noted E_g. The value of the bandgap is an intrinsic characteristic of the semiconductor, typically ranging from 0 eV to 6 eV [3, 4].

The bandgap of the semiconductor material used in a mono-junction PV cell plays a crucial role in determining the cell's efficiency and spectral response. Any incident photon with an energy lower than the bandgap will not be absorbed by the cell (red arrow in the inset of Figure 1.1), meaning that it can not contribute to electricity generation. As represented in red in Figure 1.1, for a GaAs PV cell, which bandgap is 1.42 eV, under standard solar illumination (AM1.5G spectrum), these non-absorption losses account for more than 30 % of the incoming power.

On the other hand, when photons with energy greater than the bandgap of the semiconductor material reach the cell, they transfer energy to the electrons in the material, causing them to be excited from the valence band to the conduction band (see inset of Figure 1.1). This creates electron-hole pairs, which can then be separated by the electric field within the material and collected, resulting in the generation of a current. However, the excess energy of the excited electron, meaning

the difference between the energy of the incoming photon and the bandgap (blue part of the arrow, in the inset of Figure 1.1), is rapidly lost by interaction with the lattice vibrations (phonons) of the semiconductor material. This process, called thermalization and represented in blue in Figure 1.1, results in energy dissipation as heat within the cell, increasing its temperature.

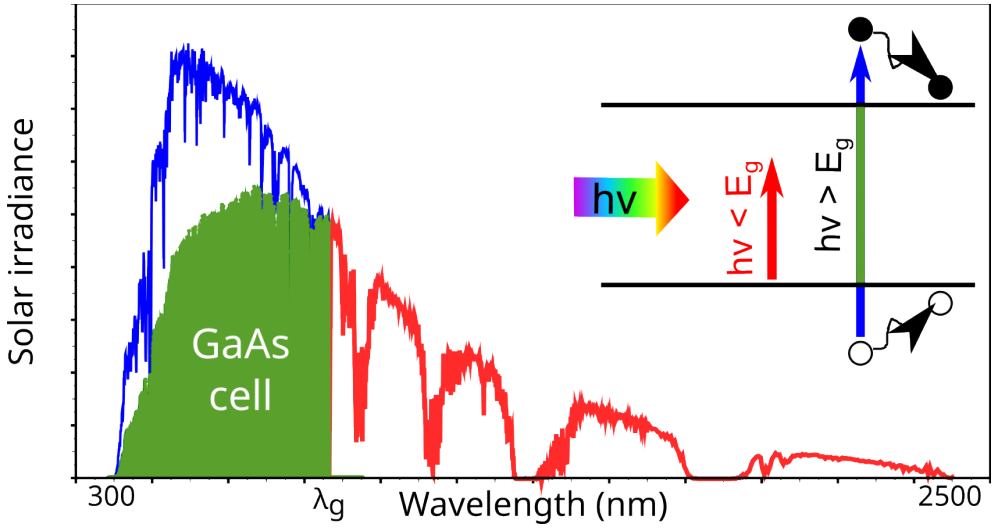

Figure 1.1: Intrinsic limitations of mono-junction photovoltaic cells. Spectrum of the AM1.5G solar irradiance showing the maximum energy converted by a GaAs solar cell with E_g = 1.42 eV according to the Shockley-Queisser limit (green) and the intrinsic losses of the cell (thermalization, blue; non-absorption, red) with the corresponding loss processes schematized in the inset. Reprinted with permission from ACS Appl. Energy Mater. 2023, 6, 4, 2128–2133. Copyright 2023 American Chemical Society.

The Shockley-Queisser limit [6] describes the maximum theoretical efficiency of mono-junction solar cells at 25 °C, with respect to their bandgap, under illumination by the standard AM1.5G solar spectrum. For a GaAs solar cell, the photovoltaic conversion efficiency is limited to 33 %, which corresponds to the power available in the green zone in Figure 1.1. The Shockley-Queisser limit is represented in black in Figure 1.2 for bandgaps between 0.5 eV and 2 eV. In the same figure, it can be seen that state-of-the art PV cells are close to reach the Shockley-Queisser limit, leaving little room for further enhancement.

An other issue faced by PV cells is the heat generated by thermalization, due to its significant impact on the performance of most inorganic mono-junction PV cells. As the temperature of the cell increases, the open-circuit voltage tends to decrease due to an increase in the intrinsic carrier concentration and the recombination rate of electron-hole pairs [7, 8]. This phenomenon leads to a decrease in cell efficiency with rising temperatures (around -0.08 %/°C for GaAs [9]). Moreover, elevated temperatures can also accelerate degradation mechanisms within the cell, reducing its lifespan and long-term stability.

Thus, selecting an appropriate bandgap to make the most efficient solar cell is a trade-off. A smaller bandgap enables efficient absorption of a broader range of photons but may also lead to increased thermalization losses, as excess energy carried by high-energy photons is dissipated as heat. On the other hand, a larger

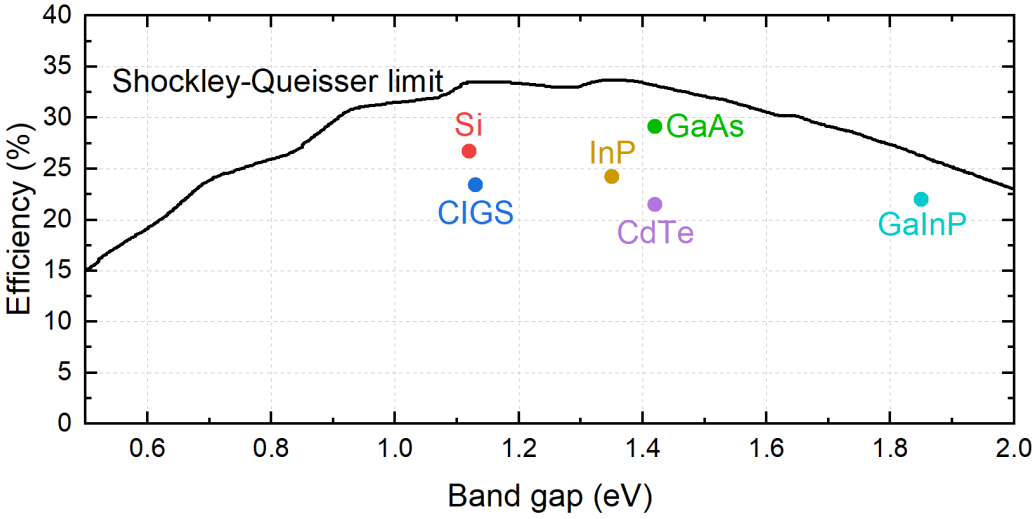

Figure 1.2: Maximum conversion efficiency of mono-junction solar cells with respect to their gap, according to the Shockley-Queisser limit (black line), and record efficiency in 2020 for several materials, adapted from [5].

bandgap reduces thermalization losses but limits the cell's ability to utilize low-energy photons. Therefore, there exists an optimal bandgap for each specific application, which balances absorption and thermalization losses.

1.1.2 Strategies for photovoltaic conversion enhancement

To overcome the limitations associated with the bandgap of semiconductor materials, thermalization losses, and the effects of heat on performance, researchers have explored various strategies in the literature. These strategies aim to improve the efficiency, spectral response, and long-term reliability of mono-junction PV cells. This section presents some of the notable approaches that have been investigated:

Bandgap engineering involves tailoring the bandgap of the semiconductor material to optimize its absorption characteristics. This can be achieved through techniques such as alloying [10, 11, 12], doping [13, 14, 15], or strain engineering [16, 17]. By carefully selecting the composition or modifying the lattice structure of the material, it is possible to fine-tune the bandgap, allowing for improved absorption of photons across the solar spectrum. Bandgap engineering strategies aim to strike a balance between absorption and thermalization losses, thereby maximizing the efficiency of the mono-junction PV cell.

Tandem and multi-junction cells [18, 19, 20, 21, 22] involve the stacking of multiple semiconductor materials with varying bandgaps into a single PV cell. By placing materials with high bandgaps on top of the stack and low bandgaps at the bottom, each subcell can efficiently absorb a specific range of photons, thereby enhancing the overall spectral response of the device. Additionally, multi-junction cells can mitigate thermalization losses by reducing the excess energy of high-energy photons, as the energy cascades through the different subcells, increasing the overall

voltage and efficiency of the device. Multi-junction photovoltaics is a mature technology, which currently achieves the highest conversion efficiency, with a record of 47.6 % for a 4-junction GaInP/AlGaAs/GaInAsP/GaInAs cell [2].

Intermediate band materials (IBMs) [23, 24, 25, 26] have attracted considerable attention as a mean to improve the efficiency of mono-junction PV cells. IBMs possess an energy level within the bandgap of the semiconductor material, allowing for additional absorption of photons that would otherwise be sub-bandgap. This approach enables more efficient utilization of a broader range of photon energies, thereby reducing thermalization losses and enhancing the overall performance of the cell.

Nanostructured materials [27, 28] have shown potential in enhancing the performance of mono-junction PV cells. Nanostructured surfaces can be used as efficient antireflection coatings, allowing more light to reach the active layer of the PV cell [29], or for advanced light trapping within the cell, drastically increasing its absorption [30].

Light management techniques have been explored to enhance the light absorption and utilization in mono-junction PV cells. These techniques include the incorporation of antireflection coatings [31, 32], textured surfaces [33, 34], and photonic structures [35, 30]. Antireflection coatings minimize the reflection losses at the cell surface, allowing for increased photon absorption. Textured surfaces or nanostructures can trap light within the cell, prolonging its interaction with the absorber material. Photonic structures, such as photonic crystals or plasmonic structures, can manipulate the propagation and absorption of light, enabling improved spectral response and light trapping.

Thermal management strategies [36, 37, 38, 39] have been explored to address the effects of heat on the performance of mono-junction PV cells. These include the incorporation of passive cooling techniques, active cooling systems, and thermal interface materials. Passive cooling techniques, such as natural convection or radiation, exploit thermal gradients to remove heat. Active cooling systems, such as fans or liquid cooling, actively circulate a coolant to extract heat. Thermal interface materials, such as liquid metal [40] or graphene-charged mineral oil [41], enhance the thermal coupling between the cell and the heat sink, improving heat dissipation.

Advanced device architectures have been developed to enhance the performance of mono-junction PV cells. These include concentrator systems, where optical elements focus sunlight onto a smaller area, increasing the photon flux and improving rentability [42]. Furthermore, novel cell designs, such as cells with a rear surface mirror [43], back-contact cells [44], which include the promising interdigitated back-contact cells [45], or passivated emitter and rear-contact (PERC) cells [46], offer improved light trapping, reduced recombination, and enhanced electrical properties, leading to higher overall performance.

In conclusion, the literature provides a wide array of strategies aimed at overcoming the limitations of mono-junction PV cells. By leveraging these approaches, researchers aim to achieve higher efficiency, improved spectral response, and in-

creased long-term reliability for mono-junction photovoltaic cells.

1.2 Working principle of thermoelectric generators

Thermoelectric generators rely on the Seebeck effect, which states that a temperature gradient across a thermocouple, i.e. a junction of dissimilar materials A and B, can induce an electric voltage [47]. If the extremity of two wires made of different electrically conductive materials are connected at a hot point with temperature T_H, while the other end of each wire is kept at a cold temperature T_C, then a difference of electric potential ΔV arises between the wires at the cold point. The link between ΔV and $\Delta T = T_H - T_C$ depends on the couple $A - B$, and is expressed as:

$$\Delta V = \alpha_{AB} \Delta T \tag{1.1}$$

where α_{AB} is the Seebeck coefficient of the $A - B$ couple in V/K, defined as the difference between α_B, the Seebeck coefficient of material B, and α_A, the Seebeck coefficient of material A:

$$\alpha_{AB} = \alpha_B - \alpha_A \tag{1.2}$$

The reciprocal of the Seebeck effect is the Peltier effect, which corresponds to a heat transfer from one junction of a thermocouple to the other in the presence of an electric current I. The heat Q removed at one junction, which is equal to the heat generated at the other, is expressed as

$$Q = (\Pi_A - \Pi_B) I \tag{1.3}$$

where Π_A and Π_B are the Peltier coefficients of materials A and B respectively.

Thus, for a thermocouple connected to a load and exposed to a temperature difference between the two junctions, an electric current will be generated through Seebeck effect. Due to the Peltier effect, this current will in turn extract heat from the hot junction to the cold one, reducing the temperature gradient.

As represented in Figure 1.3, a thermoelectric generator involves multiple thermocouples connected electrically in series and thermally in parallel. Each thermocouple consists of two dissimilar thermoelectric elements, a p-type semiconductor and an n-type semiconductor. When a temperature gradient is applied across the thermocouples, it induces a potential difference or voltage due to the Seebeck effect, as expressed in Equation 1.1. This voltage drives an electric current I_{TEG} through an external load R_L, producing electrical power [48].

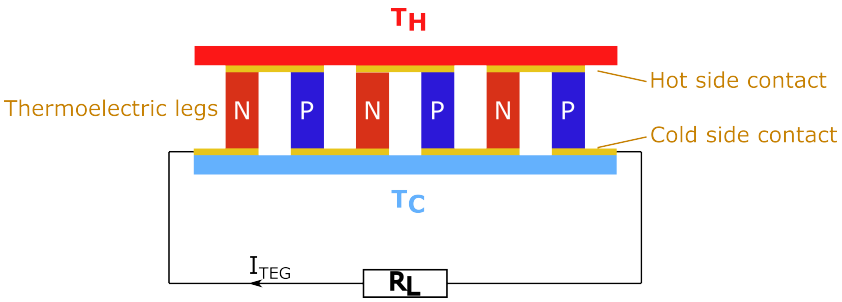

Figure 1.3: Schematic representation of a TEG delivering the current I_{TEG} to a load R_L when a temperature difference $(T_H - T_C)$ is applied.

The core component of a thermoelectric generator is a thermoelectric material, typically a semiconductor, which possesses a high Seebeck coefficient. Commonly used thermoelectric materials include bismuth telluride (Bi_2Te_3), lead telluride (PbTe), and silicon-germanium (SiGe) alloys.

One of the primary limitations of thermoelectric generators is their relatively low energy conversion efficiency. The efficiency of a thermoelectric generator is determined by the dimensionless figure of merit zT, which depends on the Seebeck coefficient α, electrical conductivity ρ, and thermal conductivity κ of the thermoelectric material at temperature T, according to Equation 1.4. A high zT value indicates efficient conversion of heat into electrical energy [49].

$$zT = \frac{\sigma \alpha^2 T}{\kappa} \tag{1.4}$$

However, achieving high zT values is challenging due to the interdependence of these material properties. For instance, materials with high electrical conductivity often exhibit high thermal conductivity as well, leading to reduced efficiency. Additionally, the Seebeck coefficient of many high-performance thermoelectric materials is relatively low, limiting the voltage output and thus the efficiency of energy conversion. Therefore, improving the figure of merit and overall efficiency of thermoelectric generators remains an active area of research.

Furthermore, thermoelectric generators have a limited operating temperature range, which restricts their applicability to specific heat sources. The efficiency of thermoelectric generators is highly dependent on the temperature difference between the hot and cold sides of the device. Higher temperature differences result in greater voltage outputs and improved performance. However, some thermoelectric materials may exhibit a significant drop in performance at high temperatures due to increased thermal conductivity or reduced Seebeck coefficient. On the other hand, operating at lower temperatures may lead to reduced voltage outputs and lower efficiency. Therefore, matching the temperature range of the thermoelectric generator to the heat source is crucial for optimal performance.

Thermoelectric generators typically have lower power densities (< 200 mW/cm^2 [50, 51]) compared to other energy conversion technologies [52], such as combustion engines or solar cells. The power density of a thermoelectric generator is limited by

their relatively low thermal-to-electric conversion efficiency. As a result, they are best suited for low-power applications or situations where waste heat recovery is the primary objective rather than high-power electricity generation.

In summary, thermoelectric generators offer the potential to convert waste heat into usable electrical energy. However, they face intrinsic limitations related to energy conversion efficiency, material selection, operating temperature range, power density, cost, and scalability.

1.3 State-of-the-art of PV-TE cogeneration

Photovoltaic (PV) and thermoelectric (TE) technologies have emerged as promising avenues to harness renewable energy and convert it into electricity. Each technology has its advantages and limitations, but combining them in a cogeneration system offers the potential to synergistically enhance overall energy efficiency. This section presents a comprehensive overview of the state-of-the-art in photovoltaic-thermoelectric cogeneration, exploring the historic development, fundamental principles, and recent advancements in these devices.

1.3.1 Principle of PV-TE cogeneration

The concept of photovoltaic-thermoelectric cogeneration can be traced back to the early 21th century when researchers began exploring the potential benefits of combining PV and TE technologies in order to overcome intrinsic limitations of photovoltaic conversion [53]. As discussed in Section 1.1.1, mono-junction PV cells are unable to efficiently exploit the whole solar spectrum, due to thermalization and non-absorption of sub-bandgap photons. The advantages of combining a PV cell and a TEG in a hybrid device is to enhance the output electrical power by taking advantage of these losses. Indeed, the waste heat generated in the PV cell by thermalization, and the photothermal conversion of infrared solar photons, can be used to increase the temperature of the hot side of a TEG, thus generating an electrical current.

Two different types of coupling are studied in the literature: **direct coupling** and **spectrum splitting**.

In the spectrum splitting configuration, the PV cell and the TEG are physically separated, and a spectral splitter is used to direct the incident optical power toward one or the other, according to the cutoff wavelength of the splitter. Many designs are described in the literature, but a general example is presented in Figure 1.4A. This approach allows to make sure that only photons with an energy superior to the bandgap reach the PV cell. On the other hand, the sub-bandgap photons are directed toward the TEG, generally coated with an absorber to allow the absorption and photothermal conversion of these photons. The advantage of this configuration is that both the PV cell and the TEG can be equipped with a heat sink. Thus, in

spectral splitting, the PV cell operates at lower temperature, ensuring maximized performances. The drawback is that the heat power generated in the PV cell is lost, as it cannot be converted by the TEG.

In the direct coupling configuration, the TEG is placed in physical contact behind the PV cell, as illustrated in Figure 1.4B. The waste heat generated by the operating PV cell can thus be exploited by the TEG to create additional electrical power. An absorbing layer can be placed at the interface between the two devices to absorb radiation transmitted by the PV cell and increase the temperature at the hot side of the TEG. This configuration maximizes the temperature at the interface between the PV cell and the TEG, which is beneficial to the TEG as it increases its power output, but detrimental to most PV cells, which conversion efficiency decreases with increased temperature.

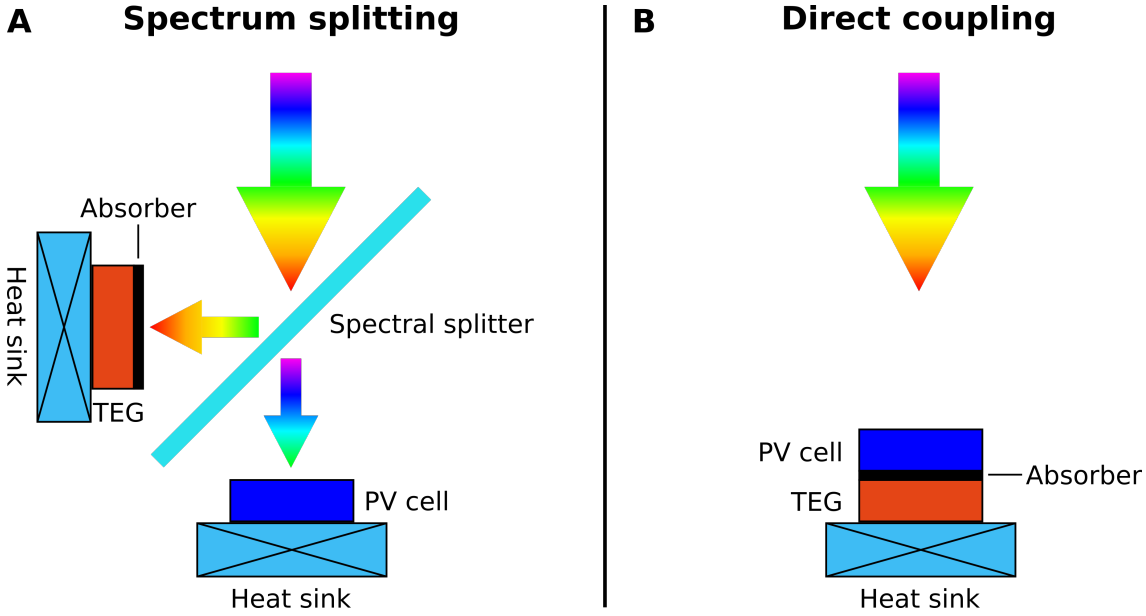

Figure 1.4: Scheme of two configurations of PV-TE coupling: (A) spectrum splitting and (B) direct coupling.

Spectrum splitting PV-TE allows to work under highly concentrated solar power, where the operating temperature limit of both the PV cell and the TEG would be exceeded in direct coupling. However, direct coupling in a monolithic device is the most compact of the two configurations, and the one we will focus on in this thesis.

1.3.2 Is PV-TE hybridization actually viable ?

Prof. Dario Narducci and his team at the University of Milano-Bicocca produced prolific work on PV-TE hybridization. In 2015, Lorenzi et al. [54] used a theoretical model to estimate the amount of thermal power recoverable from four different mono-junction PV cells (crystalline silicon (c-Si), amorphous silicon (a-Si), CIGS and CdTe) when coupled with a TEG. Their results showed that the benefits of hybridization strongly depend on the optical properties of the PV cell, and mainly of its bandgap. According to them, low bandgap PV cells are more favorable to

PV-TE coupling due to the increased thermalization losses. It is however important to note that they did not use an absorbing interface, instead supposing that the energy of non-absorbed sub-bandgap photons was not recoverable by the system.

In parellel, Bjork et al. [55] studied the theoretical performances of the same four PV cells when combined with a commercial bismuth telluride TEG. They concluded that the PV-TE coupling is detrimental to the overall electrical power output for the c-Si, CIGS and CdTe cells, because the loss of power from the PV cell due to the increased temperature is not compensated by the low conversion efficiency of the TEG. However, they highlighted a small gain in efficiency when combining the TEG with the a-Si PV cell. Once again, it is assumed that all the energy corresponding to non-absorbed photons is lost.

In 2015, the team of Prof. Narducci investigated the effect of adding an absorbing layer at the bottom of the PV cell for partial photothermal conversion of sub-bandgap photons [56]. The simulation results were encouraging, as the hybrid system was more efficient than the PV cell alone, exceeding its Shockley-Queisser limit. In 2017, the same team published another computational study on PV-TE hybridization, this time including a configuration for which the sub-bandgap photons are absorbed at the bottom of the PV cell by a highly absorbing and thermally conductive back-contact [57]. In this case, they evidenced that hybrid PV-TE system exhibits increased efficiency with respect to the PV cell alone, for a wide range of ambient conditions (i.e. ambient temperature, incident solar power, wind speed).

Bjork et al. later published another study on the maximum theoretical performance of unconcentrated PV-TE systems [58]. Their model included a PV cell operating at the Shockley-Queisser limit and a TEG with varying zT. In this case, the sub-bandgap photons were assumed to be fully converted to heat. They concluded that an increase in conversion efficiency for a combined PV-TE device compared to the PV cell alone would only occur for TEGs having unrealistically high zT values, and would still be insignificant (<1 %).

In 2011, Wang et al. reported the first experimental PV-TE device [59]. It was made of a dye-sensitized solar cell (DSSC) and a commercial TEG, between which was inserted a solar selective absorber (SSA) able to convert the radiation transmitted through the PV cell into heat. The hybrid device was tested under standard solar illumination and showed a conversion efficiency of 13.8 %, which is significantly higher than the DSSC alone (9.26 %) and the hybrid device without SSA (12.8 %). The use of a DSSC is interesting here, as this type of PV cell usually reaches its maximum efficiency at around 30-40 °C [60], which means that the addition of the TEG and subsequent temperature increase of the PV cell is actually beneficial to its performances.

Since then, several teams have fabricated and characterized PV-TE hybrid devices, showing efficiency gains with respect to the PV cell alone in various conditions [61, 62, 63, 64, 65, 66].

The strong differences in conversion enhancement resulting from PV-TE coupling between experimental and theoretical works can be explained by the fact that

theoretical models usually assume that the PV cell is operating at the Shockley-Queisser limit, which is not the case of commercial PV cells. Indeed, the power available for thermoelectric conversion is higher in the case of inefficient PV cells, for which PV-TE hybridization is thus more beneficial.

Another bias arises when the PV-TE device is compared to the PV cell alone in standard conditions. Standard conditions imply that the temperature of the PV cell is kept constantly at 25 °C, canceling the detrimental impact of heat generation, which would reduce the performance of the cell in real operating conditions. Rather, the two system should be compared within the same environment (same illumination, ambient temperature, wind speed, and eventually same heat sink or heat extraction power).

1.3.3 Work on the physical interface between the photovoltaic cell and the thermoelectric generator

As mentioned in the previous section, a critical aspect of PV-TE viability lies in the physical interface between the PV cell and the TEG, as it plays a pivotal role in dictating the device's performance. A well-engineered interface has the potential to significantly enhance the overall efficiency of the integrated system. This enhancement arises from two primary factors: improved thermal conduction and increased availability of thermal energy.

Efficient thermal conduction across the photovoltaic-thermoelectric interface is paramount for maintaining optimal operating temperatures of both components, by enabling the efficient transfer of heat between the photovoltaic cell to the thermoelectric generator. It has been experimentally proven that reducing the thermal resistance at the PV-TEG interface can lead to significant increases in the power output of the device [67]. This reduction in thermal resistance allows better heat extraction from the PV cell, reducing its temperature, while increasing the temperature at the hot side of the TEG, both effects being generally beneficial to the PV-TE device's performance.

Utilizing the maximum amount of energy from the solar spectrum is another way to improve the conversion efficiency of a PV-TE system. Most PV cells are transparent to sub-bandgap photons and generate heat mostly through thermalization, which limits the amount of thermal energy available for thermoelectric conversion by the TEG. Through judicious interface engineering, an augmented supply of thermal energy can be achieved. This is primarily facilitated by the introduction of photothermal conversion mechanisms at the interface. Photothermal interfaces can effectively capture a broader spectrum of incident light, converting a portion of it into thermal energy that can then be efficiently channeled to the thermoelectric generator. This additional thermal energy bolsters the temperature gradient across the generator, consequently enhancing the generated voltage (Equation 1.1). A downside of this approach is that a temperature increase at the hot side of the TEG will also give rise to a temperature increase of the PV cell, which is often detrimental to its performances. However, several studies showed that the addition

of a photothermal interface in PV-TE hybrid devices enhances the power output of the global system.

For example, Kim et al. proposed a PV-TE design integrating en exothermic reactive layer between the PV cell and the TEG [68]. This layer was made of an acrylic film died with black colored AZO dye, exhibiting an optical absorptivity of around 50 % in the solar infrared wavelengths and an efficient photothermal conversion. To further increase the performances of the PV-TE device, the TEG's top ceramic substrate was removed, enhancing heat conduction from the photothermal layer to the thermoelectric elements. This optimized design was compared to a PV cell alone, and two PV-TE devices with different interfaces: a normal acrylic film and an acrylic film coated with common black dye. The results show that all 3 PV-TE devices are able to generate more power than the PV cell alone under standard solar illumination, when the cold side is kept constant at 25 °C. The device with the AZO dyed acrylic exhibited the best performance due to its higher photothermal conversion, resulting in a temperature gradient of 18 °C through the TEG and a conversion efficiency of 20.1 %, when the conversion efficiency of the PV cell alone was only 16.4 %.

Furthermore, Park et al. compared a PV-TE hybrid devices without interface to PV-TE devices with interfaces made of pure boron nitride (BN) with high thermal conductivity, or boron nitride loaded with reduced graphen oxide (BN-rGO), which exhibits high thermal conductivity and absorptivity [69]. The authors showed that the high thermal conductivity of the BN interfaces allowed to increase the temperature gradient through the TEG, and thus the electrical power generated by the hybrid device. However, this effect was even more significant in the case of the BN-rGO interface, due to the combination of thermal conductivity and photothermal conversion.

In summary, the interface between the photovoltaic cell and the thermoelectric generator represents a critical focal point for improving the performance of photovoltaic-thermoelectric cogeneration devices. The ability to manipulate thermal conduction and augment available thermal energy through interface engineering offers a pathway towards achieving higher overall energy conversion efficiencies. As such, a comprehensive exploration of interface design and its impact on the integrated system is essential for realizing the full potential of this promising technology fusion.

1.4 Thermoplasmonic nanoantennas

Plasmonics is a field of research that explores the unique properties and interactions of surface plasmons, which are collective oscillations of electrons in metallic nanostructures or at metal-dielectric interfaces. These plasmonic phenomena have garnered significant interest due to their unique ability to manipulate and control light at the nanoscale. These peculiar properties have led to exciting advancements in various areas of science and technology, including sensing [70], imaging [71], energy conversion [72], and information processing [73]. This section aims to provide

an overview of the field of plasmonics, emphasizing the fundamental principles, key concepts, and applications, with a specific focus on thermoplasmonic nanoantennas and their applications to solar energy harvesting.

1.4.1 Plasmonics

Introduction

Plasmonics is the study of the interaction between light and free electrons in metallic nanostructures. Light, or electromagnetic waves, consist of oscillating electric and magnetic fields that propagate through space at the speed of light. The interaction between light and materials is fundamental in plasmonics, where the incident electromagnetic waves can dramatically affect the behavior of electrons in metals, resulting to interesting phenomena.

When light interacts with metallic nanoparticles or nanostructures, the free electrons at the metal's surface can oscillate collectively, resonating at specific frequencies, resulting in the formation of surface plasmons [74, 75]. The plasmonic resonance frequency can be tuned by adjusting the size, shape, and material properties of the nanostructures.

These surface plasmons are characterized by their localized or propagating nature, depending on the geometry and arrangement of the metallic nanostructures. Two fundamental types of plasmons are localized surface plasmons (LSPs) and surface plasmon polaritons (SPPs) [76]. LSPs occur in small metallic nanostructures, such as nanoparticles, where the plasmonic resonance is confined to a localized region [77, 78]. SPPs, on the other hand, are propagating plasmons that can be excited at metal-dielectric interfaces [79, 80]. These surface waves can guide light along the interface, confining it to subwavelength dimensions and enabling novel waveguiding [81] and nanofocusing capabilities [82].

The choice of materials is crucial in plasmonics, as different metals exhibit distinct plasmonic properties. Noble metals such as gold, silver, and copper are widely used due to their excellent plasmonic behavior in the visible and near-infrared regions [83, 84]. Transition metals like aluminum also show promise in the ultraviolet region [85]. Additionally, alternative plasmonic materials, such as doped semiconductors [86] and graphene [87], are also being explored.

Surface plasmons exhibit unique properties that can be exploited for various applications. One key property is the strong confinement of electromagnetic fields at the nanoscale [88], which allows for efficient light manipulation and enhancement of local electromagnetic fields. Another crucial characteristic is the dependence of surface plasmons on the material and geometry of the nanostructures, enabling the engineering of plasmonic resonances and the tailoring of their spectral response.

Plasmonic nanostructures are designed to exploit the unique properties of surface plasmons. These nanostructures can take various forms, such as nanocavities [89,

90], nanoantennas [91, 92], nanostructured surfaces [93, 94] and metamaterials [95, 96], among others. The choice of nanostructure geometry depends on the desired plasmonic properties and specific applications.

Localized Surface Plasmon Resonance

Localized surface plasmon resonance (LSPR) is a fundamental phenomenon in plasmonics that occurs when metallic nanoparticles or nanostructures support collective oscillations of free electrons at their surfaces. Unlike propagating surface plasmons, which involve the coherent motion of electrons along extended interfaces, LSPR is confined to and localized around individual metallic nanostructures.

The LSPR phenomenon arises from the interaction between incident electromagnetic waves and the plasmonic nanostructures. When the frequency of the incident light matches the resonant frequency of the localized surface plasmons, a strong coupling occurs, leading to the excitation of the LSPR mode. The free-electron cloud resonantly oscillates with the incident electric field, resulting in an induced oscillating dipole, as presented in Figure 1.5. This interaction leads to a strong enhancement of the electromagnetic field in the vicinity of the nanoparticle. The resonant frequency depends on various factors, including the size, shape, and composition of the nanostructures, as well as the surrounding medium [97].

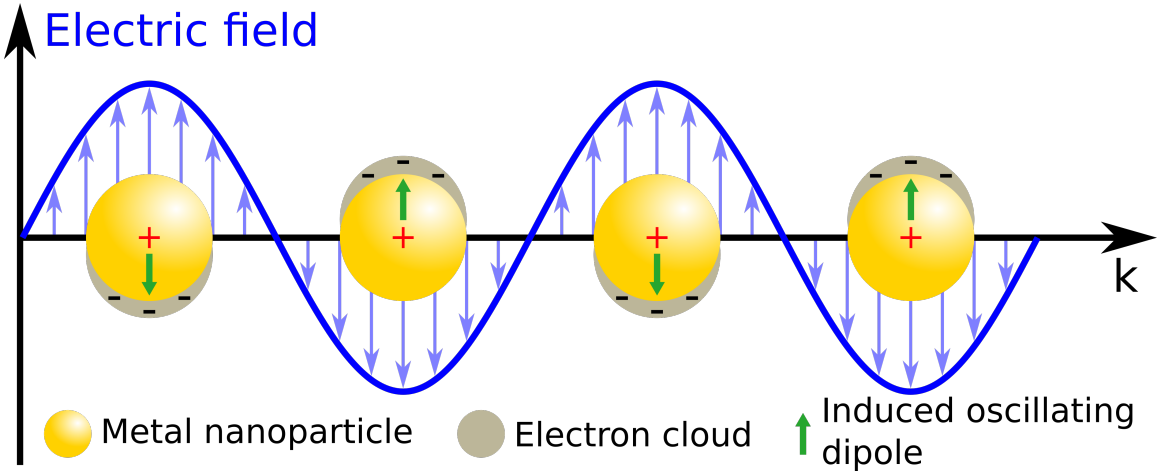

Figure 1.5: Schematic representation of the excitation of Localized Surface Plasmon Resonances in metallic nanosphere by an incident electric field.

As an example, a metallic sphere with a radius R, illuminated by a wavelength $\lambda \gg R$, can be considered as an electromagnetic dipole. Thus, its polarizability α can be calculated at the frequency ω as:

$$\alpha(\omega) = 4\pi R^3 \frac{\epsilon(\omega) - \epsilon_m}{\epsilon(\omega) + 2\epsilon_m} \tag{1.5}$$

where $\epsilon(\omega)$ is the complex relative permittivity of the metal and ϵ_m the real permittivity of the surrounding medium, at frequency ω. It can be seen from

Equation 1.5 that the polarizability of a metallic sphere exhibits a resonance when $\epsilon(\omega) = -2\epsilon_m$.

For larger spheres and more complex geometries, other models should be used to calculate the polarizability. However, for any metallic nanoparticle, the absorption and scattering cross-section at a wavelength λ can be expressed based on the polarizability:

$$\sigma_{abs}(\lambda) = kIm(\alpha(\lambda)) - \frac{8\pi^3}{3\lambda^4}|\alpha(\lambda)|^2 \tag{1.6a}$$

$$\sigma_{scat}(\lambda) = \frac{8\pi^3}{3\lambda^4}|\alpha(\lambda)|^2 \tag{1.6b}$$

LSPR is accompanied by enhanced near-field electromagnetic effects, such as increased electric field intensity and electromagnetic energy confinement, within the vicinity of the nanostructures. These enhanced fields enable the manipulation and control of light at the nanoscale, opening up possibilities for applications in sensing, imaging, and light-matter interactions. For example, in surface-enhanced Raman spectroscopy (SERS), the strong electromagnetic fields in the vicinity of plasmonic nanostructures are used to enhance the Raman scattering of molecules [98].

1.4.2 Nanoantennas for photothermal conversion

Nanoantennas have emerged as a captivating approach for photothermal conversion. The fundamental principle underlying the photothermal conversion effect in nanoantennas involves the excitation of LSPRs, which efficiently convert incident light into heat through non-radiative processes.

Nanoantennas, and more generally metallic nanostructures, can be tailored to resonate at specific wavelengths. When exposed to light, these nanoantennas experience resonant oscillations of conduction electrons in response to the incident electromagnetic field. Through this phenomenon, photons are absorbed and their energy is transferred to oscillating electrons. These so-called "hot carriers" will dissipate their energy through electron-electron scattering, followed by emission of phonons, thus increasing the temperature of the metallic lattice [99]. The heat power $Q(\lambda)$ generated in a nanoantenna, under illumination at a wavelength λ and irradiance $I(\lambda)$ (power per unit surface), is directly linked to its spectral absorption cross-section $\sigma_{abs}(\lambda)$ as:

$$Q(\lambda) = \sigma_{abs}(\lambda) \cdot I(\lambda) \tag{1.7}$$

For a polychromatic incident illumination, the total heat Q generated in the nanoantenna can simply be derived from $Q(\lambda)$:

$$Q = \int_0^\infty Q(\lambda) \cdot d\lambda = \int_0^\infty \sigma_{abs}(\lambda) \cdot I(\lambda) \cdot d\lambda \tag{1.8}$$

This heat power will increase the temperature of the nanoantenna and its surroundings. However, in order to calculate the steady-state temperature distribution around the antenna, the heat diffusion equations need to be solved. It is a complex problem that requires to take into account the thermal conductivity and emissivity of the materials at play, the ambient conditions such as temperature and convective heat transfer, as well as the shape of the nanoantenna [100]. When several nanoantennas are placed in proximity, collective thermal effects can occur, further complexifying the computation of temperature distribution [101, 102].

Thermoplasmonic nanoantennas are often compared to their thin film solar absorbers counterpart. The choice between one or the other hinges on specific application requirements and desired outcomes. While both approaches offer distinct advantages, thermoplasmonic nanoantennas exhibit unique features that make them particularly advantageous in certain scenarios.

Thermoplasmonic nanoantennas offer the ability to precisely engineer their optical properties, including shape, size, and composition, to achieve resonances at specific wavelengths. This spectral tunability enables selective absorption of light within narrow bandwidths, which is valuable for applications demanding precise wavelength matching. Unlike conventional thin film absorbers with broad absorption profiles, thermoplasmonic nanoantennas excel in situations where targeted absorption and enhanced efficiency within specific spectral regions are essential.

One of the standout advantages of thermoplasmonic nanoantennas lies in their ability to generate localized heating at nanoscale hotspots. This feature is particularly advantageous in applications where controlled and highly localized heating is required. In contrast, thin film absorbers distribute absorbed energy more uniformly across their entire volume, which may not be as effective for applications reliant on localized heating effects. The nanoscale nature of thermoplasmonic nanoantennas provides inherent advantages in miniaturization and precise control. Thin film absorbers are often limited by thickness considerations and can lack the spatial precision achievable with nanoantennas. This attribute is especially relevant in emerging nanoscale technologies, such as on-chip energy harvesting and nanoscale sensing platforms, where compactness and precise energy localization are critical.

The application of thermoplasmonic nanoantennas spans various disciplines and technologies [103]. One of the most exciting is in photothermal therapy, as nanoantennas can be used to selectively target and heat cancer cells, inducing controlled cell death and offering a potential avenue for cancer therapy. Other applications include sensing [104, 105], imaging [106] or catalysis [107, 108].

1.4.3 Applications to solar energy harvesting

Thermoplasmonic nanoantennas have garnered substantial attention in the realm of solar energy harvesting due to their distinctive capability to convert incident sunlight into localized heat. Researchers have identified several applications for which solar harvesting by thermoplasmonic nanoantennas could prove useful:

Water desalination. Water scarcity is a global challenge, and solar-powered desalination holds promise for addressing this issue sustainably. Thermoplasmonic nanoantennas have shown potential in enhancing solar-driven water desalination processes. When integrated into desalination systems, nanoantennas can efficiently concentrate solar energy to induce rapid vaporization of saline water. The localized heating effect at the nanoantenna hotspots facilitates the separation of fresh water vapor from saline solutions, enabling efficient and energy-saving water desalination with reduced reliance on external heating sources [109, 110, 111].

Solar water splitting. Thermoplasmonic nanoantennas play a pivotal role in advancing solar water splitting, a critical process for sustainable hydrogen production. By integrating nanoantennas into photocatalytic systems, solar water splitting reactions can be accelerated through localized heating. The absorbed sunlight generates intense thermal gradients at the nanoantenna surface, enhancing the rates of catalytic reactions involved in water splitting. This localized heating effect promotes the dissociation of water molecules into hydrogen and oxygen gases, thereby increasing overall solar-to-fuel conversion efficiency and facilitating the production of clean and renewable hydrogen fuel. The precise spatial control of heat generation provided by thermoplasmonic nanoantennas is of paramount importance in this process, where efficient reaction kinetics and localized temperature gradients are crucial [112, 113, 114].

Smart windows. Thermoplasmonic nanoantennas can be strategically integrated into window coatings or films. By exploiting their distinctive plasmonic characteristics, these nanoantennas can selectively modulate the transmission and reflection of solar radiation in response to external stimuli, such as temperature or sunlight intensity. This tunable light control capability allows the dynamic tuning of smart windows optical properties, enabling efficient management of indoor temperature, light levels, and energy consumption [115, 116, 117, 118].

While the utilization of thermoplasmonic nanoantennas in solar energy harvesting presents exciting opportunities, challenges remain in optimizing the design, scalability, and stability of these nanostructures for practical applications. Further research is needed to explore novel materials, enhance heat management strategies, and advance fabrication techniques to unlock the full potential of thermoplasmonic nanoantennas.

1.5 Objective of the thesis

The primary objective of this PhD thesis is to investigate the feasibility and potential benefits of incorporating photothermal interfaces based on thermoplasmonic nanoantennas into photovoltaic-thermoelectric cogeneration systems, in order to enhance their conversion efficiency. Such a system is represented in Figure 1. The fundamental aim is to harness the capabilities of nanoantennas to efficiently absorb infrared radiation traversing photovoltaic cells, converting it into heat that can be utilized to enhance the efficiency of thermoelectric generators.

To achieve this objective, a comprehensive research approach has been adopted, which encompasses both computational simulations and experimental characterizations.

In the initial phase of this research, extensive numerical simulations were conducted to calculate the optical properties of nanoantennas of varying shapes and dimensions. This computational exploration enabled the identification of nanoantenna configurations that exhibit optimal efficiency for infrared solar absorption. Importantly, the simulations also considered the influence of manufacturing defects to ensure that these imperfections do not compromise the performance of the nanoantennas.

Following the computational investigations, nanostructured interfaces were fabricated over large surfaces to facilitate practical characterization. The measurement of the thermal heating induced by these nanostructured interfaces under infrared solar illumination provided insights into the strategies for maximizing their temperature elevation. This experimental aspect sheds light on the practical implications of employing these photothermal interfaces in real-world photovoltaic-thermoelectric devices.

Last but not least, a significant advancement of this research involves the development of a multiphysics model. This model was specifically designed to simulate the behavior of a photovoltaic-thermoelectric system incorporating a nanostructured photothermal interface. By combining various physical phenomena such as optical absorption, heat generation, electrical power generation, and thermal transport, this model enables a comprehensive assessment of the impact of the photothermal interface on the electrical power output of the system. This computational framework ultimately aims at providing valuable insights to optimize the performance of the integrated energy system.

It is important to emphasize that the methodologies and findings of this research are versatile and adaptable to diverse types of photovoltaic cells and thermoelectric generators. The outcomes of this study have the potential to offer innovative strategies for enhancing the efficiency of cogeneration systems through the integration of nanostructured photothermal interfaces.

Chapter 2

Numerical and experimental methods

The aim of this chapter is to describe the different numerical and experimental methods used to obtain the results presented in the manuscript, including electromagnetic simulations, nanofabrication processes and characterization techniques. In each case, an overview of the technique is presented in order to give the reader a general understanding of its advantages and drawbacks. Then, more details are shared about the use of the technique in the specific scope of this work. The reader is encouraged to refer to this chapter whenever information about a specific process is needed in the rest of the manuscript.

Contents

2.1 DDA electromagnetic simulations

2.1.1 Presentation of the DDA method

The Discrete Dipole Approximation (DDA) is a numerical method used in computational electromagnetics to model light scattering by complex and irregularly shaped objects. In the DDA method, an object is divided into an array of polarizable dipoles, and each dipole is treated as a point source of electromagnetic radiation. Each dipole is defined by its position and complex refractive index or dielectric function. The oscillating moment of a dipole depends on its polarizability and the local electric field, the latter resulting from the combination of the incident electromagnetic wave and the electric field generated by the neighboring dipoles. The interactions between the dipoles are computed using the electric and magnetic fields generated by each dipole, and the total scattered field is obtained by summing up the contributions of all the dipoles. Given a specific discretized target and incident wave, the oscillating dipole moment can be exactly calculated at each point. It is then possible to compute the absorption and scattering cross-sections of the particle, as well as a cartography of the electromagnetic field in its vicinity [119, 120, 121].

In practice, the object is first divided into a large number of small dipoles (see Figure 2.1), with the electric dipole moment of each dipole calculated based on its polarizability and local electric field. Then, the electric field generated by each dipole at the positions of all other dipoles is calculated using numerical techniques such as the Fast Fourier Transform (FFT), and the electric dipole moment of each dipole is updated based on the interaction with the electric field generated by all other dipoles. Finally, the scattered field is obtained by summing up the contributions of all the dipoles. The process is repeated until convergence is achieved, meaning that the scattered field does not change significantly between successive iterations.

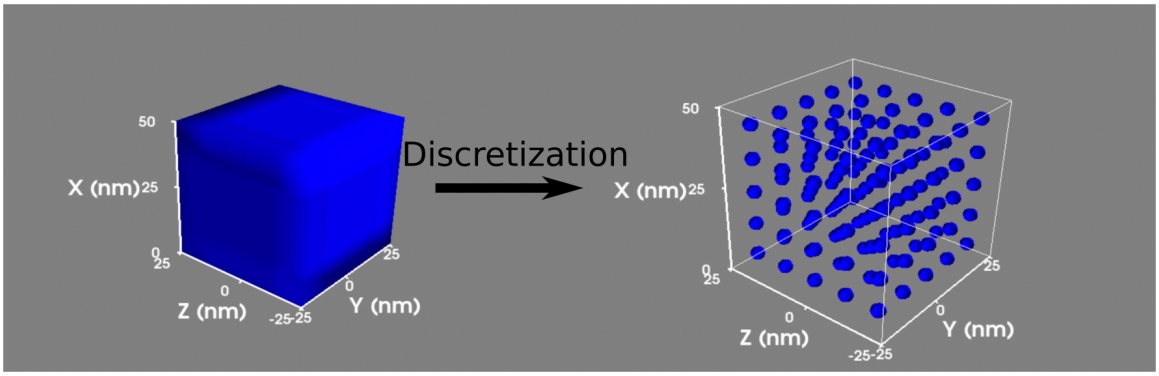

Figure 2.1: Cubic particle with 50x50x50 nm dimensions and the resulting simulation target discretized with an interdipole distance of 10 nm.

The DDA method has several advantages, including its ability to handle com-

plex and irregularly shaped objects, its ease of implementation, and its ability to handle large numbers of dipoles. However, it also has some limitations, including the difficulty in accurately modeling the interactions between closely spaced dipoles and the need for a large number of dipoles to achieve convergence.

In our case, DDA simulations are mainly used to calculate absorption and scattering spectra of isolated nanoantennas with a volume smaller than 0.1 µm^3. Such small simulation targets can be generated with a good resolution (interdipole distance of 10 nm) while limiting the number of dipoles to a maximum of 100 000, thus ensuring acceptable calculation durations (around 30 minutes). We have also done several simulations on systems made of a nanoantenna sitting on top of a thin substrate. However, due to the high number of dipoles needed to simulate the substrate, we limited the number of these time-consuming calculations.

2.1.2 Parameters of the DDA simulations

In the work presented in this thesis, the discretized targets are generated by custom codes running on the software Octave, allowing for complete control over the geometry of the simulated structures. In all cases, a cubic meshing with an interdipole spacing between 2 and 10 nm is used. The dielectric function of each dipole is attributed according to the material it represents, based on the data from Rakić et al. [122]. The numerical simulations of the nanoantennas' optical properties (namely absorption and scattering cross-sections) using the DDA method have been performed with the open-source code DDSCAT [120]. A number of input parameters can be tuned to match virtually any illumination conditions. Typically, the simulations are conducted in air (refractive index of 1), under illumination by two orthogonal linear polarizations (along the y and z axis) at normal incidence (along the x axis). The resulting cross-sections are averaged over the two polarizations. This process is repeated for a given number of incident wavelengths, linearly distributed over the waverange of interest, to generate cross-section spectra. The following calculation parameters are used: no torque calculation, BiConjugate Gradient with Stabilization (PBCGS2) iterative algorithm, GPFA (GPFAFT) as the fast Fourier transform algorithm and modified Lattice Dispersion Relation (GKDLDR) as the DDA method. The error tolerance and the maximum number of iterations have been set respectively to 0.001 and 10 000 in order to ensure convergence with a satisfactory precision.

2.1.3 Processing the data to assess the performances of simulated nanoantennas

For each DDA simulation, the absorption σ_{abs} and scattering σ_{scat} cross-sections are calculated between the wavelengths λ_{min} and λ_{max}. The resulting spectra give useful information about the optical response of the simulated structures, showing the position and intensity of absorption.

In the context of the design of an absorbing interface, these spectra need to be compared to the incoming solar spectrum in order to identify the most effective structures for solar light harvesting. Thus, we implemented two key figures of merit, to better estimate the matching of the antennas properties to the solar spectrum. First, the power absorbed by the structure under solar illumination, denoted P_{abs}, is determined by weighing σ_{abs} by the AM1.5G solar spectral irradiance (ϕ) and integrating across the wavelength range of interest:

$$P_{abs} = \int_{\lambda_{min}}^{\lambda_{max}} \sigma_{abs}(\lambda)\phi(\lambda)d\lambda \tag{2.1}$$

P_{abs} represents the optical power that can be absorbed by the simulated structure when illuminated by the solar spectrum limited to the λ_{min} - λ_{max} range. In particular, it can be used to calculate the power absorbed by a particle located below a solar cell, that is supposed to absorb all radiation above its gap.

However, this absorbed power is not always relevant for estimating the performance of a photothermal interface. The essential aspect to take into account when designing an absorbing interface is the absorption per unit surface. For the same absorbing surface, an array of small nanoparticles with low σ_{abs} could actually gather more power than one larger particle. Therefore, we define the absorbed solar power normalized by the footprint of the particle S_{NP} as the absorbed power per unit surface, or P_{abs}^{S}:

$$P_{abs}^{S} = \frac{P_{abs}}{S_{NP}} \tag{2.2}$$

As an example, the absorption cross-section of a 300x300x150 nm nickel pad is shown in black in Figure 2.2, where it is compared to the irradiance of the AM1.5G solar spectrum for wavelengths between 0.875 µm and 2.5 µm. These two spectra are used to calculate the power absorbed by the pad over the wavelength range of interest, which is P_{abs} = 29 pW. This absorbed power is divided by the footprint of the pad (S_{NP} = 0.09 µm²) to get the power absorbed per unit surface (P_{abs}^{S} = 0.32 nW/µm²). In Figure 2.2, the red curve, representing the spectral distribution of P_{abs}^{S}, shows that around 10 % of the incoming solar irradiance is absorbed by the simulated particle.

In the following chapters, these two figures of merit are used to compare the absorption efficiency of simulated nanoantennas on the spectral range 0.875-2.5 µm. This range was selected as it corresponds to the part of the solar spectrum with an energy below the bandgap of a GaAs solar cell, which is the reference PV cell used for this work. This way, it allows to estimate the power absorbed by a particle located below said solar cell.

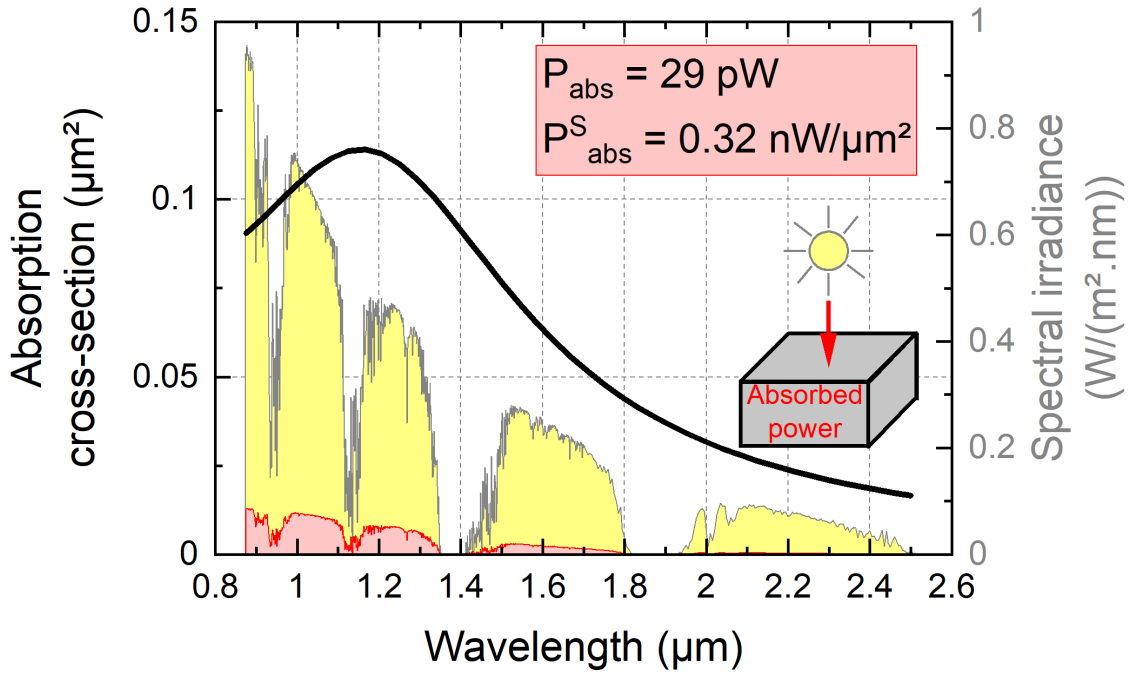

Figure 2.2: Illustration of the calculation of P_{abs} and P^S_{abs}, with the example of nickel pad with a side length of 300 nm (footprint of 0.09 µm²) and a height of 150 nm. The black curve represents the absorption cross-section of the pad, calculated by DDA between 0.875 µm and 2.5 µm wavelengths. It is weighted by the irradiance of the AM1.5G solar spectrum (in yellow) and integrated to determine P_{abs}, and then divided by the footprint of the pad to determine P^S_{abs}. The red curve represents the absorbed spectral irradiance (P^S_{abs}).

2.2 Nanopatterning techniques

Many techniques can be used to fabricate nano- or microscopic structures on a substrate. In this thesis, most samples were made using lithography of a resist, followed by a lift-off. This section is dedicated to the description of these different technological processes. First, the lift-off process, which allows to fabricate patterns onto a substrate using a resist, is presented. Prior to the lift-off, it is necessary to pattern the resist. For this purpose, two lithography techniques were used: electron-beam lithography, offering a high precision and control over the patterned structures; and hole-mask colloidal lithography, which enables quick patterning over large surfaces.

2.2.1 Principle and challenges of the lift-off process

The lift-off technique is a widely used method in the field of micro- and nanofabrication for the creation of metal patterns on substrate materials. It first requires the substrate to be coated with a resist, and the resist to be patterned using photolithography or other patterning techniques. Then, a metal layer is deposited on the resist layer and on the substrate according to the pattern. The resist is finally

dissolved, resulting in the unwanted metal being lifted off to leave behind the desired pattern on the substrate. The detailed steps required prior to the lift-off technique are:

1. **Substrate preparation:** The substrate material is cleaned and prepared to ensure a smooth and uniform surface.
2. **Resist coating:** The substrate is coated with a positive or negative resist, which is sensitive to light or other forms of radiation.
3. **Photolithography or other patterning technique:** The coated substrate is exposed to light or other forms of radiation, thereby defining the desired pattern. The exposed resist is then developed to remove the exposed areas in the case of a positive resist, or the non-exposed areas in the case of a negative resist, and leave behind a patterned resist.
4. **Metal deposition:** A layer of metal is then deposited over the patterned resist. The metal deposition process can be performed using a variety of techniques, including evaporation, sputtering, and electroplating.

As the final step, the metal is lifted off the substrate to leave behind the desired metal pattern. This can be achieved by dissolving the remaining resist in a solvent, which lifts off the undesired metal along with the resist, as presented in Figure 2.3A.

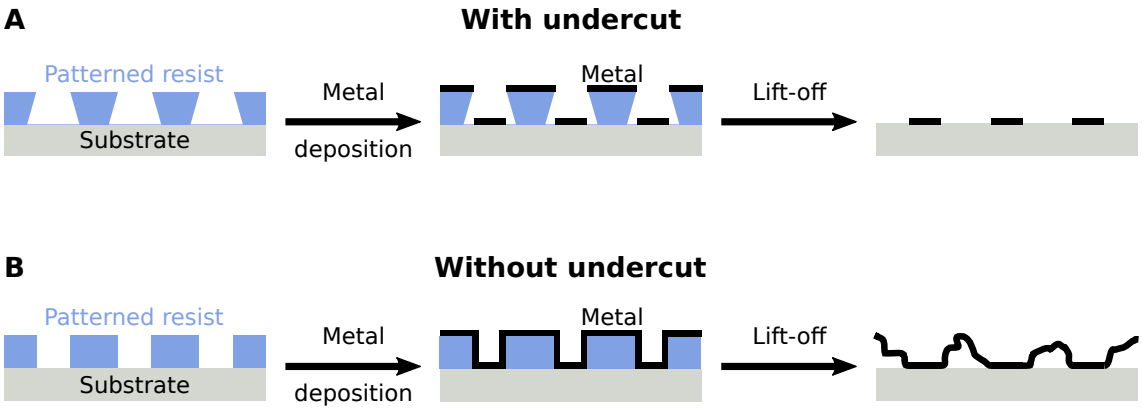

Figure 2.3: Scheme representing the lift-off process with (A) a patterned resist with undercut, leading to a successful lift-off and (B) a patterned resist without undercut, preventing the detachment of the undesired metal after dissolving the resist.

A key aspect of the lift-off technique is the undercut profile of the patterned resist. This undercut profile is often induced by the lithography technique or the etching process, and is necessary to create a discontinuous metal film by preventing metal deposition on the sides of the patterned apertures (see Figure 2.3A). Without undercut, the unwanted metal layer that should be lifted off would remain attached to the substrate and could not be removed, as illustrated in Figure 2.3B.

In our case, the substrate is covered by a poly(methyl methacrylate) (PMMA) layer, which is either exposed by electron-beam lithography and developed, or etched through in the case of colloidal lithography, to create the patterned mask. In both

cases, as discussed previously, it is important to make sure that lateral etching also takes place, resulting in holes with undercut profiles. Physical vapor deposition (PVD) is then used to cover the samples with metal. The lift-off is finally done in anisole to dissolve the PMMA layer. During the PVD, metal is also deposited on the edges of the holes, slowly closing them. Thus, the dimensions of the holes decrease during the deposition. This leads to structures with tilted walls, as can be seen on Figure 2.4, which shows the SEM image of a nickel pad fabricated through a lift-off process, using electron-beam lithography as the patterning technique. The slope of the walls, which is linked to the closing rate of the mask holes, is the same for all structures. After a given amount of metal is deposited, the holes will be completely closed, which happens sooner for small holes. There is thus a maximal height achievable for a structure with given lateral dimensions. This limitation can be overcome by using a different deposition technique, such as electroplating, in which the metal layer is grown from the substrate in a bottom-up fashion.

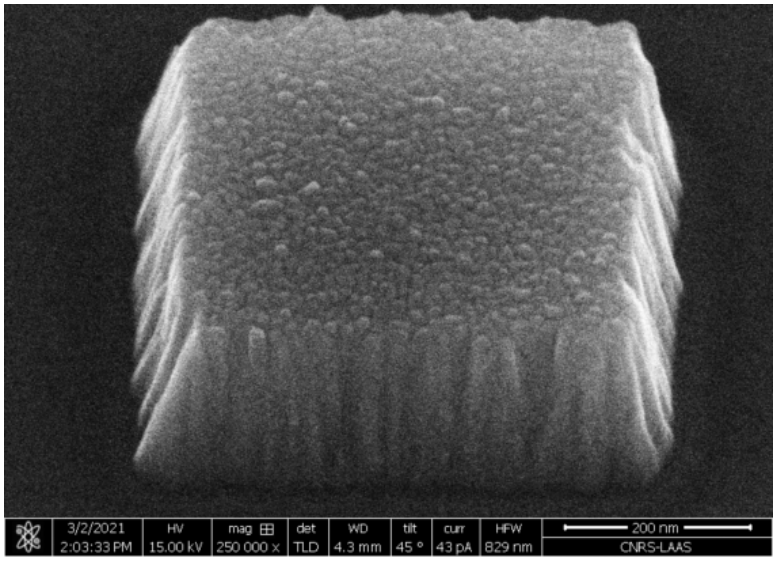

Figure 2.4: SEM image of a 540x540x150 nm pad-shaped nickel nanoantenna on silicon substrate fabricated through electron-beam lithography and lift-off process.

The lift-off technique is relatively simple and cost-effective compared to other patterning techniques, and is compatible with a wide range of substrate materials, including silicon, glass, and polymer films. Disadvantages of the lift-off technique include the need for a cleanroom environment, the difficulty in creating high-aspect-ratio structures, and the potential for metal residue or contamination of the substrate during the lift-off process. In terms of important details, it is crucial to properly control the metal deposition process to ensure an uniform thickness of the metal layer. Additionally, it is important to carefully select the resist material and solvent used for the lift-off process to ensure that the resist is easily removable and that the solvent does not damage the substrate or the metal pattern.

2.2.2 Electron-beam lithography

Description of the process

Electron-beam lithography (EBL) is a fabrication technique used to produce structures and patterns at the nanometer scale. In EBL, a beam of electrons is focused onto a substrate material, first coated with a layer of electrosensitive resist. When the electron beam passes over the resist, it causes chemical changes that alter the solubility of the resist. The resist is then developed to reveal the desired pattern, which can be used to transfer the pattern onto the underlying substrate material through a process such as etching or lift-off. EBL is a direct-write technique, as it does not require the use of a mask to transfer patterns onto the substrate. Its main advantage is its ability to create high-resolution and fine structures with feature sizes in the nanometer range, making it a valuable tool for applications such as the production of integrated circuits and the fabrication of nanoscale devices. However, EBL is typically slower and more expensive than other forms of lithography. Additionally, it requires specialized equipment and a cleanroom environment, which can increase the cost of fabrication.

The process of EBL can be divided into several steps, that are presented on Figure 2.5:

(a) **Substrate preparation:** The substrate material is carefully cleaned and prepared to ensure a smooth and uniform surface. This step is important to ensure that the resist coating is of high quality and that the patterns created during the EBL process are accurate and well-defined.

(b) **Resist coating:** The substrate is coated with a layer of electrosensitive resist. The resist coating thickness is typically in the range of a few hundred nanometers to a few micrometers.

(c) **Electron-beam exposure:** The coated substrate is then placed in the electron-beam lithography system and exposed to a focused beam of electrons. The electron beam is scanned over the substrate in a pattern defined by the user, causing chemical changes in the resist material. The formation of an undercut profile results from the interaction of backscattered electrons with the resist around the electron beam's point of focus on the substrate. The exposed areas of the resist are altered in a way that makes them more or less soluble in the developing solution, allowing for the creation of the desired pattern.

(d) **Resist development:** After exposure, the substrate is then treated with a developing solution to remove either the exposed (positive resist, see Figure 2.5d1) or unexposed (negative resist, see Figure 2.5d2) portions of the resist. The remaining resist acts as a mask, which can be used to transfer the pattern onto the substrate through a process such as lift-off or etching.

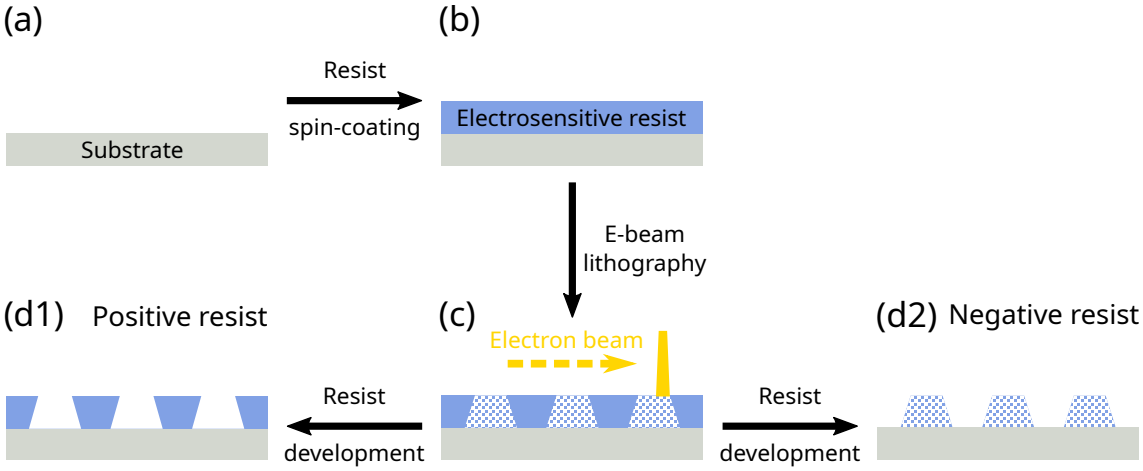

Figure 2.5: Scheme representing the patterning of an electrosensitive resist using electron-beam lithography.

Process parameters

The important parameters in electron-beam lithography include:

- **Beam energy:** The energy of the electron beam determines the depth of penetration into the substrate material, which is important for creating high-resolution patterns in a variety of materials.
- **Beam current:** The current of the electron beam is proportional to the dose of electrons delivered to the substrate per unit of time. The beam current determines the rate of exposure of the substrate and can be adjusted to control the thickness of the patterned layer.
- **Beam focus:** The focus of the electron beam is critical for achieving high-resolution patterns, as it determines the size of the electron beam spot on the substrate. A well-focused beam can produce patterns with resolutions in the sub-10 nm range.
- **Area dose:** The quantity of electric charge delivered to the substrate per unit area ($\mu C/cm^2$) determines the thickness of the patterned layer and affects the final pattern resolution. When exposing a new pattern or changing patterning conditions (substrate, resist thickness, ...), it is often necessary to first conduct a dose test in order to determine the optimal dose. An example of such a dose test is presented in Figure 2.6, where five doses are used to fabricate nickel pads with a nominal lateral side length of 540 nm. It can be seen that low doses result in defective structures, while high doses generate pads with larger dimensions. Finally, a dose of 120 $\mu C/cm^2$ would be selected in this case, as it allow a faithful replication of the shape with lateral dimensions close to the nominal ones.
- **Step size:** The distance between two exposure points of the pattern plays an important role in the final resolution. Increasing the step size results in a better resolution, but also in an increase of the process' time.

- **Pattern size:** The size of the pattern to be fabricated is an important parameter in electron-beam lithography, as it affects the beam current, dose, and focus required to achieve a desired resolution.

- **Substrate properties:** The properties of the substrate material, such as its electrical and thermal conductivity, chemical stability, and crystal structure, are important factors in electron-beam lithography. The substrate must be carefully chosen to ensure that it is compatible with the electron beam and the desired patterning process. For example, if using an electrically insulating substrate, it is necessary to add a conductive layer on top of the electrosensitive resist in order to prevent charging of the substrate that would result in a deviation of the electron beam.

- **Writing speed:** the time T needed to pattern a given area A is determined by the previous parameters. It depends on the beam current I and wanted dose D, according to $T = D \cdot A / I$. Increased beam currents allow to increase the writing speed but result in wider electron beam spots, thus reducing the final resolution.

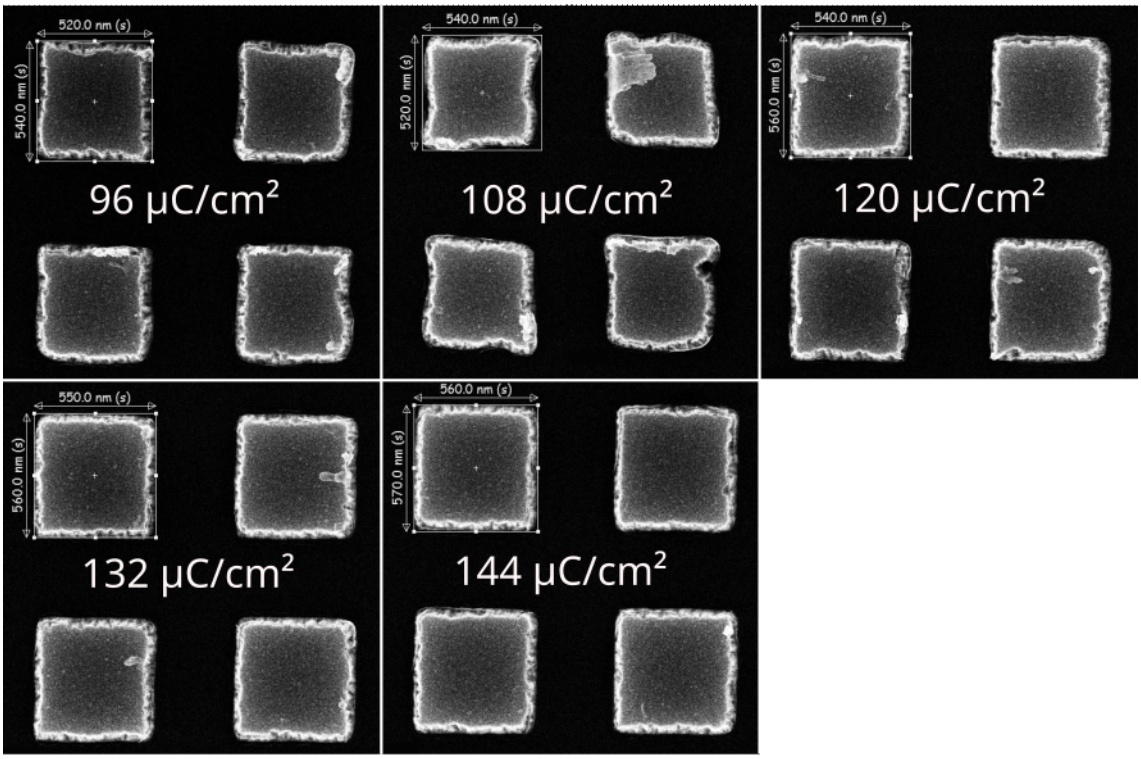

Figure 2.6: SEM images of pad-shaped nickel nanoantennas, with nominal dimensions 540x504x150 nm, made by electron-beam lithography with various beam doses on silicon substrate.

In this work, different substrates have been used to fabricate nanoantennas by EBL in the LAAS cleanroom. In any case, the substrate is always washed in acetone and water, and then dried. A 5-minute oxygen plasma treatment (0.8 mbar, 800 W) is then used as a last cleaning step to get rid of contaminants. A 300 nm thick resist layer is produced by spin-coating a 70 g/L solution of PMMA ($M_W = 996000$

from Sigma-Aldrich) in anisole at 4000 rpm for 60 s, followed by a 60 s annealing at 180 °C on a hot plate. A final cleaning is then done by a 5 min long oxygen plasma treatment (0.8 mb, 800 W) in order to remove impurities. For electrically insulating substrates such as glass, a layer of Electra 92 conductive resist is spin-coated on top of PMMA at 2000 rpm for 60 s and annealed at 90 °C for 2 min. The exposure is carried out in a Raith150 E-beam writer at 20 kV, 30 µm of aperture, and 7 mm of working distance. To ensure accurate pattern replication even for objects with acute angles, the step size is set at 10 nm. The Electra 92 layer is removed with water following the lithography step, and the sample is then dried. To reveal the pattern, the resist is developed for 60 s in a MIBK:IPA (1:3) solution. After that, PVD is used to deposit the metal layer. For the final lift-off stage, the sample is kept in a beaker of anisole until the PMMA resist is completely dissolved, which typically takes a few minutes.

2.2.3 Hole-mask colloidal lithography

Description of the process

Hole-mask colloidal lithography [123] is a patterning technique that utilizes the self-assembly of charged colloidal particles to create micro- and nanostructures on a substrate. The colloidal lithography technique has several key steps, illustrated in Figure 2.7:

1. **Preparation of the colloidal suspension:** A suspension of spherical nanoparticles, in our case polystyrene beads, is prepared in a solvent, typically with a diameter range of 10 to 1 000 nanometers. The choice of nanoparticle material and size is important for controlling the final pattern resolution and determining the pattern quality. The beads are negatively charged to allow their self-assembly and prevent aggregation.

2. **Substrate preparation:** The substrate material is cleaned and prepared to ensure a smooth and uniform surface.

3. **Resist coating:** The substrate is coated with a layer of resist or other sacrificial layer. The resist coating thickness is typically in the range of a few hundred nanometers to a few micrometers. The resist often undergoes a quick plasma treatment to ensure its hydrophilicity.

4. **Charging of the resist:** The resist is covered by a charged polymer solution then rinsed, creating a positively charged monolayer on top of it. The role of this charged layer is to attract and anchor the negatively charged beads on the surface.

5. **Self-assembly of nanoparticles:** The colloidal suspension is then dropcasted on the resist-covered substrate. The self-assembly process is driven by interparticle electrostatic interactions and the surface energy of the substrate, leading to the formation of a nanoparticle pattern with no long-range order.

The conditions of the deposition process, such as the deposition time, need to be carefully controlled to ensure that the final nanoparticle pattern is uniform and well-defined. After a few minutes, when the surface is saturated with nanoparticles, the suspension is rinsed away from the sample, which is then carefully dried. At the end of this step, a disordered arrangement of particles covers the surface, as shown in Figure 2.8A.

6. **Creation of the hole-mask:** A thin layer of metal, typically chromium, is deposited on top of the resist and the beads. Then, the beads are removed using an adhesive tape or a solvent, leaving holes in the chromium layer.

7. **Etching:** The resist is etched through the holes by a wet or dry approach. This final step results in a patterned resist (visible in Figure 2.8B) that can be used to make nanostructures on the substrate by a lift-off process.

Hole-mask colloidal lithography (HCL) is highly versatile, compatible with a wide range of materials and substrates, and can be used to create large-area patterns with high precision and uniformity. Additionally, HCL is a relatively simple and cost-effective process that can be easily integrated into existing fabrication techniques. Its main drawbacks are the limitation to circular or elliptical patterns, and the lack of control over the long-range ordering.

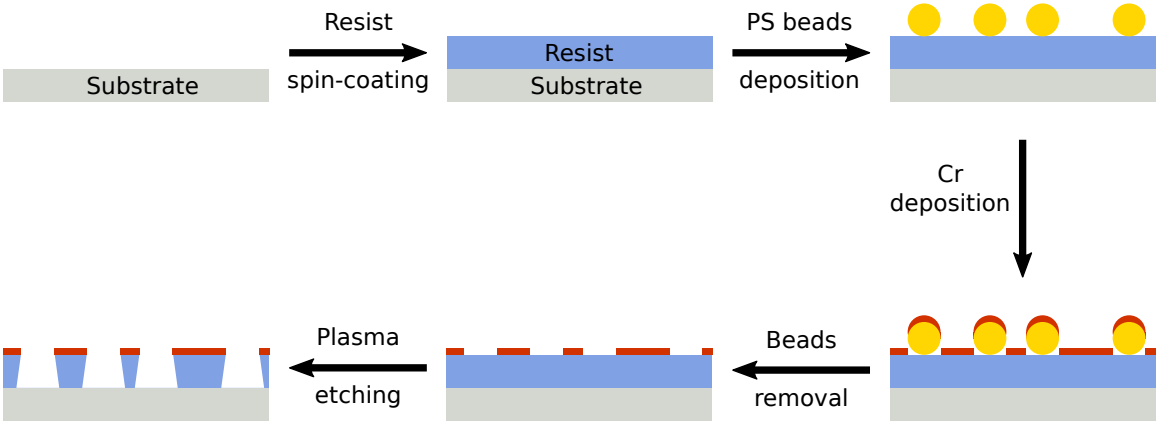

Figure 2.7: Scheme representing the patterning of a resist using hole-mask colloidal lithography.

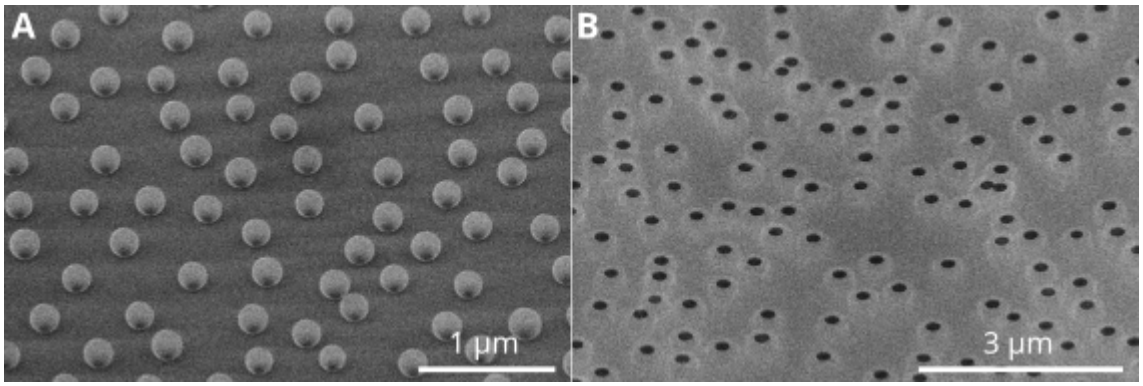

Figure 2.8: SEM images taken with a 53° tilt, at different steps of the HCL process: (A) After self-assembly of colloidal particles, and (B) after etching through the chromium mask.

Process parameters

The important parameters in colloidal lithography are listed below:

- **Particle size and size distribution:** The size and size distribution of the colloidal particles are important for determining the resolution and uniformity of the final pattern. The size of the particles can be controlled using techniques such as centrifugation or filtration to achieve a desired size range and size distribution. In our case, we used commercial dispersions of polystyrene beads in water, with a nominal diameter of 200, 300 or 500 nm and a size dispersion of $\pm$ 5 %.

- **Particle concentration:** The concentration of the colloidal particles in the solution affects the overall packing density of the particles and the final pattern resolution. A higher concentration of particles leads to a higher packing density and improved resolution, but also increases the risk of particle aggregation and defects in the final pattern. Typically, the particle concentration is between 0.02 and 1 wt. %.

- **Electrostatic interactions:** The particles need to be charged to prevent aggregation during the self-assembly. The force of the electrostatic interaction determines the average inter-particular distance of the final pattern. It can be tuned by adding ionic species in the solution to screen interparticle repulsion [124, 125] or modifying the pH.

- **Self-assembly time:** it corresponds to the time during which the dispersion is allowed to sit on the substrate before being rinsed. During that time, the particles are pulled toward the substrate's surface by gravity, and self-assemble according to the electrostatic interactions. Longer self-assembly durations lead to higher particle density on the substrate and higher short-range order, until saturation of the substrate. Generally, the deposition time, which depends on the particle size and the ionic strength of the solution, is chosen to reach saturation.

Moreover, the conditions under which the colloidal particles are deposited onto the substrate, such as the solution flow rate or the substrate temperature and inclination, can affect the final pattern resolution and uniformity. These conditions must be carefully controlled to achieve a high-quality pattern.

In the framework of this thesis, the fabrication of nanoantennas by hole-mask colloidal lithography was done in the Nanofabrication Laboratory, at Chalmers University of Technology. We first wash the substrates with acetone and isopropyl alcohol. Then, PMMA resist (Microchem Corporation, 5 wt % PMMA diluted in anisole, $M_W = 950000$) is spin-coated at 3000 rpm for 45 s before annealing the sample for 2 min on a hot plate heated at 180 °C. The sample is subsequently treated by oxygen plasma for 20 s at 50 W to improve the hydrophilicity of the top interface. In order to positively charge the surface, a 0.2 wt% solution of poly(diallyldimethylammonium chloride) (Sigma-Aldrich, M_W = 200000-350000) in water is drop-casted on the sample and allowed to sit for 30 s before rinsing with deionized water and drying. A few drops of a dispersion of polystyrene beads (Invitrogen, sulfate latex) in water is then immediately deposited on the sample. The beads are adsorbed on the sample for typically 2 min before gently rinsing under a flow of water and drying. The following deposition of a 10 nm thick Cr layer and removal of the beads with tape leads to the reveal of the patterning mask in the Cr layer. The PMMA layer is finally etched through the holes in the Cr layer by oxygen plasma for 6 min at 50 W, before deposition of a metal layer by PVD and lift-off of the PMMA layer in acetone.

2.3 Characterization of the nanoantennas' photothermal properties

This section is dedicated to the presentation of the tools used in this thesis for the characterization of photothermal interfaces. Fourier Transform Infrared Spectroscopy is used to measure their optical properties, mainly absorption and reflection spectra. We also describe an experimental setup based on infrared thermography to estimate their temperature under solar illumination.

2.3.1 FTIR spectroscopy

Fourier Transform Infrared (FTIR) spectroscopy is a type of spectroscopy traditionally used to study the molecular vibrations and chemical bonds of a sample. The FTIR spectroscopy is based on the interaction between infrared radiation and the sample molecules. Infrared radiation, with a wavelength longer than visible light, has sufficient energy to cause vibrational transitions in the sample molecules, leading to a change in their absorption or transmission properties. However, using the right source and detector, the technique can also be used in other wavelength ranges, such as visible or near-infrared.

In all cases, radiation is generated by a light source and directed onto the sample through an optical path. The radiation interacts with the sample and is either reflected, scattered, absorbed or transmitted, leading to a change in the beam intensity. The interaction between the incident radiation and the sample depends on the energy levels of the molecular vibrations and electronic transitions and the frequency of the radiation. The transmitted or reflected radiation is collected and passed through a Fourier Transform (FT) analyzer, which converts the time-domain signal into a frequency-domain signal, also known as the interferogram. The interferogram is transformed using mathematical algorithms, such as the Fast Fourier Transform, to obtain the FTIR spectrum, which represents the absorption or transmission properties of the sample as a function of frequency. The FTIR spectrum can be used to identify the molecular vibrations and chemical bonds of the sample, and to obtain information on the sample's composition, structure, and properties. FTIR spectroscopy is a powerful and versatile tool for analyzing a wide range of samples, including gases, liquids, solids, and polymers. It is widely used in fields such as chemistry, biology, materials science, and environmental science, and provides information that is not accessible by other analytical methods.

In the scope of this thesis, FTIR spectroscopy has been used to measure the absorption and reflection spectra of bare substrates and substrates covered with nanoparticles or thin films. These spectra were usually acquired in the visible to near infrared range from the front of the substrate, in order to analyze their interaction with the solar spectrum. Spectra were also acquired from the back of the samples in the mid-infrared range (between 5 and 20 µm), which corresponds to the window of black body radiation for objects around ambient temperature.

2.3.2 Temperature measurement by infrared thermography

The goal of our photothermal interfaces is to generate heat under solar infrared illumination. To measure the temperature of irradiated samples, we devised an experimental setup based on infrared thermography, using a solar simulator and an infrared camera. Prior to these measurements, it is necessary to determine the emissivity of the samples, as it is of crucial importance in the operation of the camera.

Emissivity

A black body is a perfect absorber, a theoretical system that absorbs 100 % of the incoming radiation (A=1), at any wavelength. This absorbed power is converted into heat, which results in an increase of the black body's temperature. In vacuum, the only way for this system to dissipate energy is through radiation. The Planck's law describes the radiance L^{BB} of a black body in thermal equilibrium at temperature T and wavelength λ:

$$L^{BB}(\lambda, T) = \frac{2hc^2}{\lambda^5} \frac{1}{e^{\frac{hc}{\lambda k_B T}} - 1} \tag{2.3}$$

where h is the Planck constant, c the speed of light, and k_B the Boltzmann constant. The Stefan-Boltzmann law, which describes the emittance (total power radiated by unit surface) of a black body can be obtained by integrating the radiance over all wavelengths:

$$M^{BB}(T) = \int_0^\infty L^{BB}(\lambda, T)\, d\lambda = \sigma T^4 \tag{2.4}$$

Hence the definition of the Stefan-Boltzmann constant σ:

$$\sigma = \frac{2\pi^5 k_B^4}{15c^2h^3} \approx 5.670374 \times 10^{-8}\ \mathrm{W\,m^{-2}\,K^{-4}} \tag{2.5}$$

In practice, real materials only emit a fraction of the black body's power, which is why they are called "gray bodies". For a wavelength λ, the radiance of a gray body L is that of a black body L^{BB} weighted by the spectral emissivity $\epsilon(\lambda)$, a factor comprised between 0 and 1.

$$L(\lambda, T) = \epsilon(\lambda) L^{BB}(\lambda, T) \Rightarrow \epsilon(\lambda) = \frac{L(\lambda, T)}{L^{BB}(\lambda, T)} \tag{2.6}$$

A material with an emissivity of 1 is a black body, while an emissivity of 0 characterizes a white body, a material that doesn't absorb nor emit any electromagnetic radiation. The Stefan-Boltzmann law can be rewritten in the general case of the gray body:

$$M(T) = \int_0^\infty L(\lambda, T)\, d\lambda = \int_0^\infty \epsilon(\lambda) L^{BB}(\lambda, T)\, d\lambda = \epsilon_M(T)\sigma T^4 \tag{2.7}$$

Where ϵ_M is the spectral emissivity weighted by the black body radiance over the whole spectrum:

$$\epsilon_M(T) = \frac{\int_0^\infty \epsilon(\lambda) L^{BB}(\lambda, T)\, d\lambda}{\int_0^\infty L^{BB}(\lambda, T)\, d\lambda} \tag{2.8}$$

Infrared camera

Temperature measurements of photothermal interfaces were conducted using an infrared camera. When pointing toward a sample at temperature T, the Focal Plane Array (FPA) detectors matrix of the camera absorbs radiations with wavelengths

between 7.5 and 14 µm, resulting in the heating of the detectors and a change of their electrical resistance, which can be measured by the camera. The optical power detected at a pixel P_{det} originates from external and internal sources. The general relation between P_{det}, the radiance of the combined external sources $L_{ext}(T,\lambda)$ and the radiance of the internal source $L_{int}(\lambda)$ is:

$$P_{det} = A \int_{7.5\,\mu m}^{14\,\mu m} L_{ext}(T,\lambda)\, d\lambda + B \int_{7.5\,\mu m}^{14\,\mu m} L_{int}(\lambda)\, d\lambda \tag{2.9}$$

A and B are coefficients with dimensions m^2 related to the camera's properties, taking into account the area and transmittance of the lens, the area and field-of-view of the pixel, and the detector's responsivity. The internal source is the black body emission of the lens in front of the detector.

External sources include the black body emission of the sample ($L^{BB}(\lambda,T)$), which is the parameter of interest, as well as the radiation transmitted through and reflected by the sample, as described in Equation 2.10.

$$L_{ext}(T,\lambda) = \epsilon(\lambda) L^{BB}(\lambda,T) + (\rho(\lambda) + \tau(\lambda)) L^{BB}(\lambda, T_{amb}) \tag{2.10}$$

The ratio of emission to combined transmission and reflection depends on the emissivity of the sample. Indeed, according to Kirchhoff's law, emissivity is equal to absorptivity. Equation 2.11 presents the relationship between emissivity, absorptivity $\alpha(\lambda)$, reflectivity $\rho(\lambda)$ and transmittance $\tau(\lambda)$.

$$\alpha(\lambda) + \rho(\lambda) + \tau(\lambda) = 1 \Rightarrow \rho(\lambda) + \tau(\lambda) = 1 - \epsilon(\lambda) \tag{2.11}$$

Thus, $L_{ext}(T,\lambda)$ can be expressed as:

$$L_{ext}(T,\lambda) = \epsilon(\lambda) L^{BB}(\lambda,T) + (1 - \epsilon(\lambda)) L^{BB}(\lambda, T_{amb}) \tag{2.12}$$

Where T is the temperature of the sample and T_{amb} the ambient temperature. Finally, if the emissivity of the sample is constant over the 7.5-14 µm range, Equation 2.9 becomes:

$$P_{det} = A \cdot \epsilon \cdot \int_{7.5\,\mu m}^{14\,\mu m} L^{BB}(T,\lambda)\, d\lambda + A \cdot (1-\epsilon) \cdot \int_{7.5\,\mu m}^{14\,\mu m} L^{BB}(T_{amb},\lambda)\, d\lambda + C \tag{2.13}$$

With:

$$C = B \int_{7.5\,\mu m}^{14\,\mu m} L_{int}(\lambda)\, d\lambda \tag{2.14}$$

To sum up, when using an infrared camera to measure the temperature of a sample, it is necessary to know the emissivity of the sample $\epsilon(\lambda)$, as well as the ambient temperature T_{amb}. A lack of accuracy in the input of these parameters can result in a significant error in the temperature displayed by the camera, especially for materials with low emissivity.

2.3.3 Setup for photothermal characterization

An experimental setup was built in order to characterize the light-to-heat conversion of samples, in which the idea is to illuminate the sample from the front side while measuring its temperature on the back side (see photography of the setup in Figure 2.9A). For this purpose, it is necessary to control the incident light intensity and to be able to precisely measure temperature. Thus, a AAA class solar simulator (Pico LED simulator, G2V Optics) was used for illumination, ensuring good matching with the solar spectrum, as well as spatial and temporal uniformity. This simulator, containing 30 LEDs, can emit from 350 to 1500 nm. The intensity of each LED can be controlled independently, which allows to simulate a variety of different spectra, from AM0 to AM40, at any position on Earth, or to restrict the emission to a specific spectral range.

Here, in the context of this PhD, in order to simulate the light power reaching a photothermal interface placed below a PV cell with a 800 nm energy gap, the solar simulator was set to deliver an AM1.5G spectrum restricted to the 800-1500 nm range, which represents a power of 309 W/m^2. The incident spectrum delivered by the solar simulator is presented in Figure 2.9B.

The temperature measurements were done with a Testo 885 IR camera. Using infrared thermography instead of thermocouples allows for non-intrusive contactless measurements. Furthermore, an IR image gives information about the 2D distribution of temperature.

FTIR spectroscopy (see Section 2.3.1) has been used to determine the emissivity of the back side of the samples. Using a Bruker Vertex 70 Fourier Transform Infrared spectrometer connected to a microscope with a 15x objective and a numerical aperture of 0.4, reflection and transmission spectra of the backside of the samples were recorded under normal incidence. The absorptivity α can be computed using Equation 2.11, where τ and ρ are the observed transmittance and reflectivity, respectively. This formula works as long as the samples' rear side does not show diffuse reflectance, which is the case for smooth substrates. Rough substrates thus need to be polish before measuring their absorptivity. The average emissivity ϵ was then determined using Kirchhoff's rule after averaging the absorptivity spectra across the camera's detection range (7.5–14 µm). A K-type thermocouple is used to measure the room temperature.

The setup used for the photothermal measurements is presented in Figure 2.9A. Each sample is positioned 3 cm away from the simulator, with the top side facing the source, and separated from it by a 4-inch fused silica wafer. The fused silica wafer

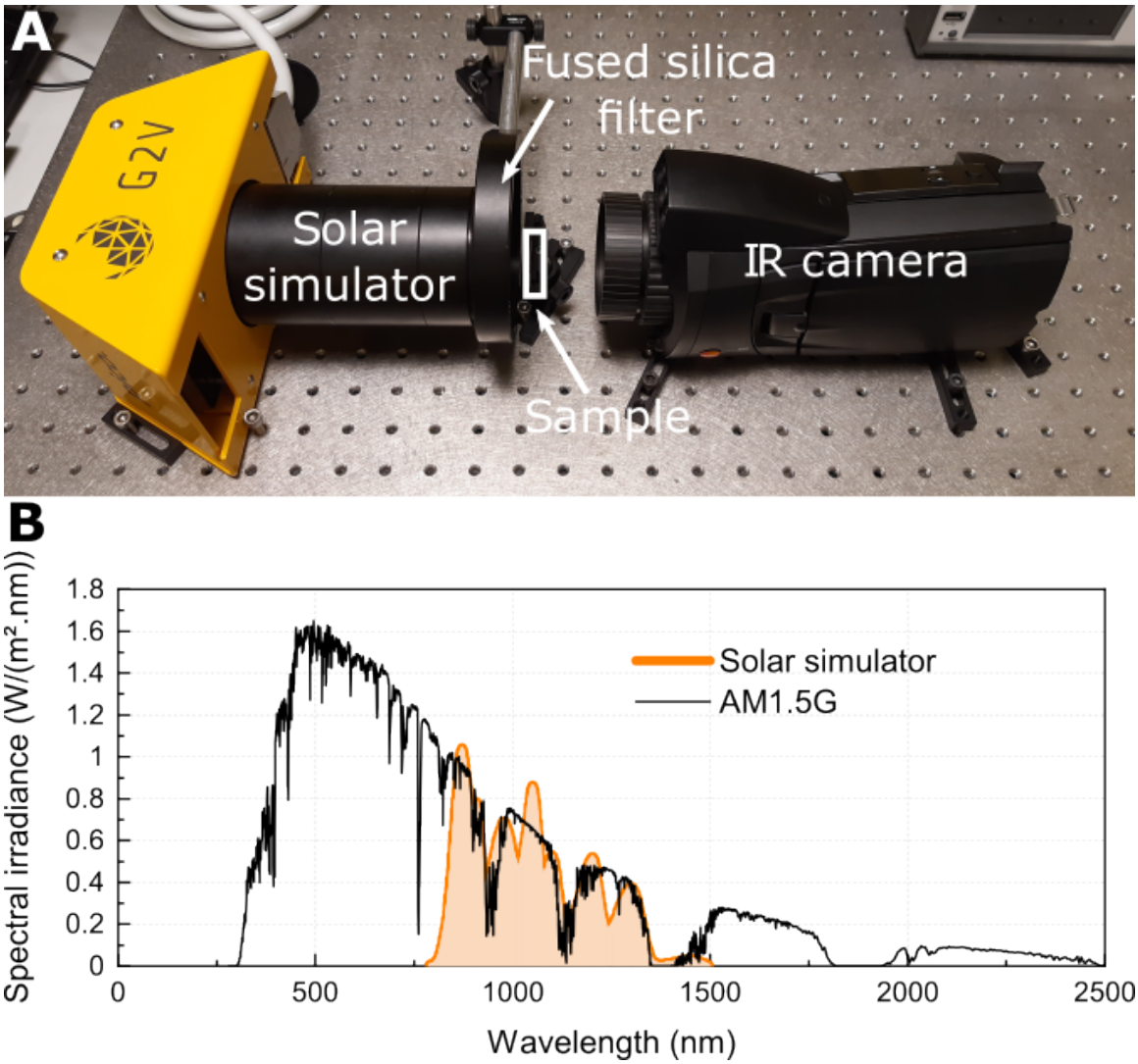

Figure 2.9: (A) Picture of the photothermal characterization setup showing the solar simulator, infrared camera, fused silica filter and positioning of the sample. (B) Illumination spectrum generated by the solar simulator when limited to the 800-1500 nm range (orange curve), compared to the standard AM1.5G solar spectrum (black curve).

is fully opaque to wavelengths between 5 and 20 µm, preventing thermal radiation from the source from reaching the sample or the camera. The IR camera is placed on the optical axis, 7 cm behind the sample. Thermal images are thus taken on the back side of the sample. By acquiring several IR photos over a period of 1 hour, ensuring temperature stabilization, the temperature increase under light for each sample is dynamically measured.

Chapter 3

Electromagnetic numerical simulations of isolated nanoantennas

In order to design an efficient nanostructured photothermal interface, we first tried to identify the optimal nanoantenna for solar infrared absorption. As the parameter space of possible geometries, sizes and compositions is virtually endless, we used electromagnetic simulations to calculate the optical response of a large number of different isolated nanoantennas. Using relevant figures of merit that take into account the incident solar spectrum, we were able to rank the structures according to their efficiency for harvesting solar infrared power. We then fabricated nanoantennas using electron-beam lithography, and studied the impact of the fabrication defects on their optical properties, in order to assess the tolerance of nanoantennas to the deviation related to technological fabrication.

Contents

3.1 Exploration of various shapes of nanoantenna for optical absorption

The study of nanoantennas has gained significant attention in recent years due to their unique ability to manipulate and control light at the nanoscale. These structures exhibit strong interactions with incident electromagnetic waves, making them promising candidates for applications in nanophotonics [126, 127, 128, 129], sensing [130, 131], and energy harvesting [132, 133]. The size and shape of a nanoparticle can strongly influence its optical properties. The variety of nanostructures already fabricated for numerous applications is huge, ranging from rather simple spheres and wires to more complex bow-tie geometries or nanostars [134, 135].

In this chapter, we present numerical simulations we have used to investigate the optical properties of isolated nanoantennas and assess their potential for solar infrared absorption. By systematically varying their geometric parameters, such as dimensions and shapes, we aimed to gain insights into how these parameters affect the absorption spectra of the nanoantennas. In our simulations, we considered the five different shapes shown in Figure 3.1: disk, pad, rod, truncated cone and diabolo. For each shape, the dimensions of the nanoantennas were systematically varied, and their absorption spectra were calculated using the DDA method (see Section 2.1 for more details on this method). The height of these simulation targets was kept constant at 150 nm in order to take into account the limitations introduced by the lift-off process described in Section 2.2.1.

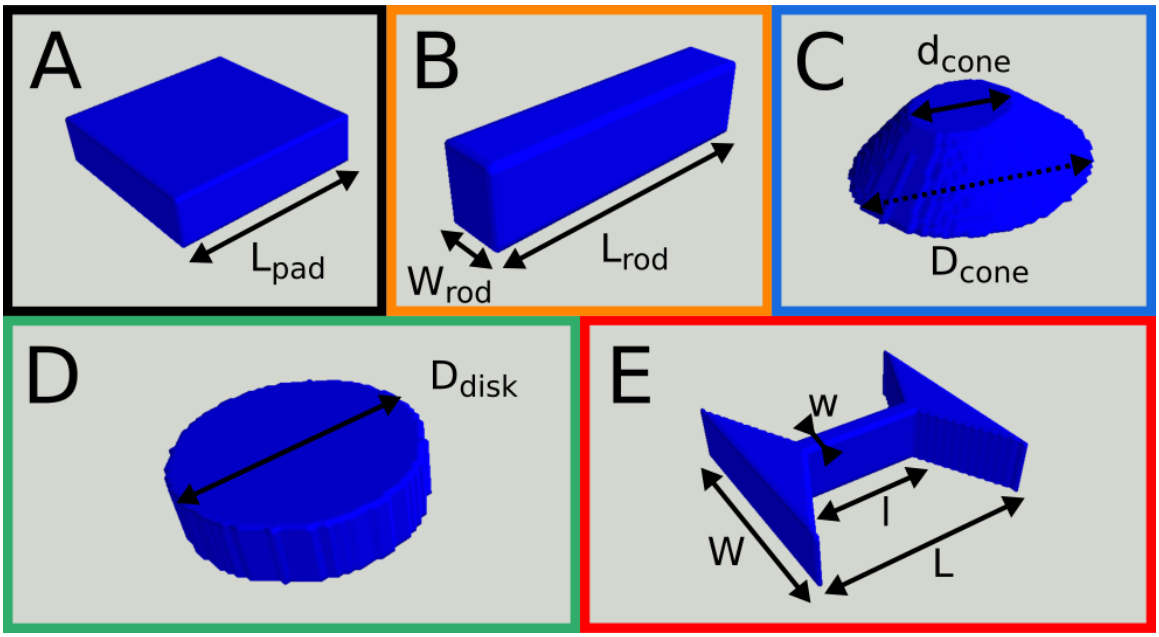

Figure 3.1: 3D representation of the models used for the DDA calculations: (A) pad, (B) rod, (C) cone, (D) disk and (E) diabolo geometries, their varying parameters marked. Reprinted with permission from ACS Appl. Energy Mater. 2023, 6, 4, 2128–2133. Copyright 2023 American Chemical Society.

3.1.1 Impact of the size for simple geometries

We first examined simple geometries such as disks (Figure 3.1D) and pads (Figure 3.1A), which only have one varying dimension: the diameter D_{disk} and side length L_{pad} respectively. Several absorption spectra were calculated by varying the lateral dimensions of these nanoantennas between 200 and 600 nm.

We started our investigation by simulating the optical properties of disk-shaped nanoantennas with varying diameters. By altering the dimensions of the disks, we observed distinct changes in their absorption spectra, as presented in Figure 3.2. Specifically, we noted a redshift of the absorption peak towards longer wavelengths and an increase in absorption intensity as the diameter of the disks increases.

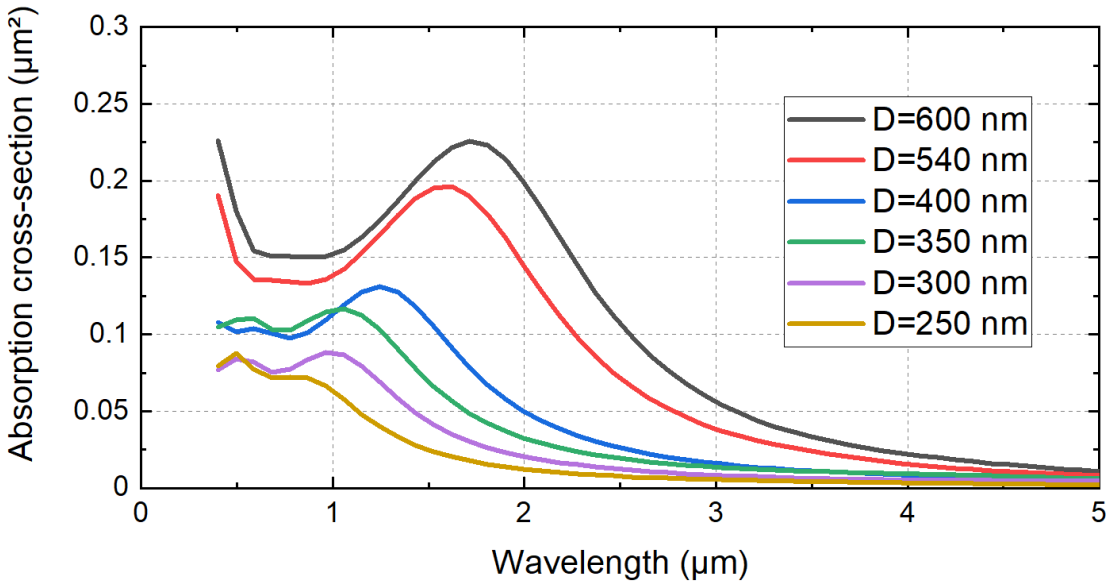

Figure 3.2: Absorption cross-section of nickel disks with varying diameter (D) and a constant height of 150 nm, calculated using the DDA method.

Continuing our exploration, we shifted our focus to pad-like nanoantennas, which possess equal length and width. We thus still consider only one varying parameter: the side length of the pad. Pads are close in shape to disks, the main difference being the presence of corners in the pad geometry. By modifying the side length while keeping the thickness constant, we calculated the absorption spectra presented in Figure 3.3. Similar to the disk simulations, increasing the side length of the pad resulted in a redshift of the absorption peak towards longer wavelengths and an increase of the absorption intensity.

The absorption spectra obtained from the simulations revealed important trends in the behavior of the nanoantennas. In both the disk and pad cases, we observed a shift of the absorption peak towards longer wavelengths with larger lateral dimensions. This is expected and in accordance with the literature [97, 136, 137]. The overall increase in absorption cross-section with increasing size is mostly attributable to the increase in the antenna's volume. Furthermore, the increase in absorption cross-section and resonance wavelength observed when switching from disks to pads, for a given size, is consistent with the fact that pads with a given side length exhibit

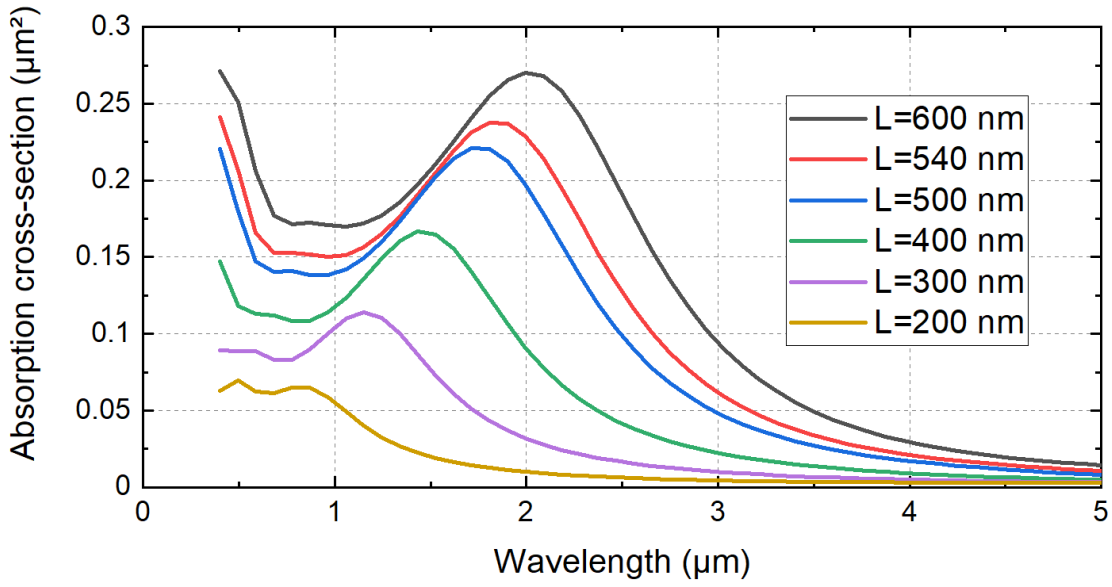

Figure 3.3: Absorption cross-section of nickel pads with varying length (L) and a constant height of 150 nm, calculated using the DDA method.

a larger volume compared to disks with the same diameter. Indeed, a pad with a side length of 600 nm has more volume (0.054 µm^3)than a disk with a diameter of 600 nm (0.042 µm^3).

In this section, we have presented the initial results of our numerical simulations on the optical properties of isolated nanoantennas. By varying the lateral dimensions of simple nanoantenna geometries such as disks and pads, we observed a redshift in the absorption peak towards longer wavelengths and an increase in absorption intensity with larger nanoantenna dimensions. Our objective is to absorb solar infrared radiation between 0.875 and 2.5 µm. Disks and pads need large dimensions to achieve strong absorption in this wavelength range, meaning that the absorption per unit surface is hindered. Thus, further investigations will be conducted to explore more complex geometries in order to find increased absorption properties for nanoantennas with a limited footprint.

3.1.2 Adding anisotropy: the rod geometry

In order to further investigate the impact of lateral dimensions on the optical properties of nanoantennas, we explored a new shape, the rod (see Figure 3.1B), which is a variation of the pad. This geometry offers two degrees of freedom in the lateral dimensions, specifically the length and width of the nanorods. We can thus define the aspect ratio (AR) of a nanorod as the ratio between its length and width. By systematically varying these parameters, we examined their effects on the calculated absorption spectra.

The following nanorod dimensions were studied: 300x200 nm (AR=1.5), 300x50 nm (AR=6), 400x200 nm (AR=2), 400x50 nm (AR=8), 500x200 nm (AR=2.5), 500x50 nm (AR=10), 600x200 nm (AR=3), and 600x50 nm (AR=12). The obtained

absorption spectra, presented in Figure 3.4, revealed interesting trends with respect to the nanorod dimensions.

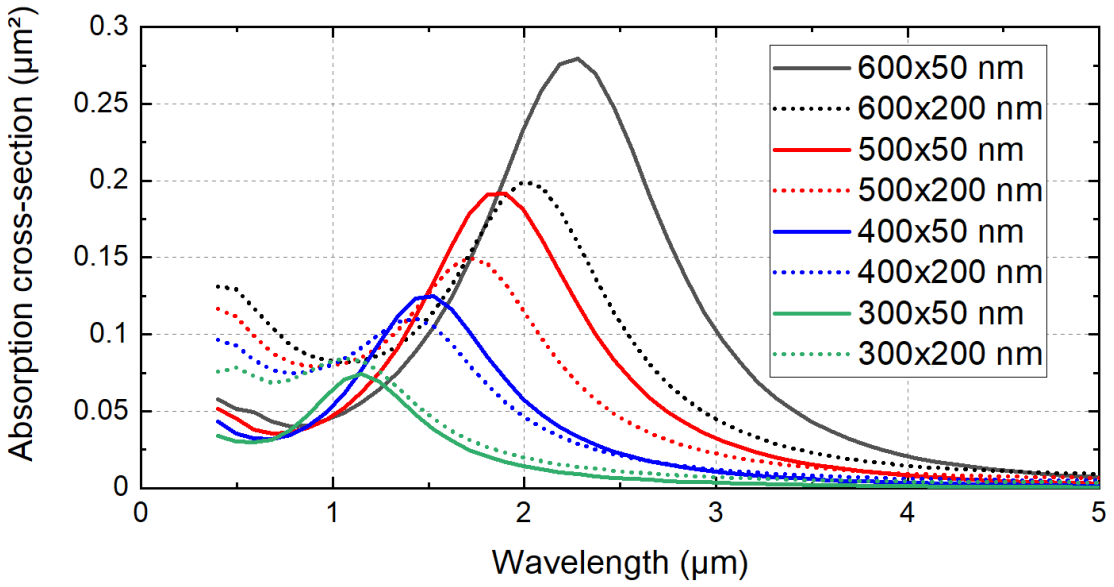

Figure 3.4: Absorption cross-section of nickel rods with varying lateral dimensions and a constant height of 150 nm, calculated using the DDA method.

By increasing the length of the nanorods while maintaining a constant width, we observed a consistent shift towards longer wavelength, as well as an intensity enhancement, of the absorption peak. This phenomenon is similar to what was observed previously for the disks and pads, which exhibited increased absorption cross-section and wavelength for particles with larger volumes.

Moreover, rods show higher absorption cross-section than disks or pads with comparable volume V. For example, the disk with a 350 nm diameter (V=0.0144 µm^3) and the pad with a side length of 300 nm (V=0.0135 µm^3) show a maximal absorption cross-section of 0.12 µm^2 and 0.11 µm^2 respectively, while the rod with dimensions 500x200 nm (V=0.0150 µm^3) reaches an absorption cross-section of 0.15 µm^2. Baffou et al. previously reported this behavior by comparing the heating, which is directly linked to optical absorption, of gold nanorods with varying aspect ratio and identical volume [138]. Their results demonstrate that the elongated geometry of rods is beneficial to their absorption-over-volume ratio.

In contrast to the length variation, increasing the width of the nanorods leads to a blueshift of the absorption peak, combined with a decrease in absorption intensity. This effect seems to be more impactful for nanorods having a high aspect ratio. Interestingly, this means that the absorption intensity of a nanorod can be enhanced by reducing its volume while increasing its aspect ratio, as can be seen in Figure 3.4, when switching from the 600x200 nm to the 600x50 nm rod for example. This effect could be leverage to create highly absorbing structures with a limited amount of material.

3.1.3 Increasing complexity: the diabolo geometry

Expanding our investigation, we introduced a novel geometry called the diabolo, which, as presented in Figure 3.1E, possesses four variable dimensions: total length (L), total width (W), neck length (l), and neck width (w). In the following paragraphs, the diabolos will be identified by their dimensions in the form $[W \times L - w \times l]$. This intricate geometry offers additional degrees of freedom for exploring the optical properties of nanoantennas. The diabolo nanoantenna is the complementary shape of the bow-tie geometry, commonly used to generate electric hotspots in the gap between two prisms [139, 140, 141]. In the diabolo geometry, the prisms are connected by a neck, resulting in a large enhancement of the current density within the antenna under illumination [142]. Our motivation for the study of this structure is that the strong current density in diabolo nanoantennas has been shown to lead to efficient photothermal conversion [143].

To evaluate the optical behavior of diabolos, we first generated a nanoantenna with dimensions $600 \times 600 - 300 \times 300$ nm, and compared its optical response to a pad having the same total dimensions (600×600 nm) and a pad having the dimensions of its neck (300×300 nm). The calculated absorption cross-section spectra of these three structures are presented in Figure 3.5A, where it can clearly be seen that the diabolo exhibits a stronger absorption than the pads over a wide range of wavelength.

In Figure 3.5B, the absorption spectrum of a second diabolo with comparable total dimensions and a thinner neck ($540 \times 540 - 300 \times 50$ nm) was also simulated and compared to a 540×540 nm pad and a 300×50 nm rod. Once again, the absorption cross-section of the diabolo is larger than that of the pad or the rod for wavelengths above 750 nm.

These results indicate that the unique geometry of the diabolo enhances its light-matter interaction, resulting in improved absorption properties for the same volume, as compared to simpler geometries.

To further unravel the impact of a diabolo's dimensions on its optical absorption, we conducted comprehensive simulations for a wide range of dimensions. Due to the high number of degrees of freedom in the dimensions of the diabolo, we divided this study into two categories:

1. **Study of the impact of the total dimensions:** Diabolos with constant neck dimensions of 300×300 nm were simulated. The total length was varied between 400 nm and 600 nm, for two different total width of 400 nm and 600 nm. The calculated absorption spectra and corresponding structures are presented in Figure 3.6A-B.

2. **Study of the impact of the neck's dimensions**: Diabolos with constant total dimensions of 540×540 nm were simulated. The length of the neck was varied between 50 nm and 300 nm, for two different neck width of 50 nm and 300 nm. The calculated absorption spectra and corresponding structures are presented in Figure 3.6C-D.

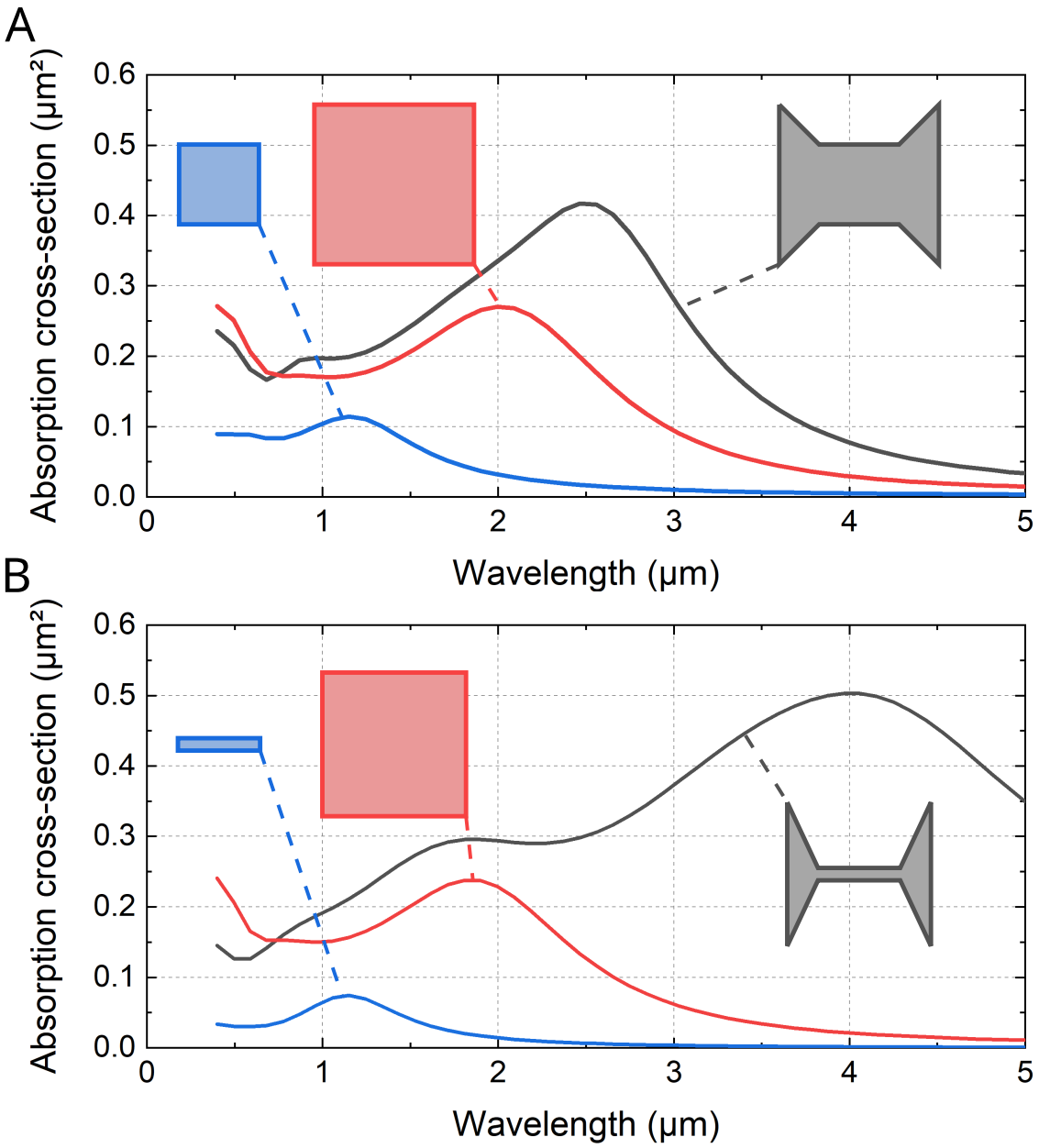

Figure 3.5: Absorption cross-sections of nickel nanoantennas with different lateral dimensions and a constant height of 150 nm, calculated using the DDA method. (A) Comparison between a $600 \times 600 - 300 \times 300$ nm diabolo, and two pads with dimensions 300×300 nm and 600×600 nm respectively. (B) Comparison between a $540 \times 540 - 300 \times 50$ nm diabolo, a rod with dimensions 300×50 nm and a pad with dimensions 540×540 nm.

For diabolos with the same neck dimensions, we investigated the impact of varying the total length and width. Increasing the total length of the diabolo leads to a redshift of the absorption peak towards longer wavelengths. On the other hand, increasing the total width of the diabolo (i.e. switching from the blue to red curves in Figure 3.6) enhances the absorption intensity, with a redshift of the absorption peak. For our targeted application of solar infrared harvesting, we aim at maximizing the absorption between 800 nm and 2500 nm. Thus, according to these results, it seems that diabolos with smaller total length should be favored to reach high absorption in shorter wavelengths, while a trade-off needs to be made between the

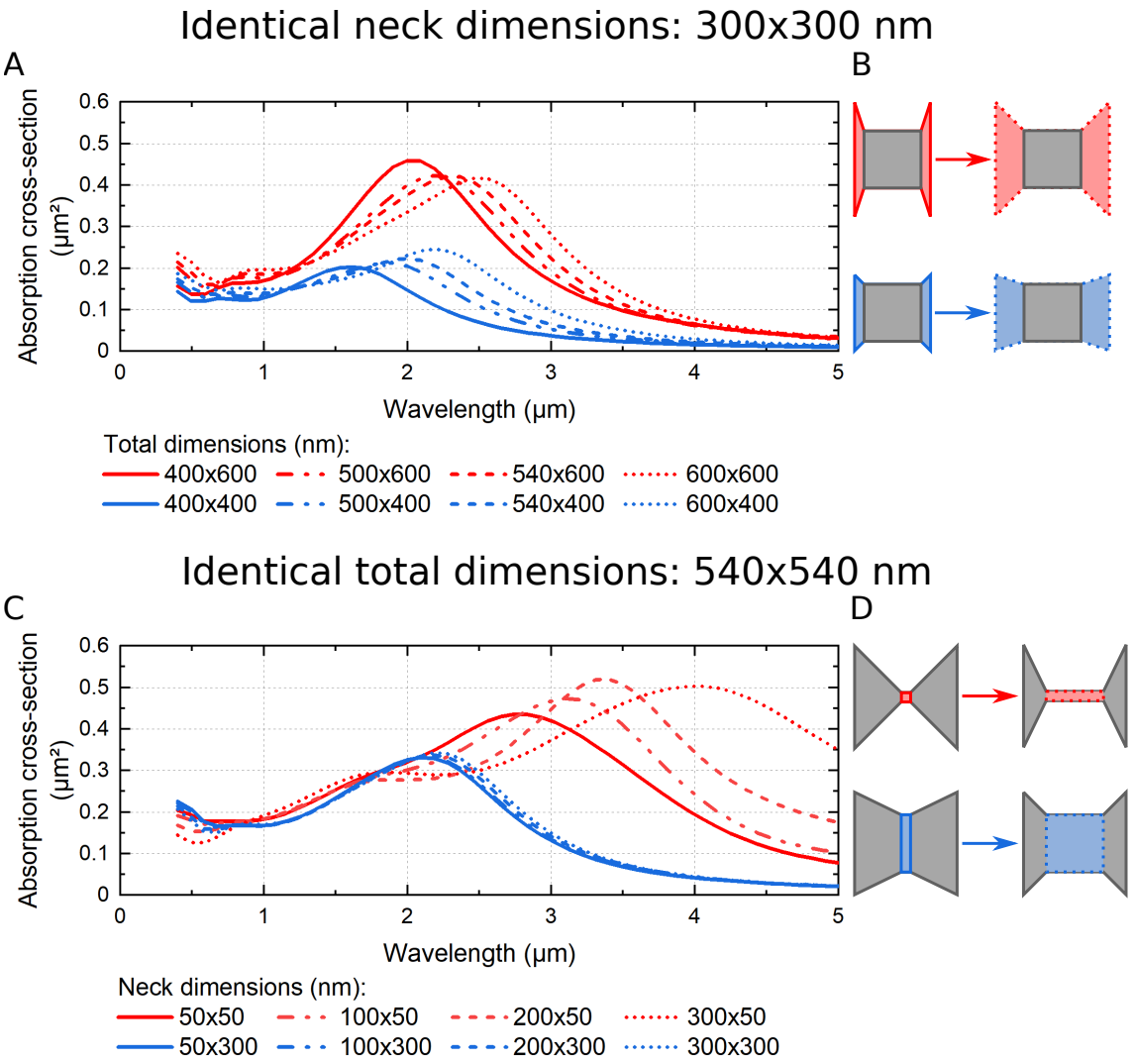

Figure 3.6: Absorption cross-sections of nickel diabolos with different lateral dimensions and a constant height of 150 nm, calculated using the DDA method. (A) Diabolos with identical neck dimensions of 300×300 nm and varying total dimensions. (B) Diabolos with identical total dimensions of 540×540 nm and varying neck dimensions.

intensity and spectral position of the absorption peak to select the optimal total width.

For diabolos with fixed total dimensions, two neck width values were studied with various neck lengths. The absorption spectra of the four diabolos with a large neck width of 300 nm (represented in blue in Figure 3.6C) show negligible change when varying the neck length. On the other hand, for diabolos with a narrow neck of 50 nm (represented in red in Figure 3.6C), increasing the neck length results in a pronounced redshift of the absorption peak. Overall, diabolos with narrow necks exhibit increased absorption cross-section as compared to diabolos with wide necks, which are closer to the pad geometry.

In this section, we introduced the diabolo geometry, defined by four variable dimensions and analyzed its optical properties through DDA calculations of absorption spectra. The results indicate that diabolos exhibit higher absorption compared

to pads with the same total dimensions, emphasizing the advantages of this geometry for light-matter interactions. By manipulating the total length, total width, and neck dimensions of the diabolos, we observed shifts in the absorption peak and enhancements in absorption intensity. These findings provide valuable insights for the design and optimization of diabolo nanoantennas for solar infrared absorption.

Highlights of the section

We have conducted numerical simulations to explore the optical properties of nanoantennas with different geometries. By investigating simple geometries such as disks and rectangular prisms, we observed consistent trends of redshift in the absorption peak and increased absorption intensity with larger dimensions. Furthermore, our exploration of nanorods revealed the impact of anisotropy on the absorption spectra. Introducing the diabolo geometry, we showcased its superior absorption compared to pads and rods and examined the influence of total dimensions and neck dimensions on the absorption spectra.

3.2 Selection of the materials

In the previous section, preliminary studies were conducted on the optical response of nickel nanoantennas with various shapes and dimensions. However, the optical behavior of metal nanoparticles can also vary drastically with their composition. In the field of plasmonics, noble metals such as gold or silver are widely used due to their strong LSPR resonances [144, 145]. Moreover, a large variety of materials [146] (non-noble metals [147], metal oxides [148, 149, 150], doped semiconductors [151, 152, 153], ...) or combinations of materials [154, 155, 156, 157, 158] have been shown to exhibit localized surface plasmon resonances. For example, alloyed [159, 160], multimetallic [161, 162] or core-shell [163, 164, 165] nanoparticles are all described in the literature. As a matter of fact, when it comes to the composition of a plasmonic structure, the possibilities are nearly endless. An important step in the identification of efficient nanoparticles for solar infrared harvesting is the selection of the particles' material.

For this purpose, our approach consisted in calculating the optical absorption of three geometries of nanoantennas with various compositions. In order to limit the number of simulations, we decided to limit ourselves to the study of monometallic nanoparticles. This choice was also made in order to simplify the further fabrication of these structures. The screened materials, selected among the most common in the literature, are aluminum (Al), chromium (Cr), copper (Cu), gold (Au), nickel (Ni), silver (Ag), titanium (Ti) and titanium nitride (TiN). For all these materials, three geometries of particles were tested: a 540x50 nm rod, a 540x540 nm pad and a diabolo with total dimensions 540x540 nm and a 300x50 nm neck, all with a height of 150 nm. These are representative of the typical geometries achievable using our nanofabrication techniques.

The absorbed solar power over the range 0.875-2.5 µm (P_{abs}) was calculated,

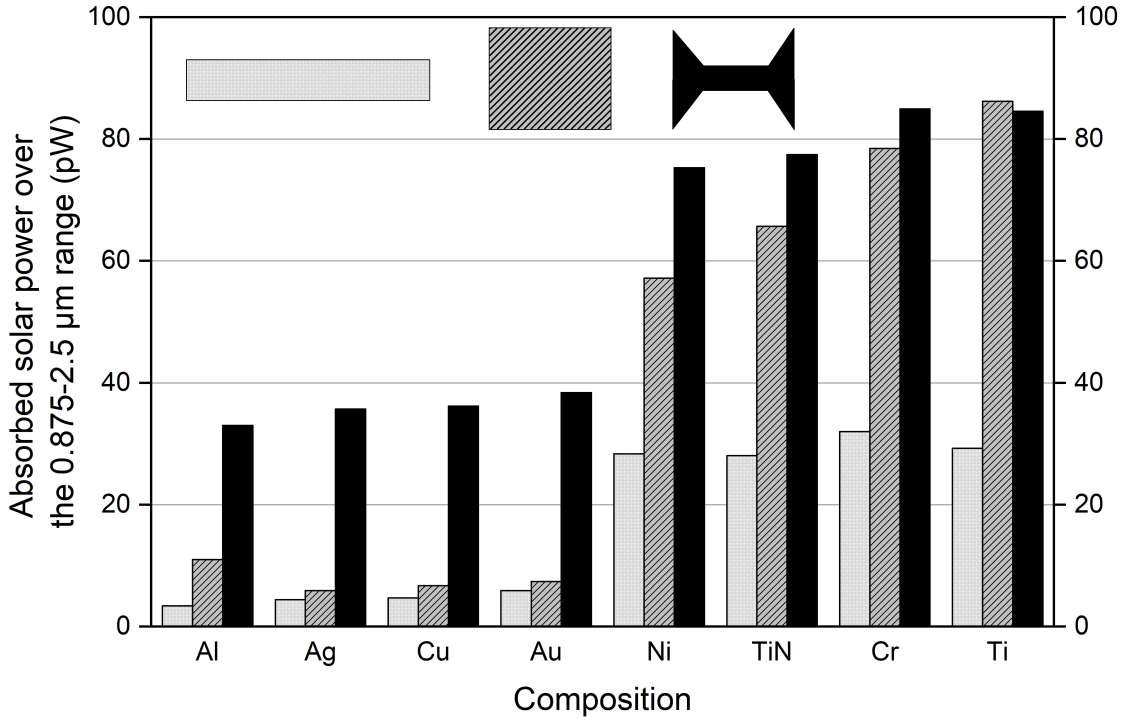

Figure 3.7: Comparison between the calculated absorbed solar power of nanoantennas made of various materials, over the range 0.875-2.5 µm. The three studied geometries are: rod (540x50 nm), pad (540x540 nm) and diabolo (total dimensions: 540x540 nm - neck dimensions: 300x50 nm). All particles have a height of 150 nm. Reprinted with permission from ACS Appl. Energy Mater. 2023, 6, 4, 2128–2133. Copyright 2023 American Chemical Society.

using Equation 2.1, for the 24 simulated structures, and the results are presented in Figure 3.7. Al, Ag, Cu and Au, although very popular for creating nanoparticles with resonances in the visible range, show poor solar infrared harvesting capabilities as compared to Ni, TiN, Cr or Ti. The best materials to fabricate rods, pads or diabolos for solar infrared absorption seem to be titanium and chromium. Finally, we selected nickel as the nanoantenna material, because it presents good absorption performances while being chemically and physically stable in ambient atmosphere. It is also cheap and abundant.

3.3 Ranking antennas for solar infrared absorption

In Section 3.1, we conducted preliminary numerical studies to understand the impact of shape and dimensions on the absorption spectrum of a variety of nanoantennas. However, based on the results obtained, we are unable to straightforwardly identify the optimal structure for solar infrared absorption. Indeed, the infrared solar spectrum is complex and has a large bandwidth (0.875-2.5 µm), meaning that we cannot simply aim at maximizing the absorption intensity of the nanoantennas at a specific wavelength. Rather, we should target the best spectral matching

between the antenna absorption spectrum and solar infrared illumination. In order to do so, we simulated a large number of nanoantennas with different shapes and dimensions, and compared their performances for solar infrared absorption using a figure-of-merit designed to take into account the spectral matching.

The disk (Figure 3.1D) and the pad (Figure 3.1A) are the most simple of the five studied shapes, as they both only have one varying parameter, namely the diameter D_{disk} for the disk and the length L_{pad} (which is equal to the width) for the pad. The rod shape (Figure 3.1B) is a variation of the pad in which the aspect ratio between the length L_{rod} and width W_{rod} is larger than five. The truncated cones (Figure 3.1C) is also defined by two parameters: the base diameter (D_{cone}) and the top diameter (d_{cone}). The most complex shape studied here is the so-called diabolo (Figure 3.1E), having four dimensional parameters: total length (L) and width (W), and length (l) and width (w) of the neck.

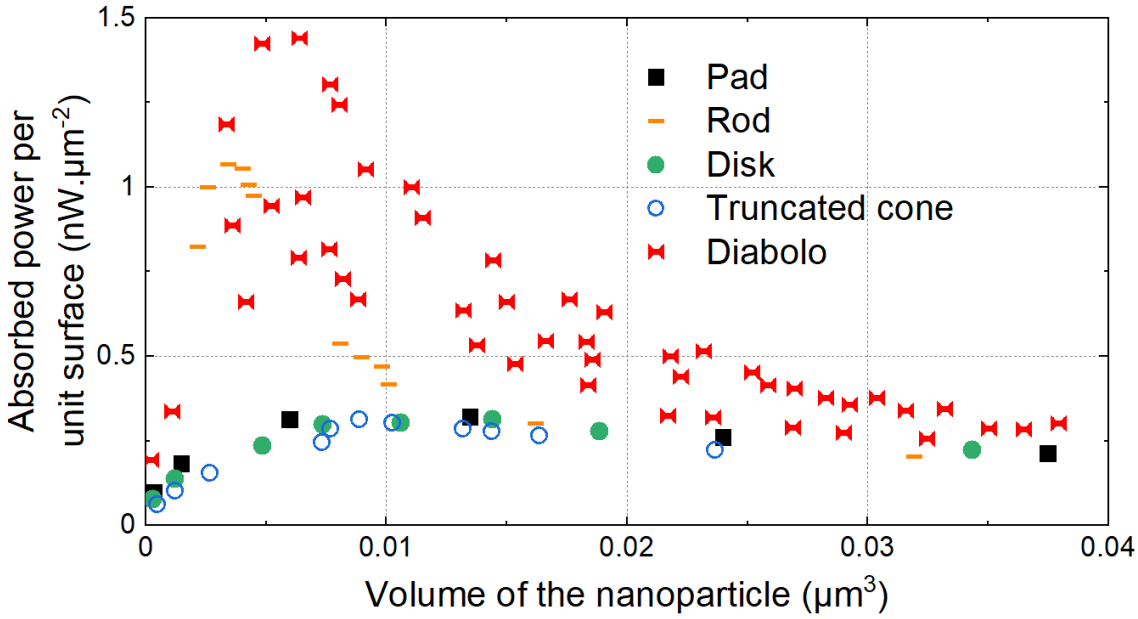

Figure 3.8: DDA-based numerical simulations of the optical absorption of various nanoantennas. Absorbed solar power per unit surface P_{abs}^{S} calculated for 150 nm-thin isolated Ni nanoantennas with different shapes (described in Figure 3.1) and dimensions. All particles have a height of 150 nm. Reprinted with permission from ACS Appl. Energy Mater. 2023, 6, 4, 2128–2133. Copyright 2023 American Chemical Society.

For each shape, the size parameters were varied between 50 and 600 nm to create nearly a hundred targets with different geometries. As described in Section 2.1, DDA simulations were conducted on these isolated nanoantennas to calculate their absorption spectra and extract the solar absorbed power per unit surface over the range 0.875-2.5 µm (Equation 2.2). The results are presented in Figure 3.8, where each particle is identified by its volume rather than its dimensions, in order to compare antennas with different shapes.

A general trend can be noticed for all five shapes, which is the presence of a maximum of P_{abs}^{S} at a given particle volume. This volume is around 0.0035 µm^3 for the rod shape, 0.0064 µm^3 for the diabolo, and between 0.0075 and 0.015 µm^3 for the

pad, disk and cone. Modifying the volume of a particle by changing its dimensions leads to two main effects on the optical absorption. First, the plasmon resonances are shifted to longer wavelengths when the size increases, or lower wavelengths when the size decreases, as shown in Section 3.1. Secondly, smaller particles tend to have a higher absorption-over-scattering ratio, as exemplified for disks in Figure 3.9, because the absorption cross-section scales with the volume of the particle while the scattering cross-section scales with the square of the volume. Thus, for a given shape, the maximization of P_{abs}^{S} results from a trade-off between:

- An optimal matching between the absorption cross-section spectrum of the particle and the solar infrared spectrum;
- A high absorption-over-scattering ratio;
- A small geometrical cross-section limiting the footprint of the particle.

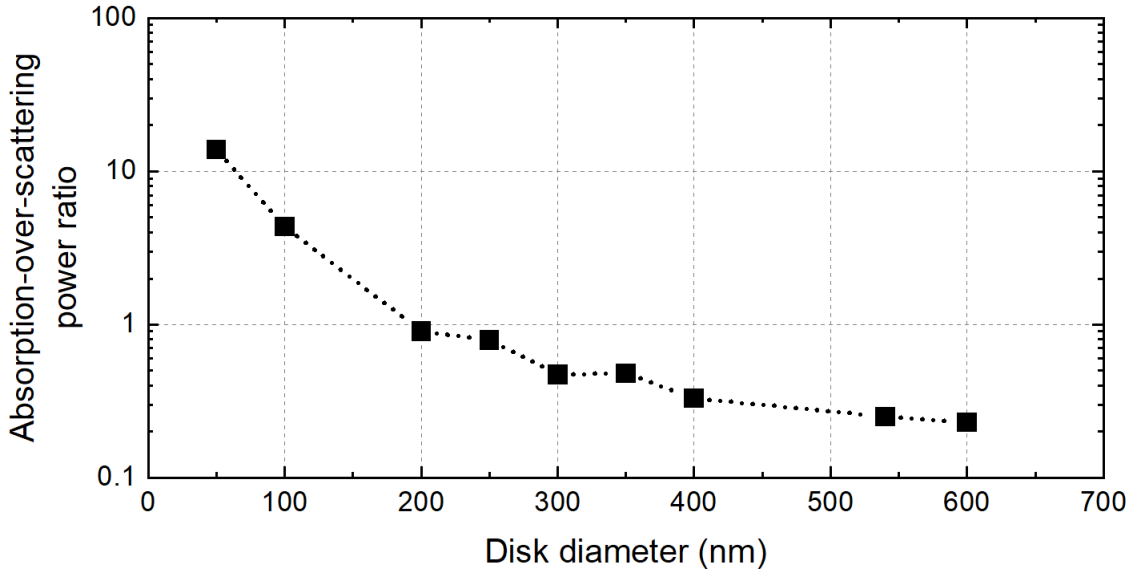

Figure 3.9: Absorption-over-scattering power ratios of nickel disks with varying diameters, calculated under illumination by the AM1.5G solar spectrum limited to the 0.875-2.5 µm range.

The absorbed power per unit surface of diabolo and rod nanoantennas shows a significant dependence on their volume, as compared to pads, disks and cones. This is probably due to their high length-to-width aspect ratios. Indeed, for these shapes, a significant increase in length, leading to an important spectral shift, can result in only a small increase in volume. On the other hand, pads, disks, and cones have a unitary aspect ratio, meaning that their length is always equal to their width.

For each studied shape, the optical properties of the best performing structure, with its lateral dimensions, are summarized in Table 3.1. The corresponding simulated absorption cross-section spectra are presented in Figure 3.10 and compared with the AM1.5G solar spectrum. It can be seen that the best pad, disk and cone have all similar spectra, with a wide absorption peak around 1.15 µm, covering a

range of wavelengths were the IR solar irradiance is strong. As a result, the best pad, disk and cone absorb a solar power of 29, 30 and 39 pW respectively. The absorption peak of the best rod is centered at 1.5 µm, in a spectral region of lower solar irradiance. However, despite its lower absorbed power of 25 pW, the best rod exhibits a high absorbed power per unit area of 1.23 nW/µm² due to its small size. Finally, the best diabolo outperforms any other structure studied with a superior absorption cross-section in almost the complete solar infrared range, which results in an absorbed solar power per unit area of 1.42 nW/µm².

Geometry and dimensions	Absorbed solar power per antenna (pW)	Absorbed solar power per unit area (nW/µm²)	Absorption/scattering power ratio
Diabolo	46	1.42	1.81
Rod	25	1.23	1.03
Pad	29	0.32	0.35
Truncated cone	39	0.31	0.67
Disk	30	0.31	0.48

Table 3.1: Optical performances of the best isolated Ni nanoantenna for each studied geometry, calculated by DDA numerical simulations. Diabolo: $400 \times 300 - 300 \times 50$ nm, rod: L_{rod}=400 nm; W_{rod}= 50 nm, pad: L_{pad}=300 nm, truncated cone: D_{cone}=400 nm; d_{cone}=100 nm, disk: D_{disk}=350 nm. The geometrical parameters are defined in Figures 3.1A-E. Reprinted with permission from ACS Appl. Energy Mater. 2023, 6, 4, 2128–2133. Copyright 2023 American Chemical Society.

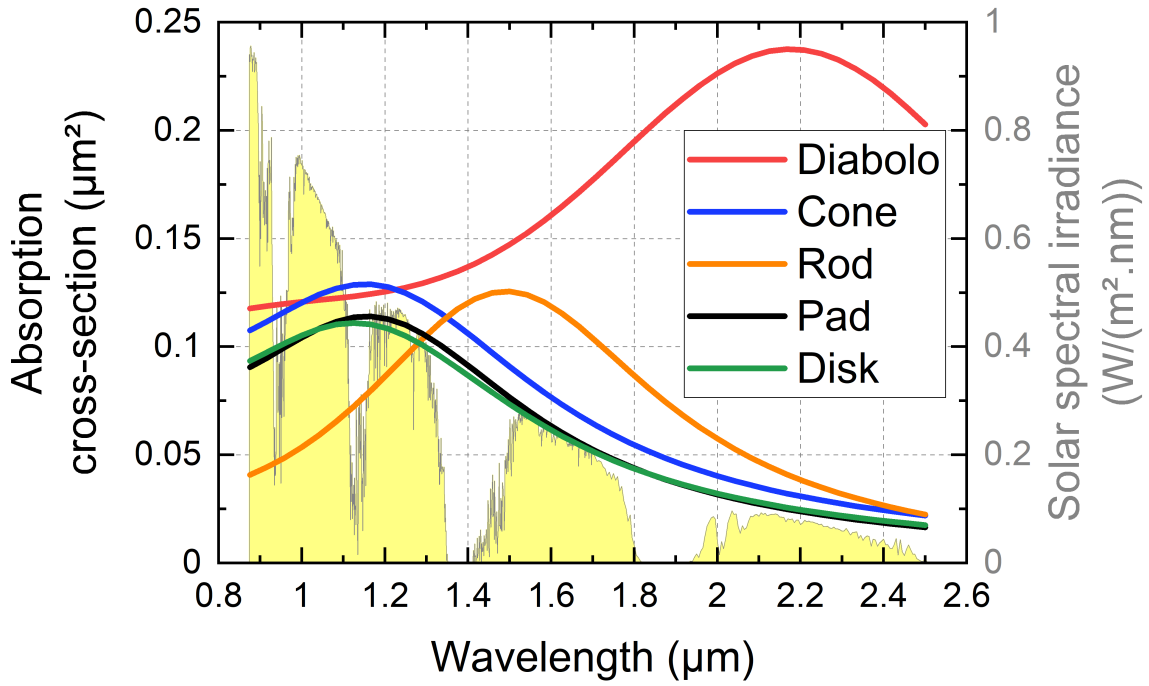

Figure 3.10: Absorption cross-section spectra of the best isolated Ni nanoantenna for each studied geometry, calculated by DDA numerical simulations, and compared to the AM1.5G solar spectrum.

Highlights of the section

In this section, we used electromagnetic simulations to calculate the absorption cross-section of a large set of nickel nanoantennas with various shapes and dimensions. By using the optical power per unit surface absorbed by each structure under solar infrared illumination, we were able to rank the nanoantennas according to their efficiency toward solar infrared absorption. We showed that the response of disks, pads and truncated cones were similar, while rods and diabolos exhibit much higher performances, due to an increased absorption intensity and a better spectral matching with the illumination spectrum.

3.4 Reconstruction of realistic simulation targets based on topographical data

As shown in the previous section, diabolo-shaped nickel nanoantennas have been identified as potentially efficient candidates for solar infrared harvesting. However, the complex shape and small dimensions of such nanoantennas render their fabrication tricky. It is thus necessary to verify the feasibility of their fabrication. Furthermore, fabricated nanoparticles usually present defects that can alter their optical properties. We have characterized these structural defects through scanning electron microscopy (SEM) and atomic force microscopy (AFM). We have then proposed to use the obtained data to reconstruct realistic simulation targets and compute the absorption of the fabricated structures.

3.4.1 Fabrication of nanodiabolos by electron-beam lithography

The targets used in the previous simulations have perfectly smooth surfaces and sharp corners, which is not the case of real structures. The nanofabrication techniques we use introduce defects such as surface roughness, tilted edges, curved corners or divergence from the nominal dimensions. In order to characterize these defects, we first fabricated the nanoantennas. Four nanodiabolos with different nominal lateral dimensions have been selected:

- Diabolo A (see Figure 3.11A): L = 400 nm, W = 500 nm, l = 300 nm, w = 50 nm
- Diabolo B (see Figure 3.11B): L = 540 nm, W = 540 nm, l = 300 nm, w = 50 nm
- Diabolo C (see Figure 3.11C): L = 540 nm, W = 540 nm, l = 200 nm, w = 50 nm
- Diabolo D (see Figure 3.11D): L = 540 nm, W = 540 nm, l = 300 nm, w = 200 nm

These structures were fabricated on a silicon substrate using electron-beam lithography, nickel deposition and a lift-off process. More details on the fabrication process can be found in Section 2.2. Prior to the electron-beam lithography step, a dose test was conducted to identify the electron dose leading to the highest patterning accuracy: 120 µC/cm². Then, 50x50 µm² arrays of 150 nm-high diabolos with a period of 900 nm were made on the same substrate. Figure 3.11E-G show representative SEM images of the fabricated diabolos A, B, C and D respectively.

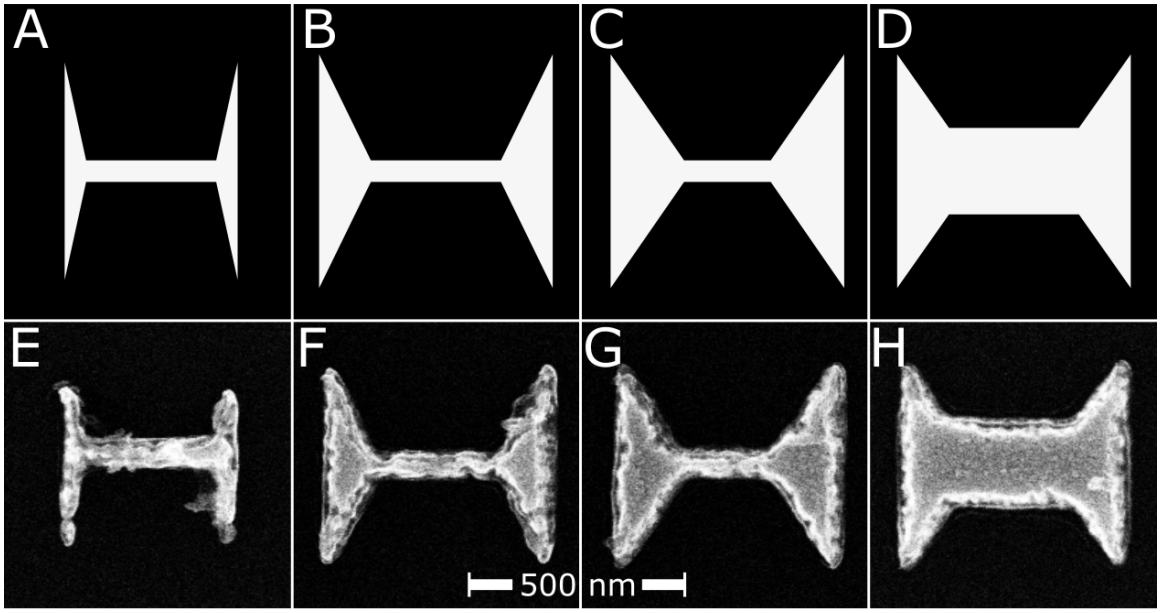

Figure 3.11: Diabolo-shaped nanoantennas fabricated using electron-beam lithography. (A-D) Representation of the nominal geometry of diabolos with (A) L = 400 nm, W = 500 nm, l = 300 nm, w = 50 nm; (B) L = 540 nm, W = 540 nm, l = 300 nm, w = 50 nm; (C) L = 540 nm, W = 540 nm, l = 200 nm, w = 50 nm and (D) L = 540 nm, W = 540 nm, l = 300 nm, w = 200 nm. (E-F) SEM images of the corresponding fabricated nickel antennas on silicon substrate.

Fabrication defects can clearly be spotted on these SEM images. As exemplified on Figure 3.11E, sharp edges are difficult to make due to the resolution limit of the technique. On Figure 3.11F-H, one can clearly notice defects along the edges of the structures, as well as the roughness of the plane surfaces.

3.4.2 Reconstruction method

In order to estimate the impact of the deviation from the nominal size and the surface roughness on the optical properties of diabolo nanoantennas, we generated two 3D models based on the fabricated diabolo B (see Figures 3.11F and 3.12A). This diabolo has been selected for this study as it shows good solar infrared absorption, according to the calculations presented in Section 3.3, while being accurately fabricated. The first model considered only the deviation in particle size, while the second model incorporated both the size deviation and the surface roughness.

The lateral dimensions of the fabricated diabolo were extracted from the SEM

image presented in Figure 3.11F, and used to generate a simulation target taking into account deviation from the nominal dimensions. This target, presented in Figure 3.12D, has straight edges and smooth surfaces, with the dimensions of the fabricated diabolo.

An AFM image of the nanodiabolo has been made using a lateral step of 8 nm (see Figure 3.12B). In the 2D AFM image, the value of each pixel corresponds to its measured height. The data from this image have been processed in order to remove the points with a height below 8 nm, which correspond to the substrate. The remaining points were used to generate a second simulation target, shown in Figure 3.12E, with an interdipole distance corresponding to the resolution of the AFM image, 8 nm. This realistic target possess the surface roughness and lateral dimensions of the fabricated diabolo.

3.4.3 Impact of the fabrication defects on the simulated optical properties

Following the method described in Section 3.4.2, three simulation targets were generated:

- A diabolo with nominal dimensions (L = 540 nm, W = 540 nm, l = 300 nm, w = 50 nm) shown in Figure 3.12C;
- A diabolo with measured dimensions (L = 570 nm, W = 490 nm, l = 270 nm, w = 80 nm) shown in Figure 3.12D;
- A diabolo with measured dimensions and surface roughness (L = 570 nm, W = 490 nm, l = 270 nm, w = 80 nm), based on AFM data and shown in Figure 3.12E.

The DDA method was employed to quantify the absorption of the solar infrared radiation by the Ni diabolos. As can be seen in Figure 3.12F, our results showed that the absorption spectrum of the Ni diabolos with measured dimensions was shifted towards longer wavelengths as compared to the nominal structure. Consequently, the absorption power decreased from 75 pW to 66 pW, as presented in Table 3.2. This clearly highlights the importance of controlling the lateral dimensions of the particles to achieve optimal absorption.

Simulated Ni diabolo	Absorbed solar power (pW)	Absorption/scattering power ratio
Nominal dimensions	75	0.89
Measured dimensions	66	0.60
Measured dimensions and surface roughness	67	0.76

Table 3.2: Calculated absorbed solar power and absorption-over-scattering power ratio over the 0.875-2.5 µm range for the diabolo B simulated with 3 different targets.

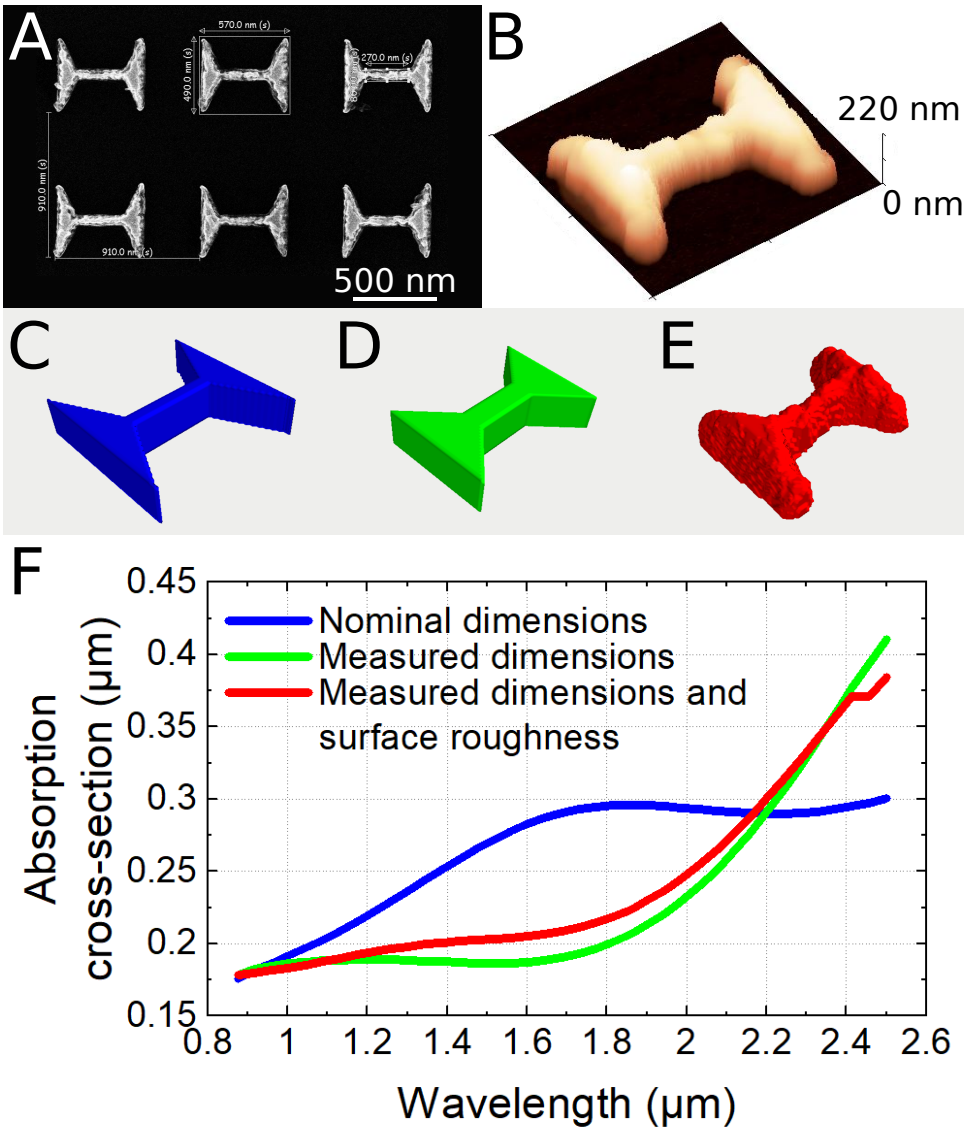

Figure 3.12: Impact of fabrication defects on the optical properties of Ni diabolo nanoantennas. The geometry chosen is the diabolo B (see Figure 3.11B,F). (A) SEM and (B) AFM images of diabolo-shaped Ni nanoantennas on Si substrate. 3D views of (C) the smooth diabolo with nominal dimensions, (D) the smooth diabolo with measured dimensions and (E) a realistic diabolo with measured dimensions and surface roughness. (F) Calculated absorption spectra of the structures C, D and E. Reprinted with permission from ACS Appl. Energy Mater. 2023, 6, 4, 2128–2133. Copyright 2023 American Chemical Society.

Furthermore, we observed that surface roughness only had a moderate impact on the absorption spectrum of the particles, which was consistent with previous findings [166, 167]. Specifically, the addition of surface roughness to the Ni diabolo with measured dimensions led to a slight increase in the absorbed power, which was calculated to be 67 pW in our case. As presented in Table 3.2, adding surface roughness to the diabolo with measured dimensions results in a higher absorption-over-scattering ratio, meaning that surface roughness actually decreases the scattered part of incoming infrared solar absorption, which is beneficial in the frame of an absorbing surface covered with an array of particles.

These findings suggest that particle size deviation is a critical factor that needs to be taken into account when designing nanoantennas for optimal solar infrared absorption. The size deviation is primarily induced by the electron-beam lithography step. Thus, we propose three modifications of the EBL process in order to address this issue. The first approach involves modifying the nominal dimensions of the structures to counteract the deviation. By adjusting the nominal dimensions, structures that have a higher likelihood of achieving the desired size and shape can be created, even with the presence of deviations. The second approach involves performing a more fine-tuned dose test before the lithography step. By selecting a more suitable electron dose, it is possible to get closer to the nominal dimensions and reduce the deviation of the final structures. Finally, the third approach involves reducing the exposure step size, which refers to the distance between two adjacent exposure points (see Section 2.2.2). By reducing the step size, it is possible to increase the resolution of the structures being fabricated, which can help to compensate for the deviation in size. However, reducing the step size also increases the exposure time, which can result in longer fabrication times.

On the other hand, the limited impact of surface roughness on the simulated optical properties of Ni diabolos suggest that the lift-off process, which is responsible for this defect, is a valid approach for the fabrication of nanoharvesters.

Highlights of the section

We fabricated diabolo-shaped nickel nanoantennas using electron-beam lithography with a lift-off process. After characterization of the samples by SEM and AFM, we noticed two main types of defects: a deviation of lateral dimensions with respect to the nominal structure, and the introduction of surface roughness. We used the measurement data to reconstruct two simulation targets: a diabolo with measured dimensions and no surface roughness, and a diabolo with measured dimensions and surface roughness. DDA simulations were conducted on these targets to calculate their optical properties. The results showed a strong impact of the variation of lateral dimensions on the absorption spectra, while surface roughness seems to slightly increase the absorption cross-section of the structure.

3.5 Conclusion

In this chapter, we studied the optical properties of isolated nickel nanoantennas, using electromagnetic simulations based on the discrete dipole approximation method. We screened through particles with various shapes, dimensions and composition, in order to identify the most suitable structures for solar infrared absorption. As the parameters space of simulated structures is large, no clear design rule could be identified to systemically point toward the optimal nanoantenna. We thus used the absorbed power per unit surface of an antenna as our main figure of merit to rank the particles according to their performance for solar infrared absorption, taking into account the spectral matching with the incident spectrum. This method

allowed to identify the diabolo geometry as the most promising among the studied geometries.

We then fabricated diabolo nanoantennas by electron-beam lithography, and measured their surface topography by Atomic Force Microscopy. We used this topographical data to reconstruct realistic simulation targets taking into account the defects introduced by the fabrication process. The electromagnetic simulations conducted on these targets showed that the deviation from nominal dimensions have a significant impact on the absorption properties of the nanoantennas, while the introduction of surface roughness seems to be slightly beneficial to their performances.

In this chapter, we used DDA simulations to calculate the optical properties of isolated nanoantennas. This approach allows to rapidly study a large number of particles with various parameters. However, with this method, we neglect the substrate and neighboring nanoantennas, which could potentially have a significant impact on the optical properties of a nanostructured surface. Moreover, we only extract the absorption and scattering cross-sections from the electromagnetic simulations, and do not consider here the photothermal conversion. These effects will be discussed in Chapter 4, in which we will study large scale photothermal interfaces.

Chapter 4

Experimental fabrication of photothermal interfaces

The diabolo-shaped nanoantennas presented in Section 3.4.1 were fabricated over small surfaces, typically around 1 mm^2, due to the use of electron-beam lithography for the patterning step, which is a costly and time-consuming technique. These limited areas are insufficient for integration in PV-TE devices, as the scale of photovoltaic cells and thermoelectric generators is the cm^2. Moreover, it is difficult to reliably characterize the optical properties and heating capabilities of such small surfaces, which is why it is necessary to fabricate large scale photothermal interfaces. To do so, we switched to a different patterning technique: hole-mask colloidal lithography (HCL). As described in Section 2.2.3, it allows to quickly pattern large surfaces, at the cost of a limited control over the nanoantennas' shape and arrangement. In particular, diabolo-shaped nanoantennas can not be made through HCL, so the only geometry fabricated in this chapter is the truncated cone. The fabricated samples are characterized using electronic microscopy and optical spectroscopy. Their heating capabilities are then measured by thermography under solar infrared illumination.

Contents

4.1 From isolated nanoantennas to photothermal interface

In Chapter 3, we studied isolated metallic nanoantennas, trying to identify structures that were efficient for solar infrared absorption, the goal being to use these nanoantennas to create a photothermal interface (PTI). However, the nanoparticles are just a part of the PTI, which also consist of a substrate and, oftentimes a capping layer.

The substrate can be a single piece of silicon or glass, for example, but it can also be multilayered to tune the optical or thermal properties. As described in Section 1.4, the substrate has an impact on the optical properties of a nanoantenna, as it modifies its environment.

The capping layer is needed in order to protect the nanoantennas from physical and chemical degradations, such as scratches or oxidation. Once again, the presence of a capping layer can change the optical properties of a nanoantenna. For our application, it should ideally be transparent in the near IR window to allow the nanoantennas to collect the solar infrared radiation. The choice of the material used for the capping layer is crucial in the performance of the PTI. For example, a capping layer with a high thermal resistance, as compared to the substrate, will result in the thermal flux generated by the nanoantennas being directed towards the substrate.

When studying a photothermal interface, we no longer face an isolated particle, but rather a 2D arrangement of nanoantennas. The presence of other particles in the vicinity of an antenna can affect its optical response. The absorption intensity can be enhanced or reduced depending on the inter-particular distance. The geometry of the arrangement can also have an impact on the optical properties. Ordered meshes often exhibit resonant absorption and scattering at specific wavelengths and angles. On the other hand, disordered arrays are less sensitive to a change in the incident illumination vector. An other effect of the switch from isolated nanoantennas to 2D arrays is the widening of the absorption peaks, which is due to the dispersion in particle size.

4.2 Fabrication of photothermal interfaces by colloidal lithography

We have used HCL to fabricate photothermal interfaces composed of a multilayered substrate covered by arrays of truncated nanocones with various compositions and heights.

4.2.1 Experimental protocol and samples description

Several photothermal interfaces were fabricated, following the same protocol. First, a glass substrate with dimensions 24x24 mm^2 is washed with acetone and isopropyl alcohol to remove impurities. Then, a 5 nm thick chromium layer is deposited on the substrate by PVD, followed by a silver layer of 80 nm and an alumina layer of 100 nm. Chromium serves as an adhesion layer between the glass and the silver, preventing delamination. On top of this multilayered sample, a short-range-ordered array of truncated nanocone antennas is fabricated by HCL, following the process described in Section 2.2.3. An example of fabricated sample is presented in Figure 4.1.

The silver layer acts as a mirror reflecting incoming radiation toward the nanoantenna array, as it is higly reflective and opaque in the solar spectral range. On the other hand, the alumina layer is used as a dielectric spacer, creating a metal-dielectric-metal photonic stack that is known to enhance optical absorption.

Five different PTIs were fabricated by changing the height and composition of the nanoantennas, while keeping the same base diameter of 200 nm:

- Ni200: 200 nm-high nickel nanoantennas
- Ni50: 50 nm-high nickel nanoantennas
- Ag50: 50 nm-high silver nanoantennas
- Al50: 50 nm-high aluminum nanoantennas
- Au50: 50 nm-high gold nanoantennas

4.2.2 Surface coverage

An important parameter of the fabricated nanoantenna arrays is their surface density d (in cm^{-2}), which is the number of particle per unit surface. It is linked to the surface coverage, or filling factor, f (the fraction of substrate covered with nanoantennas), according to:

$$f = d \cdot S_{NA} = d \cdot \pi \cdot R_{NA}^2 \tag{4.1}$$

where S_{NA} and R_{NA} are respectively the footprint of a nanocone antenna, and the radius of its base.

The surface density plays an important role in determining the optical and thermal properties of the arrays, as a more compact array will generally lead to increased absorptivity and interactions between nanoantennas.

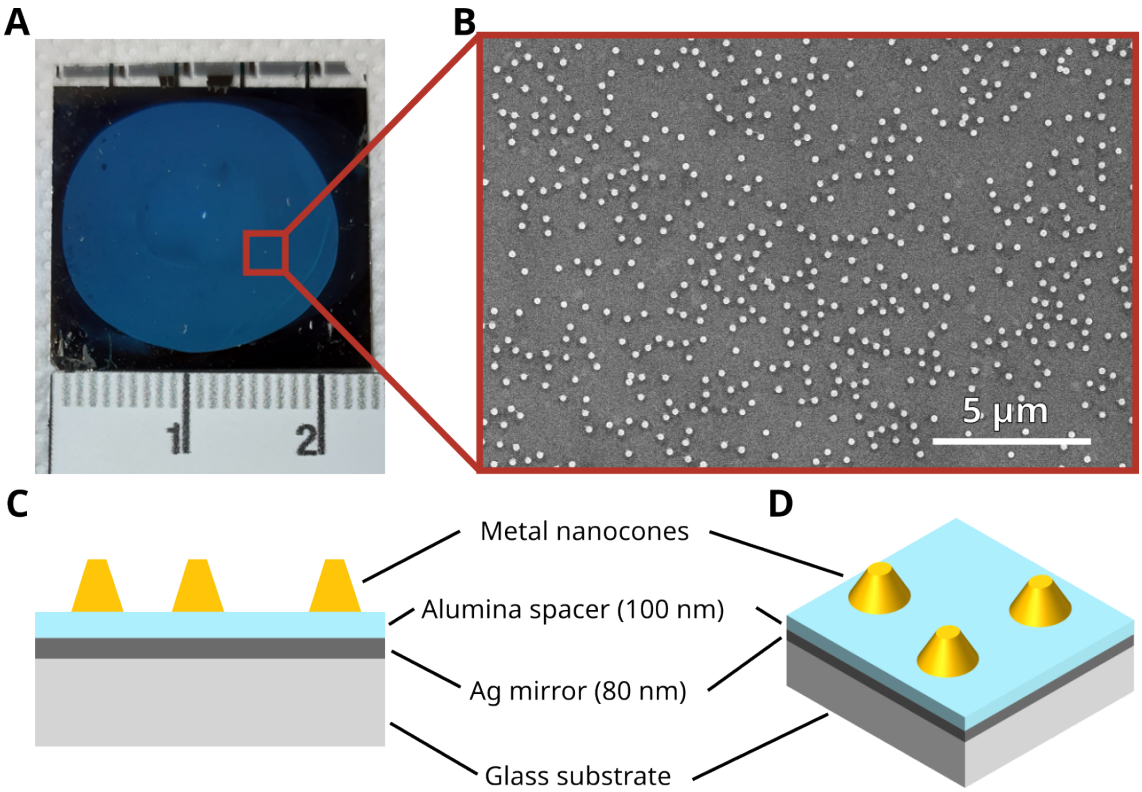

Figure 4.1: Presentation of the samples fabricated through HCL. (A) Picture of a 24x24 mm² sample covered with nickel nanocones (B) SEM image of the surface of the sample. Schematic representation of the sample (C) from the side and (D) in 3 dimensions.

SEM images of the five samples were made and analyzed to measure the surface coverage of the arrays. An example for each sample is showed in Figure 4.2, where one can clearly see a difference in density from one sample to another. The Ni50 sample has the lowest density with 4.6 % surface coverage, while the Ni200 surface coverage reaches 10.1 %.

During a controlled HCL process, negatively-charged PS beads auto-assemble on the positively-charged substrate due to electrostatic interactions. The repulsion force between beads dictates the average inter-particular distance and prevents aggregation. After a given amount of time, the surface of the substrate is saturated with PS beads and the maximum density is reached. In our case, the substrate and the beads dispersion is the same for all samples, so the surface density at saturation should also be the same. The dispersion in density we observe from sample to sample is thus due to a poor control of the HCL process used for the patterning of the nanoantenna arrays. The colloidal dispersions were made several months prior to the deposition, so they may have partially lost their electrostatic charge. It may explain the aggregates visible in Figure 4.2B, as well as the overall low density of the five arrays.

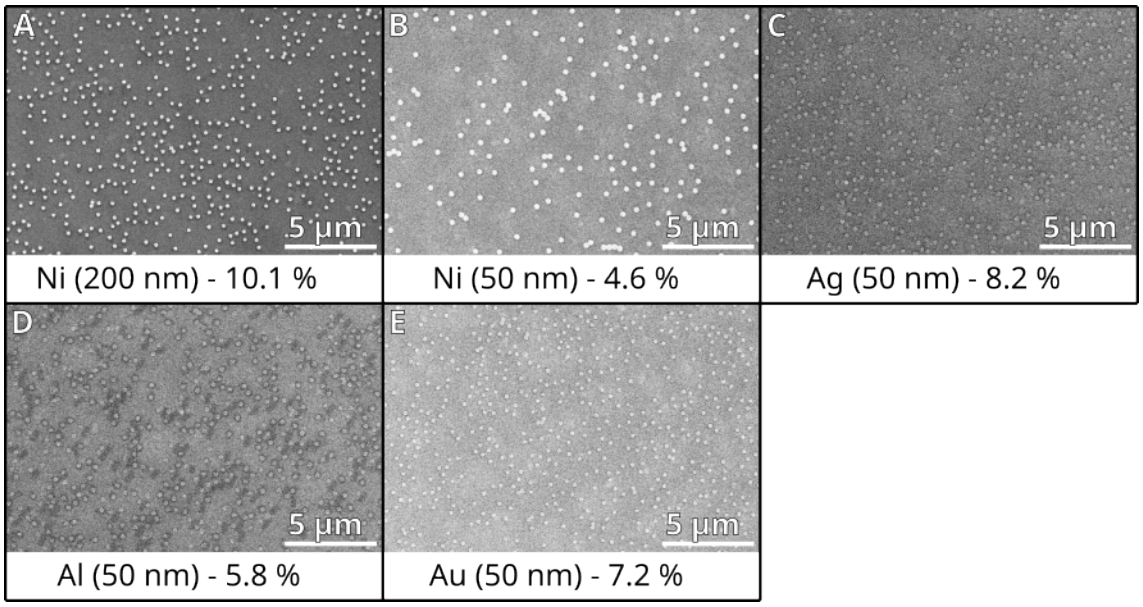

Figure 4.2: SEM images of different samples used to measure the surface coverage of nanocones. (A) Nickel cones with a height of 200 nm and a coverage of 10.1 %. (B) Nickel cones with a height of 50 nm and a coverage of 4.6 %. (C) Silver cones with a height of 50 nm and a coverage of 8.2 %. (D) Aluminum cones with a height of 50 nm and a coverage of 5.8 %. (C) Gold cones with a height of 50 nm and a coverage of 7.2 %.

Highlights of the section

We used hole-mask colloidal lithography to fabricate macroscopic photothermal interfaces covered with arrays of metallic nanocones with different heights and compositions. These self-ordered arrays exhibit no long-range order, and their densities vary from one sample to another. SEM images of the surface of each sample were analyzed to measure the surface coverage of the nanoantenna arrays.

4.3 Optical characterization

The reflectivity $R(\lambda)$ of the fabricated samples was measured using a visible spectrometer over the range 0.4-0.94 µm and an infrared spectrometer over the range 0.94-1.6 µm. The concatenated spectra are shown in Figure 4.3A, were reflectivity drops can be observed for all samples between 0.9 µm and 1.2 µm. Transmission spectra were also measured, but they showed 0 transmittance over the considered wavelength range. This means that a drop of reflectivity is linked to an increase in absorptivity or scattering.

Here, we neglect scattering and assume that the unreflected radiation is absorbed. By weighing the AM1.5G solar spectrum $\phi(\lambda)$ by the absorptivity spectrum and integrating over the wavelength range 0.8-1.5 µm, we can estimate the optical power P_{abs}^{exp} absorbed by each sample under solar illumination within this specific range:

$$P_{abs}^{exp} = \int_{0.8\,\mu m}^{1.5\,\mu m} (1 - R(\lambda))\,\phi(\lambda)\,d\lambda \tag{4.2}$$

The results, presented in Table 4.1, show that the Ni200 sample is the most promising for solar infrared absorption, with an absorbed power of 191 W/m^2 out of the 309 W/m^2 available from the sun between 0.8 µm and 1.5 µm.

Sample	Absorbed solar power over the range 0.8-1.5 µm (W/m^2)
Ni200	191
Au50	183
Ni50	175
Ag50	155
Al50	146

Table 4.1: Optical absorption of the fabricated photothermal interfaces under solar illumination, estimated from the reflectivity spectra.

We compared these results to the absorption cross-section spectra of isolated nanocones calculated by DDA (as presented in Section 2.1). On Figure 4.3B, we can see that the absorption peaks of the calculated spectra do not match the drops in the experimental reflectivity spectra. We hypothesized that this significant difference was due to the impact of the substrate on the optical properties of the samples, which was not taken into account in the simulations on isolated particles.

Thus, we conducted another set of DDA simulations, this time adding the silver and alumina layers in the calculations. The glass substrate was neglected, as the silver layer is totally opaque in the studied wavelengths. The simulation targets included a single square unit cell with lateral dimensions $L \times L$, made of a nanocone on the silver/alumina substrate. The lateral size L of the substrate was calculated so that the surface coverage of the unit cell matched the fabricated samples:

$$L = \sqrt{\frac{1}{d}} = \sqrt{\frac{S_{NA}}{f}} \tag{4.3}$$

The calculation results, presented in Figure 4.3C, show far better agreement with the experimental spectra, as the position of the absorption peaks have been shifted to the near infrared region. If we focus on the two Ni samples, we can see that the calculated absorption cross-section is larger for the nanocones with a height of 50 nm for those with a height of 200 nm, whereas the opposite trend can be seen on the experimental spectra. This is due to a difference in the size of the simulated unit cell: as the Ni200 sample is denser, its unit cell is smaller, which negatively impacts its absorption cross-section. However, for a dense sample, more unit cells are needed to cover a given surface, which results in higher absorptivity of the surface.

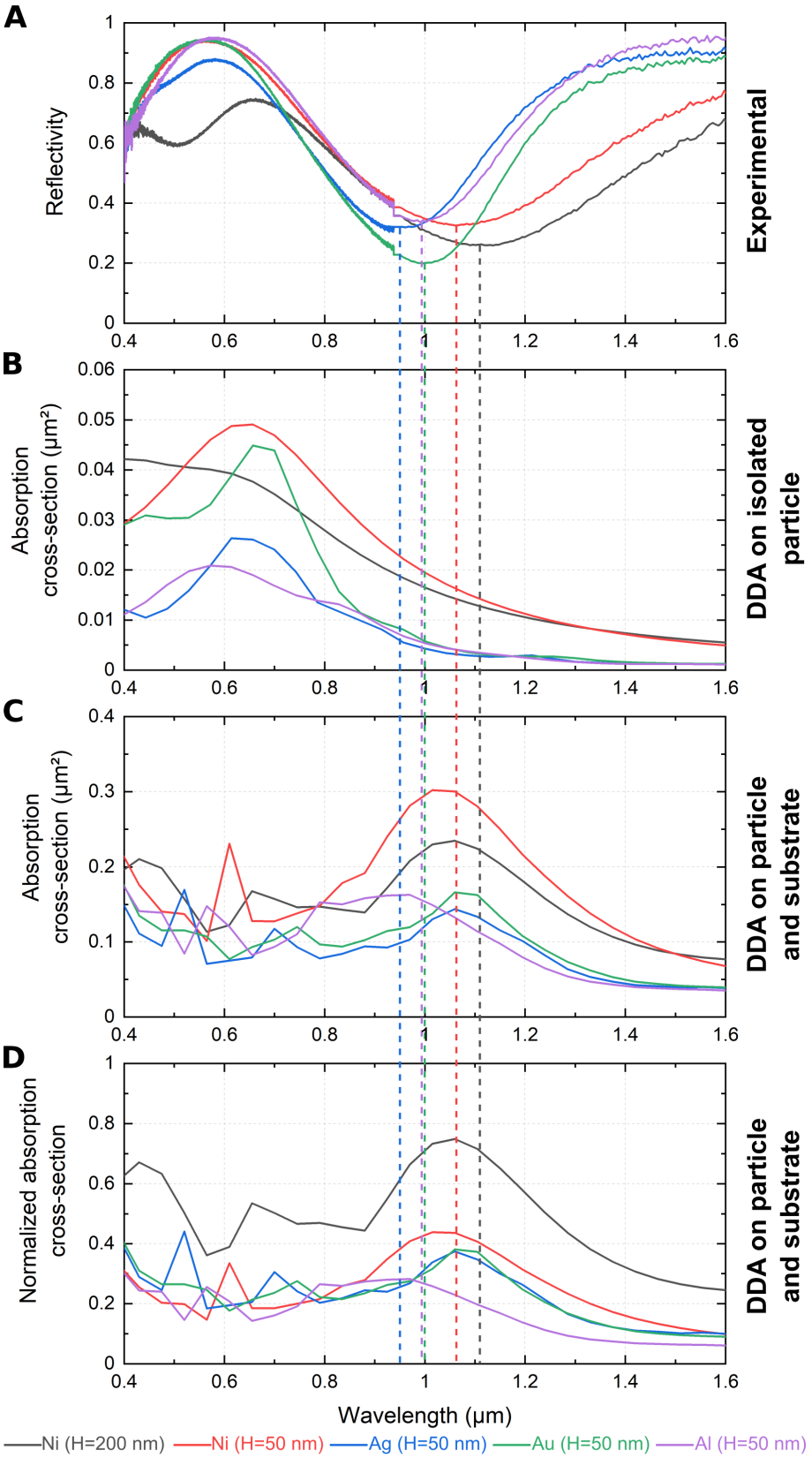

Figure 4.3: Spectra of fabricated samples covered with different nanocone arrays. (A) Experimental reflectivity. The vertical dashed lines indicate the position of the absorption peaks. (B) Calculated absorption cross-section of isolated nanocone. (C) Calculated absorption cross-section of a unit cell including a nanocone and the substrate. (D) Calculated absorption cross-section of a unit cell normalized by the surface of the unit cell.

To get rid of this bias, we normalized the absorption cross-section spectra of Figure 4.3C by the surface of the corresponding unit cell, and plotted the result in Figure 4.3D. Now, it can be seen that the simulated Ni200 sample (grey curve) clearly outperforms the other structures in terms of absorption per unit surface.

Highlights of the section

Spectroscopy measurements were conducted on the five fabricated photothermal interfaces to extract their reflectivity spectra. By comparison to simulated absorption spectra, we evidenced the necessity to take the substrate into account for representative calculations. The experimental reflectivity spectra were also used to estimate the power absorbed by the interfaces under solar infrared illumination.

4.4 Heating under solar infrared illumination

The results presented in this section, which focus on the characterization of the photothermal properties of nanostructured interfaces, were obtained by Sélyan Beldjoudi, in the framework of his Master 1 internship. First, we have compared the Ni200 sample to a reference made of the multilayered glass/silver/alumina substrate without nanoantenna, using the experimental setup presented in Section 2.3.3. The samples were illuminated from the front side by a solar simulator, emitting an AM1.5G spectrum limited to the 0.8-1.5 µm wavelength range. Initially, the sample were at room temperature, and they progressively heated up due to the photothermal conversion of incoming radiation. The temperature evolution of the back side of the samples is measured using an infrared camera and shown in Figure 4.4B, while Figure 4.4A presents thermograms of the back side of the samples after 360 s of illumination.

We can see that both samples heat up under the influence of the solar simulator to reach a steady temperature after approximately 100 s. However, the final temperature of the sample covered with nanoantennas reached almost 35 °C, which is far superior as compared to less than 29 °C for the reference sample. This result highlights the capabilities of our nickel nanocones to efficiently absorb and convert solar infrared radiation into heat.

The same experimental setup was used to measure the photothermal properties of the other samples. For better comparison, we calculated their heating with regard to their temperature without illumination T_0. For a given illumination time t, the heating $\Delta T(t)$ is expressed as:

$$\Delta T(t) = T(t) - T_0 \tag{4.4}$$

where $T(t)$ is the mean temperature of the back side of the substrate at time t, measured by the IR camera. The heating of each photothermal interface is presented in Figure 4.5, and compared to the reference.

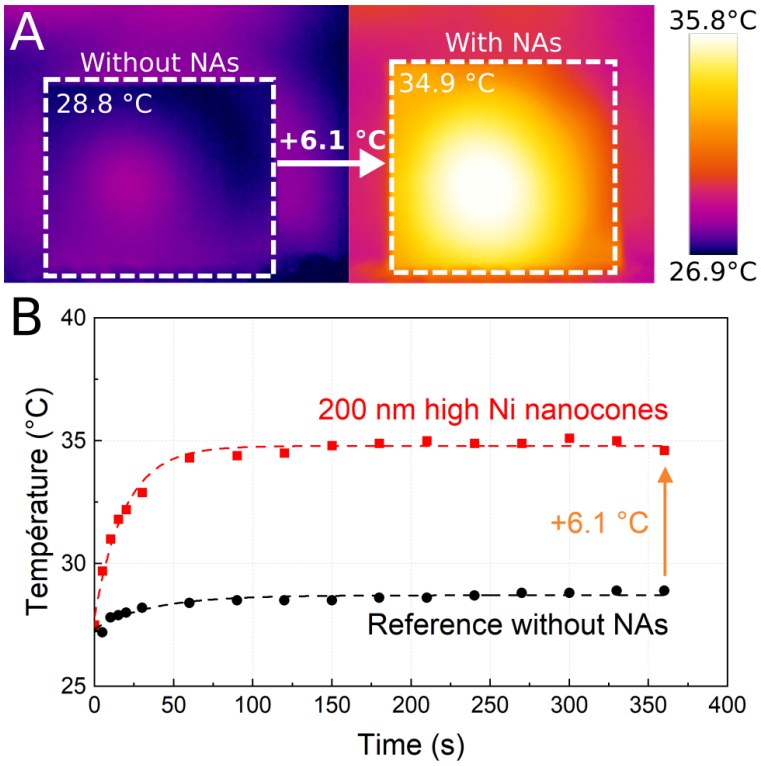

Figure 4.4: Temperature measurement under solar infrared illumination. (A) Temperature distribution at the back side of the substrate for a reference sample without nanoantennas (left), and covered by 200 nm-high nickel nanocones (right). (B) Evolution of the mean temperature of the back side of the substrates when turning on the illumination at t=0 s.

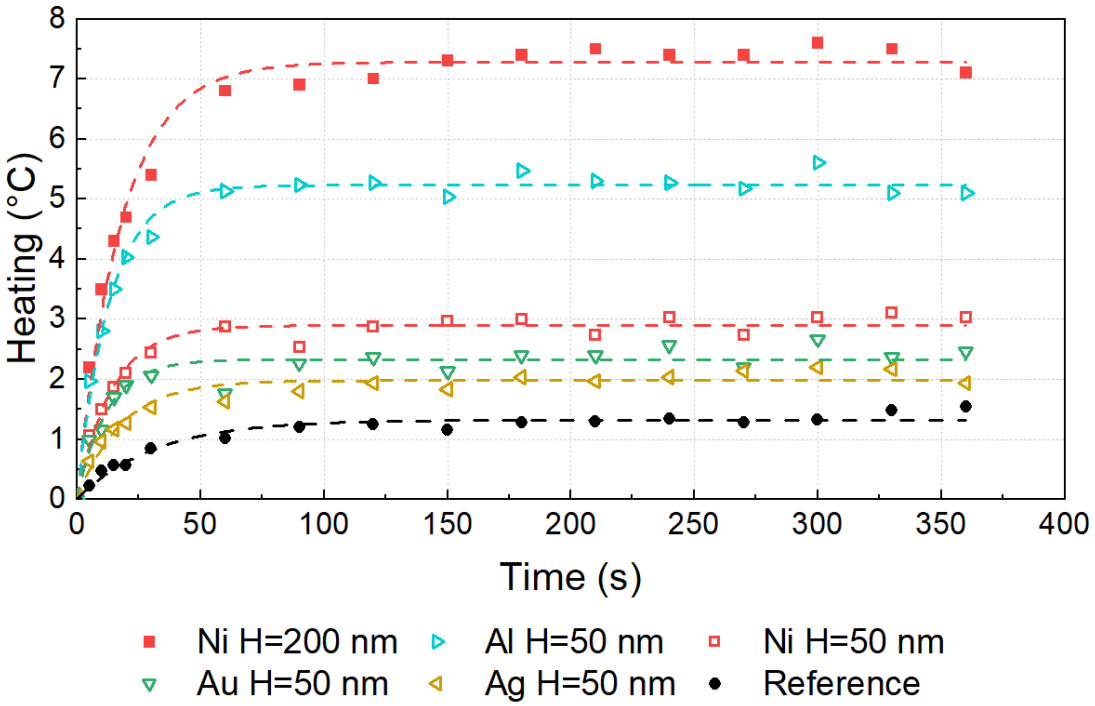

Figure 4.5: Evolution of the mean heating of the back side of the substrate under solar infrared illumination, for different samples. The illumination is turned on at t=0 s.

The heating after 6 min of illumination is stabilized for all samples and ranges from 2.1 °C for Ag50 to 7.1 °C for Ni200. We compared the measured steady-state temperature to the estimated absorbed power presented previously in Table 4.1. Intuitively, we expected that the samples showing higher solar infrared absorption should also exhibit higher heating under illumination. However, as can be seen in Figure 4.6, the two properties are not completely correlated. In particular, The Al50 PTI, in spite of having the lowest estimated absorption of the five samples, reaches a 5.1 °C temperature increase under illumination.

These qualitative discrepancies between estimated solar absorption and measured heating can have several explanations. First, in the calculation of the absorbed power with Equation 4.2, we assumed the absence of scattering by the sample. Or, scattering can occur at different intensity for each sample. Secondly, the efficiency of photothermal conversion can vary for each sample. It is possible that the aluminum nanoantenna have better photothermal properties than gold or silver. Doing additional spectroscopy measurements in an integration sphere would allow to precisely discriminate between absorption and scattering, and thus to estimate the photothermal conversion efficiency of each sample.

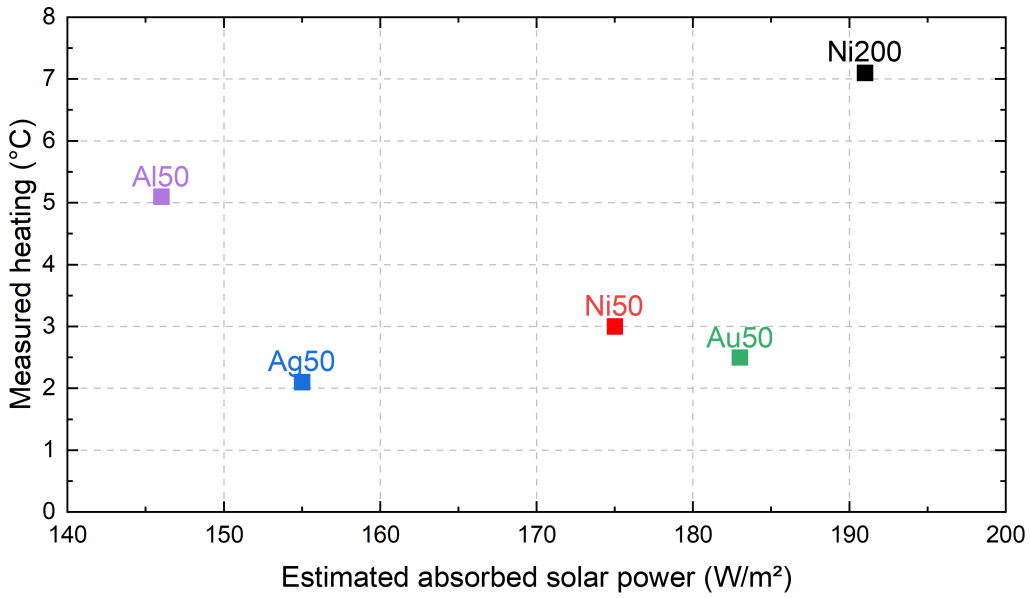

Figure 4.6: Comparison between the estimated absorbed power and measured heating, when illuminating the sample with a solar simulator limited to the 0.8-1.5 µm spectral range.

As described in Section 4.2.2, the nanocone surface density varies from one sample to the other. Thus, the best performing sample is not necessarily the one with the best performing nanocones. In order to gain more insights into the impact of the height and composition of the nanoantenna, we calculated the temperature increase per nanocone ΔT_{cone} for each photothermal interface:

$$\Delta T_{cone} = \frac{(T - T_{ref})}{d \cdot S} \tag{4.5}$$

where T_{ref} is the steady-state temperature of the reference under illumination, while T, d and S are respectively the steady-state measured temperature, the nanocone surface density and the total surface of the sample. The heating per nanoantenna is a figure-of-merit allowing to rank the nanocones with respect to their efficiency towards photothermal heating.

The results are presented in Table 4.2, where it can be seen that the contribution in the global heating of each individual Al nanocone reaches 3.8 n°C, whereas the contribution of an Ag nanocone is only 0.5 n°C. The high temperature of Ni200 can be attributed to a high heating per nanocone (3.3 n°C) combined with a high surface coverage. According to these results, even higher temperatures could be achieved by fabricating photothermal interfaces covered with Al nanocones with a high density.

Sample	Macroscopic heating (°C)	Surface coverage (%)	ΔT_{cone} (n°C)
Al (H=50 nm)	5.1	5.5	3.8
Ni (H=200 nm)	7.1	10.1	3.3
Ni (H=50 nm)	3.0	4.6	1.9
Au (H=50 nm)	2.5	7.2	0.8
Ag (H=50 nm)	2.1	8.2	0.5

Table 4.2: Heating under solar illumination limited to the 0.8-1.5 µm spectral range, for the fabricated photothermal interfaces, and heating par nanocone estimated from the surface coverage.

Highlights of the section

We first compared samples with and without 200 nm-high nickel nanoantennas to evaluate their photothermal conversion efficiency when illuminated by solar infrared light. The temperature evolution of the samples' back sides was monitored using an infrared camera. Notably, the sample with nanoantennas exhibited significantly higher temperatures, reaching +6.1 °C compared to the reference. Photothermal properties of samples with different compositions were analyzed in terms of their heating under solar infrared illumination, revealing qualitative discrepancies between the estimated solar absorption and measured heating. Possible explanations were attributed to scattering effects and variations in photothermal conversion efficiency. The influence of nanoantenna characteristics was investigated, revealing that the heating per nanoantenna varied significantly based on composition and density. Aluminum nanoantennas demonstrated superior heating efficiency per individual nanocone compared to the others. The findings suggest that the selection of nanocone material and density can influence photothermal heating efficiency, paving the way for further optimization in fabricating high-performance photothermal interfaces.

4.5 Nanoimprint lithography for quick patterning

The results presented in the previous section are encouraging, especially given that we used truncated cones as nanoantennas, which, according to the simulations made in Section 3.3, have limited absorption properties as compared to other geometries. We could expect even higher temperature increase by using diabolo nanoantennas. The reason we did not do it here is because the fabrication cost and time to make several samples with various metals would have been too high by electron-beam lithography.

However, nanoimprint lithography (NIL) could be a good alternative technique to quickly and easily fabricate several samples covered by nanoantennas with complex shapes. NIL is a fabrication technique allowing to replicate micro- and nanopatterns from a rigid mold to another substrate. In particular the so-called "Soft-NIL" process, described in Figure 4.7, is of great interest in our case, as it allows to use a single rigid mold and replicate its pattern on a large amount of samples. It first requires to fabricate a rigid mold with the negative of the desired pattern, which can be done using EBL. A thermoplastic polymer film is placed on top of the mold, as heat and pressure are applied during a step of thermal NIL (T-NIL). Under the effect of heat and pressure, the polymer takes the shape of the mold. After cooling down, the polymer film is unmold to later be used as a soft mold in a ultraviolet NIL (UV-NIL) process. Here, a substrate is covered by a sacrificial layer and a photosensitive resist, before being pressed again the soft mold. The pattern of the mold is imprinted into the resist, and a UV light is then applied to solidify the photosensitive resist. After unmolding, the sample is etched in an oxygen plasma to remove the residual resist remaining in the depths of the pattern. The sacrificial layer then undergoes wet etching to create the undercut necessary to the lift-off process.

The soft-NIL technique is already available and used in the LAAS cleanroom. However, tailoring this technique to accommodate the challenging geometry of diabolo-shaped nanoantennas demands a customized approach. Ali Msahazi Ahamada tackled this issue during his Master 2 internship. His primary objective was to adapt the soft-NIL process and subsequent lift-off to successfully fabricate 150 nm-high metallic nanodiabolos.

One of the main challenges encountered arises from the lift-off process following soft-NIL. In order to achieve successful replication of diabolo-shaped nanoantennas, an effective lift-off step is crucial to remove unwanted material and isolate the replicated structures. A bilayer lift-off process has shown to be effective in generating the necessary undercut for ensuring clean and well-defined nanoantenna structures. However, the important height of the nanoantennas adds complexity to this step. Indeed, taller structures necessitate precise control over the bilayer materials and their etching characteristics to prevent structural collapse or damage during etching.

The intern's work focused on developing an optimized bilayer lift-off process that accommodates the height of the desired nanoantennas. This involved a study of various sacrificial layers, etching solvents and etching parameters, considering both the dimensions of the nanoantennas and the constraints of the soft-NIL technique.

In the end, he managed to successfully replicate 130 nm-height nanoantennas using a NIL/lift-off process. These developments pave the way for the fabrication of large-scale photothermal interfaces covered with diabolo-shape nanoantennas.

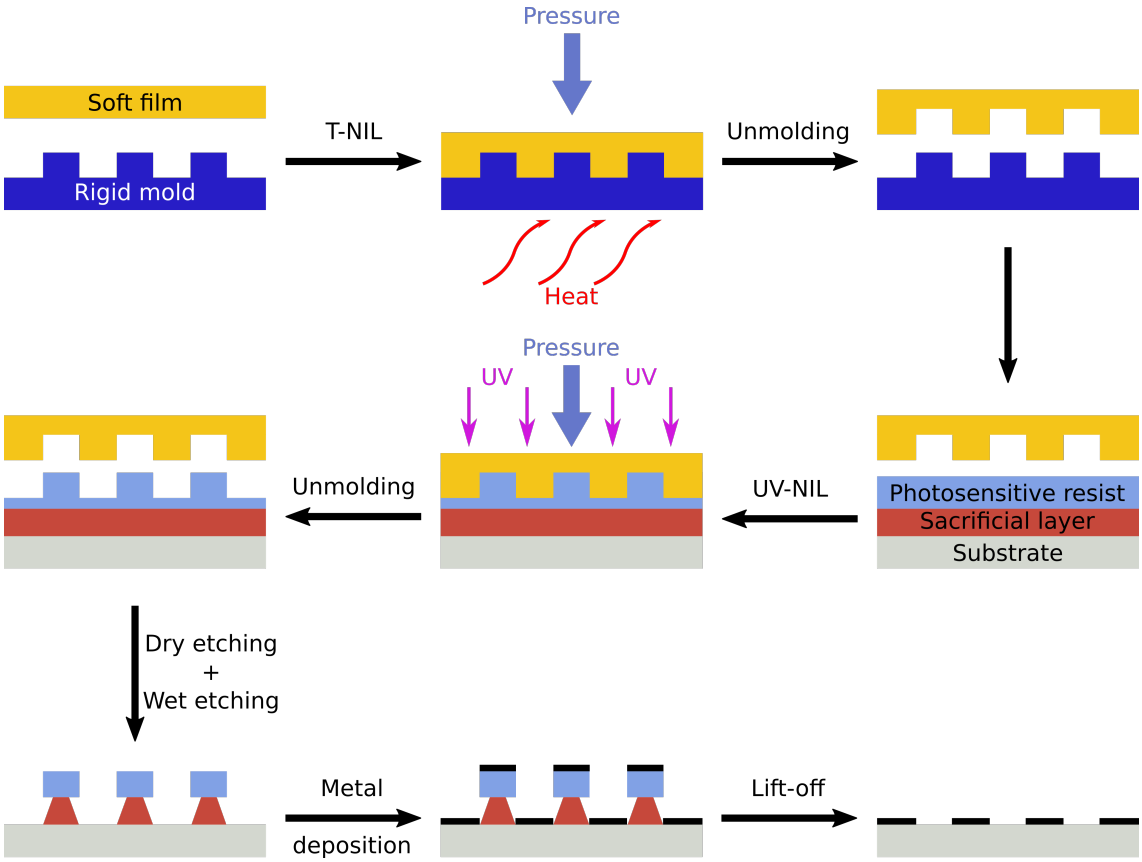

Figure 4.7: Scheme describing the use of soft nanoimprint lithography, including a step of T-NIL and UV-NIL, to replicate a pattern from a rigid mold to a substrate.

4.6 Impact of substrate and capping layer

The purpose of a photothermal interface is to be integrated in PV-TE devices, to increase the temperature at the interface between the back side of the substrate and the hot side of the TEG. We should thus aim at maximizing the temperature at the back side of the substrate. The fabricated photothermal interfaces presented in this section were all made on a glass substrate, which has a low thermal conductivity. However, in this context, the substrate plays a major role in determining the temperature distribution within the interface. A substrate with low thermal conductivity limits the conductive heat transfer from the nanoantennas, where the heat is generated, to the back of the substrate. On the other hand, using a substrate with high thermal conductivity allows to preferentially direct the heat flux toward the TEG. Aluminum nitride (AlN), which thermal conductivity can reach over 200 $\mathrm{W\,m^{-1}\,K^{-1}}$, is an excellent candidate for a photothermal interface substrate.

Moreover, in order to integrate such interfaces in a PV-TE device, the nanoantenna arrays would need to be encapsulated in a capping layer, which role is to

protect the nanoantennas from physical and chemical attacks from the environment. However, the addition of a capping layer could significantly impact the optical and thermal properties of the interface.

Of course, the capping layer needs to be optically transparent in the solar infrared region, so that the incident light can be reach the nanoantennas. Then, if the goal is to maximize the temperature at the back side of the substrate, a capping layer with low thermal conductivity would be ideal. Once again, it would allow the heat flux to be directed in the right direction, limiting losses from the top side of the interface. Deposition of a polymer layer, such as polydimethylsiloxane (PDMS), which thermal conductivity is around 0.15 $\mathrm{W\,m^{-1}\,K^{-1}}$, on top of the nanoantenna array would check these specifications [168].

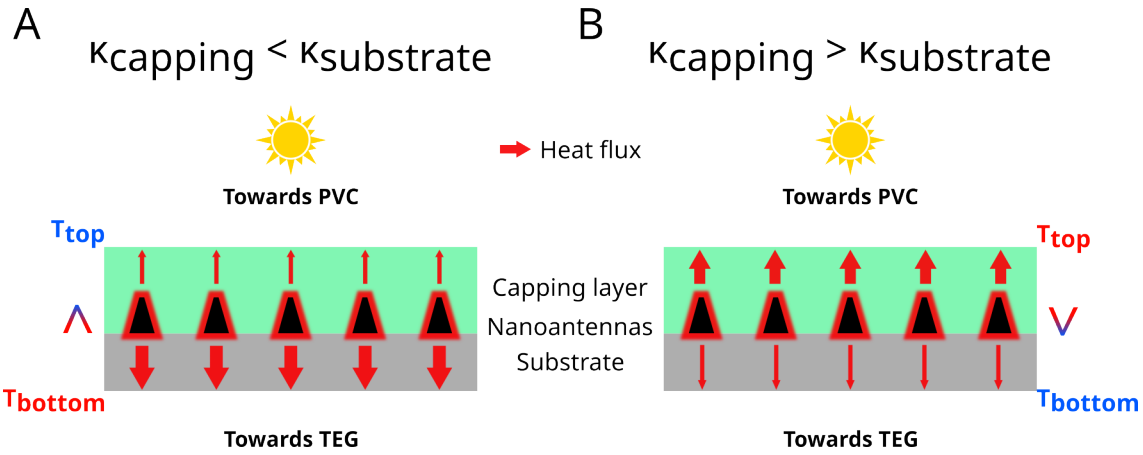

Figure 4.8: Scheme representing the distribution of the heat flux generated from photothermal conversion by the nanoantennas, when (A) the thermal conductivity of the capping layer is lower than that of the substrate and (B) the thermal conductivity of the capping layer is higher than that of the substrate.

A careful selection of the thermal conductivity of the substrate and capping layer can thus be used to tailor the temperature distribution within the photothermal interface. As shown in Figure 4.8A, if the thermal conductivity of the capping layer $\kappa_{capping}$ is lower than that of the substrate $\kappa_{substrate}$, the temperature at the interface directed towards the TEG T_{bottom} will be higher than the temperature at top interface T_{top}. The opposite behavior is expected if the thermal conductivity of the capping layer is higher than that of the substrate (see Figure 4.8B).

Preliminary work was conducted in order to quantify the impact of substrate on the photothermal properties of nanostructured interfaces. The idea was to fabricate nanoantenna arrays on different substrate, including Si and AlN, and to measure the heating under solar infrared illumination. However, a major difficulty lies in the roughness of the rear side of these substrate. Indeed, as explained in Section 4.4, the back surface of the samples must be smooth in order to correctly measure the emissivity of the back side of the samples, which is a critical parameter in the calibration of the IR camera. We thus tried to polish the substrates before fabricating the nanoantennas, but the tools available at that time were not able to sufficiently reduce the surface roughness.

When it comes to the impact of the photothermal interface's substrate and cap-

ping layer on the performances of a complete PV-TE device, the problem is far more complex. Indeed, the heat generated in the PV cell should be able to reach the TEG. Thus, using a capping layer with a low thermal conductivity could result in trapping the heat within the PV cell, increasing its temperature and reducing its performance. The trade-off between directing efficiently the heat flux from the nanoantennas to the TEG and heat dissipation and recovery from the PV cell needs to be optimized. For this purpose, it is necessary to take into account all the physical phenomena occuring in the PV-TE device, which can be done using the multiphysics model presented in Chapter 5.

4.7 Conclusion

In this chapter, large-scale photothermal interfaces (PTIs) were fabricated and investigated, with an emphasis on their optical and thermal properties. The utilization of hole-mask colloidal lithography (HCL) allowed for the creation of PTIs composed of arrays of truncated nanocones with varying compositions and heights. Spectroscopy measurements were employed to study the optical properties of the fabricated samples, revealing that the presence of the substrate plays a significant role in influencing the absorption spectra. The heating capabilities of the photothermal interfaces were rigorously examined under solar infrared illumination using an experimental setup, indicating a substantial temperature increase in the presence of nanoantennas.

Despite qualitative discrepancies between estimated solar absorption and measured heating, this work established the influence of various factors on photothermal properties, including substrate materials, nanoantenna height and composition, and density. Aluminum nanoantennas exhibited remarkable heating efficiency per individual nanocone, surpassing other materials. Moreover, the chapter introduced the potential of utilizing nanoimprint lithography (NIL) for efficient fabrication of complex-shaped nanoantennas, potentially leading to improved temperature gains. A discussion on the impact of the PTI's substrate and capping layer was also included, in order to take into account the consideration emerging from the integration in PV-TE devices.

In conclusion, this chapter provided valuable insights into the fabrication techniques, optical properties, and photothermal efficiency of large-scale photothermal interfaces. These findings pave the way for further exploration and optimization of PTIs, and the development of more intricate and efficient nanoantenna geometries using advanced fabrication techniques like nanoimprint lithography. Now rises the question of the impact of the integration of such PTIs in PV-TE device on the conversion efficiency of the global system, which will be tackled in the next chapter.

Chapter 5

Multiphysics modelling of the photovoltaic-thermoelectric device

In order to validate the use of a nanostructured photothermal interface in PV-TE devices, it is essential to estimate its impact on the electrical power output of the whole system. For this purpose, we implemented a multiphysics model of the photovoltaic cell - photothermal interface - thermoelectric generator device, based on a coupling between optical simulations, thermal transport equations and thermoelectric modeling. The working principles of this multiphysics tool are presented in this chapter, along with a comparison to results published in the literature.

Contents

5.1 General description of the multiphysics model

A complete PV-TE device is a complex system in which optical, thermal and electrical effects are tightly interlinked. The impact of the integration of a photothermal interface in such a system can not be straightforwardly estimated. For

example, it is likely that the addition of a photothermal interface (PTI) will increase the temperature of the photovoltaic cell (PVC) and of the thermoelectric generator (TEG), potentially reducing the performances of the first and increasing those of the latter. Thus, this temperature increase is beneficial to the global electrical power extracted by the system only if the extra power generated by the TEG compensates the loss of PV power. The fulfillment of this condition strongly depends on the physical characteristics of the PTI, the PV cell and the TEG.

In order to estimate the impact of the integration of a photothermal interface in a PV-TE device, it is thus necessary to model the whole system, of which an example is presented in Figure 5.1. Several numerical simulations of PV-TE systems have already been described in the literature. In 2017, Teffah & Zhang [169] integrated the output of a MATLAB/SIMULINK detailed model of a PV cell to a COMSOL Multiphysics model of a PV-TE system. Another team used the Finite Element Method and COMSOL to simulate three-dimensional PV-TE devices [170, 171]. Recently, a fully analytical PV-TE model has been proposed by Liu et al. [172]. In these studies, only the PV layer was optically active, all other layers were supposed to be transparent.

Zhou and coworkers elaborated a multiphysics model to simulate different PV-TE devices incorporating a nanostructured front surface [173, 174, 175]. The purpose of the nanostructures is to reduce reflection at the air-PVC interface. Thus, their spectral transmittance was calculated using Finite-Difference Time-Domain, and only the transmitted light reached the PV active layer. The PV model was based on Poisson's equations, continuity equations and transport equations, and included a temperature-dependent band gap. The presence of two optically active layers (the nanostructured front surface and the PV active layer) is interesting, as it induces the necessity to take into account the spectral response of the materials. Yet, in this model, only the PV active layer was able to absorb light.

In 2022, Park et al. used machine learning to estimate the performance of PV-TE devices including different interface materials [176]. The main issue with this approach is the need of large sets of experimental data for the training phase.

The multiphysics tool we propose in this chapter aims at simulating the behavior of PV-TE devices including a photothermal interface and overcoming some limitations of the previous models. The main improvements lie in the optical processing of the system. Indeed, we will consider a spectrally-dependent absorption in every layer of the PV cell and the PTI.

We will describe a **one-dimensional model** using the **steady-state assumption**. The global PVC-PTI-TEG system is represented by a stack of layers with infinite surface, each having its own thickness and thermal conductivity. The model can be divided into three sub-systems in thermal contact: the PV cell, the photothermal interface and the TEG. Based on the specific characteristics of each layer, we are able to calculate the temperature at each interface of the system, as well as the electrical power generated by the PV cell and the TEG.

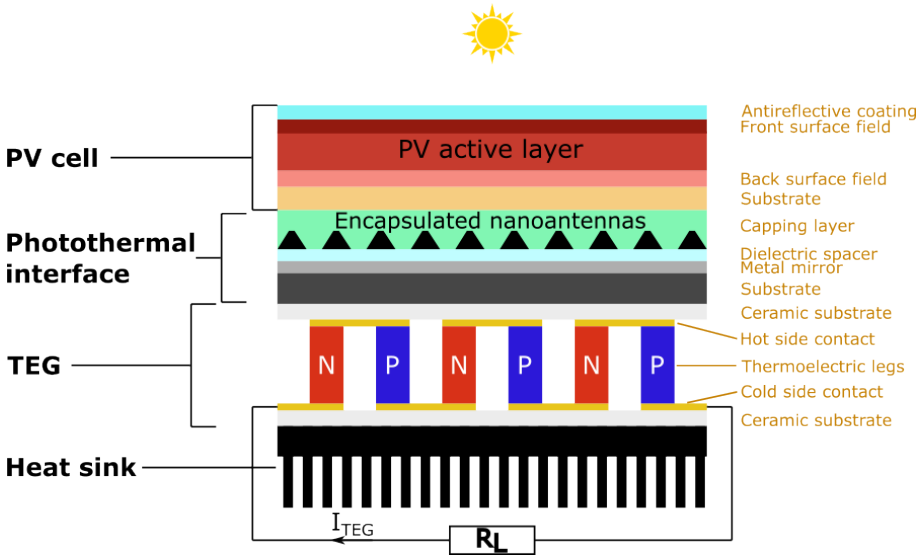

Figure 5.1: Schematic representation of a photovoltaic-thermoelectric device integrating a photothermal interface. The active layer of the PV cell generates the photocurrent I_{PV} when illuminated by the solar spectrum. The PTI is made of encapsulated nanoantennas on top of a multilayered substrate. The N- and P-doped thermoelements are connected in series to a load resistance R_L and generate the current I_{TEG} when exposed to a heat flux. The role of the passive heat sink is to dissipate heat through natural convection.

5.2 Equations of thermal transport

Figure 5.2 represents the 1D model for thermal transfer in the PV-TE system. All the layers in the stack are in thermal contact with the adjacent layers, allowing thermal transfer by conduction. The top and bottom layers are also in contact with the environment, which is air at ambient temperature, resulting in thermal transfer by convection and radiation. Due to various physical phenomena that will be detailed later on (such as photothermal conversion, Joule effect, Peltier effect, thermalization in the PV cell, ...), heat can be generated in the layers. The equations of thermal transfer presented in this section are used to calculate the temperature at each interface of the system, based on the thickness e and thermal conductivity κ of each layer.

As shown in Figure 5.2, in the general case of an inner interface i located between two layers ($i-1$ and i) of the system, the temperature T_i of this interface depends on the conduction from these layers, as well as on the heat flux generated in these layers (Q_{i-1} and Q_i) and eventually at the interface itself (Q). When assuming that the heat generated in each layer is delivered at a point source in the middle of the layer, the general heat balance equation can be written as:

$$\frac{\kappa_{i-1}}{e_{i-1}}(T_i - T_{i-1}) + \frac{\kappa_i}{e_i}(T_i - T_{i+1}) = Q + \frac{Q_{i-1}}{2} + \frac{Q_i}{2} \tag{5.1}$$

where κ_{i-1} and e_{i-1} are the thermal conductivity and thickness of the layer above the interface, while κ_i and e_i are the thermal conductivity and thickness of

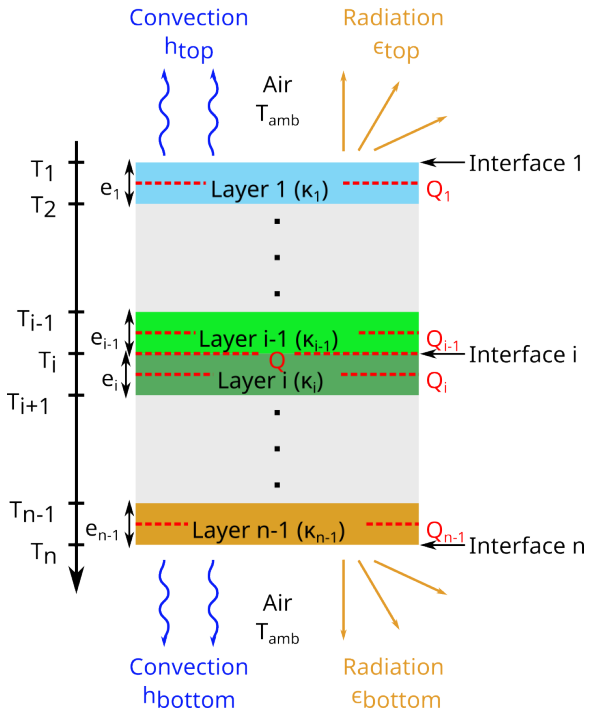

Figure 5.2: Representation of the 1 dimensional model for thermal transfer. T_1 to T_n are the temperature at each interface of the system. Q_1 to Q_{n-1} are the heat flux generated in each layer, with thermal conductivity κ_1 to κ_{n-1}.

the layer below the interface. T_{i-1} and T_{i+1} are the temperature at the interface directly above and below the one considered.

For the top and bottom interfaces of the system, heat transfer by convection and radiation toward the environment at temperature T_{amb} should be taken into account. Thus, in each case, the heat balance equation becomes:

$$\frac{\kappa_1}{e_1}(T_1 - T_2) + h_{top}(T_1 - T_{amb}) + \epsilon_{top} \cdot \sigma(T_1^4 - T_{amb}^4) = \frac{Q_1}{2} \tag{5.2a}$$

$$\frac{\kappa_{n-1}}{e_{n-1}}(T_n - T_{n-1}) + h_{bottom}(T_n - T_{amb}) + \epsilon_{bottom} \cdot \sigma(T_n^4 - T_{amb}^4) = \frac{Q_{n-1}}{2} \tag{5.2b}$$

where σ is the Stefan-Boltzmann constant, and h_{top}, ϵ_{top}, h_{bottom} and ϵ_{bottom} are the convective heat transfer coefficient and emissivity of the top and bottom interfaces respectively. Emissivity is an intrinsic property of the material, while the convective heat transfer coefficient is usually an experimental value depending on the geometry and position of the interface, and on environmental conditions such as air speed.

In order to solve these heat transfer equations, it is necessary to determine the different heat fluxes generated in the system. In the following, we will present the models of the different sub-systems as well as the calculation methods for these heat fluxes.

To summarize, here is a list of the inputs and outputs of the thermal transfer model:

- Inputs:
  1. Thermal conductivity κ of each layer ($\mathrm{W\,m^{-1}\,K^{-1}}$)
  2. Thickness e of each layer (m)
  3. Heat flux generated in each layer Q^{layer} and at each interface $Q^{interface}$ ($\mathrm{W\,m^{-2}}$)
  4. Emissivity ϵ of the top and bottom interfaces
  5. Convective heat transfer coefficient h of the top and bottom interfaces ($\mathrm{W\,m^{-2}\,K^{-1}}$)
  6. Ambient temperature T_{amb} (K)
- Outputs:
  1. Temperature T at each interface of the system (K)

5.3 Model of the photovoltaic cell

The efficiency of PV cells is measured in Standard Test Conditions, under illumination by the AM1.5G solar spectrum at 1000 W/m² and at a controlled temperature of $T_{ref} = 25$ °C, in order to extract the reference conversion efficiency η_{ref}. In normal operating conditions, the temperature of a PV cell can reach up to 60 °C due to non-radiative losses [177, 178]. These losses include thermalization of high-energy photons and Joule effect. The impact of temperature T on the conversion efficiency η of a PV cell can be described using the temperature coefficient β, as presented in detail in [179], assuming a linear variation:

$$\eta(T) = \eta_{ref} + \beta(T - T_{ref}) \tag{5.3}$$

For most PV cells, an increase in the temperature leads to a decrease of performances, in which case the temperature coefficient is negative. The power output per unit surface $P_{out}^{PV}(T)$ generated by a PV cell at temperature T is thus given by:

$$P_{out}^{PV}(T) = \eta(T) \cdot P_{sun} = (\eta_{ref} + \beta(T - T_{ref}))\, P_{sun} \tag{5.4}$$

where P_{sun} is the irradiance of the AM1.5G solar spectrum.

The model of the PV cell is made of a stack of layers, including the PV active layer in which the photovoltaic conversion is assumed to take place. As an example, for a GaAs PV cell, the active layer is the p-n junction. Using the open-source code Moosh [180], the optical absorption P_{abs}^{layer} in each layer of the PV model, as

well as the transmitted P_{trans}^{PV} and reflected P_{refl}^{PV} irradiances, are calculated under normal unpolarized solar illumination, based on the complex refractive index and thicknesses of the layers. Rigorously, the refractive index of a material depends on its temperature. However, to simplify the calculations and limit the amount of data needed to run the model, we only input the refractive index at ambient temperature. The calculated absorbed, reflected and transmitted powers are thus independent of temperature. It is assumed that the absorbed optical power is fully converted into heat for all layers ($Q^{layer} = P_{abs}^{layer}$), except for the active layer. Indeed, for this specific layer, the absorbed optical power can be converted through various physical phenomena:

- **Photovoltaic conversion**, which is the purpose of the PV cell, generates the electrical power $P_{out}^{PV}(T)$
- **Radiative recombination:** photogenerated excitons can recombine, resulting in photon emission. The power lost this way is noted $P_{rad}(T)$. In the case of classical semiconductors such as Si or GaAs, the radiative losses represent a negligible part of the incident solar power ($\approx 0.1\%$) [181].
- **Thermalization** is the non-radiative relaxation of excitons with an energy above the band gap $E_g(T)$ of the cell. The heat power generated by thermalization is expressed as:

$$Q_{therm}(T) = \int_0^{\lambda_g} \left(1 - \frac{E_g(T)}{E(\lambda)}\right) P_{abs}^{PV}(\lambda) \cdot d\lambda \tag{5.5}$$

  where λ_g is the band gap wavelength of the cell, $E(\lambda)$ the energy of a photon with wavelength λ and $P_{abs}^{PV}(\lambda)$ the optical power density absorbed by the active layer at a wavelength λ. Rigorously, the band gap of the PV cell depends on its temperature, according to the Varshni empirical law, using two constants α and γ:

$$E_g(T) = E_g(0) - \frac{\alpha T^2}{T + \gamma} \tag{5.6}$$

  Typically, for a GaAs solar cell, the values for α and γ are $5.405 \cdot 10^{-4}$ eV/K and 204 K respectively [182, 183]. The variation of $E_g(T)$ is incidentally the main source of the temperature-dependent efficiency shift described by the temperature coefficient β.
- **Non-radiative losses** include several sources of loss, such as non-radiative recombination of excitons and Joule heating, which collectively generate the heat power $Q_{NRad}(T)$.

Thus, the optical power absorbed in the PV active layer, noted P_{abs}^{PV}, is the sum of the converted powers:

$$P_{abs}^{PV} = P_{out}^{PV}(T) + P_{rad}(T) + Q_{therm}(T) + Q_{NRad}(T) \tag{5.7}$$

The heat generated in the active layer $Q^{PV}(T)$ results from the combination of thermalization and non-radiative losses, but can also be expressed as the difference between the absorbed optical power and the radiative and electrical generated powers:

$$Q^{PV}(T) = Q_{therm}(T) + Q_{NRad}(T) \tag{5.8a}$$
$$= P_{abs}^{PV} - P_{out}^{PV}(T) - P_{rad}(T) \tag{5.8b}$$

Using Equation 5.8a to calculate the heat flux generated in the active layer can be difficult, as it requires empirical data on the evolution of the band gap of the cell with temperature, as well as an estimation of the non-radiative losses. On the other hand, as radiative recombination can be neglected in Equation 5.8b, we can assume in the model that all the optical power that is absorbed and not converted into electricity generates heat. Thus, the heat flux generated in the active layer is:

$$Q^{PV}(T) = P_{abs}^{PV} - P_{out}^{PV}(T) \tag{5.9}$$

It should be noted that the output electrical power of the cell ($P_{out}^{PV}(T)$) and the heat generated in the active layer ($Q^{PV}(T)$) both depend on its temperature. This coupling adds a level of complexity to the calculation of the final temperature distribution of the system, increasing the computing time.

To summarize, here is a list of the inputs and outputs of the PV cell model:

- Inputs:
  1. Incident solar spectrum $P_{sun}(\lambda)$ ($\mathrm{W\,m^{-2}\,nm^{-1}}$)
  2. Refractive indices of the materials
  3. Structure (order of the layers in the stack) and position of the active layer
  4. Thickness e^{layer} of each layer (m)
  5. Reference efficiency η_{ref} and temperature T_{ref} (K) of the cell
  6. Temperature coefficient β ($\mathrm{K^{-1}}$)
  7. Temperature T of the active layer (K)
- Outputs:
  1. Electrical power density P_{out}^{PV} generated by the PV cell ($\mathrm{W\,m^{-2}}$)
  2. Heat flux generated in each layer Q^{layer}, including the active layer (Q^{PV}) ($\mathrm{W\,m^{-2}}$)
  3. Optical power density transmitted through P_{trans}^{PV} and reflected by P_{refl}^{PV} the PV cell ($\mathrm{W\,m^{-2}}$)

5.4 Model of the photothermal interface

5.4.1 Description of the photothermal interface model

We used the DDA method to simulate the optical properties of nanostructured photothermal interfaces. However, contrary to the studies on isolated particles presented in the Chapter 3, we now need to take into account the impact of the substrate and encapsulant. Thus, as illustrated in Figure 5.3 (inset), the simulation target representing a given PTI is made of a square unit cell, including the substrate, one particle and the encapsulating layer.

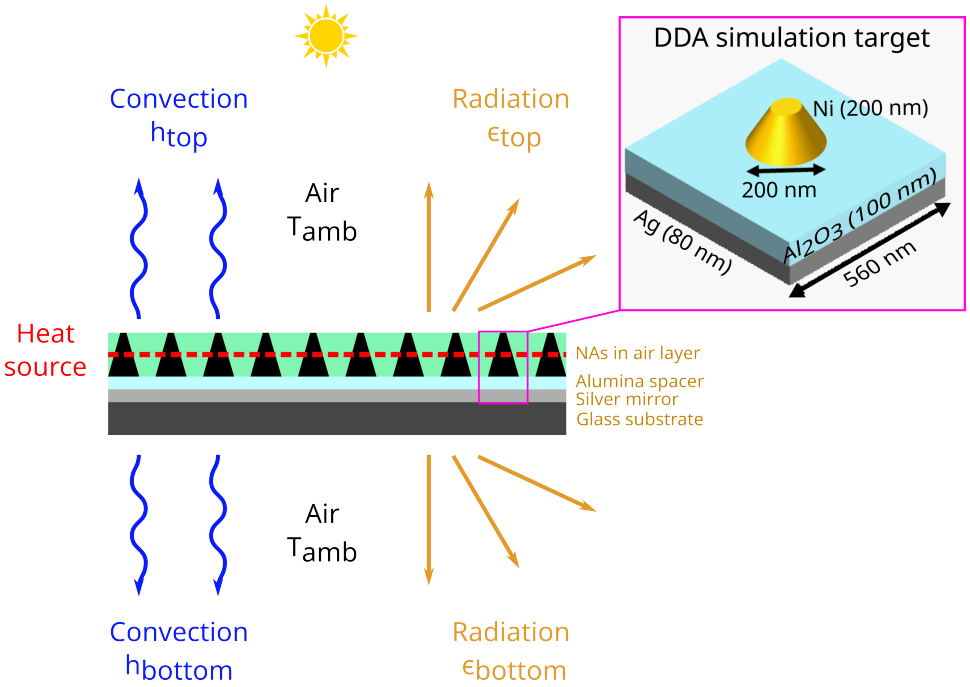

Figure 5.3: Scheme of a nanostructured photothermal interface with glass/silver/alumina substrate. The inset shows an example of DDA simulation target used to calculate the absorptivity of the interface.

The lateral size of a unit cell is set so that the filling factor of the nanoantenna on the unit cell matches the surface density of particles on the substrate of the PTI. In other words, a PTI with a surface S_{PTI}, covered by an array of N nanoantennas, is represented by a unit cell with dimensions $L \times L$ containing a single nanoantenna, with:

$$L = \sqrt{\frac{S_{PTI}}{N}} \tag{5.10}$$

The absorption cross-section of the target, $\sigma_{abs}(\lambda)$, calculated using the DDA method, is used to determine the absorptivity $A(\lambda)$ of the PTI and the optical power density P_{abs}^{PTI} it would absorb under an incident optical power density $P_{inc}(\lambda)$:

$$A(\lambda) = \frac{\sigma_{abs}(\lambda)}{L^2} \tag{5.11}$$

$$P_{abs}^{PTI} = \int_0^\infty A(\lambda) \cdot P_{inc}(\lambda) d\lambda \tag{5.12}$$

In the case of a complete PVC-PTI-TEG system, the incident spectrum is the one transmitted by the PV cell ($P_{trans}^{PV}(\lambda)$), as calculated in the previous section.

The heat Q^{PTI} generated by the PTI is calculated assuming that the optical power absorbed by the PTI is fully converted into heat at the center of this effective layer (Q^{PTI}=P_{abs}^{PTI}).

For the thermal transfer calculations, the nanoantenna layer is represented by an effective medium, which thermal conductivity $\kappa_{effective}$ is calculated by weighing the thermal resistance of the nanoantenna κ_{NA} and the encapsulant κ_{encaps} by their relative volume fraction. For an array of nanoantennas with height H_{NA} and volume V_{NA}, the effective thermal conductivity is:

$$\kappa_{effective} = \frac{V_{NA} \cdot \kappa_{NA} + \left(L^2 \cdot h_{NA} - V_{NA}\right) \kappa_{encaps}}{L^2 \cdot h_{NA}} \tag{5.13}$$

To summarize, here is a list of the inputs and outputs of the PTI model:

- Inputs:
  1. Refractive indices of the materials
  2. Structure (order of the layers in the stack)
  3. Thickness e^{layer} of each layer (m)
  4. Shape and dimensions of a nanoantenna
  5. Surface density of nanoantenna (m^{-2})
  6. Incident optical spectrum $P_{inc}(\lambda)$ ($\mathrm{W\,m^{-2}\,nm^{-1}}$)
- Outputs:
  1. Heat flux generated in the photothermal interface Q^{PTI} ($\mathrm{W\,m^{-2}}$)

5.4.2 Comparison to experimental results

The model of the nanostructured photothermal interface can be used in combination with the equations of thermal transfer described in Section 5.2 to calculate the temperature of photothermal interfaces under illumination, as presented in Figure 5.3. Thus, we can compare the heating calculated with the model to the experimental heating measured by IR thermography in Chapter 4, in order to validate the

model of the photothermal interface independently from the complete PVC-PTI-TEG device.

The PTIs presented in Chapter 4 were all made of a glass substrate covered by a 80 nm silver layer and a 100 nm-thick alumina spacer. On top of it were deposited disordered arrays of truncated nanocones with 200 nm base diameter, having different heights H and compositions: nickel (H=50 nm and H=200 nm), silver (H=50 nm), gold (H=50 nm) and aluminum (H=50 nm). The density of nanoantennas per unit surface was estimated from SEM images of each sample. Though the colloidal lithography technique used to pattern the PTIs leads to a disordered nanoantenna arrangement, the DDA simulations targets were still made of a single particle on a square substrate with dimensions $L \times L$, according to Equation 5.10. An example of simulation target is represented on Figure 5.3. As the silver layer is assumed to be fully opaque to solar radiation, the glass substrate is not included in the target, which greatly reduces the number of dipoles and the calculation time. The capping layer is made of air, with a thickness corresponding to the height of the nanoantennas.

The calculated absorptivity of these targets is plotted on Figure 5.4. Though the greater absorptivity of 200 nm-high cones is obvious compared to the 50 nm-high cones, it can be seen that all structures exhibit an absorption peak around 1 µm.

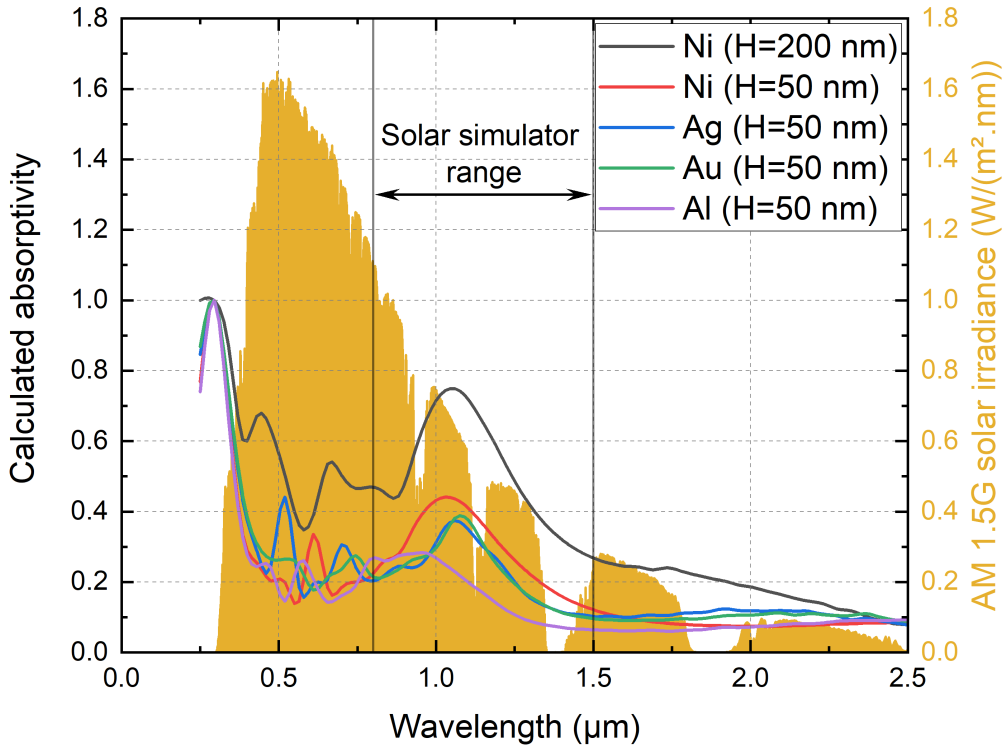

Figure 5.4: Absorptivity of photothermal interfaces covered with array of truncated nanocones, estimated based on the absorption cross-sections calculated by DDA. The AM1.5G solar spectrum is represented in yellow for comparison.

For the heating measurement of the fabricated PTI, a solar simulator limited to the 0.8-1.5 µm range was used as the illumination source (see Section 2.3.3 for more details). Thus, the same spectrum is set as the incident optical power in the simulations.

As for the thermal parameters of the simulation, they are summarized in Table 5.1. The top and bottom convective heat transfer coefficients are set to 9 $\mathrm{W\,m^{-2}\,K^{-1}}$, an empirical value for vertical surfaces in natural convection, as the PTIs are positioned vertically in the experimental setup. The emissivity of the back side of the samples was measured to be 0.86 by FTIR spectroscopy, as described in Section 2.3.3. The same value of emissivity is used for the front side. The ambient temperature, measured to be 26 °C, is the same in the simulation.

Thermal conductivity ($\mathrm{W\,m^{-1}\,K^{-1}}$))		Radiative and convective properties	
Glass	1.05	Top surface emissivity ϵ_{top}	0.86
Silver	428	Bottom surface emissivity ϵ_{bottom}	0.86
Alumina	36	Top surface convective coefficient h_{top} ($\mathrm{W\,m^{-2}\,K}-1$)	9
Air	0.03	Bottom surface convective coefficient h_{bottom} ($\mathrm{W\,m^{-2}\,K}-1$)	9
Nickel	94	Ambient temperature T_{amb} (°C)	26
Gold	318		
Aluminum	236		

Table 5.1: Thermal properties used in the simulation of photothermal interfaces. The thermal conductivities are taken from [184].

With these parameters, the heating of the back side of each sample is calculated by the model and compared to the experimental results in Figure 5.5. Table 5.2 shows that the relative error of the calculated heating ranges between −51 % and 31 %. The best prediction is made for the hottest sample (Ni 200 nm), and the agreement between measured and calculated heating seems to decrease with the calculated temperature. Overall, the calculated heating exhibits the same tendency as the measured one, with an absolute error limited to ±1 °C, except for the Al sample which shows the largest error compared to the experiment. Thus, the model of the PTI seems to be able to predict the qualitative heating generated by different samples, and thus allows to rank their photothermal conversion efficiency.

We notice an important difference between the calculated and measured heating. Several sources of error can be expected here, and it is difficult, with the data at hand, to identify the most relevant ones. First, there can be differences between the absorption spectra calculated by DDA and the experimental ones. The effect of dispersion in size of nanoantennas and inter-particular distance, which can result in a broadening of the absorption peaks, is not taken into account in the simulation, as they are conducted on a single unit cell. Also, the surface density of nanoantennas on the fabricated photothermal interfaces was measured in the center of the sample, and might not be homogeneous over the 2x2 $\mathrm{cm^2}$ substrate. It is worth noting that, in our model, the calculated absorption spectrum of the interface can easily be replaced by an experimental spectrum, which would cancel these uncertainties.

Other sources of error include the input parameters of the model, such as the convective coefficients which are not experimentally measured nor controlled. Intrinsic limitations of the model can also come into play. For example, as this is a

one dimensional model, the heat losses by the sides of the photothermal interfaces are neglected.

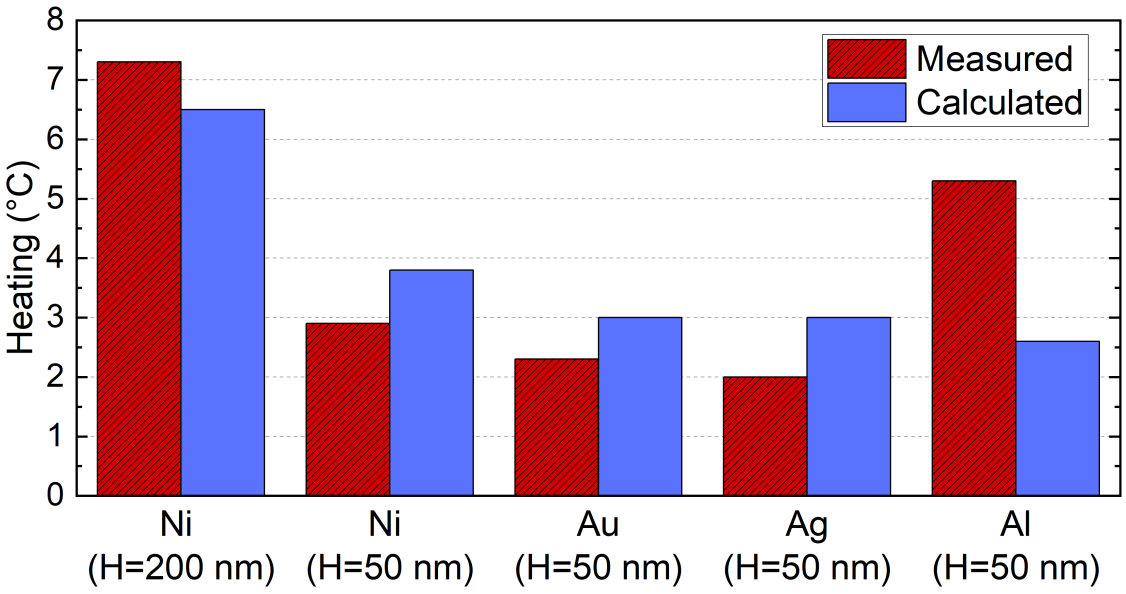

Figure 5.5: Histogram comparing the measured and calculated heating, under illumination by a solar spectrum limited to the 0.8-1.5 µm wavelength range, for different nanostructured photothermal interfaces.

Heating (°C)	Measured	Calculated	Absolute error	Relative error
Ni (H=200 nm)	7.3	6.5	−0.8	−11%
Ni (H=50 nm)	2.9	3.8	+0.9	+31%
Au (H=50 nm)	2.3	3.0	+0.7	+30%
Ag (H=50 nm)	2.0	3.0	+1.0	+50%
Al (H=50 nm)	5.3	2.6	−2.7	−51%

Table 5.2: Comparison between the experimental and calculated heating of photothermal interfaces covered with array of nanocones under illumination by a solar spectrum limited to the 0.8-1.5 µm wavelength range.

Highlights of the section

In this section, we described the model of a nanostructured photothermal interface, which allows to calculate the heat flux generated by a PTI under illumination, based on the geometrical parameters of the nanoantenna array. We used this model in combination with the equations of thermal transport to calculate the temperature increase of fabricated photothermal interfaces under solar infrared illumination. The results obtained through numerical simulations were then compared to experimental data, to which it showed quantitative errors but a good qualitative agreement.

5.5 Model of the thermoelectric generator

The TEG model is made of a stack of layers representing the heat sink, the ceramic substrates, the metallic contacts and the thermoelectric layer. The latter is made of an array of N pairs of n- and p- doped thermoelectric legs with a length L_{leg}, a cross-section A_{leg}, a thermal conductivity κ_{leg} and an electrical resistivity ρ_{leg}. The density of pairs by unit surface d is given by the ratio of N over the total surface of the TEG S_{TEG}. The internal electric resistance of a leg and the thermal conductivity of the thermoelectric layer are expressed respectively as:

$$R_{leg} = \frac{\rho_{leg} \cdot L_{leg}}{A_{leg}} \tag{5.14}$$

$$\kappa_{TE} = 2\,d \cdot A_{leg} \cdot \kappa_{leg} \tag{5.15}$$

A TEG connected to a load resistance R_L generates electric current when a temperature gradient is present between the hot side (at temperature T_H) and cold side (at temperature T_C) of the thermoelectric elements. The intensity I of this current depends on the internal electric resistance and Seebeck coefficient of a leg (R_{leg} and α_{leg} respectively), according to:

$$I = \frac{2\,N \cdot \alpha_{leg}\,(T_H - T_C)}{2\,N \cdot R_{leg} + R_L} \tag{5.16}$$

Thus, the power output per unit surface P_{out}^{TEG} generated by the TEG is:

$$P_{out}^{TEG} = \frac{I^2 \cdot R_L}{S_{TEG}} = \left(\frac{2\,N \cdot \alpha_{leg}\,(T_H - T_C)}{2\,N \cdot R_{leg} + R_L}\right)^2 \frac{R_L}{S_{TEG}} \tag{5.17}$$

Note that the maximum power output is achieved when the load resistance matches the internal resistance of the TEG ($R_L = 2\,N \cdot R_{leg}$).

The current flowing through the operating TEG is responsible for heat generation in the thermoelectric layer by Joule effect:

$$Q_{Joule}^{TE} = \frac{2\,I^2 \cdot N \cdot R_{leg}}{S_{TEG}} \tag{5.18}$$

Because a TEG is also a Peltier module, Peltier effect occurs at the top and bottom interfaces of the thermoelectric layer, heating the cold side and cooling down the hot side. The heat flux generated by Peltier effect at the hot and cold interfaces, designated as $Q_{Peltier}^{H}$ and $Q_{Peltier}^{C}$ respectively, are expressed as:

$$Q^{H}_{Peltier} = -2\,d \cdot \alpha_{leg} \cdot T_H \cdot I \tag{5.19a}$$

$$Q^{C}_{Peltier} = 2\,d \cdot \alpha_{leg} \cdot T_C \cdot I \tag{5.19b}$$

To summarize, here is a list of the inputs and outputs of the TEG model:

- Inputs:
  1. Properties of a single thermoelectric leg
     - Absolute Seebeck coefficient α_{leg} ($\mathrm{V\,K^{-1}}$)
     - Thermal conductivity κ_{leg} ($\mathrm{W\,m^{-1}\,K^{-1}}$)
     - Electrical resistivity ρ_{leg} ($\Omega\,\mathrm{m}$)
     - Length L_{leg} (m)
     - Cross-section A_{leg} ($\mathrm{m^2}$)
  2. Number of pairs of TE legs N
  3. Total surface of the TEG S_{TEG} ($\mathrm{m^2}$)
  4. Load resistance R_L (Ω)
  5. Temperature of the hot T_H and cold T_C contacts (K)
- Outputs:
  1. Electrical power P^{TEG}_{out} generated by the TEG ($\mathrm{W\,m^{-2}}$)
  2. Heat power generated in the thermoelectric layer by Joule effect Q^{TE}_{Joule} ($\mathrm{W\,m^{-2}}$)
  3. Heat power generated at the hot $Q^{H}_{Peltier}$ and cold $Q^{C}_{Peltier}$ side of the thermoelectric layer by Peltier effect ($\mathrm{W\,m^{-2}}$)

5.6 Coupling of the sub-systems

Finally, to model the complete PVC-PTI-TEG system, the three sub-systems are coupled owing to the equations of thermal transfer. Figure 5.6 presents the different steps involved to calculate the output power of the PVC and the TEG.

At the beginning of the process, the whole system is set at ambient temperature. First, based on the incident solar spectrum and the properties of the PV cell, photonic simulations using the Moosh code are conducted to compute the optical absorption in each layer of the cell, as well as the transmitted power. The heat generated in the PV cell, resulting from photothermal conversion, thermalization and non-radiative losses, is calculated using the model presented previously.

The optical power transmitted through the PV cell is then used as the incident optical spectrum in the PTI model. DDA simulations allow to estimate the absorption in the PTI, which is supposed fully opaque, so that no light is transmitted

to the TEG. The optical power scattered or reflected by the PTI is assumed to be lost from the system. As presented in Section 5.4.1, the heat generated in the PTI results from the photothermal conversion of absorbed optical power.

The model of the TEG is used to calculate the heat generated in the thermoelectric layer based on the temperatures of the hot and cold side.

Thus, the heat generated in each layer of the system is computed for a given temperature distribution (which is homogeneous in the first iteration).

The models of the PVC, the PTI and the TEG are placed in thermal contact, which means that, from the point of view of thermal transfer, the top layer of the PTI is placed directly below the bottom layer of the PVC, while the bottom layer of the PTI is placed directly above the top layer of the TEG. In both case, the interface thermal resistance is neglected and the transfer is assumed to be fully conductive.

MatLab is used to solve the system of coupled equations defining the temperature at each interface, based on the heat generated in each layer. The new set of temperatures is then used to compute the heat generation. Through an iterative process, the solver converges towards a set of positive solutions, which are used to calculate the electrical power generated by the PV cell and the TEG.

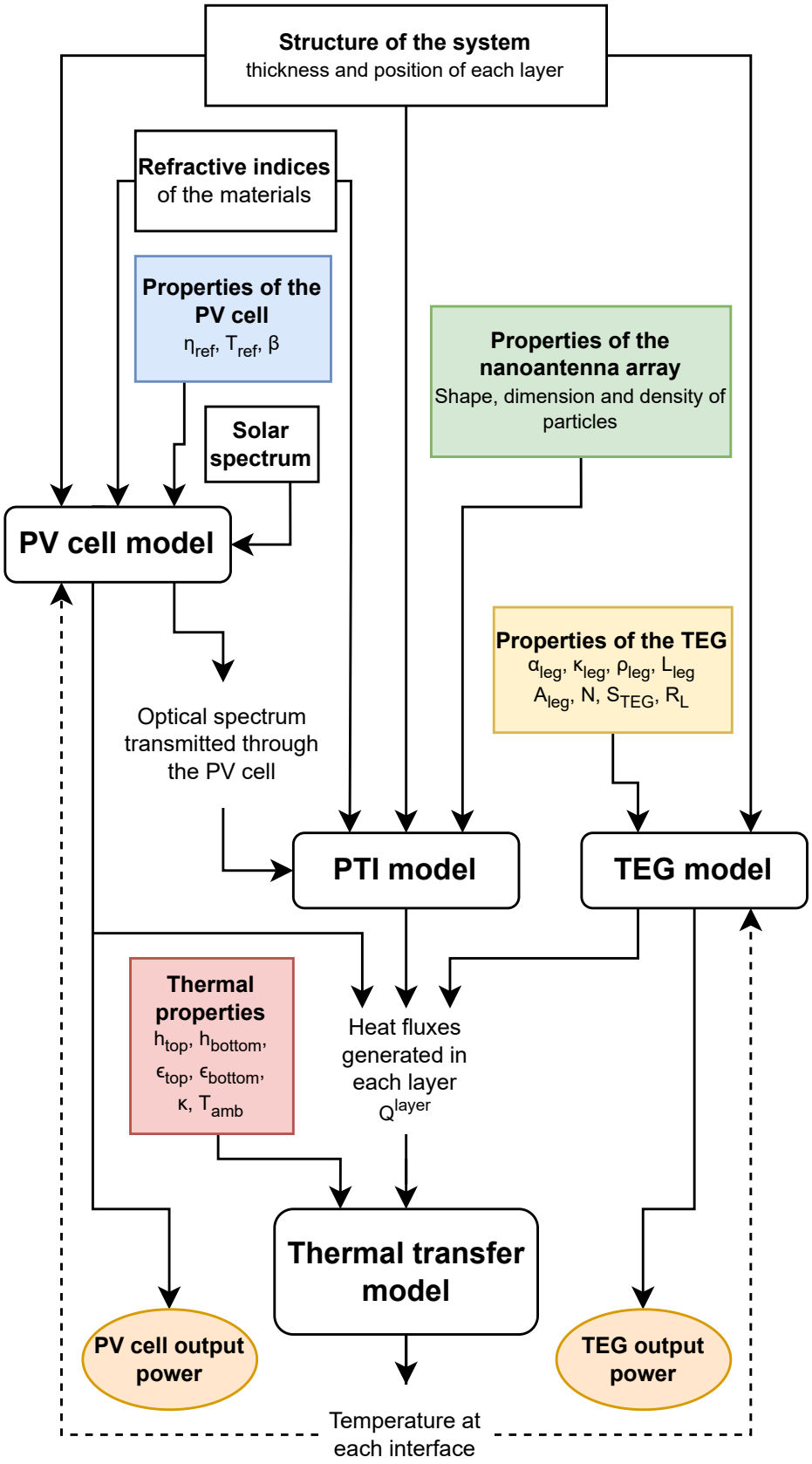

Figure 5.6: Diagram presenting the principle of the multiphysics tool allowing to calculate the electrical power generated by a PVC-PTI-TEG device based on the properties of its components.

5.7 Validation of the model by comparison to the literature

A few models of PV-TE devices have already been reported in the literature [169, 170, 173], offering opportunity for comparison with our model. However, none of them include a nanostructured photothermal interface between the PV cell and the TEG. In this section, we will compare the results obtained with our model to the results published by Zhou and coworkers in 2018 [174]. In this paper, the authors describe a 3D multiphysics model of a PV-TE device made of a silicon solar cell, a thermoelectric generator and a passive heat sink.

Their solar cell is covered by a nanostructured array encapsulated in a EVA layer, which purpose is to reduce reflection at the air-PVC interface. They use a Finite Difference Time Domain method to simulate the optical properties of this layer. In our case, this is replaced by a simple EVA layer. Thus, to account for the reflection reduction introduced by this nanostructured layer that is not calculated in our model, we assume that there is no optical reflection, meaning that all the reflected optical power reaches the active layer of the PV cell.

The PV model used in the paper is more complex than ours, and requires the input of the doping characteristics of the PV cell. These quantities are difficult to measure experimentally and are often not included in the papers on photovoltaic cells. On the other hand, the reference efficiency and temperature coefficient are routinely measured when characterizing a PV cell. From the data given by Zhou et al, we are able to deduce that the PVC used in the paper has an efficiency of 11.55 % at 120 °C and a temperature coefficient of -0.056 %/°C. In the paper, it is assumed that all the optical power reaching the active layer of the PVC is either converted in electricity or in heat, with no transmission.

To satisfy the conditions of absence of reflection and transmission, Equation 5.8b is modified to:

$$Q^{PV} = P_{abs}^{PV} + P_{refl}^{PV} + P_{trans}^{PV} - P_{out}^{PV}(T) \tag{5.20}$$

where P_{refl}^{PV} and P_{trans}^{PV} are the optical power reflected by and transmitted through the PV cell, respectively.

No modifications are made to the model of the TEG, as both are similar.

Most inputs of the system, such as thickness and thermal conductivity of the layers, and the parameters of the TEG, are taken directly from the publication. The ambient temperature is set at 300 K, and the incident optical power is the solar spectrum with a concentration ratio of 10. However, the emissivity and convection coefficients are not provided in the paper. In our model, they are set accordingly to Table 5.3.

Zhou et al. simulated two PV-TE structures:

Radiative and convective properties	
Top surface emissivity ϵ_{top}	0.85
Bottom surface emissivity ϵ_{bottom}	0.1
Top surface convective coefficient h_{top} ($\mathrm{W\,m^{-2}\,K^{-1}}$)	2
Bottom surface convective coefficient h_{bottom} ($\mathrm{W\,m^{-2}\,K^{-1}}$)	120

Table 5.3: Thermal properties used in the simulation of the PVC-TEG device

- **A standard structure**, in which the PV cell layers are, from top to bottom: glass, EVA, PV active layer, EVA and tedlar. A TEG made of ceramic, copper contacts, thermoelectric elements, copper contacts and ceramic is placed just below the PVC.
- **An optimized structure** designed to enhanced the thermal contact between the PV cell and the TEG. In this configuration, the PV cell layers are, from top to bottom: glass, EVA and PV active layer. The top and bottom ceramic substrates of the TEG, having low thermal conductivity, have been replaced by RTV silicone.

We simulated these two structures using our home-made model. The calculated temperature distributions along the devices are compared to the results of Zhou et al. in Figure 5.7. For both structures, our model shows a good agreement with the data from the literature. The main difference is a lower temperature gradient through the thermoelectric layer in our case. This can result from an underestimation of the heat generated in the PV cell.

The power outputs of the PV cell and TEG resulting from these temperature distributions are presented in Table 5.4. For both structures, the power output of the PV cell is consistent with the paper, which makes sense due to the similar temperature of the cells. The power output of the TEG is lowered with our model in both cases, due to the lower temperature gradient through the thermoelectric layer. For the traditional structure, Zhou et al. calculated a gradient of 25.1 °C, when ours is only 21.9 °C. Overall, the results of our PV-TE model seems to correspond to the state-of-the-art in PV-TE simulation.

Output power density ($\mathrm{W/m^2}$)	PV	TE	System
Traditional structure			
Zhou et al.	1051.6	112.0	1163.6
This work	1043.5	71.2	1114.7
Optimized structure			
Zhou et al.	1154.5	114.5	1269.0
This work	1166.4	73.2	1239.6

Table 5.4: Comparison between the calculated power outputs by our model and the model from Zhou et al., for the traditional and optimized structures.

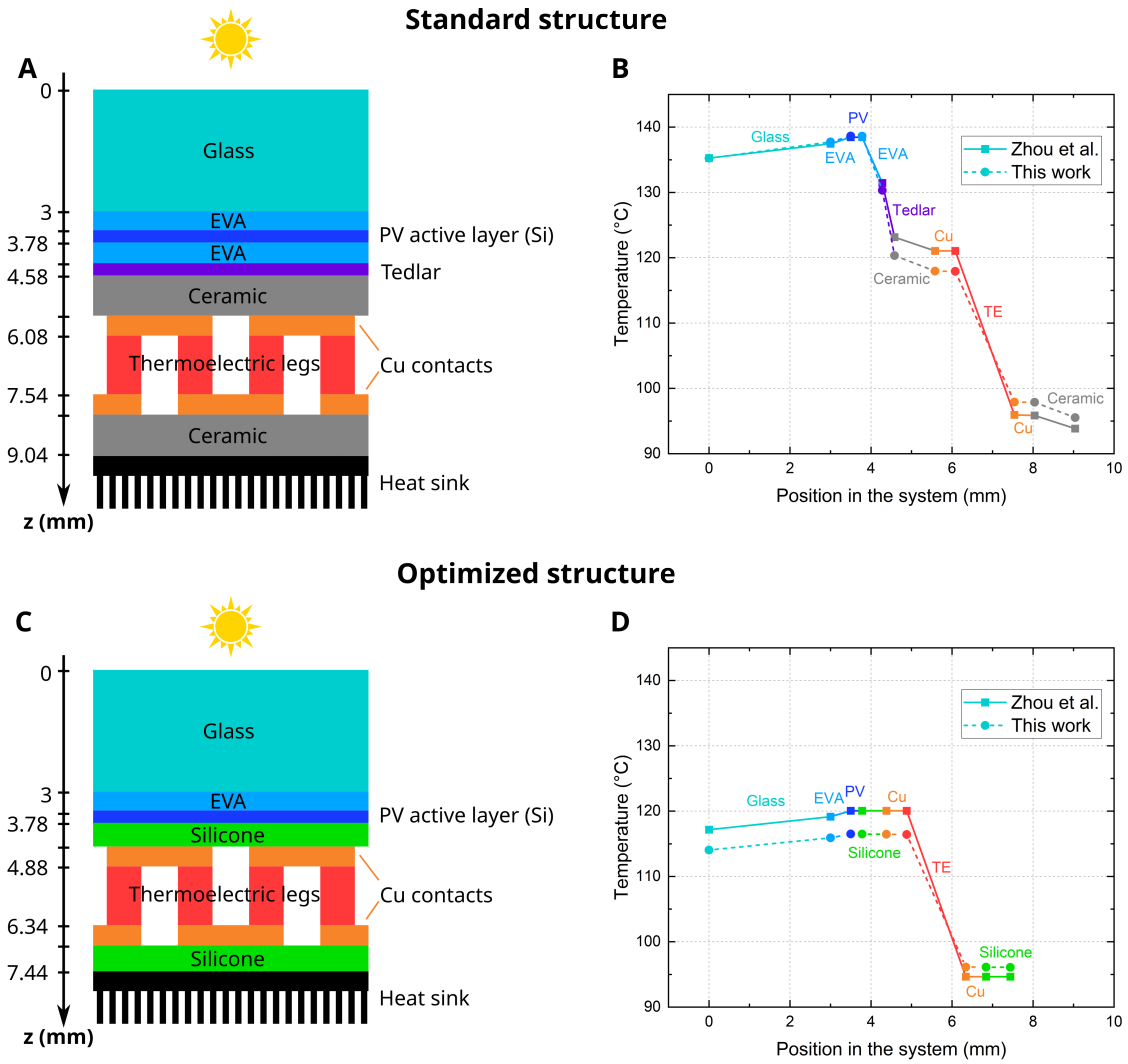

Figure 5.7: Comparison between the temperature distribution in two PV-TE devices calculated by Zhou et al. [174], and calculated using the multiphysics model presented in this work. (A) Scheme of the simulated system and (B) temperature distribution for a traditional PV-TE device. (C) Scheme of the simulated system and (D) temperature distribution for an optimized PV-TE device with enhanced thermal coupling.

Highlights of the section

Our home-made multiphysics model of PV-TE devices has been compared to a state-of-the-art model available in the literature. Based on the data provided by Zhou et al., two PV-TE structures were simulated: a standard and an optimized one. In both cases, the temperature distribution in the system resulting from our calculations is in good agreement with the results of Zhou et al. The main divergence arises from the temperature gradient through the TEG, which is smaller in our case, resulting in a significant difference of thermoelectric output power. However, the output power density of the whole system calculated using our model is very close to the results presented in the paper, with a difference of less than 5 % for both structures. These results validate our approach for the multiphysics simulation of PV-TE devices.

5.8 Limits and perspectives

The multiphysics model presented in this chapter aims at estimating the power output of a PV-TE device integrating a nanostructured photothermal interface. It combines different tools for electromagnetic and photonic simulations, analytical expressions of the behavior of the PVC, PTI and TEG, and thermal transfer equations.

The PTI and PV-TE components have been validated separately by comparing experiments and calculations. The results obtained with our model of a PV-TE device without PTI shows good agreement with state-of-the-art calculations. The model of the isolated PTI is able to provide qualitative data about the photothermal efficiency of a nanostructured interface.

The tool we designed relies completely on open-source data and code. It is highly versatile, as any component of the system is described by a small set of properties that are accessible in the literature and can be easily modified. Thus, virtually any PVC-PTI-TEG device could be simulated.

To this day, the main limitations of the model are the following:

- Due to the one dimensional nature of the model, any heat transfer occurring on the sides of the system is neglected, which could lead to a small overestimation of the temperature.
- Thermal transfer through radiation is taken into account only for the top and bottom interfaces. Rigorously, emission of thermal radiation happens at each layer of the system.
- Only the solar spectrum (concentrated or not) can be used as incident illumination. This is because we define the output power of the PV cell based on the reference efficiency and temperature coefficient, which are usually determined in standard conditions, i.e. under AM1.5G illumination. Using a different illumination spectrum would require to know the reference efficiency and temperature coefficient for this particular spectrum.
- The photovoltaic conversion efficiency of the PV cell is assumed to vary linearly with temperature, which is only valid in a specific temperature range. This could be a source of error for simulations under high concentration ratio, which would result in high temperature of the PV cell.
- The temperature dependence of the refractive indices used for the PVC and PTI is not taken into account. This could be a source of error, especially for the active layer of the PVC, which band gap is known to vary with temperature.
- The electromagnetic simulations conducted on a unit cell of the PTI could be unrepresentative of the collective response of interacting nanoantennas, especially if they are closely packed. It could be useful to conduct simulations on pairs of unit cells to verify the lack of interaction.
- The thermal resistance between adjacent layers is neglected.

Now, this operational multiphysics tool can be used to calculate the power output of a variety of PVC-PTI-TEG systems, under different environmental conditions. In the framework of this thesis, the aim would be to identify the best photothermal interface for a given PV-TE device. By varying the parameters of the interface (shape, dimension, composition and density of nanoantennas, thickness and composition of the substrate and encapsulant), it will be possible to identify the optimal design of nanostructured photothermal interface. But this model can be used more widely, to identify the best TEG for a specific PV cell, or inversely, with or without PTI. The environment can also be modified by changing the ambient temperature and convection coefficient, in order to simulate system with or without heat sink or air flow.

5.9 Conclusion

In this chapter, we have presented a multiphysics tool for PV-TE devices including a nanostructured photothermal interface. The models of the photovoltaic cell, the photothermal interface and the TEG have been described separately before being thermally and optically coupled.

Our model is able to calculate the heat flux generated by fabricated PTIs under solar infrared illumination, considering the geometrical parameters of the nanoantenna arrays. By combining the PTI model with thermal transport equations, this allowed us to determine the heating of these photothermal interfaces. We compared the results to the experimental data to assess the validity of our approach. Although there were quantitative errors when comparing our numerical simulations to experimental data, we achieved a good qualitative agreement.

Furthermore, we compared our home-made multiphysics model with a state-of-the-art model available in the literature. Our model demonstrated excellent agreement in terms of the temperature distribution in the system. The main divergence arose from the temperature gradient through the TEG, resulting in a significant difference in thermoelectric output power. However, when considering the output power density of the entire system, our model yielded results within 5% of those presented in the literature, thus validating our approach for the multiphysics simulation of PV-TE devices.

With the operational multiphysics tool we have developed, we can now calculate the power output of various PVC-PTI-TEG systems under different environmental conditions. The primary objective within the scope of this thesis is to identify the optimal photothermal interface for a given PV-TE device. By systematically varying the parameters of the interface, such as shape, dimension, composition, and density of nanoantennas, as well as the substrate and encapsulant thickness and composition, we can determine the ideal design of a nanostructured photothermal interface.

Moreover, our multiphysics model has broader applications beyond the specific optimization of the PV-TE device. It can be used to identify the best TEG for

a particular PV cell or vice versa, with or without the inclusion of a PTI. This versatility makes our model a valuable tool for studying various configurations and optimizing the performance of PV-TE devices in different settings.

Conclusion and Perspectives

This thesis has explored the integration of photothermal interfaces based on thermoplasmonic nanoantennas into photovoltaic-thermoelectric cogeneration systems, with the aim of enhancing their conversion efficiency. To this purpose, we took a multiscale approach, starting from the simulation of isolated nanoantennas before fabricating and characterizing large-scale photothermal interface, to finally model the behavior of a complete PVC-PTI-TEG device. The work undertaken in each chapter is summarized in the following section.

Main results

In the introductory chapter, the context of the global energy demand and the significance of self-sustaining energy systems were outlined. The limitations of single-junction photovoltaic cells were discussed, leading to the proposal of a PV-TE cogeneration system as a potential solution. The concept of utilizing photothermal interfaces composed of thermoplasmonic nanoantennas was introduced as a means to enhance the efficiency of this integrated energy device.

Chapter 2 provided an overview of the numerical and experimental methodologies employed throughout the thesis. These methods encompassed electromagnetic simulations, nanofabrication techniques, and characterization methods, forming the foundation for the subsequent investigations.

The third chapter delved into the electromagnetic simulations of isolated nanoantennas, aiming to identify optimal structures for solar infrared absorption. Various shapes, sizes, and compositions of nanoantennas were explored through simulations, and the nickel diabolo geometry was highlighted as particularly promising. The impact of fabrication defects on the optical properties of nanoantennas was also examined, showing the necessity to precisely control their lateral dimensions in order to achieve the desired optical response.

Chapter 4 shifted focus to the experimental fabrication of large-scale photothermal interfaces using hole-mask colloidal lithography. Truncated cone nanoantennas were fabricated, and their optical and heating properties were characterized. The influence of factors such as substrate materials, nanoantenna height, and composition on photothermal efficiency was investigated. A temperature of 35 °C under solar infrared illumination was measured for the PTI covered with 200 nm-high

nickel nanocones. Taking into account the surface density of each sample, aluminum nanocones were identified has the most efficient photothermal converters among the studied nanoantennas. This chapter laid the groundwork for understanding the practical aspects of incorporating photothermal interfaces in PV-TE systems.

The fifth chapter presented a multiphysics model of the entire PV-TE device, including the photovoltaic cell, photothermal interface, and thermoelectric generator. This model combined optical simulations, thermal transport equations, and thermoelectric modeling to estimate the electrical power output of the integrated system. The model was validated through comparison with experimental data and existing literature, demonstrating its capability to predict the behavior of PV-TE devices incorporating photothermal interfaces.

In summary, this thesis has advanced the understanding of the potential benefits of incorporating thermoplasmonic nanoantenna-based photothermal interfaces in PV-TE cogeneration systems. By combining numerical simulations, experimental characterizations, and multiphysics modeling, valuable insights have been gained into the design, fabrication, and optimization of photothermal interfaces. This research paves the way for the development of more efficient and sustainable energy conversion technologies.

Perspectives

Optimization of the design through electromagnetic simulation

We have seen in chapter 4 that the substrate plays an important role in the optical response of photothermal interfaces. Adding the substrate in DDA simulation drastically increases the computation time, but it would allow to better estimate the absorbed power of actual interfaces, and identify the optimal nanoantenna-substrate couple for a given application. This principle also holds true for the addition of a capping layer. Moreover, numerical simulation could be leverage to explore the impact of the nanoantennas surface density on the optical properties of photothermal interfaces, thus providing guidelines for the fabrication of optimal interfaces.

Fabrication of high-quality photothermal interfaces

There are promising avenues for enhancing the fabrication of nanostructured photothermal interfaces. Achieving better control over the colloidal lithography process could lead to an increase in the density of nanoantenna arrays, consequently boosting the absorbed solar power. Further advancements could be made by leveraging nanoimprint lithography to rapidly fabricate a multitude of samples covered with complex-shaped nanoantennas, such as the diabolo geometry, which holds the potential for superior solar absorption efficiency. Encapsulation of the nanoanten-

nas is of paramount importance, necessitating the development or adaptation of a thin-film deposition process compatible with the identified optimal encapsulation material. These refinements in fabrication methods hold the promise of improving the performance of photothermal interfaces, thus propelling the overall efficiency of photovoltaic-thermoelectric cogeneration systems.

Characterization

Quantification of the optical response of fabricated nanostructured interfaces is of crucial importance to validate simulation results, and to fully understand the physical phenomena occurring during photothermal conversion. Spectroscopy studies with the help of an integrating sphere would be very helpful in precisely measuring absorption, reflection, transmission and scattering spectra. As discussed in Section 4.6, it would also be interesting to measure the heating of photothermal interfaces with different substrates and capping layer, but it is first necessary to overcome the issue of substrates with rough back surfaces, by high-quality polishing for example.

Using the multiphysics model

Regarding the multiphysics model, while there is room for refinement, the immediate focus lies on capitalizing on its versatility to explore diverse optimization strategies and examine various avenues for enhancement of PV-TE cogeneration. One approach involves fixing the parameters of a photovoltaic cell and subsequently optimizing the parameters of the photothermal interface and thermoelectric generator, which could be used to discern whether the performance gains achieved through the integration of PVC-PTI-TEG systems warrant the associated costs in comparison to the performance of the standalone PVC. This targeted approach not only allows for a comprehensive assessment of the effectiveness of the combined system but also facilitates the identification of the most promising configurations for practical implementation. Additionally, the model's versatility extends to exploring optimal substrate and capping materials for a given PVC-TEG combination. This broader exploration could uncover materials that enhance overall system performance, instead of merely focusing on the temperature of the standalone PTI, by addressing factors such as thermal conductivity and optical properties, further contributing to the advancement of efficient photovoltaic-thermoelectric devices.

Appendices

Appendix A

Inputs and outputs of electromagnetic simulations on isolated nanoantennas

In Chapter 3, we presented electromagnetic numerical simulations of isolated nanoantennas of various shapes, dimensions and composition. In this section, we present the refractive indices used to simulate the different materials, as well as the complete list of simulation results obtained for isolated nanoantennas.

A.1 Refractive indices of the simulated materials

The dielectric functions of the studied materials were taken from Rakić et al. [122] and are represented in Figure A.1.

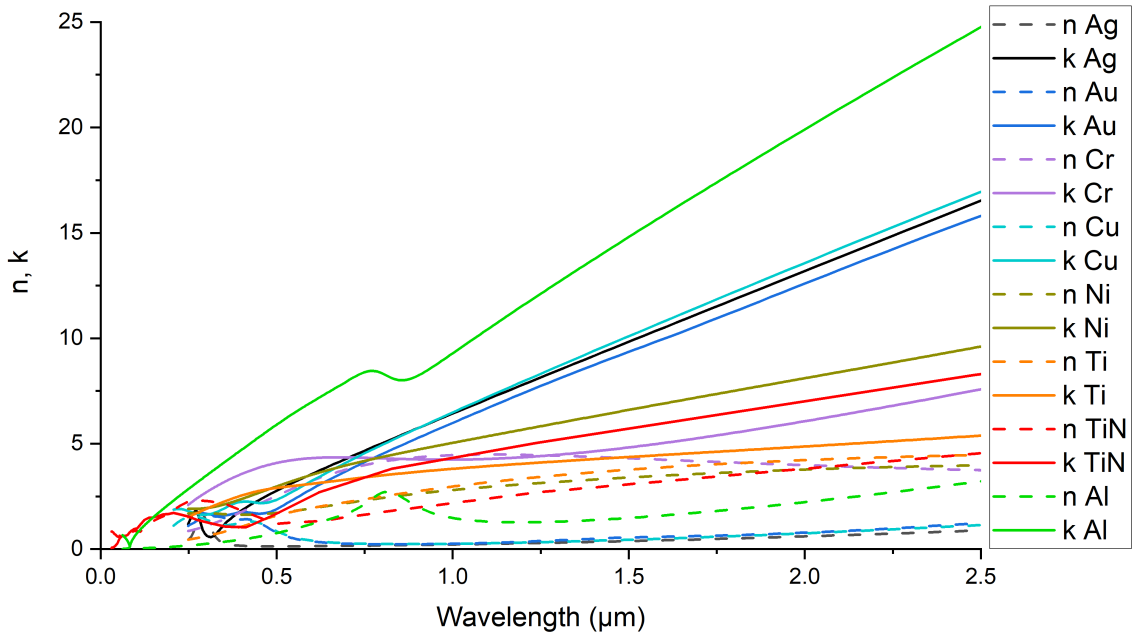

Figure A.1: Refractive index (n) and extinction coefficient (k) of the materials used in the simulation, from Rakić et al. [122].

A.2 Detailed simulation results

Table A.1 gathers all the results from the DDA simulations used in Chapter 3. All particles have a height of 150 nm. The absorbed power is calculated based on the simulated absorption cross-section and the AM 1.5G spectra. The absorption per unit surface is the absorbed power divided by the footprint of the particle on a substrate. The absorption-over-scattering ratio is calculated by dividing the absorbed power by the scattered power of the antenna.

Table A.1: Results of the optical simulations using the DDA method. The simulations were performed on 150 nm-high isolated particles under AM1.5G solar infrared (0.875-2.5 µm) illumination.

Shape	Material	Dimensions (nm)	Lattice spacing (nm)	Volume (μm^3)	Absorbed power (pW)	Absorption/ scattering power ratio	Absorption per unit surface ($nW/\mu m^2$)
Cone	Ni	1000 - 890	10	0.106	97	0.18	**0.12**
Cone	Ni	110 - 0	5	0.001	1	8.92	**0.06**
Cone	Ni	150 - 40	5	0.001	2	4.01	**0.1**
Cone	Ni	200 - 90	5	0.003	5	1.81	**0.16**
Cone	Ni	300 - 190	10	0.008	20	0.73	**0.28**
Cone	Ni	300 - 190	5	0.007	17	0.64	**0.25**
Cone	Ni	400 - 100	10	0.009	39	0.67	**0.31**
Cone	Ni	400 - 150	10	0.01	38	0.61	**0.3**
Cone	Ni	400 - 290	5	0.014	32	0.39	**0.25**
Cone	Ni	500 - 100	10	0.013	56	0.53	**0.28**
Cone	Ni	500 - 140	10	0.014	54	0.5	**0.28**
Cone	Ni	500 - 200	10	0.016	52	0.46	**0.27**
Cone	Ni	500 - 390	5	0.024	44	0.3	**0.22**
Diabolo	Ag	540x540 - 300x50	10	0.014	36	0.25	**0.37**
Diabolo	Al	540x540 - 300x50	10	0.014	33	0.23	**0.34**
Diabolo	Au	540x540 - 300x50	10	0.014	38	0.29	**0.4**
Diabolo	Cr	540x540 - 300x50	10	0.014	85	1.08	**0.88**
Diabolo	Cu	540x540 - 300x50	10	0.014	36	0.26	**0.37**
Diabolo	Ni	100x100 - 50x50	5	0.001	3	4.64	**0.33**
Diabolo	Ni	200x200 - 100x100	5	0.004	18	1.17	**0.66**
Diabolo	Ni	200x200 - 50x50	5	0.004	21	1.61	**0.88**
Diabolo	Ni	300x300 - 100x100	5	0.008	40	0.81	**0.73**
Diabolo	Ni	300x300 - 100x50	5	0.007	42	1.19	**0.97**
Diabolo	Ni	300x300 - 50x100	5	0.009	39	0.76	**0.67**
Diabolo	Ni	300x300 - 50x50	5	0.008	41	1	**0.81**

Shape	Material	Dimensions (nm)	Lattice spacing (nm)	Volume (μm^3)	Absorbed power (pW)	Absorption/ scattering power ratio	Absorption per unit surface ($nW/\mu m^2$)
Diabolo	Ni	400x100 - 100x50	5	0.004	27	1.12	**0.97**
Diabolo	Ni	400x100 - 200x50	5	0.004	27	1.21	**1.07**
Diabolo	Ni	400x100 - 300x50	5	0.003	27	1.25	**1.18**
Diabolo	Ni	400x200 - 100x50	5	0.006	34	1.17	**0.79**
Diabolo	Ni	400x200 - 200x50	5	0.005	33	1.35	**0.94**
Diabolo	Ni	400x200 - 300x50	5	0.004	32	1.51	**1.18**
Diabolo	Ni	400x300 - 100x50	5	0.009	44	1.04	**0.77**
Diabolo	Ni	400x300 - 200x50	5	0.007	43	1.25	**0.96**
Diabolo	Ni	400x300 - 300x50	5	0.005	46	1.81	**1.42**
Diabolo	Ni	400x400 - 200x200	5	0.016	52	0.49	**0.48**
Diabolo	Ni	400x400 - 300x100	5	0.009	64	1.17	**1.05**
Diabolo	Ni	400x400 - 300x300	10	0.024	50	0.33	**0.32**
Diabolo	Ni	400x400 - 300x50	5	0.006	61	1.62	**1.44**
Diabolo	Ni	400x400 - 50x300	5	0.022	47	0.33	**0.32**
Diabolo	Ni	400x400 - 50x50	5	0.013	56	0.74	**0.63**
Diabolo	Ni	400x500 - 300x100	10	0.011	74	1.21	**1**
Diabolo	Ni	400x500 - 300x300	10	0.022	65	0.46	**0.44**
Diabolo	Ni	400x540 - 300x300	10	0.023	73	0.55	**0.48**
Diabolo	Ni	400x540 - 300x50	10	0.008	67	1.43	**1.24**
Diabolo	Ni	400x600 - 300x300	10	0.023	79	0.61	**0.51**
Diabolo	Ni	500x300 - 100x100	10	0.015	49	0.62	**0.48**
Diabolo	Ni	500x300 - 100x200	10	0.017	60	0.64	**0.54**
Diabolo	Ni	500x300 - 200x100	10	0.014	49	0.68	**0.53**
Diabolo	Ni	500x400 - 100x100	10	0.019	60	0.6	**0.49**
Diabolo	Ni	500x400 - 300x300	10	0.027	52	0.31	**0.29**
Diabolo	Ni	500x500 - 100x50	5	0.018	66	0.65	**0.54**
Diabolo	Ni	500x500 - 200x50	5	0.015	66	0.73	**0.66**
Diabolo	Ni	500x500 - 300x300	10	0.029	63	0.36	**0.33**
Diabolo	Ni	500x500 - 300x50	5	0.012	70	0.95	**0.91**
Diabolo	Ni	500x540 - 300x300	10	0.029	70	0.39	**0.36**
Diabolo	Ni	500x600 - 300x100	10	0.018	78	0.77	**0.67**
Diabolo	Ni	500x600 - 300x300	10	0.03	76	0.43	**0.38**
Diabolo	Ni	50x50 - 25x25	5	0	0	19.12	**0.19**
Diabolo	Ni	540x400 - 300x300	10	0.029	53	0.3	**0.27**
Diabolo	Ni	540x500 - 300x300	10	0.031	65	0.35	**0.31**
Diabolo	Ni	540x540 - 100x100	10	0.026	71	0.52	**0.41**
Diabolo	Ni	540x540 - 100x200	10	0.03	71	0.42	**0.35**
Diabolo	Ni	540x540 - 100x300	10	0.036	68	0.33	**0.29**
Diabolo	Ni	540x540 - 100x50	10	0.022	73	0.64	**0.49**
Diabolo	Ni	540x540 - 200x100	10	0.022	73	0.6	**0.5**
Diabolo	Ni	540x540 - 200x200	10	0.028	71	0.44	**0.38**
Diabolo	Ni	540x540 - 200x300	10	0.034	68	0.34	**0.3**
Diabolo	Ni	540x540 - 200x50	10	0.019	72	0.7	**0.58**
Diabolo	Ni	540x540 - 300x100	10	0.019	76	0.72	**0.62**
Diabolo	Ni	540x540 - 300x200	10	0.025	76	0.53	**0.45**
Diabolo	Ni	540x540 - 300x300	10	0.032	69	0.36	**0.32**
Diabolo	Ni	540x540 - 300x50	10	0.014	75	0.89	**0.78**
Diabolo	Ni	540x540 - 50x100	10	0.027	73	0.51	**0.4**
Diabolo	Ni	540x540 - 50x200	10	0.032	71	0.41	**0.34**
Diabolo	Ni	540x540 - 50x300	10	0.037	69	0.33	**0.28**
Diabolo	Ni	540x540 - 50x50	10	0.025	74	0.58	**0.44**
Diabolo	Ni	540x600 - 300x300	10	0.033	76	0.4	**0.34**
Diabolo	Ni	600x300 - 100x100	10	0.018	51	0.59	**0.41**
Diabolo	Ni	600x400 - 300x300	10	0.033	55	0.29	**0.25**
Diabolo	Ni	600x500 - 300x300	10	0.035	67	0.33	**0.29**
Diabolo	Ni	600x540 - 300x300	10	0.036	71	0.35	**0.3**
Diabolo	Ni	600x600 - 300x300	10	0.038	76	0.36	**0.3**
Diabolo	Ni	600x600 - 300x50	10	0.019	80	0.73	**0.63**
Diabolo	Ti	540x540 - 300x50	10	0.014	85	1.44	**0.88**
Diabolo	TiN	540x540 - 300x50	10	0.014	78	1.12	**0.8**
Disk	Ni	Ddisk=100	5	0.001	1	4.37	**0.14**
Disk	Ni	Ddisk=200	5	0.005	8	0.9	**0.24**
Disk	Ni	Ddisk=250	10	0.007	15	0.79	**0.3**
Disk	Ni	Ddisk=300	10	0.011	21	0.47	**0.3**
Disk	Ni	Ddisk=350	10	0.014	30	0.48	**0.31**
Disk	Ni	Ddisk=400	10	0.019	35	0.33	**0.28**
Disk	Ni	Ddisk=50	5	0	0	13.83	**0.08**
Disk	Ni	Ddisk=540	10	0.034	51	0.25	**0.22**
Disk	Ni	Ddisk=600	10	0.042	57	0.23	**0.2**
Pad	Ag	540x540	10	0.044	6	0.02	**0.02**
Pad	Al	540x540	10	0.044	11	0.03	**0.04**
Pad	Au	540x540	10	0.044	7	0.02	**0.03**
Pad	Cr	540x540	10	0.044	78	0.32	**0.27**
Pad	Cu	540x540	10	0.044	7	0.02	**0.02**
Pad	Ni	100x100	10	0.002	2	3.25	**0.18**
Pad	Ni	200x200	10	0.006	12	0.65	**0.31**
Pad	Ni	300x300	10	0.014	29	0.35	**0.32**
Pad	Ni	400x400	10	0.024	42	0.26	**0.26**
Pad	Ni	500x500	10	0.038	53	0.22	**0.21**
Pad	Ni	50x50	10	0	0	11.59	**0.1**
Pad	Ni	540x540	10	0.044	57	0.21	**0.2**
Pad	Ni	600x600	10	0.054	63	0.2	**0.18**
Pad	Ti	540x540	10	0.044	86	0.39	**0.3**
Pad	TiN	540x540	10	0.044	66	0.26	**0.23**
Rod	Ag	540x50	10	0.004	4	0.07	**0.16**
Rod	Al	540x50	10	0.004	3	0.04	**0.13**
Rod	Au	540x50	10	0.004	6	0.1	**0.22**
Rod	Cr	540x50	10	0.004	32	1.3	**1.19**
Rod	Cu	540x50	10	0.004	5	0.07	**0.17**
Rod	Ni	1000x100	5	0.015	33	0.52	**0.33**
Rod	Ni	1000x200	5	0.03	43	0.35	**0.21**
Rod	Ni	1000x50	5	0.008	31	0.82	**0.62**
Rod	Ni	1080x100	10	0.016	32	0.52	**0.3**
Rod	Ni	125x25	5	0.001	1	6.06	**0.21**

Appendix A. Inputs and outputs of electromagnetic simulations on isolated nanoantennas

Shape	**Material**	**Dimensions (nm)**	**Lattice spacing (nm)**	**Volume (μm^3)**	**Absorbed power (pW)**	**Absorption/ scattering power ratio**	**Absorption per unit surface ($nW/\mu m^2$)**
Rod	Ni	250x50	5	0.002	12	1.29	**0.95**
Rod	Ni	300x50	5	0.002	17	1.15	**1.15**
Rod	Ni	400x50	5	0.003	25	1.03	**1.23**
Rod	Ni	500x100	5	0.008	28	0.57	**0.57**
Rod	Ni	500x50	5	0.004	29	0.98	**1.15**
Rod	Ni	500x75	5	0.006	28	0.76	**0.76**
Rod	Ni	540x100	10	0.008	29	0.56	**0.53**
Rod	Ni	540x50	10	0.004	28	1.01	**1.05**
Rod	Ni	600x100	5	0.009	31	0.54	**0.51**
Rod	Ni	600x100	10	0.009	30	0.55	**0.5**
Rod	Ni	600x50	10	0.005	29	0.98	**0.97**
Rod	Ni	810x75	10	0.009	29	0.64	**0.47**
Rod	Ti	540x50	10	0.004	29	1.77	**1.08**
Rod	TiN	540x50	10	0.004	28	1.34	**1.04**

Résumés des chapitres en français

Chapitre 1

Contexte, motivations et objectifs

1.1 Limites des cellules photovoltaïques mono-jonctions

Les cellules photovoltaïques (PV) sont des dispositifs optoélectroniques capables d'absorber de la lumière et de la convertir en énergie électrique. Parmi les différentes technologies de cellules PV, les plus répandues sont les cellules mono-jonctions, qui utilisent un unique matériau semi-conducteur. Les matériaux couramment utilisés comprennent des semi-conducteurs inorganiques tels le silicium (Si), l'arséniure de gallium (GaAs), le sélénium de cuivre-indium-gallium (CIGS) et le tellurure de cadmium (CdTe). Les électrons dans les semi-conducteurs existent dans deux bandes : la bande de valence et la bande de conduction, séparées par une plage d'énergie appelée la bande interdite (E_g). Une énergie au moins égale à Eg est nécessaire pour déplacer un électron de la bande de valence à la bande de conduction. La valeur de la bande interdite détermine en grande partie la réponse à la lumière des cellules photovoltaïques mono-jonctions, et donc leur efficacité de photo-conversion.

Lorsque des photons avec une énergie E_{ph} supérieure à la bande interdite atteignent la cellule, ils peuvent exciter les électrons de la bande de valence vers la bande de conduction, générant des paires électron-trou. La séparation et collection sélective de ces porteurs de charge permet de créer un courant électrique. Cependant, l'excès d'énergie ($E_{ph} - E_g$) est perdu sous forme de chaleur, ce qui a pour effet de chauffer la cellule. Ce phénomène est appelé thermalisation et est représenté en bleu sur la Figure 1.1A. De plus, les photons dont l'énergie est inférieure à la bande interdite ne sont simplement pas absorbés par le semi-conducteur (en rouge sur la Figure 1.1A), et ne participent donc pas à la génération d'électricité.

Seule une fraction du spectre solaire incident est donc converti par les cellules mono-jonctions. La limite de Shockley-Queisser [6] établit l'efficacité maximale possible d'une cellule PV mono-jonction avec une bande interdite donnée, dans des conditions standard (illumination par le spectre solaire AM1.5G, cellule refroidie à 25 °C), en prenant notamment en compte les effets de thermalisation des photons de haute énergie et la non-absorption des photons de basse énergie. Par exemple, les

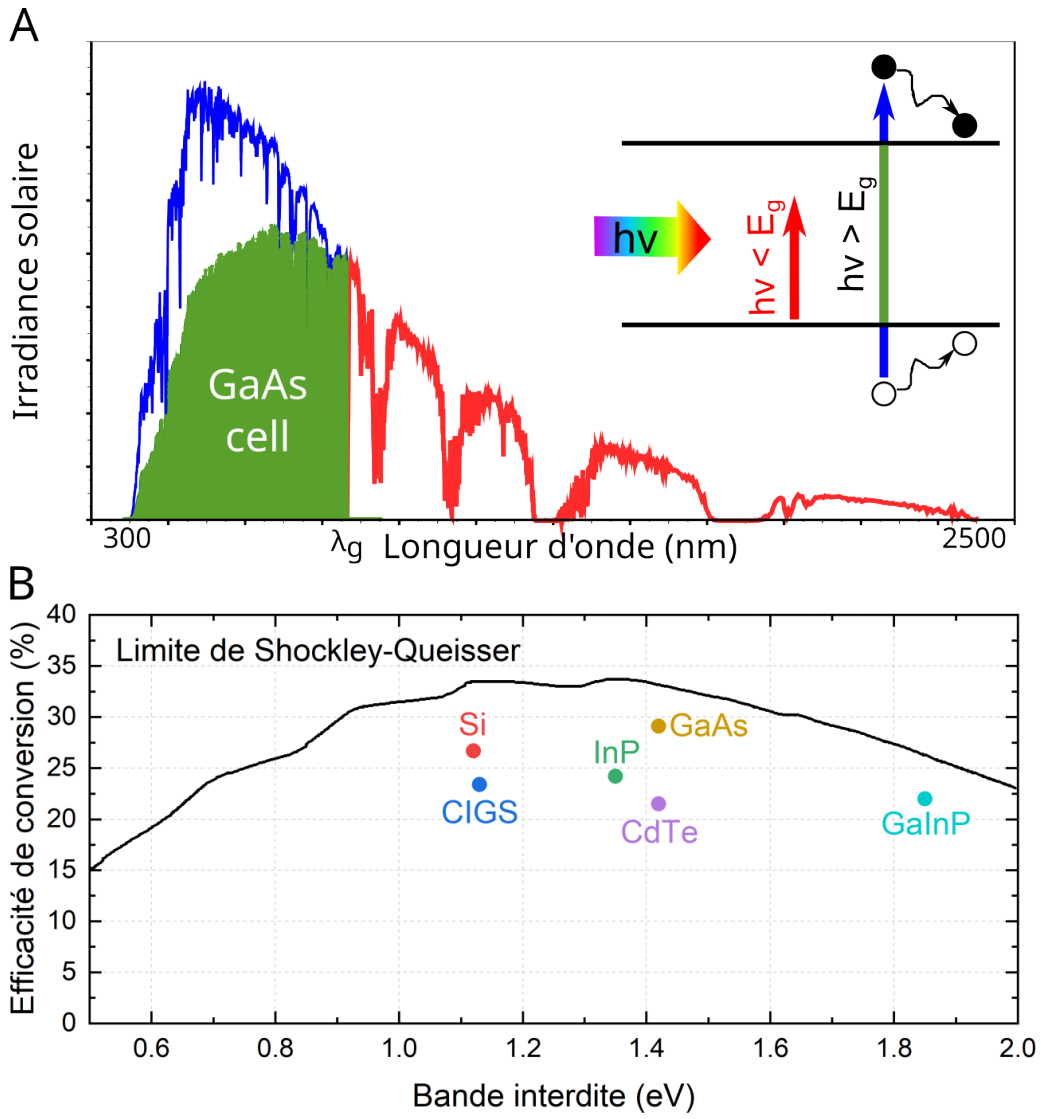

Figure 1.1 : Limitations intrinsèques des cellules photovoltaïques mono-jonctions. (A) Spectre du rayonnement solaire AM1.5G montrant l'énergie maximale convertie par une cellule solaire GaAs avec Eg = 1,42 eV, selon la limite de Shockley-Queisser (en vert) et les pertes intrinsèques de la cellule (thermalisation, en bleu ; non-absorption, en rouge) avec les processus de perte correspondants schématisés dans l'encart. Réimprimé avec la permission de ACS Appl. Energy Mater. 2023, 6, 4, 2128–2133. Copyright 2023 American Chemical Society. (B) Efficacité de conversion maximale des cellules solaires mono-jonctions en fonction de leur bande interdite, selon la limite de Shockley-Queisser (ligne noire), et efficacité record en 2020 pour plusieurs matériaux, adapté de [5].

cellules solaires à base de GaAs sont limitées à une efficacité de 33 % en raison de la valeur de leur bande interdite, comme illustré en Figure 1.1B. Les performances des cellules photovoltaïques actuelles (29,1 % de rendement pour GaAs [2]) approchent de la limite théorique de Shockley-Queisser (courbe noire sur la Figure 1.1B), ce qui réduit le gain en rendement encore possible.

Une autre limitation à laquelle font face les cellules PV est leur perte d'efficacité avec l'augmentation de la température. En effet, la chaleur provenant de la thermalisation conduit à une hausse de température de la cellule en fonctionnement, ce qui a un impact négatif sur les performances de la plupart des cellules inorganiques. À mesure que la température augmente, l'efficacité de la cellule PV diminue en raison de la recombinaison accrue des paires électron-trou [7, 8]. Des températures élevées entraînent également une dégradation des matériaux composants la cellule, réduisant sa durée de vie.

Le choix d'une bande interdite implique un compromis entre l'absorption efficace des photons et les pertes par thermalisation, ce qui aboutit à une bande interdite optimale pour chaque application.

1.2 Principe de la cogénération photovoltaïque-thermoélectrique

Le concept de cogénération photovoltaïque-thermoélectrique (PV-TE) remonte au début du 21ème siècle, lorsque la combinaison des technologies photovoltaïque et thermoélectrique fut explorée dans le but de surpasser les limites intrinsèques des cellules PV [53]. L'idée est d'utiliser un générateur thermoélectrique, un dispositif capable de générer de l'énergie électrique lorsqu'il est parcouru par un flux de chaleur, afin de récupérer les pertes thermiques de la cellule PV.

Les générateurs thermoélectriques (TEG) fonctionnent grâce à l'effet Seebeck, qui dicte qu'un gradient de température au sein d'un thermocouple, i.e. une jonction de deux matériaux, l'un dopé N et l'autre dopé P, peut produire une tension électrique [47]. Les TEGs sont faits d'une série de thermocouples connectés électriquement en série et thermiquement en parallèle, comme présenté sur la Figure 1.2.

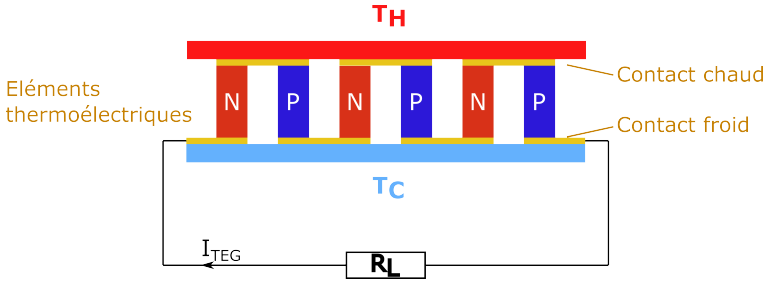

Figure 1.2 : Schéma d'un TEG générant un courant électrique sous l'effet d'un gradient de température lorsqu'il est connecté à une résistance R_L.

Dans la configuration de couplage direct, le TEG est positionné sous la cellule PV, en contact physique avec celle-ci, et un dissipateur thermique est généralement placé en dessous. La lumière incidente interagit donc en premier lieu avec la cellule PV, dont la température augmente. Le TEG voit alors un gradient thermique s'établir entre le côté chaud (cellule PV) et le côté froid (dissipateur thermique), ce qui lui permet de générer une tension électrique. Le dispositif PV-TE est ainsi capable de générer une puissance électrique supérieure à celle de la cellule PV seule [54].

L'interface physique entre la cellule PV et le TEG joue un rôle crucial dans les performances du dispositif. Une interface bien conçue peut considérablement améliorer l'efficacité globale du système intégré, principalement grâce à une conduction thermique optimisée et une disponibilité d'énergie thermique accrue [57].

Une conduction thermique efficace à travers l'interface photovoltaïque-thermoélectrique est essentielle pour maintenir les températures de fonctionnement optimales des deux composants en permettant un transfert de chaleur efficace entre la cellule PV et le TEG. Il a été montré que réduire la résistance thermique à l'interface PV-TE permet d'augmenter considérablement la puissance de sortie du dispositif [67]. Cette réduction de la résistance thermique permet une meilleure extraction de chaleur de la cellule PV, abaissant sa température, tout en augmentant la température du côté chaud du TEG, ce qui est généralement bénéfique pour les performances du dispositif PV-TE.

Une autre approche pour améliorer l'efficacité de conversion d'un système PV-TE consiste à exploiter au maximum l'énergie du spectre solaire. Les cellules PV sont en grande partie transparentes aux photons en dessous de l'énergie de bande interdite, ce qui limite la quantité d'énergie exploitable par le système. En optimisant l'interface, il est possible d'augmenter l'énergie thermique disponible pour le TEG en utilisant des mécanismes de conversion photothermique. Les interfaces photothermiques (PTIs) capturent efficacement un spectre plus large de lumière incidente, convertissant une partie en énergie thermique, qui peut ensuite être canalisée efficacement vers le TEG, comme illustré en Figure 1.3. Cette énergie thermique supplémentaire renforce le gradient de température à travers le TEG, améliorant ainsi son efficacité de conversion thermoélectrique [68, 69].

En résumé, l'interface physique entre la cellule photovoltaïque et le générateur thermoélectrique est un élément-clé pour améliorer les performances des dispositifs de cogénération photovoltaïque-thermoélectrique. L'optimisation de la conduction thermique et l'augmentation de l'énergie thermique disponible grâce à l'ingénierie d'interface ouvrent la voie à des efficacités de conversion énergétique globale plus élevées. Par conséquent, une exploration approfondie de la conception de l'interface et de son impact sur le système intégré est essentielle pour réaliser le plein potentiel de cette technologie.

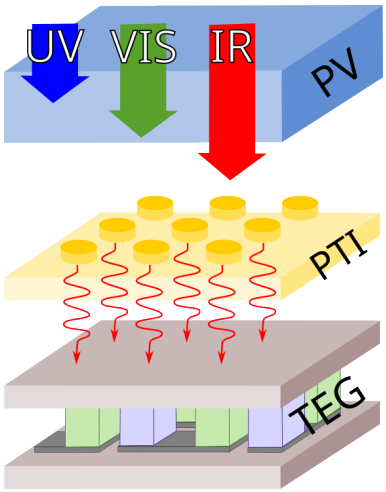

Figure 1.3 : Schéma d'un dispositif hybride photovoltaïque-thermoélectrique, comprenant une interface photothermique nanostructurée pour convertir le rayonnement solaire infrarouge en chaleur. Dans le dispositif réel, les trois composants sont en contact physique. Réimprimé avec la permission de ACS Appl. Energy Mater. 2023, 6, 4, 2128–2133. Copyright 2023 American Chemical Society.

1.3 Interface photothermique nanostructurée

Différents types d'interfaces PV-TE ont été étudiés dans la littérature. Nous proposons ici une nouvelle approche basée sur l'utilisation de nanoantennes thermoplasmoniques.

Les nanoantennes plasmoniques sont connues pour leurs propriétés optiques particulières. Lorsqu'une nanoparticule interagit avec certaines longueurs d'ondes du spectre lumineux, les électrons libres présents dans la nanoparticule peuvent osciller de manière collective [74, 75]. Cette résonance plasmonique induit une forte absorption optique aux longueurs d'ondes considérées. La fréquence de résonance dépend de la forme, taille et composition de la nanoparticule, ainsi que de la nature du milieu environnant [97]. L'énergie ainsi absorbée par une nanoantenne peut être convertie sous forme de chaleur pour augmenter sa température [99, 100], d'où le nom de nanoantenne thermoplasmonique.

Les nanoantennes plasmoniques combinent une forte absorption et une taille réduite, ce qui est idéal pour leur intégration au sein de dispositifs PV-TE. En effet, la puissance optique absorbée, convertie en chaleur, permet d'augmenter la température au contact chaud du TEG, tandis qu'une faible épaisseur permet de réduire la résistance thermique entre la cellule PV et le TEG. De plus, leurs spectres d'absorption peuvent être facilement adaptés en modifiant leur forme, taille ou composition, ce qui permet de les faire correspondre au spectre solaire incident.

Chapitre 2

Méthodes expérimentales et numériques

2.1 Simulations électromagnétiques par la méthode DDA

L'Approximation Dipolaire Discrète (Discrete Dipole Approximation ou DDA, en anglais) est une méthode numérique utilisée pour étudier la diffusion de la lumière par des nanoparticules complexes et irrégulières. Elle offre une approche efficace pour modéliser les interactions entre les champs électromagnétiques et les structures nanométriques, permettant ainsi d'obtenir des informations précises sur les propriétés optiques et les champs électromagnétiques à l'échelle nanométrique.

La méthode DDA consiste à discrétiser la cible de simulation en un réseau de dipôles polarisables. Chaque dipôle est traité comme une source élémentaire de rayonnement électromagnétique et est caractérisé par sa position et son indice de réfraction complexe. L'oscillation du moment dipolaire de chaque dipôle est déterminée par la polarisabilité du dipôle et le champ électrique local, qui résulte de l'interaction entre l'onde électromagnétique incidente et les champs électriques induits par les dipôles voisins. La somme des contributions de tous les dipôles permet de déterminer le champ électromagnétique aux alentours et au sein de la nanoparticule, et ainsi de remonter à ses spectres de sections efficaces d'absorption et de diffusion [119, 120, 121].

La méthode DDA présente des avantages significatifs dans la modélisation de la diffusion de la lumière par des structures complexes. Elle peut traiter des objets de formes irrégulières, ce qui est particulièrement important pour les nanoparticules dont la géométrie peut être très variable. De plus, sa mise en œuvre est relativement simple et elle permet de gérer un grand nombre de dipôles, ce qui est crucial pour capturer les détails à l'échelle nanométrique. Cependant, la méthode DDA présente également des limites. L'une des principales difficultés réside dans la modélisation précise des interactions entre les dipôles qui sont très proches les uns des autres. De plus, l'obtention de la convergence du calcul peut nécessiter un grand nombre de

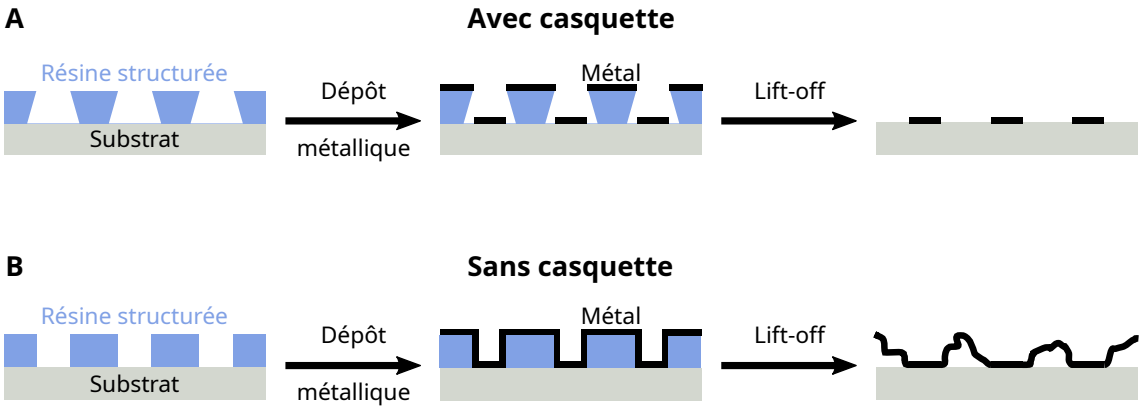

Figure 2.1 : Schéma illustrant le processus de lift-off avec (A) une résine structurée avec casquette, conduisant à un décollement réussi, et (B) une résine structurée sans casquette, empêchant le détachement du métal indésirable après dissolution de la résine.

dipôles, ce qui peut entraîner des temps de calcul importants, en particulier pour des structures volumineuses.

Dans le cadre de cette thèse, nous utilisons la méthode DDA pour calculer les spectres d'absorption et de diffusion de nanoparticules isolées, à partir du code libre DDSCAT [120]. Cette méthode nous permet d'étudier en détail les réponses optiques de nanoantennes de volume réduit (inférieur à 0,1 μm^{-3}), en générant des simulations avec une résolution élevée et un nombre de dipôles limité pour des durées de calcul raisonnables. Nous avons également effectué plusieurs simulations sur des systèmes composés d'une nanoantenne placée sur un substrat mince. Cependant, en raison du grand nombre de dipôles nécessaires pour simuler le substrat, nous avons limité le nombre de ces calculs chronophages.

2.2 Techniques de nanofabrication

Au cours de cette thèse, des échantillons recouverts de nanoantennes métalliques ont été réalisés en utilisant différentes techniques. Cette section décrit le procédé de lift-off permettant de transférer un motif depuis une résine vers un substrat, ainsi que les deux principales techniques de nanofabrication utilisées dans ces travaux de thèse pour structurer la résine, à savoir la lithographie électronique et la lithographie colloïdale.

2.2.1 Le procédé de lift-off

Le procédé de lift-off est largement employé en micro- et nanofabrication, pour la création de motifs métalliques sur un substrat. Tout d'abord, cette technique nécessite que le substrat soit recouvert d'une résine, préalablement structurée par photolithographie ou à l'aide d'autres techniques de structuration. Ensuite, une couche métallique est déposée à la fois sur la couche de résine et sur le substrat conformé-

ment au motif prédéfini. Enfin, la résine est dissoute, entraînant le décollement du métal indésirable pour ne laisser que le motif souhaité sur le substrat.

Un aspect essentiel de la technique de lift-off réside dans le profil en casquette de la résine structurée, visible sur la Figure 2.1A. Ce profil est souvent créé par la technique de lithographie ou le processus de gravure, et est nécessaire pour obtenir un film métallique discontinu en empêchant le dépôt de métal sur les côtés des ouvertures structurées. Sans cette casquette, la couche indésirable de métal qui devrait être retirée resterait fixée au substrat et ne pourrait pas être éliminée, comme illustré dans la Figure 2.1B.

2.2.2 La lithographie électronique

La lithographie électronique est une technique de fabrication utilisée pour produire des structures et des motifs à l'échelle nanométrique. Le principe de cette technique est schématisé en Figure 2.2. Elle consiste à focaliser un faisceau d'électrons sur un substrat, préalablement recouvert d'une couche de résine électrosensible. Lorsque le faisceau d'électrons traverse la résine, il provoque des changements chimiques qui modifient sa solubilité. La résine est ensuite développée pour révéler le motif souhaité, qui peut être transféré sur le substrat sous-jacent grâce à un processus tel que la gravure ou le lift-off. La lithographie électronique est une technique d'écriture directe, car elle ne nécessite pas l'utilisation d'un masque pour transférer les motifs sur le substrat. Son principal avantage réside dans sa capacité à créer des structures haute résolution avec des tailles de motifs dans la plage nanométrique, ce qui en fait un outil précieux pour des applications telles que la production de circuits intégrés et la fabrication de dispositifs nanométriques. Cependant, la lithographie électronique est généralement plus lente et plus coûteuse que d'autres formes de lithographie. De plus, elle nécessite un équipement spécialisé ainsi qu'un environnement de salle blanche, ce qui peut encore augmenter le coût de fabrication. Dans le cadre de cette thèse, la fabrication par lithographie électronique a été entreprise au sein de la salle blanche du LAAS.

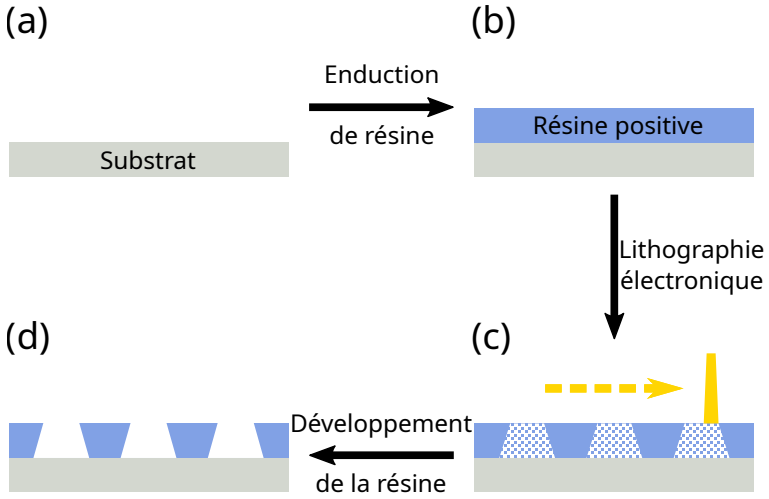

Figure 2.2 : Schéma représentant la structuration d'une résine électrosensible par lithographie électronique.

2.2.3 La lithographie colloïdale

La lithographie colloïdale permet la fabrication de surfaces nanostructurées par l'auto-assemblage de particules colloïdales chargées [123], comme présenté sur la Figure 2.3. Ces particules, typiquement des billes de polystyrène chargées négativement, sont dispersées dans un solvant puis déposées sur un substrat recouvert d'une résine chargée positivement. Les billes s'auto-arrangent sous l'effet de la gravité et des interactions électrostatiques. Les forces de répulsion entre billes dictent la distance inter-particulaire moyenne et empêchent l'agrégation. Il en résulte un arrangement désordonné de billes. L'échantillon est ensuite recouvert d'une fine couche de chrome de 10 nm d'épaisseur. Les billes sont ensuite retirées à l'aide d'une bande adhésive, laissant des trous circulaires dans la couche de chrome, qui servent de masque pour graver la résine.

La lithographie colloïdale est hautement polyvalente, compatible avec une vaste gamme de matériaux et de substrats, et peut être utilisée pour créer des motifs à grande échelle avec une grande précision et une uniformité élevée. De plus, cette

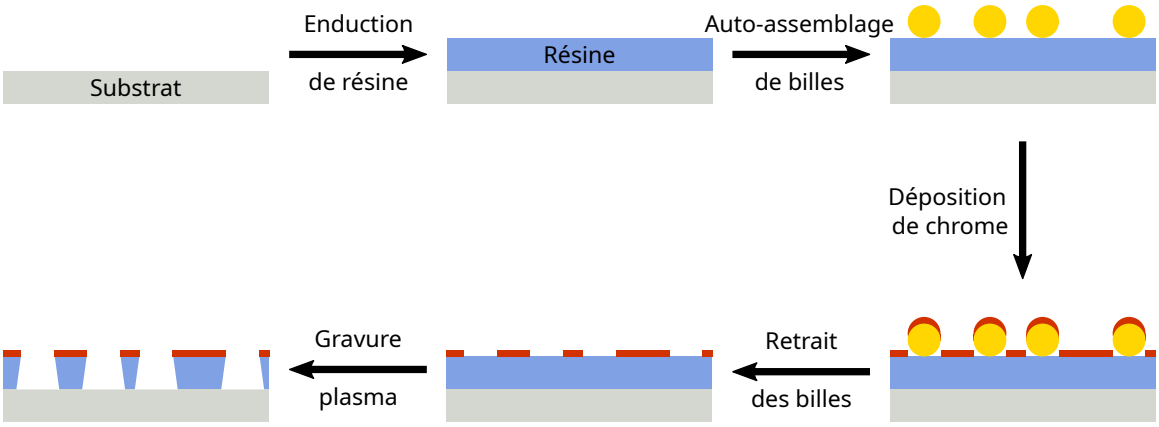

Figure 2.3 : Schéma représentant la structuration d'une résine par lithographie colloïdale.

technique est relativement simple et peu coûteuse. Ses principaux inconvénients sont la limitation aux motifs circulaires ou elliptiques et le manque de contrôle sur l'ordre de l'arrangement colloïdal à longue distance. Les échantillons réalisés par lithographie colloïdale présentés dans cette thèse ont été fabriquées au sein du Nanofabrication Laboratory, à Göteborg.

2.3 Mesure de l'échauffement sous illumination solaire infrarouge

Afin de mesurer les propriétés photothermiques des échantillons fabriqués, le dispositif de caractérisation présenté en Figure 2.4 a été mis en place. L'idée est d'illuminer un échantillon à l'aide d'un simulateur solaire en face, et de mesurer sa température en face arrière par thermographie infrarouge. Pour cela, un simulateur solaire à spectre accordable (Pico LED simulator, G2V Optics) a été utilisé. Ce simulateur contient 30 diodes électroluminescentes (DEL) dont les longueurs d'ondes d'émission sont réparties entre 350 et 1500 nm. L'intensité de chaque DEL pouvant être contrôlée indépendamment, nous avons réglé le simulateur pour qu'il émette le spectre standard AM1.5G limité aux longueurs d'onde infrarouges entre 800 et 1500 nm, dans le but de simuler l'illumination solaire après filtration par une cellule PV. Un filtre en silice fondue est placé devant le simulateur solaire, afin d'empêcher le rayonnement thermique parasite du simulateur d'atteindre l'échantillon. Une caméra infrarouge est utilisée pour mesurer la température en face arrière de l'échantillon. Une détermination préalable de l'émissivité de la face arrière de l'échantillon est nécessaire pour calibrer la caméra IR.

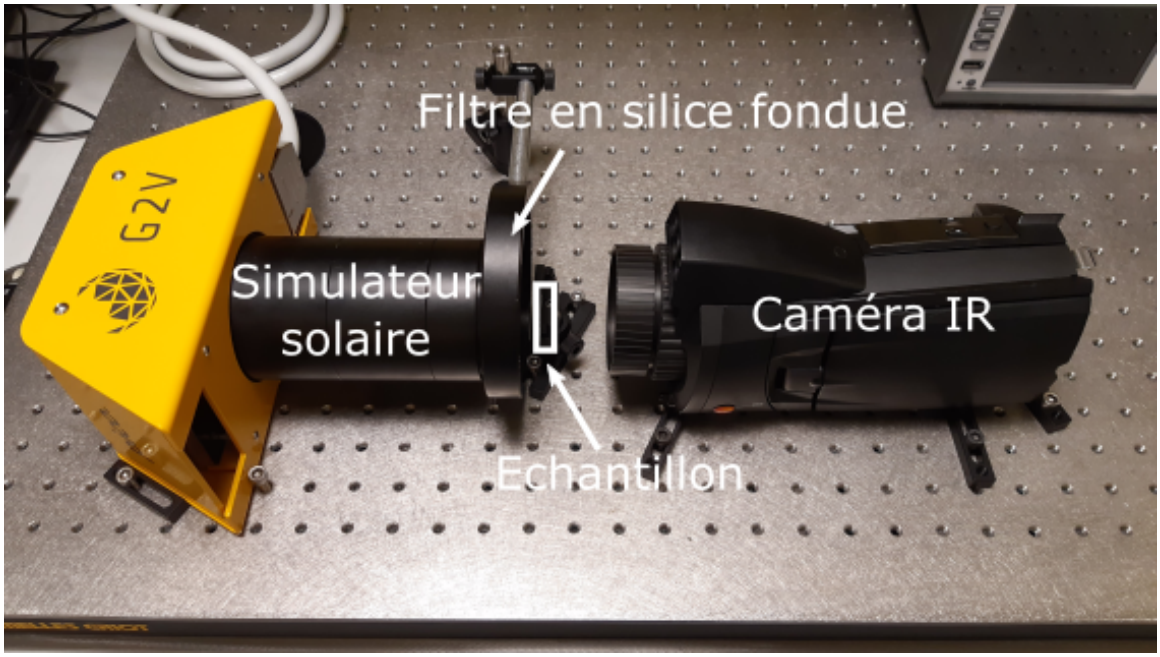

Figure 2.4 : Photographie du dispositif de caractérisation photothermique mis en place au LAAS, comprenant le simulateur solaire, la caméra infrarouge, le filtre en silice fondue et la position de l'échantillon.

Chapitre 3

Simulations électromagnétiques de nanoantennes isolées

3.1 Classement des nanoantennes pour l'absorption solaire infrarouge

Les propriétés optiques de nanoparticules isolées peuvent fortement varier en fonction de leur forme, taille et composition. Créer la structure idéale pour une application spécifique n'est pas une tâche facile, en raison de la grande variété de géométries disponibles avec les techniques de nanofabrication actuelles. Ainsi, nous avons commencé par mener une étude numérique afin d'identifier les nanoantennes les plus prometteuses pour l'absorption solaire infrarouge. Dans cette optique, nous avons utilisé DDSCAT [120], un code de calcul libre reposant sur la méthode de l'approximation des dipôles discrets (voir Chapitre 2.1), pour calculer les spectres de sections efficaces d'absorption $\sigma(\lambda)$ de différents types de particules.

Ces simulations numériques ont été limitées à l'étude de 5 formes de particules présentées en Figure 3.1 A-E : le pavé, le bâtonnet, le cône tronqué, le disque et le diabolo. La composition et les dimensions latérales ont été variées pour ces différentes géométries, tandis que l'épaisseur a été maintenue à 150 nm.

Puisque ces nanoantennes ont vocation à être intégrées à l'interface entre une cellule PV et un TEG, le paramètre à optimiser est la puissance absorbée par unité de surface sous illumination solaire infrarouge P_{abs}^{S}. En effet, pour une cellule PV en GaAs, seules les longueurs d'ondes supérieures à la longueur d'onde de la bande interdite λ_g sont transmises à l'inteface photothermique. Nous avons donc choisi P_{abs}^{S} comme figure de mérite, afin de comparer l'efficacité des nanoantennes simulées :

$$P_{abs}^{S} = \frac{\int_{\lambda_g}^{\infty} \sigma_{abs}(\lambda)\phi(\lambda)d\lambda}{S_{NP}} \tag{3.1}$$

Avec $\lambda_g = 875$ nm la longueur d'onde de la bande interdite du GaAs, $\phi(\lambda)$

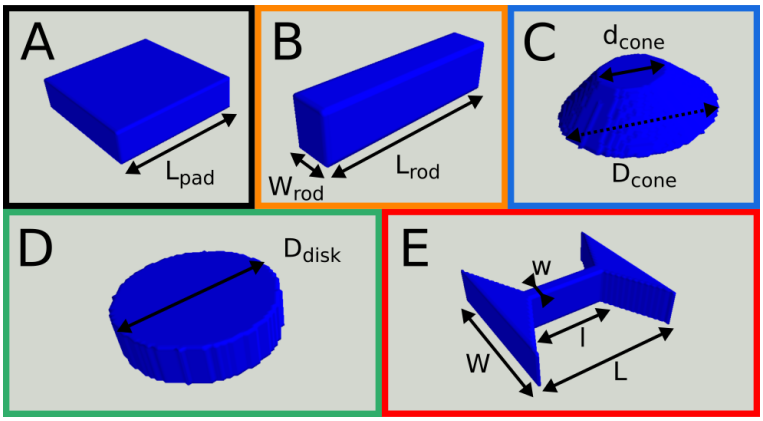

Figure 3.1 : Modèles en 3D des géométries simulées, dont les dimensions variables sont indiquées : (A) pavé, (B) bâtonnet, (C) cône tronqué, (D) disque et (E) diabolo. Réimprimé avec la permission de ACS Appl. Energy Mater. 2023, 6, 4, 2128–2133. Copyright 2023 American Chemical Society.

l'irradiance du spectre solaire AM1.5G, et S_{NP} l'empreinte de la nanoantenne, c'est-à-dire la surface qu'elle occupe sur un substrat.

La figure 3.2 montre les résultats obtenus pour des nanoantennes en nickel, matériau retenu car il offre un bon compromis entre intensité de l'absorption dans la gamme d'intérêt, stabilité chimique, et facilité de déposition dans la salle blanche du LAAS.

Une tendance générale peut être observée pour les cinq formes, à savoir la présence d'un maximum de P^S_{abs} à un volume de particule donné. Modifier le volume d'une nanoantenne en modifiant ses dimensions entraîne deux effets principaux sur l'absorption optique. Tout d'abord, les résonances plasmoniques sont déplacées vers des longueurs d'onde plus élevées lorsque la taille de la nanoantenne augmente, ou vers des longueurs d'onde plus courtes lorsque sa taille diminue. Deuxièmement, les particules plus petites ont tendance à avoir un rapport absorption-sur-diffusion plus élevé. On observe que la réponse des disques, pavés et cônes tronqués est similaire, tandis que les bâtonnets et les diabolos présentent des performances nettement supérieures, en raison d'une intensité d'absorption plus importante et d'un meilleur recouvrement spectral avec le spectre d'illumination. Parmi toutes les structures étudiées, les nanoantennes en forme de diabolo semblent être les plus efficaces pour l'absorption solaire infrarouge.

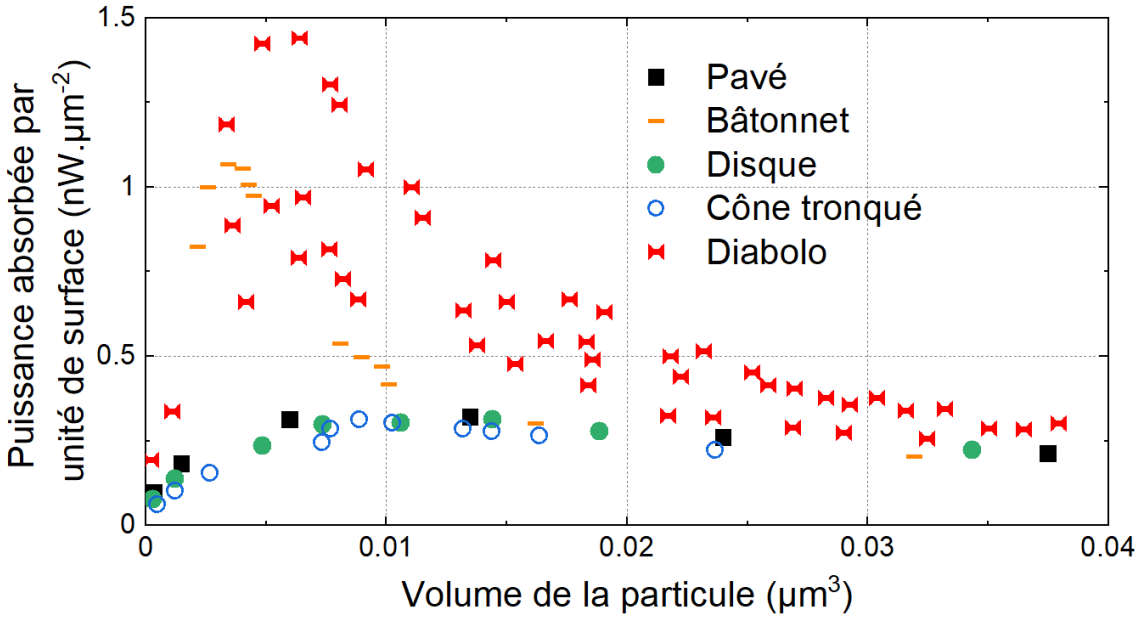

Figure 3.2 : Simulations numériques par la méthode DDA de l'absorption optique de diverses nanoantennes. Puissance solaire infrarouge absorbée par unité de surface P^S_{abs} calculée pour des nanoantennes isolées en nickel d'une épaisseur de 150 nm et de différentes formes et dimensions. Réimprimé avec la permission de ACS Appl. Energy Mater. 2023, 6, 4, 2128–2133. Copyright 2023 American Chemical Society.

3.2 Impact des défauts de fabrication

Les simulations réalisées précédemment ont permis d'identifier les diabolos en nickel comme étant des nanoantennes efficaces pour l'absorption solaire infrarouge. Nous avons donc entrepris de fabriquer ces structures sur un substrat par lithographie électronique.

Une image par microscopie électronique à balayage (MEB) des nanodiabolos obtenus est visible en Figure 3.3A, et une représentation en trois dimensions de leur topographie de surface, obtenue par microscopie à force atomique (AFM), est présentée en Figure 3.3B. Ces images montrent clairement la présence de défauts de fabrication, à savoir une déviation des dimensions latérales vis-à-vis de la structure nominale, visible en Figure 3.3C, ainsi que l'introduction de rugosité de surface.

Afin de quantifier l'impact de ces défauts de fabrication sur les propriétés optiques des nanodiabolos, deux nouvelles cibles de simulation ont été générées, dont les dimensions latérales sont celles mesurées au MEB. La première est un diabolo lisse (Figure 3.3D), et la deuxième est un diabolo dont la rugosité de surface correspond aux données AFM (Figure 3.3E).

Des simulations DDA ont été conduites sur ces deux cibles, et leurs spectres de section efficace d'absorption sont comparés à la structure nominale en Figure 3.3F. Les résultats montrent un fort impact de la variation des dimensions latérales sur les propriétés d'absorption, alors que l'effet de la rugosité de surface est, quant à lui, très faible.

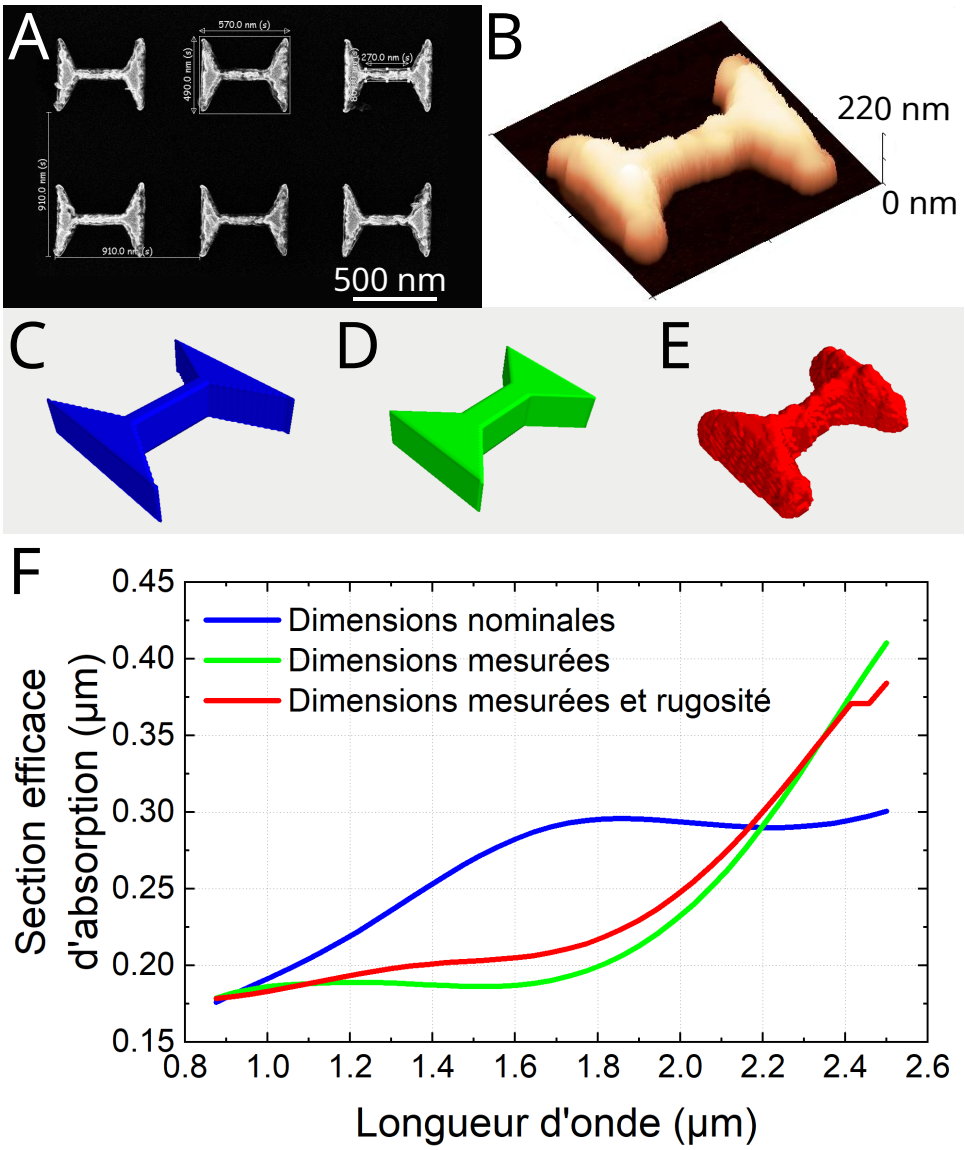

Figure 3.3 : Impact des défauts de fabrication sur les propriétés optiques de nanodiabolos en nickel. Images (A) MEB et (B) AFM des nanodiabolos fabriqués sur un substrat silicium. Modèles 3D (C) de la structure nominale, (D) de la structure lisse avec dimensions réelles et (E) d'une structure réaliste avec dimensions réelles et rugosité de surface. (F) Spectres d'absorption calculés pour les trois structures. Réimprimé avec la permission de ACS Appl. Energy Mater. 2023, 6, 4, 2128–2133. Copyright 2023 American Chemical Society.

Ainsi, afin de s'assurer d'obtenir les propriétés optiques souhaitées, il est crucial de pouvoir maîtriser précisément les dimensions des nanoantennes fabriqués. Cela peut se faire relativement aisément par une calibration préalable des procédés de fabrication. D'un autre côté, la rugosité de surface, qui est inhérente à la méthode de dépôt métallique utilisée, ne représente pas un obstacle à l'obtention de nanoantennes performantes.

Chapitre 4

Fabrication et caractérisation d'interfaces photothermiques nanostructurées

4.1 Fabrication par lithographie colloïdale

Afin de caractériser les propriétés photothermiques de nos nanoantennes, nous avons fabriqué six échantillons à partir d'un substrat de verre recouvert d'un miroir d'argent de 80 nm d'épaisseur, puis d'une couche d'alumine de 100 nm d'épaisseur. Des arrangements de nanocônes tronqués, de différentes compositions et hauteurs, sont ensuite fabriqués par lithographie colloïdale sur la face supérieure du substrat, pour aboutir au résultat présenté en Figure 4.1. Quatre échantillons sont recouverts de nanocônes de 50 nm d'épaisseur en aluminium (Al50), argent (Ag50), nickel (Ni50) ou or (Au50), et le dernier est recouvert de nanocônes en nickel de 200 nm d'épaisseur (Ni200). Tous les cônes ont un diamètre de base de 200 nm. Un dernier échantillon de référence, dépourvu de nanocônes, est également fabriqué.

L'observation par microscopie électronique à balayage a permis de mettre en évidence une forte fluctuation de la densité surfacique de nanoantennes d'un échantillon à l'autre, due à un mauvais contrôle lors de l'étape de lithographie colloïdale. Ainsi, le taux de recouvrement du substrat varie de 4,6 % pour Ni50 à 10,1 % pour Ni200.

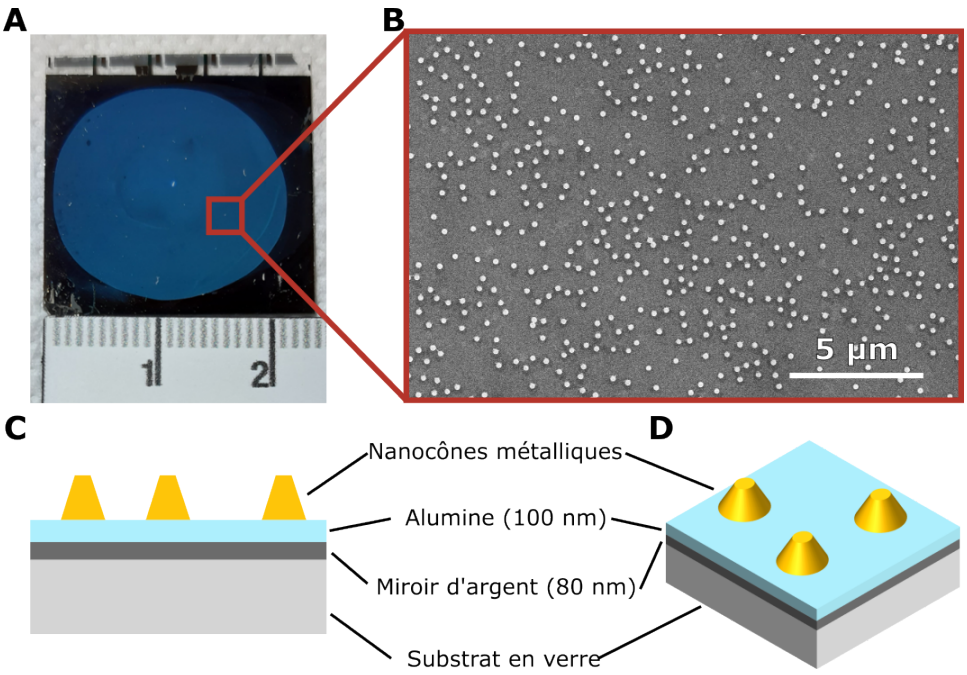

Figure 4.1 : Exemple d'échantillon fabriqué par lithographie colloïdale. (A) Photographie d'un échantillon de 24x24 mm² recouvert de nanocônes en nickel de 200 nm d'épaisseur. (B) Image MEB de la surface de l'échantillon. Représentation schématique de l'échantillon (C) en coupe et (D) en 3 dimensions.

4.2 Échauffement sous illumination solaire infrarouge

Le dispositif expérimental utilisé pour caractériser les propriétés photothermiques des interfaces nanostructurées est présenté en Section 2.3. Les échantillons fabriqués ont été illuminés par l'avant (côté nanoantennes) par un simulateur solaire dont le spectre est limité aux longueurs d'ondes comprises entre 0,8 et 1,5 µm. Les échantillons, initialement à température ambiante, s'échauffent progressivement sous l'effet de la conversion photothermique du rayonnement incident. La température en face arrière des échantillons (côté verre) est mesurée à l'aide d'une caméra thermique. L'évolution temporelle de l'échauffement de chaque interface photothermique est représentée en Figure 4.2.

L'échauffement après 6 min d'illumination est stabilisé pour chaque échantillon, et systématiquement supérieur à celui de la référence sans nanoantennes, ce qui met en évidence les capacités de nos nanostructures métalliques à absorber le rayonnement solaire infrarouge et à le convertir en chaleur. L'échantillon Ni200 montre l'élévation de température la plus importante, avec un échauffement de +6,1 °C par rapport à la référence.

Cependant, ces résultats ne permettent pas de comparer l'efficacité des nanocônes utilisés. En effet, considérer uniquement l'échauffement global de l'échantillon revient à occulter l'impact de la densité surfacique de nanocônes qui, comme nous l'avons montré précédemment, varie grandement d'un échantillon à l'autre. Ainsi,

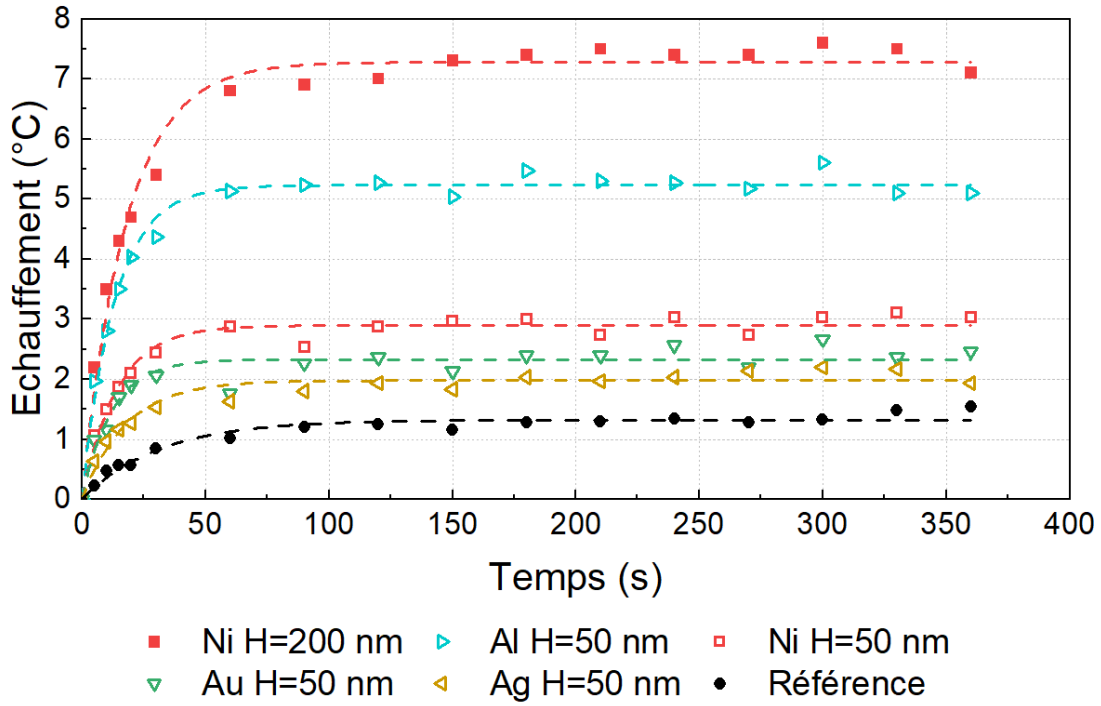

Figure 4.2 : Évolution de l'échauffement moyen de la face arrière du substrat sous illumination solaire infrarouge, pour différents échantillons. L'illumination est activée à t=0 s.

afin d'obtenir davantage d'information sur les performances des nanoantennes, nous avons calculé l'échauffement par nanocône ΔT_{cone} pour chaque interface photothermique :

$$\Delta T_{cone} = \frac{(T - T_{ref})}{d \cdot S} \tag{4.1}$$

avec T_{ref} la température d'équilibre de la référence sous illumination, et T, d et S la température d'équilibre mesurée, la densité surfacique en nanocônes, et la surface totale de l'échantillon, respectivement. ΔT_{cone} nous permet de classer les nanoantennes selon leur efficacité pour l'échauffement photothermique.

Les résultats sont présentés dans le Tableau 4.1, qui montre que la contribution dans l'échauffement global de chaque nanocône en aluminium atteint 3,8 n°C, alors que la contribution d'un nanocône en argent est de seulement 0,5 n°C. Ainsi, optimiser la température globale d'une interface photothermique nanostructurée requiert de combiner une forte densité de nanoantennes et une forte capacité d'absorption et de conversion photothermique par les nanoantennes individuellement. Selon ces résultats, des températures encore plus élevées pourraient être atteintes en fabriquant des interfaces photothermiques recouvertes de nanocônes en aluminium avec une forte densité.

Échantillon	Échauffement (°C)	Taux de recouvrement (%)	ΔT_{cone} (n°C)
Al (H=50 nm)	5,1	5,5	3,8
Ni (H=200 nm)	7,1	10,1	3,3
Ni (H=50 nm)	3,0	4,6	1,9
Au (H=50 nm)	2,5	7,2	0,8
Ag (H=50 nm)	2,1	8,2	0,5

Table 4.1 : Échauffement sous illumination solaire limitée à la gamme 0,8-1,5 µm, pour les interfaces photothermiques fabriquées, et échauffement par nanocône estimé à partir du taux de recouvrement surfacique.

Chapitre 5

Modélisation multiphysique du dispositif PV-TE

5.1 Description générale du modèle

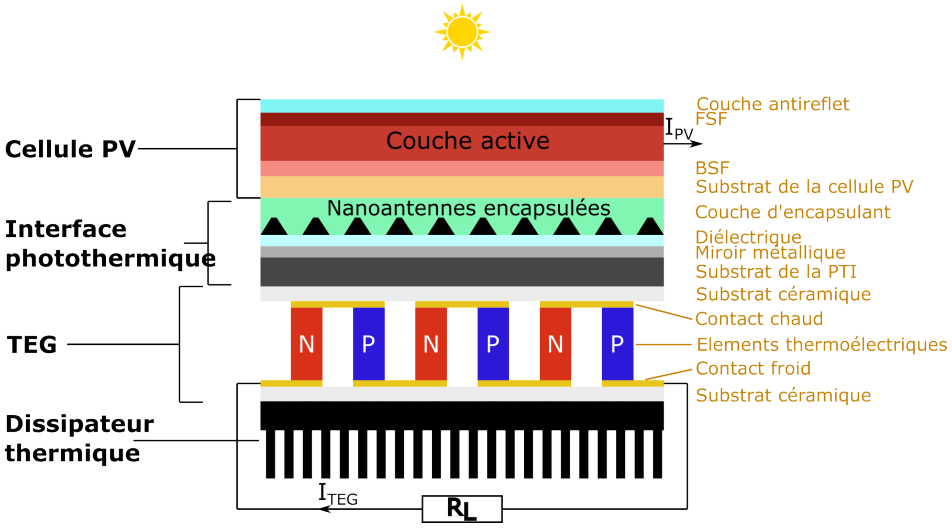

Figure 5.1 : Représentation schématique d'un dispositif PV-TE intégrant une interface photothermique nanostructurée. La couche active de la cellule photovoltaïque génère le photocourant I_{PV} lorsqu'elle est éclairée par le spectre solaire. L'interface photothermique est composée de nanoantennes encapsulées sur un substrat multicouche. Les thermocouples dopés N et P sont connectés en série à une résistance de charge R_L et génèrent le courant I_{TEG} lorsqu'ils sont exposés à un flux de chaleur. Le rôle du dissipateur thermique est de dissiper la chaleur par convection naturelle.

Un dispositif PV-TE complet est un système complexe dans lequel les effets optiques, thermiques et électriques sont étroitement liés. L'impact de l'intégration d'une interface photothermique dans un tel système ne peut pas être estimé de manière directe. Par exemple, il est probable que l'ajout d'une interface photothermique augmentera la température de la cellule photovoltaïque et du générateur thermoélectrique, réduisant potentiellement les performances de la première et augmentant

celles du second. Ainsi, cette augmentation de température n'est bénéfique pour la puissance électrique globale extraite par le système seulement si la puissance supplémentaire générée par le TEG compense la perte de puissance de la cellule photovoltaïque (PVC). La réalisation de cette condition dépend fortement des caractéristiques physiques de la PTI, de la cellule photovoltaïque et du TEG.

Afin d'estimer l'impact de l'intégration d'une interface photothermique dans un dispositif PV-TE, il est donc nécessaire de modéliser l'ensemble du système, dont un exemple est présenté sur la Figure 5.1. L'outil multiphysique que nous proposons dans ce chapitre vise à simuler le comportement des dispositifs PV-TE comprenant une interface photothermique, en considérerons une absorption dépendante du spectre dans chaque couche de la cellule photovoltaïque et de l'interface photothermique. Cet outil combine simulations optiques, équations de transport thermique et modèles électriques.

Nous décrirons un modèle unidimensionnel en état d'équilibre. Le système global PVC-PTI-TEG est représenté par un empilement de couches de surface infinie, chacune ayant son épaisseur et sa conductivité thermique propres. Le modèle peut être divisé en trois sous-systèmes placés en contact thermique : la cellule photovoltaïque, l'interface photothermique et le TEG. En fonction des caractéristiques spécifiques de chaque couche, nous sommes en mesure de calculer la température à chaque interface du système, ainsi que la puissance électrique générée.

5.2 Couplage multiphysique

Le modèle implique trois sous-systèmes interconnectés, à savoir la PVC, la PTI et le TEG. Les équations de transfert thermique sont utilisées pour coupler ces sous-systèmes. La Figure 5.2 illustre les différentes étapes du processus visant à déterminer la puissance de sortie de la PVC et du TEG, en prenant en compte leurs propriétés structurelles, optiques, thermiques et électriques.

Initialement, des simulations photoniques sont réalisées à l'aide du code Moosh [180], en utilisant le spectre solaire incident et les propriétés de la cellule PV. Ces simulations permettent de calculer l'absorption optique dans chaque couche de la cellule ainsi que la puissance transmise. Ensuite, la chaleur générée dans la PVC sous l'effet de la conversion photothermique, de la thermalisation et des autres pertes non radiatives est évaluée.

La puissance optique transmise à travers la cellule PV est ensuite introduite comme spectre optique incident dans le modèle de l'interface photothermique. Des simulations DDA sont utilisées pour estimer l'absorption par la PTI, qui est considérée totalement opaque, empêchant toute transmission de lumière au TEG. La chaleur générée par la PTI résulte de la conversion photothermique de la puissance optique absorbée, supposée avoir lieu au niveau de la couche nanostructurée.

Le modèle du TEG permet de calculer la puissance électrique et la chaleur générées dans la couche thermoélectrique en fonction des températures des contacts

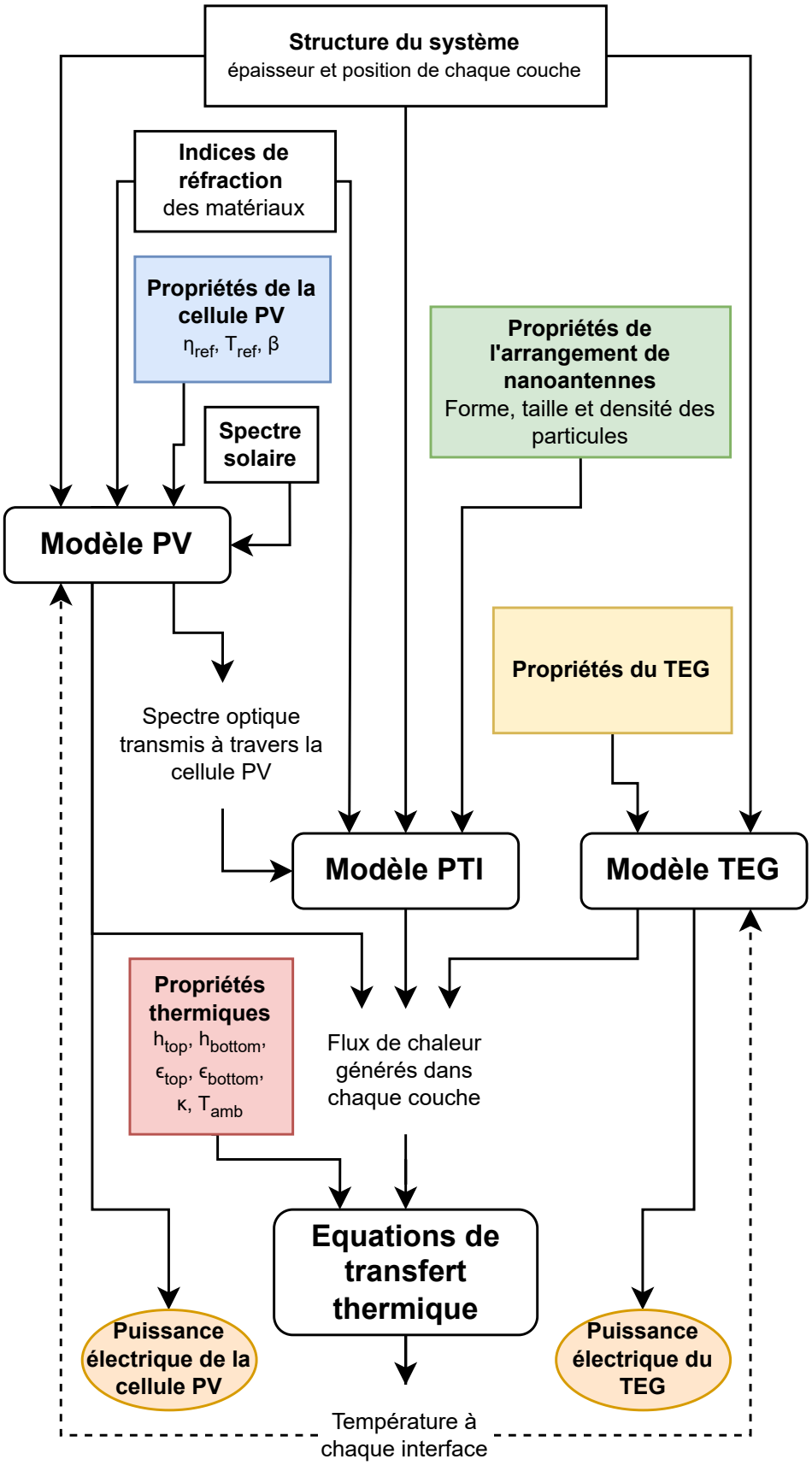

Figure 5.2 : Schéma présentant le principe de l'outil multiphysique permettant de calculer la puissance électrique générée par un dispositif PVC-PTI-TEG en fonction des propriétés de ses composants.

chaud et froid.

Les modèles de la PVC, de la PTI et du TEG sont mis en contact thermique, avec la couche supérieure de la PTI directement sous la couche inférieure de la PVC et la couche inférieure de la PTI directement au-dessus de la couche supérieure du TEG. Les résistances thermiques d'interface sont négligées et le transfert thermique est considéré comme entièrement conductif au sein du système. Le transfert de chaleur par convection et rayonnement est pris en compte pour l'interface supérieure (air/PVC) et inférieure (TEG/air).

L'outil de simulation utilise MatLab pour résoudre les équations couplées qui définissent la chaleur générée dans chaque couche, en fonction de la température à chaque interface. Le processus débute par le calcul de la chaleur générée lorsque le système est à température ambiante, ce qui permet de d'évaluer une nouvelle distribution de température. Ce processus itératif est répété jusqu'à convergence vers un couple températures-chaleur stable, qui est ensuite utilisé pour calculer la puissance électrique générée par la PVC et le TEG.

5.3 Validation expérimentale du modèle de l'interface photothermique

Le modèle de la PTI peut être utilisé, en combinaison avec les équations de transfert thermique, afin de simuler le comportement photothermique d'une PTI isolée, indépendamment du reste du système. Ainsi, il est possible de comparer les résultats de simulation de l'interface seule aux résultats expérimentaux du Chapitre 4, afin de vérifier la validité du modèle.

Les paramètres des interfaces photothermiques nanostructurées présentées dans le Chapitre 4 ont été entrés dans le modèle de la PTI. Le spectre incident a été fixé au spectre solaire AM1.5G, limité à la gamme 0,8-1,5 µm, afin de correspondre à l'illumination fournie par le simulateur solaire.

L'échauffement de la face arrière des interfaces photothermiques est calculé par le modèle à partir de ces paramètres, et comparé aux résultats expérimentaux en Figure 5.3.

La meilleure prédiction est obtenue pour l'échantillon le plus chaud (Ni200), et l'accord entre l'échauffement mesuré et calculé semble diminuer avec la température calculée. Dans l'ensemble, l'échauffement calculé présente la même tendance que celui mesuré, avec une erreur absolue limitée à ±1 °C, à l'exception de l'échantillon en aluminium, qui montre la plus grande erreur par rapport à l'expérience. Ainsi, le modèle de la PTI semble capable de prédire qualitativement le chauffage généré par différents échantillons, ce qui permet de classer leur efficacité de conversion photothermique.

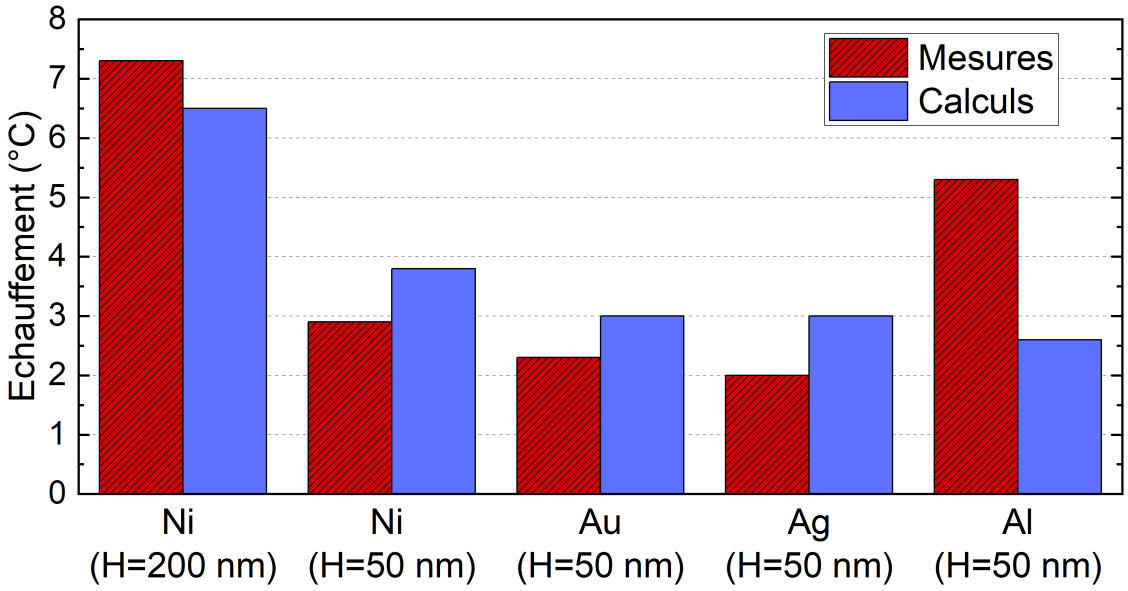

Figure 5.3 : Histogramme comparant le chauffage mesuré et calculé, sous illumination solaire limitée à la plage de longueurs d'onde de 0,8 à 1,5 µm, pour différentes interfaces photothermiques nanostructurées.

5.4 Validation du modèle PV-TE par comparaison à la littérature

Dans cette section, nous allons comparer les résultats obtenus avec notre modèle aux résultats publiés par Zhou et al. en 2018 [174], qui décrivent la modélisation multiphysique du dispositif PV-TE visible en Figure 5.4A, composé d'une cellule solaire en silicium, d'un générateur thermoélectrique et d'un dissipateur thermique passif, .

La plupart des paramètres d'entrée de notre modèle, tels que l'épaisseur et la conductivité thermique des couches, ainsi que les paramètres du TEG, sont directement extraits de la publication. La température ambiante est fixée à 300 K, et la puissance optique incidente correspond au spectre solaire avec un rapport de concentration de 10. Les coefficients d'émissivité et de convection utilisés dans notre modèle sont donnés en Table 5.1.

Paramètres de radiation et convection	
Émissivité de l'interface supérieure ϵ_{sup}	0,85
Émissivité de l'interface inférieure ϵ_{inf}	0,1
Coef. de convection de l'interface supérieure $h_{sup}(W/(m^2 \cdot K))$	2
Coef. de convection de l'interface inférieure $h_{inf}(W/(m^2 \cdot K))$	120

Table 5.1 : Paramètres thermiques utilisés dans la simulation du dispositif PVC-TEG.

À partir des données fournies par Zhou et al., nous sommes en mesure de déduire que la cellule solaire utilisée dans l'article présente un rendement de 11,55 % à 120

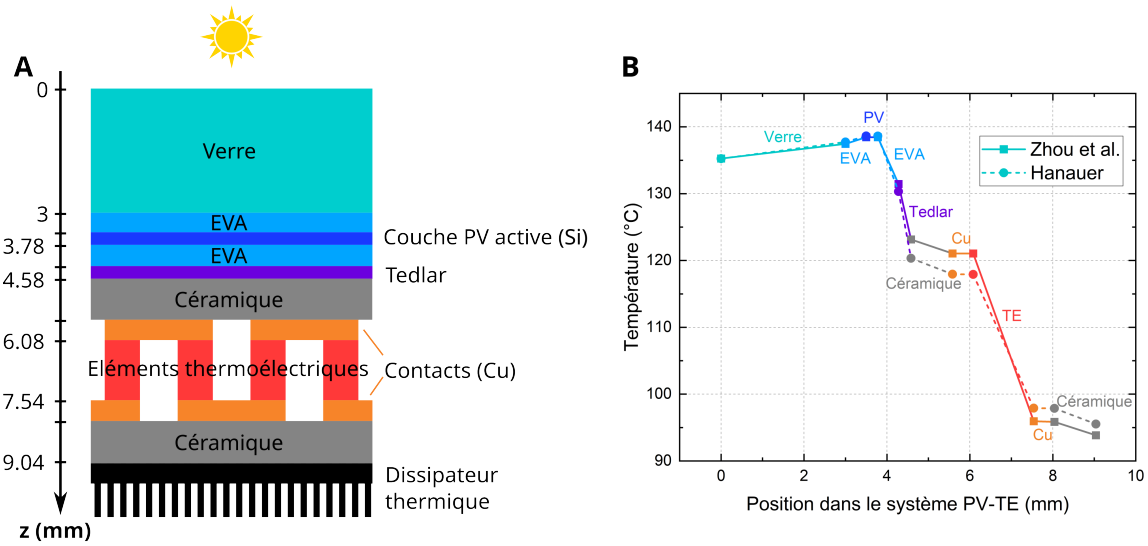

Figure 5.4 : Comparaison entre la distribution de température au sein d'un dispositif PV-TE calculée par Zhou et al. [174], et calculée à l'aide du modèle multiphysique présenté dans cette thèse. (A) Schéma du système simulé et (B) distribution de température.

°C et un coefficient de température de -0,056 %/°C. Dans l'article, il est supposé que toute la puissance optique atteignant la couche active de la PVC est soit convertie en électricité, soit en chaleur, sans transmission. Nous avons donc modifié notre modèle pour satisfaire cette hypothèse.

La distribution de température calculée par notre modèle au sein du dispositif est comparée aux résultats de Zhou et al. dans la Figure 5.4B, où l'on peut voir que notre modèle présente une bonne concordance quantitative avec les données de la littérature. La principale différence réside en un gradient de température plus faible à travers la couche thermoélectrique dans notre cas. Cela peut découler d'une sous-estimation de la chaleur générée dans la cellule PV.

Les puissances électriques générées par la cellule PV et le TEG dans ces conditions de température sont présentées dans le Tableau 5.2. La puissance de sortie de la cellule PV est en accord avec l'article, ce qui est cohérent en raison de la similarité des températures des cellules. La puissance de sortie du TEG est réduite avec notre modèle, en raison du gradient de température plus faible à travers la couche thermoélectrique : Zhou et al. ont calculé un gradient de 25,1 °C, tandis que le nôtre est seulement de 21,9 °C. Dans l'ensemble, les résultats de notre modèle PV-TE semblent correspondre à l'état de l'art dans la simulation PV-TE, avec une différence inférieure à 5% dans le calcul des puissances générées.

Puissance électrique générée (W/m^2)	PV	TE	PV-TE
Zhou et al.	1051.6	112.0	1163.6
Notre modèle	1043.5	71.2	1114.7

Table 5.2 : Comparaison entre les puissances électriques générées par la cellule PV et le TEG, calculées par notre modèle et le modèle de Zhou et al.

Conclusion

Cette thèse avait pour objectif d'étudier les propriétés d'interfaces photothermiques à base de nanoantennes thermoplasmoniques, et d'explorer leur intégration au sein de dispositifs de cogénération photovoltaïque-thermoélectrique. Pour cela, nous avons suivi une approche multi-échelle, allant de la simulation de nanoantennes isolées à la modélisation d'un système PV-TE complet, en passant par la fabrication et la caractérisation d'interfaces photothermiques.

Nous avons tout d'abord présenté les limites des cellules photovoltaïques monojonctions, afin d'expliciter les avantages des dispositifs de cogénération PV-TE. Nous avons alors proposé l'utilisation d'interfaces photothermiques composées de nanoantennes thermoplasmoniques pour améliorer l'efficacité de ces systèmes.

Nous avons ensuite donné un aperçu des méthodes numériques et expérimentales utilisées au cours de la thèse, à savoir les méthodes de simulations électromagnétiques, les techniques de nanofabrication et les moyens de caractérisation.

Les simulations électromagnétiques sur nanoantennes isolées ont permis d'identifier des structures efficaces pour l'absorption solaire infrarouge. La géométrie prometteuse des diabolos en nickel a été mise en avant, et l'impact des défauts de fabrication a été exploré.

Des interfaces photothermiques macroscopiques ont été fabriquées par lithographie colloïdale. Ces interfaces ont été caractérisées, et les facteurs affectant leur efficacité photothermique ont été étudiés.

Finalement, un modèle multiphysique de l'ensemble du dispositif PV-TE a été développé, permettant de calculer l'impact de l'intégration d'une interface photothermique nanostructurée sur la puissance électrique générée par le système. La précision du modèle est validée par rapport aux données expérimentales et à la littérature, démontrant sa capacité prédictive.

Pour conclure, cette thèse a permis de mieux comprendre les phénomènes en jeu lors de l'intégration d'interfaces photothermiques à base de nanoantennes thermoplasmoniques au sein de dispositifs PV-TE. La combinaison de simulations numériques, d'expérimentation et de modélisation offre des éclairages sur la conception, la fabrication et l'optimisation d'interfaces photothermiques..

Bibliography

[1] "Evolution of solar PV module cost by data source, 1970-2020 – Charts – Data & Statistics - IEA."

[2] M. Green, E. Dunlop, J. Hohl-Ebinger, M. Yoshita, N. Kopidakis, and X. Hao, "Solar cell efficiency tables (version 57)," *Progress in Photovoltaics: Research and Applications*, vol. 29, pp. 3–15, Jan. 2021.

[3] J. Haiwei, Q. Li, Z. Lan, Z. Xinlin, and Y. Rui, "Review of wide band-gap semiconductors technology," *MATEC Web of Conferences*, 2015.

[4] M. Shur, "Wide band gap semiconductor technology: State-of-the-art," *Solid-State Electronics*, vol. 155, pp. 65–75, May 2019.

[5] B. Ehrler, E. Alarcón-Lladó, S. W. Tabernig, T. Veeken, E. C. Garnett, and A. Polman, "Photovoltaics Reaching for the Shockley–Queisser Limit," *ACS Energy Letters*, vol. 5, pp. 3029–3033, Sept. 2020.

[6] W. Shockley and H. J. Queisser, "Detailed Balance Limit of Efficiency of p-n Junction Solar Cells," *Journal of Applied Physics*, vol. 32, pp. 510–519, Mar. 1961.

[7] M. B. Prince, "Silicon Solar Energy Converters," *Journal of Applied Physics*, vol. 26, no. 5, pp. 534–540, 1995.

[8] M. A. Green, "General temperature dependence of solar cell performance and implications for device modelling," *Progress in Photovoltaics: Research and Applications*, vol. 11, no. 5, pp. 333–340, 2003.

[9] E. Chahid, M. I. Oumhanad, M. Feddaoui, and A. Malaoui, "Study of the physical parameters on the GaAs solar cell efficiency," *Journal of Ovonic Research*, vol. 13, pp. 119–128, June 2017.

[10] A. Badawi, A. H. Al Otaibi, A. M. Albaradi, N. Al-Hosiny, and S. E. Alomairy, "Tailoring the energy band gap of alloyed Pb1-xZnxS quantum dots for photovoltaic applications," *Journal of Materials Science: Materials in Electronics*, vol. 29, pp. 20914–20922, Dec. 2018.

[11] A. Lambertz, V. Smirnov, T. Merdzhanova, K. Ding, S. Haas, G. Jost, R. E. I. Schropp, F. Finger, and U. Rau, "Microcrystalline silicon–oxygen alloys for application in silicon solar cells and modules," *Solar Energy Materials and Solar Cells*, vol. 119, pp. 134–143, Dec. 2013.

[12] J. F. Geisz, D. J. Friedman, J. M. Olson, S. R. Kurtz, R. C. Reedy, A. B. Swartzlander, B. M. Keyes, and A. G. Norman, "BGaInAs alloys lattice matched to GaAs," *Applied Physics Letters*, vol. 76, pp. 1443–1445, Mar. 2000.

[13] M. N. Islam and J. Podder, "The role of Al and Co co-doping on the band gap tuning of TiO2 thin films for applications in photovoltaic and optoelectronic devices," *Materials Science in Semiconductor Processing*, vol. 121, p. 105419, Jan. 2021.

[14] U. Jabeen, S. M. Shah, N. Hussain, Fakhr-e-Alam, A. Ali, A. khan, and S. U. Khan, "Synthesis, characterization, band gap tuning and applications of Cd-doped ZnS nanoparticles in hybrid solar cells," *Journal of Photochemistry and Photobiology A: Chemistry*, vol. 325, pp. 29–38, July 2016.

[15] G. Borghs, K. Bhattacharyya, K. Deneffe, P. Van Mieghem, and R. Mertens, "Band-gap narrowing in highly doped n- and p-type GaAs studied by photoluminescence spectroscopy," *Journal of Applied Physics*, vol. 66, pp. 4381–4386, Nov. 1989.

[16] N. T. Kaner, Y. Wei, Y. Jiang, W. Li, X. Xu, K. Pang, X. Li, J. Yang, Y. Jiang, G. Zhang, and W. Q. Tian, "Enhanced Shift Currents in Monolayer 2D GeS and SnS by Strain-Induced Band Gap Engineering," *ACS Omega*, vol. 5, pp. 17207–17214, July 2020.

[17] J. Zhang, X. Y. Lang, Y. F. Zhu, and Q. Jiang, "Strain tuned InSe/MoS2 bilayer van der Waals heterostructures for photovoltaics or photocatalysis," *Physical Chemistry Chemical Physics*, vol. 20, pp. 17574–17582, July 2018.

[18] C. Zhang, S. W. Tong, C. Jiang, E. T. Kang, D. S. H. Chan, and C. Zhu, "Simple tandem organic photovoltaic cells for improved energy conversion efficiency," *Applied Physics Letters*, vol. 92, p. 083310, Feb. 2008.

[19] J. Kim, Z. Hong, G. Li, T.-b. Song, J. Chey, Y. S. Lee, J. You, C.-C. Chen, D. K. Sadana, and Y. Yang, "10.5% efficient polymer and amorphous silicon hybrid tandem photovoltaic cell," *Nature Communications*, vol. 6, p. 6391, Mar. 2015.

[20] R. I. Rabady, "Optimized multi-junction photovoltaic solar cells for terrestrial applications," *Solar Energy*, vol. 106, pp. 72–81, Aug. 2014.

[21] C. Zhang, J. Gwamuri, R. Andrews, and J. M. Pearce, "Design of Multijunction Photovoltaic Cells Optimized for Varied Atmospheric Conditions," *International Journal of Photoenergy*, vol. 2014, p. e514962, Nov. 2014.

[22] E. Jackson, "Areas for improvement of the semiconductor solar energy converter," *Trans.Intern.Conf.on the Use of Solar Energy-The Scientific Basis*, vol. 5, p. 122, 1955.

[23] A. Luque, A. Martí, and C. Stanley, "Understanding intermediate-band solar cells," *Nature Photonics*, vol. 6, pp. 146–152, Mar. 2012.

[24] Y. Okada, N. J. Ekins-Daukes, T. Kita, R. Tamaki, M. Yoshida, A. Pusch, O. Hess, C. C. Phillips, D. J. Farrell, K. Yoshida, N. Ahsan, Y. Shoji, T. Sogabe, and J.-F. Guillemoles, "Intermediate band solar cells: Recent progress and future directions," *Applied Physics Reviews*, vol. 2, p. 021302, Apr. 2015.

[25] I. Ramiro and A. Martí, "Intermediate band solar cells: Present and future," *Progress in Photovoltaics: Research and Applications*, vol. 29, no. 7, pp. 705–713, 2021.

[26] A. Luque and A. Martí, "The Intermediate Band Solar Cell: Progress Toward the Realization of an Attractive Concept," *Advanced Materials*, vol. 22, no. 2, pp. 160–174, 2010.

[27] K. Nikolaidou, S. Sarang, and S. Ghosh, "Nanostructured photovoltaics," *Nano Futures*, vol. 3, p. 012002, Feb. 2019.

[28] R. R. Lunt, T. P. Osedach, P. R. Brown, J. A. Rowehl, and V. Bulović, "Practical Roadmap and Limits to Nanostructured Photovoltaics," *Advanced Materials*, vol. 23, no. 48, pp. 5712–5727, 2011.

[29] E. E. Perl, C.-T. Lin, W. E. McMahon, D. J. Friedman, and J. E. Bowers, "Ultrabroadband and Wide-Angle Hybrid Antireflection Coatings With Nanostructures," *IEEE Journal of Photovoltaics*, vol. 4, pp. 962–967, May 2014. Conference Name: IEEE Journal of Photovoltaics.

[30] C. Trompoukis, I. Abdo, R. Cariou, I. Cosme, W. Chen, O. Deparis, A. Dmitriev, E. Drouard, M. Foldyna, E. G. Caurel, I. Gordon, B. Heidari, A. Herman, L. Lalouat, K.-D. Lee, J. Liu, K. Lodewijks, F. Mandorlo, I. Massiot, A. Mayer, V. Mijkovic, J. Muller, R. Orobtchouk, G. Poulain, P. Prod'Homme, P. R. i. Cabarrocas, C. Seassal, J. Poortmans, R. Mertens, O. E. Daif, and V. Depauw, "Photonic nanostructures for advanced light trapping in thin crystalline silicon solar cells," *physica status solidi (a)*, vol. 212, no. 1, pp. 140–155, 2015.

[31] J. Zhao and M. Green, "Optimized antireflection coatings for high-efficiency silicon solar cells," *IEEE Transactions on Electron Devices*, vol. 38, pp. 1925–1934, Aug. 1991.

[32] C. Ji, W. Liu, Y. Bao, X. Chen, G. Yang, B. Wei, F. Yang, and X. Wang, "Recent Applications of Antireflection Coatings in Solar Cells," *Photonics*, vol. 9, p. 906, Dec. 2022.

[33] C. Cho, H. Kim, S. Jeong, S.-W. Baek, J.-W. Seo, D. Han, K. Kim, Y. Park, S. Yoo, and J.-Y. Lee, "Random and V-groove texturing for efficient light trapping in organic photovoltaic cells," *Solar Energy Materials and Solar Cells*, vol. 115, pp. 36–41, Aug. 2013.

[34] M.-J. Sher, M. T. Winkler, and E. Mazur, "Pulsed-laser hyperdoping and surface texturing for photovoltaics," *MRS Bulletin*, vol. 36, pp. 439–445, June 2011.

[35] M. Peters, J. C. Goldschmidt, P. Löper, B. Groß, J. Üpping, F. Dimroth, R. B. Wehrspohn, and B. Bläsi, "Spectrally-Selective Photonic Structures for PV Applications," *Energies*, vol. 3, pp. 171–193, Feb. 2010.

[36] D. Du, J. Darkwa, and G. Kokogiannakis, "Thermal management systems for Photovoltaics (PV) installations: A critical review," *Solar Energy*, vol. 97, pp. 238–254, Nov. 2013.

[37] C. G. Popovici, S. V. Hudişteanu, T. D. Mateescu, and N.-C. Cherecheş, "Efficiency Improvement of Photovoltaic Panels by Using Air Cooled Heat Sinks," *Energy Procedia*, vol. 85, pp. 425–432, Jan. 2016.

[38] L. Chen, D. Deng, Q. Ma, Y. Yao, and X. Xu, "Performance evaluation of high concentration photovoltaic cells cooled by microchannels heat sink with serpentine reentrant microchannels," *Applied Energy*, vol. 309, p. 118478, Mar. 2022.

[39] M. C. Browne, B. Norton, and S. J. McCormack, "Phase change materials for photovoltaic thermal management," *Renewable and Sustainable Energy Reviews*, vol. 47, pp. 762–782, July 2015.

[40] T. G. van Kessel, Y. C. Martin, R. L. Sandstrom, and S. Guha, "Extending photovoltaic operation beyond 2000 suns using a liquid metal thermal interface with passive cooling," in *2008 33rd IEEE Photovoltaic Specialists Conference*, pp. 1–3, May 2008. ISSN: 0160-8371.

[41] B. K. Mahadevan, S. Naghibi, F. Kargar, and A. A. Balandin, "Non-Curing Thermal Interface Materials with Graphene Fillers for Thermal Management of Concentrated Photovoltaic Solar Cells," *C*, vol. 6, p. 2, Mar. 2020.

[42] A. Hasan, J. Sarwar, and A. H. Shah, "Concentrated photovoltaic: A review of thermal aspects, challenges and opportunities," *Renewable and Sustainable Energy Reviews*, vol. 94, pp. 835–852, Oct. 2018.

[43] G. Yue, L. Sivec, J. M. Owens, B. Yan, J. Yang, and S. Guha, "Optimization of back reflector for high efficiency hydrogenated nanocrystalline silicon solar cells," *Applied Physics Letters*, vol. 95, p. 263501, Dec. 2009.

[44] E. V. Kerschaver and G. Beaucarne, "Back-contact solar cells: a review," *Progress in Photovoltaics: Research and Applications*, vol. 14, no. 2, pp. 107–123, 2006.

[45] E. Franklin, K. Fong, K. McIntosh, A. Fell, A. Blakers, T. Kho, D. Walter, D. Wang, N. Zin, M. Stocks, E.-C. Wang, N. Grant, Y. Wan, Y. Yang, X. Zhang, Z. Feng, and P. J. Verlinden, "Design, fabrication and characterisation of a 24.4% efficient interdigitated back contact solar cell," *Progress in Photovoltaics: Research and Applications*, vol. 24, no. 4, pp. 411–427, 2016.

[46] A. Blakers, "Development of the PERC Solar Cell," *IEEE Journal of Photovoltaics*, vol. 9, pp. 629–635, May 2019.

[47] A. W. Van Herwaarden and P. M. Sarro, "Thermal sensors based on the seebeck effect," *Sensors and Actuators*, vol. 10, pp. 321–346, Nov. 1986.

[48] H. Jouhara, A. Żabnieńska Góra, N. Khordehgah, Q. Doraghi, L. Ahmad, L. Norman, B. Axcell, L. Wrobel, and S. Dai, "Thermoelectric generator (TEG) technologies and applications," *International Journal of Thermofluids*, vol. 9, p. 100063, Feb. 2021.

[49] G. J. Snyder and A. H. Snyder, "Figure of merit ZT of a thermoelectric device defined from materials properties," *Energy & Environmental Science*, vol. 10, no. 11, pp. 2280–2283, 2017.

[50] M. T. Dunham, M. T. Barako, S. LeBlanc, M. Asheghi, B. Chen, and K. E. Goodson, "Power density optimization for micro thermoelectric generators," *Energy*, vol. 93, pp. 2006–2017, Dec. 2015.

[51] H. You, Z. Li, Y. Shao, X. Yuan, W. Liu, H. Tang, Q. Zhang, Y. Yan, and X. Tang, "Flexible Bi2Te3-based thermoelectric generator with an ultra-high power density," *Applied Thermal Engineering*, vol. 202, p. 117818, Feb. 2022.

[52] N. E. Dutoit, B. L. Wardle, and S.-G. Kim, "Design Considerations for Mems-Scale Piezoelectric Mechanical Vibration Energy Harvesters," *Integrated Ferroelectrics*, vol. 71, pp. 121–160, July 2005.

[53] Y. Vorobiev, J. González-Hernández, P. Vorobiev, and L. Bulat, "Thermal-photovoltaic solar hybrid system for efficient solar energy conversion," *Solar Energy*, vol. 80, pp. 170–176, Feb. 2006.

[54] B. Lorenzi, M. Acciarri, and D. Narducci, "Analysis of Thermal Losses for a Variety of Single-Junction Photovoltaic Cells: An Interesting Means of Thermoelectric Heat Recovery," *Journal of Electronic Materials*, vol. 44, pp. 1809–1813, June 2015.

[55] R. Bjørk and K. K. Nielsen, "The performance of a combined solar photovoltaic (PV) and thermoelectric generator (TEG) system," *Solar Energy*, vol. 120, pp. 187–194, Oct. 2015.

[56] B. Lorenzi, M. Acciarri, and D. Narducci, "Conditions for beneficial coupling of thermoelectric and photovoltaic devices," *Journal of Materials Research*, vol. 30, pp. 2663–2669, Sept. 2015.

[57] G. Contento, B. Lorenzi, A. Rizzo, and D. Narducci, "Efficiency enhancement of a-Si and CZTS solar cells using different thermoelectric hybridization strategies," *Energy*, vol. 131, pp. 230–238, July 2017.

[58] R. Bjørk and K. K. Nielsen, "The maximum theoretical performance of unconcentrated solar photovoltaic and thermoelectric generator systems," *Energy Conversion and Management*, vol. 156, pp. 264–268, Jan. 2018.

[59] N. Wang, L. Han, H. He, N.-H. Park, and K. Koumoto, "A novel high-performance photovoltaic–thermoelectric hybrid device," *Energy & Environmental Science*, vol. 4, no. 9, p. 3676, 2011.

[60] S. Ruiz Raga and F. Fabregat-Santiago, "Temperature effects in dye-sensitized solar cells," *Physical chemistry chemical physics : PCCP*, vol. 15, Jan. 2013.

[61] K.-T. Park, S.-M. Shin, A. S. Tazebay, H.-D. Um, J.-Y. Jung, S.-W. Jee, M.-W. Oh, S.-D. Park, B. Yoo, C. Yu, and J.-H. Lee, "Lossless hybridization between photovoltaic and thermoelectric devices," *Scientific Reports*, vol. 3, p. 2123, July 2013.

[62] Y. Zhang, J. Fang, C. He, H. Yan, Z. Wei, and Y. Li, "Integrated Energy-Harvesting System by Combining the Advantages of Polymer Solar Cells and Thermoelectric Devices," *The Journal of Physical Chemistry C*, vol. 117, pp. 24685–24691, Nov. 2013.

[63] O. Beeri, O. Rotem, E. Hazan, E. A. Katz, A. Braun, and Y. Gelbstein, "Hybrid photovoltaic-thermoelectric system for concentrated solar energy conversion: Experimental realization and modeling," *Journal of Applied Physics*, vol. 118, p. 115104, Sept. 2015.

[64] T.-J. Hsueh, J.-M. Shieh, and Y.-M. Yeh, "Hybrid Cd-free CIGS solar cell/TEG device with ZnO nanowires," *Progress in Photovoltaics: Research and Applications*, vol. 23, no. 4, pp. 507–512, 2015.

[65] D. N. Kossyvakis, G. D. Voutsinas, and E. V. Hristoforou, "Experimental analysis and performance evaluation of a tandem photovoltaic–thermoelectric hybrid system," *Energy Conversion and Management*, vol. 117, pp. 490–500, June 2016.

[66] T.-H. Kil, S. Kim, D.-H. Jeong, D.-M. Geum, S. Lee, S.-J. Jung, S. Kim, C. Park, J.-S. Kim, J. M. Baik, K.-S. Lee, C. Z. Kim, W. J. Choi, and S.-H. Baek, "A highly-efficient, concentrating-photovoltaic/thermoelectric hybrid generator," *Nano Energy*, vol. 37, pp. 242–247, July 2017.

[67] J. Zhang, H. Zhai, Z. Wu, Y. Wang, and H. Xie, "Experimental investigation of novel integrated photovoltaic-thermoelectric hybrid devices with enhanced performance," *Solar Energy Materials and Solar Cells*, vol. 215, p. 110666, Sept. 2020.

[68] Y. J. Kim, H. Choi, C. S. Kim, G. Lee, S. Kim, J. Park, S. E. Park, and B. J. Cho, "High-Performance Monolithic Photovoltaic–Thermoelectric Hybrid Power Generator Using an Exothermic Reactive Interlayer," *ACS Applied Energy Materials*, vol. 2, pp. 2381–2386, Apr. 2019.

[69] Y. Park, K. Cho, S. Yang, T. Park, S. Park, H.-e. Song, S. M. Kim, and S. Kim, "Performance of Hybrid Energy Devices Consisting of Photovoltaic Cells and Thermoelectric Generators," *ACS Applied Materials & Interfaces*, vol. 12, pp. 8124–8129, Feb. 2020.

[70] L. Tong, H. Wei, S. Zhang, and H. Xu, "Recent Advances in Plasmonic Sensors," *Sensors*, vol. 14, pp. 7959–7973, May 2014.

[71] G. Deka, C.-K. Sun, K. Fujita, and S.-W. Chu, "Nonlinear plasmonic imaging techniques and their biological applications," *Nanophotonics*, vol. 6, pp. 31–49, Jan. 2017.

[72] S. K. Cushing and N. Wu, "Progress and Perspectives of Plasmon-Enhanced Solar Energy Conversion," *The Journal of Physical Chemistry Letters*, vol. 7, pp. 666–675, Feb. 2016.

[73] T. J. Davis, D. E. Gómez, and A. Roberts, "Plasmonic circuits for manipulating optical information," *Nanophotonics*, vol. 6, pp. 543–559, May 2017.

[74] T. V. Shahbazyan and M. I. Stockman, *Plasmonics: Theory and Applications*, vol. 15 of *Challenges and Advances in Computational Chemistry and Physics*. Springer Dordrecht, 2013.

[75] S. A. Maier, *Plasmonics: Fundamentals and Applications*. New York, NY: Springer US, 2007.

[76] J. M. Pitarke, V. M. Silkin, E. V. Chulkov, and P. M. Echenique, "Theory of surface plasmons and surface-plasmon polaritons," *Reports on Progress in Physics*, vol. 70, p. 1, Dec. 2006.

[77] E. Hutter and J. H. Fendler, "Exploitation of Localized Surface Plasmon Resonance," *Advanced Materials*, vol. 16, no. 19, pp. 1685–1706, 2004.

[78] J. R. Krenn, J. C. Weeber, A. Dereux, E. Bourillot, J. P. Goudonnet, B. Schider, A. Leitner, F. R. Aussenegg, and C. Girard, "Direct observation of localized surface plasmon coupling," *Physical Review B*, vol. 60, pp. 5029–5033, Aug. 1999.

[79] J. Zhang, L. Zhang, and W. Xu, "Surface plasmon polaritons: physics and applications," *Journal of Physics D: Applied Physics*, vol. 45, p. 113001, Feb. 2012.

[80] A. V. Zayats, I. I. Smolyaninov, and A. A. Maradudin, "Nano-optics of surface plasmon polaritons," *Physics Reports*, vol. 408, pp. 131–314, Mar. 2005.

[81] P. Berini, R. Charbonneau, N. Lahoud, and G. Mattiussi, "Characterization of long-range surface-plasmon-polariton waveguides," *Journal of Applied Physics*, vol. 98, p. 043109, Aug. 2005.

[82] D. K. Gramotnev and S. I. Bozhevolnyi, "Nanofocusing of electromagnetic radiation," *Nature Photonics*, vol. 8, pp. 13–22, Jan. 2014.

[83] P. K. Jain, X. Huang, I. H. El-Sayed, and M. A. El-Sayed, "Review of Some Interesting Surface Plasmon Resonance-enhanced Properties of Noble Metal Nanoparticles and Their Applications to Biosystems," *Plasmonics*, vol. 2, pp. 107–118, Sept. 2007.

[84] P. K. Jain and M. A. El-Sayed, "Plasmonic coupling in noble metal nanostructures," *Chemical Physics Letters*, vol. 487, pp. 153–164, Mar. 2010.

[85] G. Maidecchi, G. Gonella, R. Proietti Zaccaria, R. Moroni, L. Anghinolfi, A. Giglia, S. Nannarone, L. Mattera, H.-L. Dai, M. Canepa, and F. Bisio, "Deep Ultraviolet Plasmon Resonance in Aluminum Nanoparticle Arrays," *ACS Nano*, vol. 7, pp. 5834–5841, July 2013.

[86] I. Kriegel, F. Scotognella, and L. Manna, "Plasmonic doped semiconductor nanocrystals: Properties, fabrication, applications and perspectives," *Physics Reports*, vol. 674, pp. 1–52, Feb. 2017.

[87] A. N. Grigorenko, M. Polini, and K. S. Novoselov, "Graphene plasmonics," *Nature Photonics*, vol. 6, pp. 749–758, Nov. 2012.

[88] B. Lee, I.-M. Lee, S. Kim, D.-H. Oh, and L. Hesselink, "Review on subwavelength confinement of light with plasmonics," *Journal of Modern Optics*, vol. 57, pp. 1479–1497, Sept. 2010.

[89] R. B. Jaculbia, H. Imada, K. Miwa, T. Iwasa, M. Takenaka, B. Yang, E. Kazuma, N. Hayazawa, T. Taketsugu, and Y. Kim, "Single-molecule resonance Raman effect in a plasmonic nanocavity," *Nature Nanotechnology*, vol. 15, pp. 105–110, Feb. 2020.

[90] A. N. Koya, J. Cunha, T.-L. Guo, A. Toma, D. Garoli, T. Wang, S. Juodkazis, D. Cojoc, and R. Proietti Zaccaria, "Novel Plasmonic Nanocavities for Optical Trapping-Assisted Biosensing Applications," *Advanced Optical Materials*, vol. 8, no. 7, p. 1901481, 2020.

[91] V. Giannini, A. I. Fernández-Domínguez, S. C. Heck, and S. A. Maier, "Plasmonic Nanoantennas: Fundamentals and Their Use in Controlling the Radiative Properties of Nanoemitters," *Chemical Reviews*, vol. 111, pp. 3888–3912, June 2011.

[92] H. Fischer and O. J. F. Martin, "Engineering the optical response of plasmonic nanoantennas," *Optics Express*, vol. 16, pp. 9144–9154, June 2008.

[93] M. Ghidelli, L. Mascaretti, B. R. Bricchi, A. Zapelli, V. Russo, C. S. Casari, and A. Li Bassi, "Engineering plasmonic nanostructured surfaces by pulsed laser deposition," *Applied Surface Science*, vol. 434, pp. 1064–1073, Mar. 2018.

[94] A. Minopoli, A. Acunzo, B. Della Ventura, and R. Velotta, "Nanostructured Surfaces as Plasmonic Biosensors: A Review," *Advanced Materials Interfaces*, vol. 9, no. 2, p. 2101133, 2022.

[95] K. Yao and Y. Liu, "Plasmonic metamaterials," *Nanotechnology Reviews*, vol. 3, pp. 177–210, Apr. 2014.

[96] A. Christ, O. J. F. Martin, Y. Ekinci, N. A. Gippius, and S. G. Tikhodeev, "Symmetry Breaking in a Plasmonic Metamaterial at Optical Wavelength," *Nano Letters*, vol. 8, pp. 2171–2175, Aug. 2008.

[97] X. Huang and M. El-Sayed, "Gold nanoparticles: Optical properties and implementations in cancer diagnosis and photothermal therapy," *Journal of Advanced Research*, vol. 1, pp. 13–28, Jan. 2010.

[98] S. J. Lee, Z. Guan, H. Xu, and M. Moskovits, "Surface-Enhanced Raman Spectroscopy and Nanogeometry: The Plasmonic Origin of SERS," *The Journal of Physical Chemistry C*, vol. 111, pp. 17985–17988, Dec. 2007.

[99] J. B. Khurgin, "How to deal with the loss in plasmonics and metamaterials," *Nature Nanotechnology*, vol. 10, pp. 2–6, Jan. 2015.

[100] G. Baffou and R. Quidant, "Thermo-plasmonics: using metallic nanostructures as nano-sources of heat: Thermoplasmonics," *Laser & Photonics Reviews*, vol. 7, pp. 171–187, Mar. 2013.

[101] H. H. Richardson, M. T. Carlson, P. J. Tandler, P. Hernandez, and A. O. Govorov, "Experimental and Theoretical Studies of Light-to-Heat Conversion and Collective Heating Effects in Metal Nanoparticle Solutions," *Nano Letters*, vol. 9, pp. 1139–1146, Mar. 2009.

[102] G. Baffou, R. Quidant, and C. Girard, "Thermoplasmonics modeling: A Green's function approach," *Physical Review B*, vol. 82, p. 165424, Oct. 2010.

[103] G. Baffou, F. Cichos, and R. Quidant, "Applications and challenges of thermoplasmonics," *Nature Materials*, vol. 19, pp. 946–958, Sept. 2020.

[104] F. Yi, H. Zhu, J. C. Reed, A. Y. Zhu, and E. Cubukcu, "Thermoplasmonic Membrane-Based Infrared Detector," *IEEE Photonics Technology Letters*, vol. 26, pp. 202–205, Jan. 2014.

[105] M. Essone Mezeme and C. Brosseau, "Engineering nanostructures with enhanced thermoplasmonic properties for biosensing and selective targeting applications," *Physical Review E*, vol. 87, p. 012722, Jan. 2013.

[106] D. Boyer, P. Tamarat, A. Maali, B. Lounis, and M. Orrit, "Photothermal Imaging of Nanometer-Sized Metal Particles Among Scatterers," *Science*, vol. 297, pp. 1160–1163, Aug. 2002.

[107] Z. Li, J. Liu, Y. Zhao, R. Shi, G. I. N. Waterhouse, Y. Wang, L.-Z. Wu, C.-H. Tung, and T. Zhang, "Photothermal hydrocarbon synthesis using alumina-supported cobalt metal nanoparticle catalysts derived from layered-double-hydroxide nanosheets," *Nano Energy*, vol. 60, pp. 467–475, June 2019.

[108] Y. Qi, Z. Yang, Y. Jiang, H. Han, T. Wu, L. Wu, J. Liu, Z. Wang, and F. Wang, "Platinum-Copper Bimetallic Nanoparticles Supported on TiO2 as Catalysts for Photo-thermal Catalytic Toluene Combustion," *ACS Applied Nano Materials*, vol. 5, pp. 1845–1854, Feb. 2022.

[109] S. Santoro, A. H. Avci, A. Politano, and E. Curcio, "The advent of thermoplasmonic membrane distillation," *Chemical Society Reviews*, vol. 51, no. 14, pp. 6087–6125, 2022. Publisher: Royal Society of Chemistry.

[110] A. Politano, P. Argurio, G. Di Profio, V. Sanna, A. Cupolillo, S. Chakraborty, H. A. Arafat, and E. Curcio, "Photothermal Membrane Distillation for Seawater Desalination," *Advanced Materials*, vol. 29, no. 2, p. 1603504, 2017.

[111] D. Ding, H. Wu, X. He, F. Yang, C. Gao, Y. Yin, and S. Ding, "A metal nanoparticle assembly with broadband absorption and suppressed thermal radiation for enhanced solar steam generation," *Journal of Materials Chemistry A*, vol. 9, no. 18, pp. 11241–11247, 2021.

[112] P. Subramanyam, B. Meena, V. Biju, H. Misawa, and S. Challapalli, "Emerging materials for plasmon-assisted photoelectrochemical water splitting," *Journal of Photochemistry and Photobiology C: Photochemistry Reviews*, vol. 51, p. 100472, June 2022.

[113] L. Mascaretti, A. Dutta, S. Kment, V. M. Shalaev, A. Boltasseva, R. Zbořil, and A. Naldoni, "Plasmon-Enhanced Photoelectrochemical Water Splitting for Efficient Renewable Energy Storage," *Advanced Materials*, vol. 31, no. 31, p. 1805513, 2019.

[114] Y. Zhao, L. Sang, and C. Wang, "Thermoplasmonics effect of Au-rGO/TiO2 photoelectrode in solar-hydrogen conversion," *Solar Energy Materials and Solar Cells*, vol. 255, p. 112306, June 2023.

[115] M. Guo, Q. Yu, X. Wang, W. Xu, Y. Wei, Y. Ma, J. Yu, and B. Ding, "Tailoring Broad-Band-Absorbed Thermoplasmonic 1D Nanochains for Smart Windows with Adaptive Solar Modulation," *ACS Applied Materials & Interfaces*, vol. 13, pp. 5634–5644, Feb. 2021.

[116] Q. Yu, M. Guo, W. Xu, X. Shi, Y. Ma, J. Yu, and B. Ding, "Spray-assembly of thermoplasmonic nanoparticles: A speed-up fabrication strategy for energy-saving smart windows," *Solar Energy*, vol. 238, pp. 9–16, May 2022.

[117] F. Pierini, A. Guglielmelli, O. Urbanek, P. Nakielski, L. Pezzi, R. Buda, M. Lanzi, T. A. Kowalewski, and L. De Sio, "Thermoplasmonic-Activated Hydrogel Based Dynamic Light Attenuator," *Advanced Optical Materials*, vol. 8, no. 12, p. 2000324, 2020.

[118] G. Jönsson, D. Tordera, T. Pakizeh, M. Jaysankar, V. Miljkovic, L. Tong, M. P. Jonsson, and A. Dmitriev, "Solar Transparent Radiators by Optical Nanoantennas," *Nano Letters*, vol. 17, pp. 6766–6772, Nov. 2017.

[119] E. M. Purcell and C. R. Pennypacker, "Scattering and Absorption of Light by Nonspherical Dielectric Grains," *The Astrophysical Journal*, vol. 186, p. 705, Dec. 1973.

[120] B. T. Draine and P. J. Flatau, "Discrete-Dipole Approximation For Scattering Calculations," *Journal of the Optical Society of America A*, vol. 11, p. 1491, Apr. 1994.

[121] M. Yurkin and A. Hoekstra, "The discrete dipole approximation: An overview and recent developments," *Journal of Quantitative Spectroscopy and Radiative Transfer*, vol. 106, pp. 558–589, July 2007.

[122] A. D. Rakić, A. B. Djurišić, J. M. Elazar, and M. L. Majewski, "Optical properties of metallic films for vertical-cavity optoelectronic devices," *Applied Optics*, vol. 37, pp. 5271–5283, Aug. 1998.

[123] H. Fredriksson, Y. Alaverdyan, A. Dmitriev, C. Langhammer, D. S. Sutherland, M. Zäch, and B. Kasemo, "Hole–Mask Colloidal Lithography," *Advanced Materials*, vol. 19, no. 23, pp. 4297–4302, 2007.

[124] P. Hanarp, D. S. Sutherland, J. Gold, and B. Kasemo, "Control of nanoparticle film structure for colloidal lithography," *Colloids and Surfaces A: Physicochemical and Engineering Aspects*, vol. 214, pp. 23–36, Mar. 2003.

[125] P. M. Piechulla, L. Muehlenbein, R. B. Wehrspohn, S. Nanz, A. Abass, C. Rockstuhl, and A. Sprafke, "Fabrication of Nearly-Hyperuniform Substrates by Tailored Disorder for Photonic Applications," *Advanced Optical Materials*, vol. 6, no. 7, p. 1701272, 2018.

[126] F. Monticone and A. Alù, "Metamaterial, plasmonic and nanophotonic devices," *Reports on Progress in Physics*, vol. 80, p. 036401, Feb. 2017.

[127] D. Brinks, M. Castro-Lopez, R. Hildner, and N. F. van Hulst, "Plasmonic antennas as design elements for coherent ultrafast nanophotonics," *Proceedings of the National Academy of Sciences*, vol. 110, pp. 18386–18390, Nov. 2013.

[128] A. Habib, X. Zhu, S. Fong, and A. A. Yanik, "Active plasmonic nanoantenna: an emerging toolbox from photonics to neuroscience," *Nanophotonics*, vol. 9, pp. 3805–3829, Sept. 2020.

[129] I. S. Maksymov, "Magneto-plasmonic nanoantennas: Basics and applications," *Reviews in Physics*, vol. 1, pp. 36–51, Nov. 2016.

[130] F. Zang, Z. Su, L. Zhou, K. Konduru, G. Kaplan, and S. Y. Chou, "Ultrasensitive Ebola Virus Antigen Sensing via 3D Nanoantenna Arrays," *Advanced Materials*, vol. 31, no. 30, p. 1902331, 2019.

[131] D. Rodrigo, A. Tittl, A. John-Herpin, O. Limaj, and H. Altug, "Self-Similar Multiresonant Nanoantenna Arrays for Sensing from Near- to Mid-Infrared," *ACS Photonics*, vol. 5, pp. 4903–4911, Dec. 2018.

[132] Y. M. El-Toukhy, M. Hussein, M. F. O. Hameed, A. M. Heikal, M. M. Abd-Elrazzak, and S. S. A. Obayya, "Optimized tapered dipole nanoantenna as efficient energy harvester," *Optics Express*, vol. 24, pp. A1107–A1122, July 2016. Publisher: Optica Publishing Group.

[133] N. F. F. Areed, S. M. El Malt, and S. S. A. Obayya, "Broadband Omnidirectional Nearly Perfect Plasmonic Absorber For Solar Energy Harvesting," *IEEE Photonics Journal*, vol. 8, pp. 1–18, Oct. 2016.

[134] F. Kretschmer, S. Mühlig, S. Hoeppener, A. Winter, M. D. Hager, C. Rockstuhl, T. Pertsch, and U. S. Schubert, "Survey of Plasmonic Nanoparticles: From Synthesis to Application," *Particle & Particle Systems Characterization*, vol. 31, pp. 721–744, July 2014.

[135] X. Lu, M. Rycenga, S. E. Skrabalak, B. Wiley, and Y. Xia, "Chemical Synthesis of Novel Plasmonic Nanoparticles," *Annual Review of Physical Chemistry*, vol. 60, pp. 167–192, May 2009.

[136] E. Ringe, J. Zhang, M. R. Langille, K. Sohn, C. Cobley, L. Au, Y. Xia, C. A. Mirkin, J. Huang, L. D. Marks, and R. P. Van Duyne, "Effect of Size, Shape,

Composition, and Support Film on Localized Surface Plasmon Resonance Frequency: A Single Particle Approach Applied to Silver Bipyramids and Gold and Silver Nanocubes," *MRS Proceedings*, vol. 1208, pp. 1208–O10–02, 2009.

[137] K.-C. Lee, S.-J. Lin, C.-H. Lin, C.-S. Tsai, and Y.-J. Lu, "Size Effect of Ag Nanoparticles on Surface Plasmon Resonance," *Surface & Coatings Technology - SURF COAT TECH*, vol. 202, pp. 5339–5342, Aug. 2008.

[138] G. Baffou, R. Quidant, and C. Girard, "Heat generation in plasmonic nanostructures: Influence of morphology," *Applied Physics Letters*, vol. 94, p. 153109, Apr. 2009.

[139] S. Dodson, M. Haggui, R. Bachelot, J. Plain, S. Li, and Q. Xiong, "Optimizing Electromagnetic Hotspots in Plasmonic Bowtie Nanoantennae," *The Journal of Physical Chemistry Letters*, vol. 4, pp. 496–501, Feb. 2013.

[140] B. Wang, S. C. Singh, H. Lu, and C. Guo, "Design of Aluminum Bowtie Nanoantenna Array with Geometrical Control to Tune LSPR from UV to Near-IR for Optical Sensing," *Plasmonics*, vol. 15, pp. 609–621, June 2020.

[141] N. Pfullmann, C. Waltermann, M. Noack, S. Rausch, T. Nagy, C. Reinhardt, M. Kovačev, V. Knittel, R. Bratschitsch, D. Akemeier, A. Hütten, A. Leitenstorfer, and U. Morgner, "Bow-tie nano-antenna assisted generation of extreme ultraviolet radiation," *New Journal of Physics*, vol. 15, p. 093027, Sept. 2013.

[142] T. Grosjean, M. Mivelle, F. I. Baida, G. W. Burr, and U. C. Fischer, "Diabolo Nanoantenna for Enhancing and Confining the Magnetic Optical Field," *Nano Letters*, vol. 11, pp. 1009–1013, Mar. 2011.

[143] Z. J. Coppens, W. Li, D. G. Walker, and J. G. Valentine, "Probing and Controlling Photothermal Heat Generation in Plasmonic Nanostructures," *Nano Letters*, vol. 13, pp. 1023–1028, Mar. 2013.

[144] P. K. Jain, K. S. Lee, I. H. El-Sayed, and M. A. El-Sayed, "Calculated Absorption and Scattering Properties of Gold Nanoparticles of Different Size, Shape, and Composition: Applications in Biological Imaging and Biomedicine," *The Journal of Physical Chemistry B*, vol. 110, pp. 7238–7248, Apr. 2006.

[145] L. Khosravi Khorashad, L. V. Besteiro, Z. Wang, J. Valentine, and A. O. Govorov, "Localization of Excess Temperature Using Plasmonic Hot Spots in Metal Nanostructures: Combining Nano-Optical Antennas with the Fano Effect," *The Journal of Physical Chemistry C*, vol. 120, pp. 13215–13226, June 2016.

[146] J. Zhou, Y. Wang, L. Zhang, and X. Li, "Plasmonic biosensing based on non-noble-metal materials," *Chinese Chemical Letters*, vol. 29, pp. 54–60, Jan. 2018.

[147] W. Li, K. Ren, and J. Zhou, "Aluminum-based localized surface plasmon resonance for biosensing," *TrAC Trends in Analytical Chemistry*, vol. 80, pp. 486–494, June 2016.

[148] A. Agrawal, R. W. Johns, and D. J. Milliron, "Control of Localized Surface Plasmon Resonances in Metal Oxide Nanocrystals," *Annual Review of Materials Research*, vol. 47, no. 1, pp. 1–31, 2017.

[149] T. M. Mattox, X. Ye, K. Manthiram, P. J. Schuck, A. P. Alivisatos, and J. J. Urban, "Chemical Control of Plasmons in Metal Chalcogenide and Metal Oxide Nanostructures," *Advanced Materials*, vol. 27, no. 38, pp. 5830–5837, 2015.

[150] B. M. Crockett, A. W. Jansons, K. M. Koskela, D. W. Johnson, and J. E. Hutchison, "Radial Dopant Placement for Tuning Plasmonic Properties in Metal Oxide Nanocrystals," *ACS Nano*, vol. 11, pp. 7719–7728, Aug. 2017.

[151] X. Ma, Y. Dai, L. Yu, and B. Huang, "Noble-metal-free plasmonic photocatalyst: hydrogen doped semiconductors," *Scientific Reports*, vol. 4, p. 3986, Feb. 2014.

[152] O. A. Balitskii, "Recent energy targeted applications of localized surface plasmon resonance semiconductor nanocrystals: a mini-review," *Materials Today Energy*, vol. 20, p. 100629, June 2021.

[153] A. Agrawal, S. H. Cho, O. Zandi, S. Ghosh, R. W. Johns, and D. J. Milliron, "Localized Surface Plasmon Resonance in Semiconductor Nanocrystals," *Chemical Reviews*, vol. 118, pp. 3121–3207, Mar. 2018.

[154] M. S. Islam, A. Z. Kouzani, X. J. Dai, W. P. Michalski, and H. Gholamhosseini, "Design and Analysis of a Multilayer Localized Surface Plasmon Resonance Graphene Biosensor," *Journal of Biomedical Nanotechnology*, vol. 8, pp. 380–393, June 2012.

[155] S. Lee, M. h. Lee, H.-j. Shin, and D. Choi, "Control of density and LSPR of Au nanoparticles on graphene," *Nanotechnology*, vol. 24, p. 275702, June 2013.

[156] R. Alharbi, M. Irannejad, and M. Yavuz, "A Short Review on the Role of the Metal-Graphene Hybrid Nanostructure in Promoting the Localized Surface Plasmon Resonance Sensor Performance," *Sensors*, vol. 19, p. 862, Jan. 2019.

[157] R. Jiang, B. Li, C. Fang, and J. Wang, "Metal/Semiconductor Hybrid Nanostructures for Plasmon-Enhanced Applications," *Advanced Materials*, vol. 26, no. 31, pp. 5274–5309, 2014.

[158] S. Khanam and S. K. Rout, "Plasmonic Metal/Semiconductor Heterostructure for Visible Light-Enhanced H2 Production," *ACS Omega*, vol. 7, pp. 25466–25475, July 2022.

[159] C.-c. Jian, J. Zhang, and X. Ma, "Cu–Ag alloy for engineering properties and applications based on the LSPR of metal nanoparticles," *RSC Advances*, vol. 10, no. 22, pp. 13277–13285, 2020.

[160] P. K. Kuiri, "Tailoring localized surface plasmons in Ag–Al alloys' nanoparticles," *Journal of Alloys and Compounds*, vol. 826, p. 154250, June 2020.

[161] A. Bansal, J. S. Sekhon, and S. S. Verma, "Scattering Efficiency and LSPR Tunability of Bimetallic Ag, Au, and Cu Nanoparticles," *Plasmonics*, vol. 9, pp. 143–150, Feb. 2014.

[162] M. Sui, S. Kunwar, P. Pandey, S. Pandit, and J. Lee, "Improved localized surface plasmon resonance responses of multi-metallic Ag/Pt/Au/Pd nanostructures: systematic study on the fabrication mechanism and localized surface plasmon resonance properties by solid-state dewetting," *New Journal of Physics*, vol. 21, p. 113049, Nov. 2019.

[163] N. Zhou, C. Ye, L. Polavarapu, and Q.-H. Xu, "Controlled preparation of Au/Ag/SnO 2 core–shell nanoparticles using a photochemical method and applications in LSPR based sensing," *Nanoscale*, vol. 7, no. 19, pp. 9025–9032, 2015.

[164] J. Deng, J. Du, Y. Wang, Y. Tu, and J. Di, "Synthesis of ultrathin silver shell on gold core for reducing substrate effect of LSPR sensor," *Electrochemistry Communications*, vol. 13, pp. 1517–1520, Dec. 2011.

[165] K. Zhang, Y. Xiang, X. Wu, L. Feng, W. He, J. Liu, W. Zhou, and S. Xie, "Enhanced Optical Responses of Au@Pd Core/Shell Nanobars," *Langmuir*, vol. 25, pp. 1162–1168, Jan. 2009.

[166] A. Trügler, J.-C. Tinguely, J. Krenn, A. Hohenau, and U. Hohenester, "Influence of surface roughness on the optical properties of plasmonic nanoparticles," *Physical Review B*, vol. 83, p. 081412(R), Feb. 2011.

[167] A. V. Kildishev, J. D. Borneman, K.-P. Chen, and V. P. Drachev, "Numerical Modeling of Plasmonic Nanoantennas with Realistic 3D Roughness and Distortion," *Sensors*, vol. 11, pp. 7178–7187, July 2011.

[168] J. González-Colsa, A. Franco, F. Bresme, F. Moreno, and P. Albella, "Janus-Nanojet as an efficient asymmetric photothermal source," *Scientific Reports*, vol. 12, p. 14222, Aug. 2022.

[169] K. Teffah and Y. Zhang, "Modeling and experimental research of hybrid PV-thermoelectric system for high concentrated solar energy conversion," *Solar Energy*, vol. 157, pp. 10–19, Nov. 2017.

[170] G. Li, S. Shittu, X. Ma, and X. Zhao, "Comparative analysis of thermoelectric elements optimum geometry between photovoltaic-thermoelectric and solar thermoelectric," *Energy*, vol. 171, pp. 599–610, Mar. 2019.

[171] S. Shittu, G. Li, X. Zhao, X. Ma, Y. G. Akhlaghi, and Y. Fan, "Comprehensive study and optimization of concentrated photovoltaic-thermoelectric considering all contact resistances," *Energy Conversion and Management*, vol. 205, p. 112422, Feb. 2020.

[172] C. Liu, Y. J. Cui, K. F. Wang, and B. L. Wang, "Interlaminar mechanical performance of a multi-layered photovoltaic-thermoelectric hybrid device," *Applied Mathematical Modelling*, June 2023.

[173] Y.-P. Zhou, M.-J. Li, Y.-L. He, and Y.-S. Li, "Multi-physics analysis: The coupling effects of nanostructures on the low concentrated black silicon photovoltaic system performances," *Energy Conversion and Management*, vol. 159, pp. 129–139, Mar. 2018.

[174] Y.-P. Zhou, M.-J. Li, W.-W. Yang, and Y.-L. He, "The effect of the full-spectrum characteristics of nanostructure on the PV-TE hybrid system performances within multi-physics coupling process," *Applied Energy*, vol. 213, pp. 169–178, Mar. 2018.

[175] Y.-H. Hu, M.-J. Li, Y.-P. Zhou, H. Xi, and T.-C. Hung, "Multi-physics investigation of a GaAs solar cell based PV-TE hybrid system with a nanostructured front surface," *Solar Energy*, vol. 224, pp. 102–111, Aug. 2021.

[176] Y. Park, K. Cho, and S. Kim, "Performance Prediction of Hybrid Energy Harvesting Devices Using Machine Learning," *ACS Applied Materials & Interfaces*, vol. 14, pp. 11248–11254, Mar. 2022.

[177] A. Muzathik, "Photovoltaic Modules Operating Temperature Estimation Using a Simple Correlation," *International Journal of Energy Engineering*, vol. 4, pp. 151–158, Aug. 2014.

[178] S. Odeh and M. Behnia, "Improving Photovoltaic Module Efficiency Using Water Cooling," *Heat Transfer Engineering*, vol. 30, pp. 499–505, May 2009.

[179] O. Dupré, R. Vaillon, and M. A. Green, *Thermal Behavior of Photovoltaic Devices*. Cham: Springer International Publishing, 2017.

[180] F. Krayzel, R. Pollès, A. Moreau, M. Mihailovic, and G. Granet, "Simulation and analysis of exotic non-specular phenomena," *Journal of the European Optical Society - Rapid publications*, vol. 5, June 2010.

[181] A. Shang and X. Li, "Photovoltaic Devices: Opto-Electro-Thermal Physics and Modeling," *Advanced Materials*, vol. 29, no. 8, p. 1603492, 2017.

[182] C. D. Thurmond, "The Standard Thermodynamic Functions for the Formation of Electrons and Holes in Ge, Si, GaAs , and GaP," *Journal of The Electrochemical Society*, vol. 122, pp. 1133–1141, Aug. 1975.

[183] J. C. Fan, "Theoretical temperature dependence of solar cell parameters," *Solar Cells*, vol. 17, pp. 309–315, Apr. 1986.

[184] "Solids, Liquids and Gases - Thermal Conductivities."